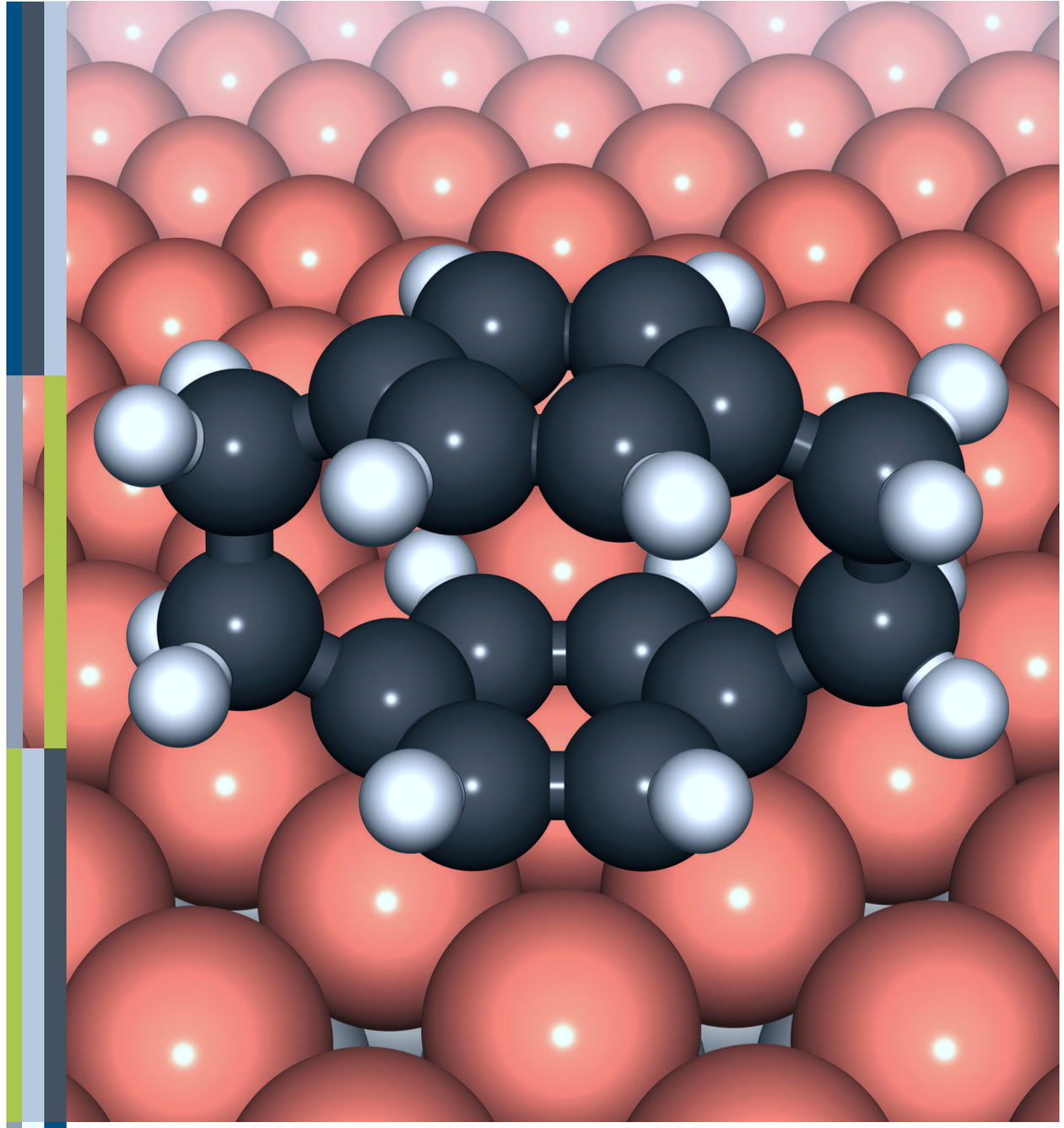

Member of the Helmholtz Association

Ab initio investigations of π-conjugated-molecule-metal interfaces for molecular electronics and spintronics

Martin Callsen

JÜLICH
FORSCHUNGSZENTRUM

Ab initio investigations of π-conjugated-molecule-metal interfaces for molecular electronics and spintronics

Von der Fakultät für Mathematik, Informatik und Naturwissenschaften
der RWTH Aachen University zur Erlangung des akademischen
Grades eines Doktors der Naturwissenschaften genehmigte Dissertation

vorgelegt von

Dipl.-Phys. Martin Callsen

aus Itzehoe

Berichter: Univ.-Prof. Dr. Stefan Blügel
Univ.-Prof. Dr. Arne Lüchow

Tag der mündlichen Prüfung: 26. Mai 2014

Forschungszentrum Jülich GmbH
Peter Grünberg Institute (PGI)
Quantum Theory of Materials (PGI-1 / IAS-1)

Ab initio investigations of π-conjugated-molecule-metal interfaces for molecular electronics and spintronics

Martin Callsen

Schriften des Forschungszentrums Jülich
Reihe Schlüsseltechnologien / Key Technologies Band / Volume 92

ISSN 1866-1777 ISBN 978-3-89336-992-8

Bibliographic information published by the Deutsche Nationalbibliothek.
The Deutsche Nationalbibliothek lists this publication in the Deutsche
Nationalbibliografie; detailed bibliographic data are available in the
Internet at http://dnb.d-nb.de.

Publisher and Distributor: Forschungszentrum Jülich GmbH
Zentralbibliothek
52425 Jülich
Tel: +49 2461 61-5368
Fax: +49 2461 61-6103
Email: zb-publikation@fz-juelich.de
www.fz-juelich.de/zb

Cover Design: Grafische Medien, Forschungszentrum Jülich GmbH

Printer: Grafische Medien, Forschungszentrum Jülich GmbH

Schriften des Forschungszentrums Jülich
Reihe Schlüsseltechnologien / Key Technologies, Band / Volume 92

D 82 (Diss. RWTH Aachen University, 2014)

ISSN 1866-1807
ISBN 978-3-89336-992-8

The complete volume is freely available on the Internet on the Jülicher Open Access Server (JUWEL)
at www.fz-juelich.de/zb/juwel

Kurzfassung

Der stete Wunsch nach Miniaturisierung stellt die konventionelle Elektronik vor eine enorme Herausforderung. Elektronische Bauelemente nach der "bottom up" Strategie zu entwerfen, ist eine viel versprechende Alternative zur weiteren Verkleinerung der bereits etablierten, Silizium basierten Technologie. Als derzeit kleinste vorstellbare Elemente elektronischer Bauteile sind auf Oberflächen adsorbierte Atome und Moleküle im Fokus aktueller Forschung auf dem Gebiet der Molekularelektronik. Weitere Vorteile gegenüber konventioneller Elektronik, wie z.B. ein geringerer Energieverbrauch, verspricht das schnell wachsende Feld der Molekularspintronik, in dem der Ladungsstrom durch einen Spinstrom ersetzt wird. Um neue Bauteile zu entwickeln, ist sowohl für die Molekularelektronik als auch für die Molekularspintronik eine realistische theoretische Modellierung unverzichtbar. Wenn es um die mikroskopische Beschreibung von Grenzflächen zwischen Molekülen und Oberflächen geht, ist Dichtefunktionaltheorie die Methode der Wahl. Für eine realistische Simulation der betrachteten Systeme muss eine angemessene Näherung für das Austausch-Korrelations-Funktional gemacht werden. Gerade bei schwach gebundenen, auf Oberflächen adsorbierten organischen Molekülen, für welche die van der Waals Wechselwirkungen der dominierende Beitrag zur Bindung sind, gelangen verbreitete Näherungen für das Austausch-Korrelations-Funktional an ihre Grenzen. Eine Lösung für dieses Problem zu finden, ist Gegenstand aktueller Forschung.

In dieser Arbeit untersuchen wir die Adsorption π konjugierter Moleküle auf Metall-Oberflächen. Thiophen chemisorbiert schwach auf der Cu(111) Oberfläche, während Cyclooctatetraen auf der Au(111) Oberfläche physisorbiert und auf den (100) Oberflächen von Au, Ag und Cu chemisorbiert. Für all diese Bereiche der Bindungsstärke testen wir neuartige semi-empirische und *ab initio* Formulierungen der bis dato unzureichenden Beschreibung von van der Waals Wechselwirkungen in Dichtefunktionaltheorie. Basierend auf den dabei gewonnenen Erkenntnissen über die Schnittstelle zwischen organischen Molekülen und Metall-Oberflächen bei verschiedenen Bindungsstärken, schlagen wir zwei viel versprechende magnetische Systeme für Anwendungen in der Molekularspintronik vor. Die elektronische Struktur von Cyclooctatetraen adsorbiert auf Übergangsmetall-Adatomen auf der Au(111) Oberfläche zeigt scharfe, Austausch aufgespaltene, Molekülorbital ähnliche Merkmale, welche die Charakteristiken eines Spinfilters erfüllen. Paracyclophan adsorbiert auf der ferromagnetischen Fe/W(110) und der antiferromagnetischen Fe/W(100) Oberfläche ist neben seiner Eigenschaft als Spinfilter ein Beispiel für die Modifikation magnetischer Eigenschaften von Oberflächen durch die Adsorption organischer Moleküle. Insbesondere wird die magnetische Austauschwechselwirkung unter den direkt mit dem Molekül wechselwirkenden Fe Atomen verstärkt, was zu einer Erhöhung des Koerzivitätsfeldes und der Curie-Temperatur führt.

Abstract

The demand for continuous miniaturization of electronic devices poses an enormous challenge to conventional electronics. Instead of further miniaturizing the already established silicon based technology beyond the nanoscale, designing electronic devices by the bottom-up strategy is a promising alternative. As the currently smallest imaginable parts for electronic devices, single atoms or molecules adsorbed on a substrate are the subject of research in the field of molecular electronics. In addition molecular spintronics is a quickly rising field, which promises advantages over electronics like a lower power consumption. In spintronics the charge current is replaced by a spin current. Both molecular electronics and molecular spintronics require a proper theoretical description to design new materials and to propose candidates for future devices. Density functional theory is the method of choice to efficiently describe the molecule surface interfaces under consideration. For a realistic description of the system a suitable approximation for the exchange correlation functional has to be made. In particular for weakly bound organic molecules adsorbed on surfaces common approximations to the exchange correlation functional fail to correctly account for van der Waals interactions, which are in this case the dominant contribution to the binding. To find a correction for this deficiency is still subject of current research.

In this thesis we investigate molecule surface systems of small π conjugated molecules adsorbed on metal surfaces. For thiophene on Cu(111) we find weak chemisorption as binding mechanism while cyclooctatetraene is physisorbed on Au(111) and chemisorbed on the metal (100) surfaces of Au, Ag and Cu. In all these regimes of binding strength we asses semi-empirical and *ab initio* approaches to correct for vdW interactions in DFT. Based on the insights gained about the organic metal interfaces for different molecule surface interaction strengths, we propose two promising magnetic systems for molecular spintronics applications. Cyclooctatetraene adsorbed on magnetic transition metal adatoms on Au(111) shows sharp spin split molecular orbital like features, which are characteristic for a spin filter. Paracyclophane adsorbed on the ferromagnetic Fe/W(110) surface and the antiferromagnetic Fe/W(100) surface in addition to the spin filter characteristics is an example for the modification of the magnetic properties of a surface by the adsorption of organic molecules. In particular the exchange coupling strength between the Fe atoms directly interacting with the molecule is increased, which leads to higher coercivity fields and Curie temperatures of the sample.

Contents

1 Molecular electronics and spintronics: an introduction

Molecular electronics [1–6] and spintronics [7–11] offer both fundamental scientific and technological perspectives. On the technological side, the need for further miniaturization of existing electronic devices is the driving force behind the research dedicated to single molecule electronics [2]. While silicon based electronics has become a nanotechnology in the sense that scales inside devices are now measured in nanometers, there are clear physical limits for a continuing decrease of the size of this kind of conventional electronic devices along Moore's law, due to the increasing importance of quantum effects with decreasing device size [12]. In contrast, molecules are those stable and reproducible ensembles of a small set of atoms that at the moment are considered the smallest possible building blocks for electronic devices. In fact, when the size of conventional electronic devices will be further reduced, the silicon structures forming the electronic devices, which will at that point consist only of a few to several atoms, will just turn into molecular electronic devices [12]. Another idea followed in conventional technologies is spintronics, where the objective is to move away from electric currents using the charge degree of freedom to spin currents using the spin degree of freedom, due to potential advantages over conventional electronics [13] in speed and reduced power consumption. Molecular spintronics combines both streams of thought and implements this new functionalities in devices based on single molecules [11].

But there is only limited technological progress without a thorough comprehension of the fundamental processes occurring in such nanoscale devices. In this theoretical thesis we contribute to the deeper understanding by density functional theory (DFT) simulations. We explore and extend the idea to change the magnetic properties of magnetic materials by the adsorption of molecules with unpaired spins [14] to the adsorption of nonmagnetic π-conjugated organic molecules. In particular, as published in [15], we show that paracyclophane (PCP) adsorbed on Fe/W(110) serves two purposes: (i) it

has the characteristics of a spin filter and (ii) in addition it leads to an increase of the magnetic exchange interaction between those Fe atoms interacting directly with the molecule and thus a local magnetic hardening of the magnetic interactions. This leads to an increase of the coercivity field and the Curie-temperature. For the adsorption of organic molecules on metal substrates van der Waals (vdW) interactions have a large contribution to the binding. Due to the well-known insufficient description of vdW interactions within DFT, we dedicate a part of our study to the assessment of different correction-schemes on suitable molecule surface systems [16, 17].

The thesis is organized in the following way: In the next sections a brief overview about the wide field of molecular electronics will be given and the typical binding mechanisms – physisorption and chemisorption – for ensembles of atoms adsorbed on surfaces will be introduced. After that, molecular spintronics and important definitions of magnetic properties necessary for this thesis will be in the focus of the introduction. In Chapter 2, the theoretical concept of DFT will be introduced, which is the method of choice for an efficient and realistic description of systems relevant for molecular electronics and spintronics. Within this we will point out the known deficiency of DFT in correctly describing vdW interactions. Therefore, we have dedicated Chapter 3 to vdW interactions, describing semi-empirical and *ab initio* approaches how vdW interactions can be included in DFT calculations. From the semi-empirical methods the scheme proposed by S. Grimme [18] referred to as DFT-D and from the *ab initio* methods the vdW density functional following M. Dion *et al.* [19] referred to as vdW-DF will be used for the calculations in this thesis. In Chapter 4, we assess the performance of these methods for thiophene adsorbed on Cu(111), for which extensive experimental data are available for comparison. We also investigate the influence of vdW interactions at different binding strengths for cyclooctatetraene (COT) provided by adsorption on different noble metal surfaces. In Chapter 5 we extend our study to magnetic systems, in particular COT adsorbed on magnetic adatoms on Au(111) and PCP adsorbed on Fe/W(110), relevant for molecular spintronics applications. The Summary concludes the thesis. In the appendices a detailed derivation of the vdW-DF and an efficient scheme for implementation will be given.

1.1. Molecular electronics

The prospect of molecular electronics is to implement electronic devices like wires, transistors and rectifiers by using single molecules. This should be clearly distinguished from organic electronics where thick layers of organic materials replace conventional materials in electronic devices like e.g. organic field effect transistors. However, the latter has been the original use of the term "molecular electronics", which had been brought up to describe a new "bottom up" approach in electronics opposed to the conventional "top down" strategy applied at that time. Instead of implementing electronic functionalities to materials e.g. by lithographically carving nanostructures into a silicon sample the in-

tention was to design new materials, which inherently have the desired properties from the very beginning. If one strictly follows this idea the next consequence is to build electronic devices based on single specifically designed molecules, which implement the dedicated electronic functionality. The information provided in this section has been collected from [1–6].

The first electronic device that uses a single molecule is the molecular rectifier proposed in 1974 by A. Aviram and M. A. Ratner [20] based on semi quantitative independent electron calculations, which later has been experimentally realized [21–25]. The molecular rectifier shown in [20] consists of a donor and an acceptor type molecule connected by a methylene spacer adsorbed between two Au electrodes. The task of the spacer is to separate the molecular orbitals of the donor and the acceptor in order to increase the tunneling barrier between the left electrode and the acceptor and thus suppress superexchange type electron transfer [3]. Then electron or hole hopping becomes the dominant conductance channel. The molecule is adsorbed between two Au electrodes to which an AC bias voltage can be applied. Ideally conduction of electrons through the molecule occurs only in the direction from the donor to the acceptor, which leads to a rectifying ability of the junction. In the experiment done by M. Metzger *et al.* [25] on a Langmuir-Blodgett film[1] of dimethyanilinoaza[C_{60}]fullerene between two Au electrodes an asymmetric conduction behavior for positive and negative voltages has been measured. Although the conductance for the negative voltages has not been zero like it would be in the ideal case, a moderate rectification ratio has been observed. I. Oleynik *et al.* [27] explained based on a model the rectification behavior of diblock oligomers between metal contacts. While the tunneling current is symmetric for a neutral molecule in the resonant tunneling regime, the authors argue that under the influence of the applied bias voltage the wavefunction of the tunneling electron becomes strongly asymmetric [27]. This asymmetry of the wavefunction of the tunneling electrons breaks the symmetry in the tunneling current for electrons tunneling from the left to the right electrode or the opposite way, when the tunneling probabilities to the two electrodes are not equal [27].

For implementing higher order functionalities like logic operations or memory devices in a molecular electronic circuit, the basic part is a molecular switch. A switch is defined as a system with two metastable states, which can reversibly be switched from one to the other and for which both states can be distinguished by for instance their conductive properties. For systems based on nonmagnetic molecules there are mainly two different concepts: the conformational switch and the redox switch. For conformational switching the two required metastable states are two different geometries of a molecule, which can be switched by exciting vibrational modes of the molecule by e.g. electric impulses or light. Examples for conformational molecular switches are dithienylcyclopentene on Au nanoparticles reported by T. Kudernac *et al.* [28] and between two Au electrodes by

[1] A Langmuir-Blodgett film is a monolayer or a few monolayers of organic molecules adsorbed on a substrate after pulling out the solid from or diving it into a liquid [26].

D. Dulić [29], azobenzene adsorbed on Au(111) proposed by B. Choi *et al.* [30], and Zinc-phthalocyanine (ZnPC) adsorbed on Ag(111) shown by Y. Wang *et al.* [31]. The dithienylcyclopentene molecule adsorbed on Au nanoparticles can be switched between a conducting "on" state and a nonconducting "off" state by visible light and back by UV light [28]. When this molecule is adsorbed in a junction between two Au electrodes the reversed switching process does not work [29]. The conformation of azobenzene adsorbed on a Au(111) surface can reversibly be switched between the cis and the trans isomer by tunneling electrons [30]. In a ZnPC molecule the central Zn atom is due to its size shifted away from the molecular plane defined by the rest of the PC molecule. When adsorbed flat on a substrate the Zn atom is either between the molecule and the surface or above the molecule, which can be used to reversibly switch the molecule between these two conformations by applying a bias voltage with the tip of a scanning tunneling microscope (STM) [31]. Arrays of such individually switchable molecules adsorbed on a surface could be used as a memory device.

One of the most important electronic devices in conventional electronics is the transistor as a basic requirement for logic operations with electronics. Hence, there has been a lot of effort to implement a single molecule transistor [32–34]. Besides the molecular rectifier A. Aviram proposed also a field effect transistor (FET) used to implement simple logic functions and amplifiers based on single molecules [32]. The FET consists of two long oligothiophene chains. One molecule is oxidized and thus conducting, while the other is semiconducting. The two chains are linked at the centre by a nonconducting bridge. An electric field applied along the connection of the two oligothiophene chains can switch the conduction across them by allowing electron tunneling [32]. J. S. Tans *et al.* [33] used semiconducting single wall carbon nanotubes contacted to Pt electrodes and an oxidized silicon backgate as a molecular FET operated at room temperature and demonstrated promising high switching speeds. The authors were able to connect a few of these molecular FET devices and have implemented basic logical functions [33]. Recently M. M. Shulaker *et al.* [35] managed to overcome intrinsic problems of the fabrication of carbon nanotube based FETs by a new imperfection-immune design methodology. With their new method the authors were able to build a computer based solely on carbon nanotube FETs. The computer was capable of multitasking which has been demonstrated by simultaneous counting and integer sorting operations. Besides this a set of computing instructions has been implemented to prove the generality of the computer. H. Song *et al.* [34] investigated an octanedithiol molecule and a three terminal active electronic device based on a 1,4-benzenedithiol molecule between two Au electrodes. The molecules together with the two Au electrodes have been adsorbed on an Al_2O_3 contact, which served as the gate electrode. The energies of the molecular orbitals and thus the conductive properties of the 1,4-benzenedithiol molecule within the junction can be tuned by a gate voltage modulation.

To connect molecular electronic devices to each other and to build electric circuits on a molecular level, molecular wires are required in addition. Conductance measurements of alkanedithiols in a Au junction by B. Xu and N. Tao have revealed an exponential

increase of the resistance from 10.5 MΩ to 630 MΩ when going from hexanedithiol to decanedithiol [36]. S. Ho Choi *et al.* showed that for very large conjugated hydrocarbon chains however this exponential dependence is weakened due to a change of the dominant transport mechanism from direct tunneling to hopping [37]. Carbon nanotubes have been proposed early as potential candidates to implement molecular wires. The electric properties of carbon nanotubes have been predicted by N. Hamada *et al.* [38] to vary from semiconducting with moderate gap over semiconducting with a small gap to metallic depending on the diameter of the tubes and their wrapping angle. The concept of using single walled carbon nanotubes as molecular wires has been validated by electron transport measurements of nanotubes connected to Pt contacts on silicon oxide by S. Tans *et al.* [39]. Due to the large degree of conjugation [40] porphyrin oligomers are another promising class of molecules for molecular wires. The size of the porphyrin oligomers is large enough to connect molecular electronic devices at realistic distances of several nm [40]. K. Dongho and A. Osuka [41] found comparably small HOMO-LUMO gaps[2] and oxidation potentials for tape shaped triple fused multiporphyrin arrays, which makes these directly coupled Zn-porphyrin arrays very attractive for potential usage as an efficient molecular wire.

Understanding the interaction of the molecules with the electrodes at the interface is critical for the progress in developing molecular electronics devices. Up to now the choice of the electrodes for particular devices is done based on practical considerations like e.g. the convenient adsorption behavior of thiolate groups on Au substrates [3]. The second equally important point is the appropriate choice of the electronic properties of the interface. Only those combinations of molecules and substrate materials which provide both experimental feasibility and the desired electronic properties are real candidates for future electronic devices. Hence, in addition to improved characterization and construction techniques for molecular electronic devices a reliable theoretical prediction of molecule surface interfaces by means of first-principles calculations to choose appropriate combinations of molecules and electrodes is necessary for future developments.

1.2. Physisorption and chemisorption

When adsorbates like atoms, clusters of atoms or molecules, which are considered as molecular electronic devices, adsorb on surfaces, their binding is classified by the terms physisorption and chemisorption for weak and strong interaction of the adsorbate with the substrate. The distinction is made upon whether there is or there is not a chemical interaction between the adsorbate and the surface. If the adsorbate is bound to the surface by chemical interaction that involves electron sharing, the bonding mechanism is chemisorption. If there is no chemical interaction and no electrostatic interaction due to charge transfer, which leads to ionic binding, the binding mechanism is referred to

[2]The HOMO-LUMO gap is the energy difference between the highest occupied molecular orbital (HOMO) and the lowest unoccupied molecular orbital (LUMO).

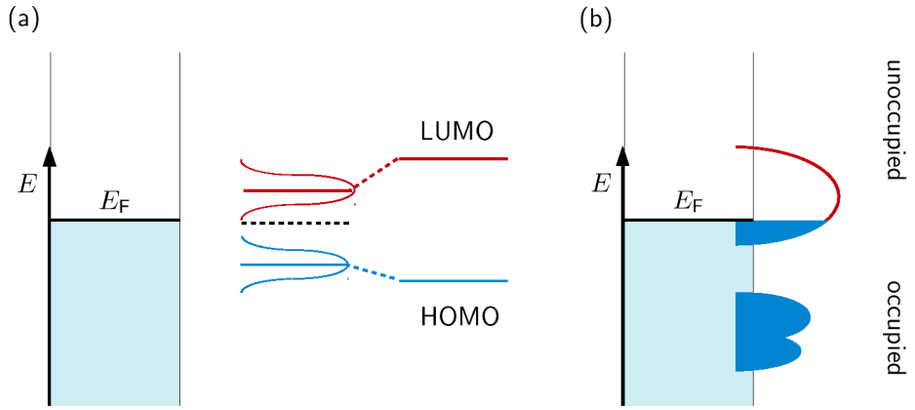

Figure 1.1.: Sketch of the change of the electronic structure of an adsorbate upon physisorption (a) and chemisorption (b) on a substrate. In the case of physisorption the discrete states of the adsorbate align with the substrates Fermi level and the gap between HOMO and LUMO decreases. In the case of chemisorption a new compound with broad hybrid states is formed.

as physisorption. In real systems the binding mechanism lies somewhere in between physisorption and chemisorption.

Starting with physisorption the binding of the adsorbate to the substrate is not due to chemical interaction. This means that the electronic structures of the surface and the adsorbate can be considered in first approximation as almost not affected by the adsorption process and no chemical bond is formed. Thus, in this case it is valid to still speak of atomic or molecular orbitals of the adsorbate after the adsorption on the surface, although in reality a small hybridization of the involved orbitals cannot be avoided. The fingerprint of a physisorption type of bonding is the almost not broadened peak structure in the density of states (DOS) resembling the DOS of the adsorbate in the gas-phase as sketched in Figure 1.1. The energy levels of the adsorbate align with the vacuum level when the molecule and the substrate are well separated [42] or with the Fermi level of the substrate [43]. The gap between the highest occupied and the lowest unoccupied molecular orbital decreases due to dynamical polarization effects [44, 45]. This weak interaction of the adsorbate with the substrate leads to rather small adsorption energies of a few 10 meV for noble gas atoms, $\approx$ 100 meV for small organic molecules and $\approx$ 1 eV for large organic molecules. The adsorption energy however depends on the substrate under investigation and on the size of the adsorbate. In the true physisorption regime without covalent or ionic binding between the substrate and the adsorbate, the van der Waals-forces, which will be subject to the next chapter, are responsible for the binding [46]. In one sentence, the spontaneous fluctuations of the charge density distribution of the adsorbate and the substrate can lead to an attractive interaction even when both of

them are neutral and do not have a permanent multipole moment. Together with the Pauli-repulsion occurring for short distances r the atom-atom interaction potential $V(r)$ for this case can be approximated by the Lennard-Jones-potential:

$$V(r) = \epsilon \left[\left(\frac{r_0}{r} \right)^{12} - 2 \left(\frac{r_0}{r} \right)^{6} \right], \tag{1.1}$$

where ϵ is the depth of the potential well and r_0 the position of the minimum. The exponent of the repulsive term can be chosen differently, but the most common form of the Lennard-Jones-potential uses twelve.

The second limiting case of bonding mechanism is chemisorption, which governs the regime of strong interaction between the adsorbate and the substrate. In this case the adsorbate and the surface chemically interact with each other via strong chemical bonds, which leads to the formation of a new compound. This includes not only the adsorption of molecules or clusters strongly interacting with the surface but also dissociation of the adsorbate together with a strong adsorption of the non desorbing parts [47, 48]. The electronic structure of the newly generated material does not necessarily resemble one of the constituents and the appearance of the density of states is usually dominated by the formation of broad hybrid bands [49, 50]. In the process of forming a chemical bond between the adsorbate and the substrate a charge rearrangement at the adsorbates site takes place and some amount of charge is "transferred" from the surface and the adsorbate between the two components at the interface. Both effects are due to the hybridization of the adsorbate orbitals with those of the substrate. Charge transfer in the usual ionic sense that an electron from the occupied states of the adsorbate or the substrate is transferred to an unoccupied state can occur on top of that. In general, chemisorbed systems have large adsorption energies of a few to several eV even for small adsorbates.

1.3. Molecular spintronics

The development of molecular spintronics as a field of research is in many ways analogue to that of molecular electronics with the main difference that spintronics itself in contrast to conventional electronics is at the beginning and therefore a fast developing field of research. While at the beginning the main focus was on replacing conventional semiconductor materials by organic materials now the direction has changed towards using the particular properties of single molecules for spintronics applications. There is a number of review articles [7–11] which introduce the subject and on which this section is based.

An example of a spintronic device is the spin valve that consists of two ferromagnets separated by a nonmagnetic spacer. The resistance of the spin valve depends on the relative orientation of the magnetization of the two ferromagnetic materials. The change of the devices resistance by applying a magnetic field is called magnetoresistance.

When the two ferromagnets in a spintronic device are separated by a thick nonmagnetic material, tunneling is the main conductance channel of the device. Since the tunneling current depends on the product of the DOS of both ferromagnetic contacts at the Fermi level, which in turn depends on the relative magnetization of the contacts, the resistance of these devices can be changed by external magnetic fields. This is called tunneling magneto resistance (TMR) which has been discovered by M. Jullière [51]. While studying layered Fe-Cr-Fe systems G. Binasch *et al.* [52] and M. N. Baibich *et al.* [53] independently discovered the giant magneto resistance (GMR) effect. Under the assumption that spin flip processes are negligible, the two spin channels can be considered as independent conducting channels [54]. In a device where the current flows perpendicular to the plane of the contact the current injected into the nonmagnetic spacer is polarized, which leads to a finite spin accumulation. The injected spin polarization is largest at the injection point and decays exponentially as a function of the distance to the injection point. If the second ferromagnet is placed at a distance larger than the spin relaxation length, then there will be no spin polarization at the interface. If the second ferromagnetic contact is however placed within the spin relaxation length, the spin polarization at the interface will be finite. When the magnetization of the second contact is parallel to the spin polarization at the interface the transmission of the device is larger than in the anti parallel case [11]. To decide whether tunneling or spin injection with diffusive transport is the dominating transport channel is not straight forward in an organic spintronic device [7]. For tunneling transport the temperature dependence of the conductance is weak, the device area is proportional to the conductance and increasing the thickness of the tunneling barrier leads to an exponential decrease of the conductance [55]. In the spin injection case the conductance is still proportional to the device area, but the temperature and layer thickness dependence of the conductance follows a power law [56].

A. N. Pasupathy *et al.* [57] found TMR ratios larger than predicted by the Jullière formula [51] in a Ni junction containing a C_{60} fullerene molecule. This is explained by the presence of a Kondo resonance in the system which changes its energetic position depending on an applied magnetic field. In the case that the magnetizations of the Ni electrodes are anti parallel the Kondo resonance is closer to the Fermi level, which leads to an enhancement of the conductance and a large negative TMR ratio [57], due to an additionally available tunneling channel. J. R. Petta *et al.* [58] reported transport measurements on a self assembled monolayer of octanethiol adsorbed between two Ni electrodes. They observed spin polarized tunneling and TMR where careful control experiments ensured that TMR is present only in samples containing an octanethiol monolayer [58].

Direct spin injection into and spin transport through a semiconducting organic sexithiophene layer at room temperature has been reported first by V. Dediu *et al.* [59]. The measured long spin lifetimes together with small relaxation lengths due to a low mobility are typical for organic spintronic devices [7]. The observed MR for thin layers disappeared at a thickness of the organic layer larger than 200 nm [59]. In the experi-

ment of Ref. [59] both contacts were made of the same material and thus not individually switchable [59]. Thus, the reported magnetoresistance ratio[3] of 30% is given between a random relative orientation at zero field to a parallel orientation of the ferromagnetic contacts [59]. Z. H. Xiong *et al.* [60] found a GMR effect of 40% at low temperatures for an organic spin valve containing an 8-hydroxy quinoline aluminium (Alq_3) layer, which is comparable to GMR effects measured in metallic devices. At higher temperatures the GMR disappears and instead an high field MR (HFMR) effect occurs, which is increasing with the temperature [60]. In a later experiment the authors replaced the Alq_3 layer by different small molecule or polymer layers [61]. They studied the HFMR effect in more detail and ascribe it to a field dependent carrier injection at the interface between the ferromagnet and the organic layer, which is due to an unusual Fermi level shift in the ferromagnet. In addition to TMR and GMR recently organic magneto resistance for a purely organic semiconductor without ferromagnetic contacts has been observed by T. L. Francis *et al.* [62]. Their device based on polyfluorene sandwiches reaches a magneto resistance of 16% in a field of 10 mT at room temperature [62].

Besides of the great commercial success of GMR based devices for the production of hard disks, research on molecular spintronic devices also goes into the direction of reading, writing and manipulating the orientation of single spins. In a theoretical transport study on a single molecular magnet (SMM) adsorbed on a metal surface and contacted with a STM tip G. Kim and T. Kim [63] put forward the idea of detecting the spin state of the SMM by conductance measurements. R. Vincent *et al.* [64] read the magnetization direction of a single molecular magnet, consisting of a Pc double decker molecule hosting a magnetic Tb atom, within a Au junction. The current flowing through the ligand of the molecule depends on the magnetization direction of the centre Tb atom, which can be altered by an applied magnetic field [64].

1.4. Magnetic exchange and anisotropy

In real magnetic materials at not too large temperatures the orientation of the magnetization is not arbitrary. The individual spins align in certain patterns of which the simplest phase would be the ferromagnetic structure where all magnetic moments point into the same direction. In an antiferromagnetic structure the neighboring magnetic moments have opposite orientations such that the total magnetization of the system is zero. A ferrimagnet is a structure of two ferromagnetic sublattices with different magnetic moments. For these types of magnetic structures the magnetic exchange interaction decides which one is stable. The just mentioned magnetic structures belong to the non exotic class of structures. Higher order terms of magnetic interaction like four spin and Dzaloshinskii-Moriya interactions can lead to the even more complicated

[3] To quantify magnetoresistance the ratio $(R(H) - R(0))/R(0)$ of the resistance $R(H)$ with applied magnetic field H and $R(0)$ without magnetic field is given.

skyrmion structures [65]. In a crystal or at surfaces another quantity, namely the magnetic anisotropy, which determines along which crystal direction the magnetic moments are oriented, adds to the variety of possible magnetic structures. In macroscopic samples the total energy can be reduced by minimization of the internal magnetic field due to the formation of magnetic domains. In the simplest case two neighboring domains have opposite magnetization directions, which, on the expense of exchange interaction at the domain boundaries, reduces the internal magnetic field and thus the total energy. In general, the detailed balance of all the involved interactions and the symmetry of the sample can lead to more diverse domain structures. Between these magnetic domains domain walls occur in which the magnetization direction is continuously rotated from one domains orientation to the neighboring domains orientation. The strength of the magnetic exchange and the magnetic anisotropy determines the size of such domains and domain walls, which in turn is important for the magnetization switching behavior. In this section we will have a brief overview of the Heisenberg model, magnetic exchange and magnetic anisotropy based on a lecture by S. Blügel [66] and the book by R. Skomski [67].

The Hamiltonian of a system of N spins $\mathbf{S}_i$ on a lattice in a magnetic field $\mathbf{H}$ is given by the Heisenberg Hamiltonian with second order magnetocrystalline anisotropy and Zeeman terms:

$$\mathcal{H} = -\frac{1}{2}\sum_{i,j} J_{ij}\mathbf{S}_i\mathbf{S}_j - \sum_i \mathbf{S}_i\mathbf{K}\mathbf{S}_i - \sum_i \mathbf{H}_i\mathbf{S}_i, \tag{1.2}$$

where the sum indices i, j run over all spins in the system, J_{ij} are the magnetic exchange coupling constants between spin i and j, $\mathbf{K}$ is the matrix of magnetic anisotropy constants and $\mathbf{H}_i$ is an external magnetic field acting on the ith spin. The last term favors orientations of the magnetization which are parallel to the external magnetic field. In the following a short discussion of the involved magnetic exchange coupling and magnetic anisotropy contributions will be given.

The contribution of the magnetic exchange term is determined by the relative orientation of two spins i and j. The form of the magnetic exchange term comes from the original Heisenberg-model [68] for a two electron system, where properties of the electron wavefunction like Coulomb repulsion and the Pauli principle are mapped onto a model of spin variables, which do not explicitly include the wavefunctions. The energy difference between the ferromagnetically coupled and the antiferromagnetically coupled system divided by two yields the exchange integral J. The definition of J_{ij} has to be done with care because in the literature there are different versions differing by a factor of two or one half depending on e.g. whether or not a factor stemming from double counting in the sum has been absorbed into J_{ij}. When J_{ij} is positive a parallel alignment of the spins i and j is favored while a negative coupling constant leads to an antiparallel orientation. The exchange coupling constants J_{ij} go to zero as a function of the distance between the spins i and j and thus often only the nearest neighbor contribution is taken into account. The increase of the total energy by the magnetic exchange term when

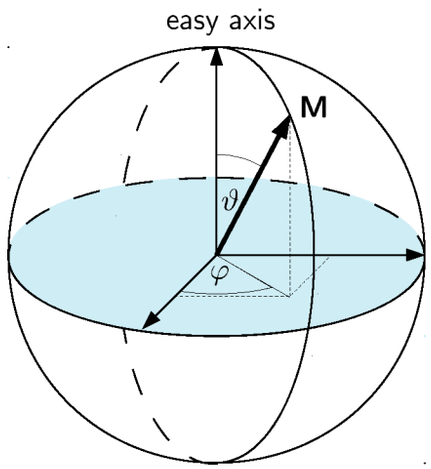

Figure 1.2.: Coordinate system for the definition of the polar and azimuthal angles ϑ and φ with respect to the direction of the magnetic easy-axis. In the magnetic configuration with the lowest energy the magnetization is oriented along the easy-axis.

two neighboring spins are not oriented parallel or antiparallel leads to the formation of domain walls at the domain boundaries as mentioned above. Over the domain wall the deviation from a parallel orientation is adjusted such that the loss of total energy due to the rotation of spins from one domains orientation to the others is minimized. From the quantum mechanical point of view the magnetic exchange term in Equation 1.2 is only an approximation. The magnetic exchange coupling constant is in general a tensor which also allows an extension of the model to anisotropic magnetic exchange. In this thesis we will restrict the considerations to isotropic magnetic exchange interactions.

The magnetic anisotropy determines the orientation of the magnetization within a sample with respect to the crystal directions. There are two different contributions: the shape anisotropy and the magnetocrystalline anisotropy. The shape anisotropy is responsible for the orientation of the magnetization with respect to the shape of the magnetic sample. For nonspherical geometries of the sample the magnetic dipole interactions lead to a preference of a certain magnetization direction. The magnetocrystalline anisotropy is an intrinsic property of the material under consideration due to spin orbit coupling. It determines how the magnetization is oriented with respect to the crystal directions of the material. The magnetocrystalline anisotropy branches again into bulk and surface anisotropy of which the second one is usually dominant in cubic crystals [67]. In this thesis only thin layers consisting of one or two monolayers of magnetic material will be considered. Thus, we will neglect the bulk anisotropy. It has been shown [69] that the Gibbs free energy density for the magnetocrystalline anisotropy can be expanded in a

power series of of the components of the magnetization direction $\mathbf{M} = (\alpha_1, \alpha_2, \alpha_3)$:

$$G(T, H_{\mathbf{M}}, \mathbf{M}) = K_0 + \sum_{\mu} K_\mu \alpha_\mu + \sum_{\mu,\nu} K_{\mu\nu} \alpha_\mu \alpha_\nu + \sum_{\mu,\nu,\tau} K_{\mu\nu\tau} \alpha_\mu \alpha_\nu \alpha_\tau + \ldots \tag{1.3}$$

where T is the temperature and $H_{\mathbf{M}}$ is the external magnetic field projected onto to magnetization direction $\mathbf{M}$. Depending on the symmetry of the crystal only specific terms from this power series do not vanish. Of importance for this thesis are expressions for the bcc (110) and fcc (111) surfaces and for the bcc (100) surface. With the direction of the magnetization $\mathbf{M} = (\sin\vartheta \sin\varphi, \sin\vartheta \cos\varphi, \cos\vartheta)$ the terms for the second order magnetocrystalline anisotropy in Equation 1.2 as a function of the polar angle ϑ and the azimuthal angle φ are $K_1 \sin^2\vartheta + K_1' \cos 2\varphi \sin^2\vartheta$ and $K_1 \sin^2\vartheta$. Within the coordinate system shown in Figure 1.2 these angles are defined with respect to the easy-axis which is the magnetization direction with the lowest total energy.

2 Density functional theory

In this chapter the necessary theoretical concepts used in this thesis will be introduced. The starting point is the formulation of the full quantum-mechanical many-body problem by the Schrödinger-equation (SGE). The dynamics of a quantum mechanical system of N_I ions and N_e electrons is described by the in general time-dependent SGE in atomic units ($\hbar = m_\mathrm{e} = e = 1$):

$$i\frac{\partial}{\partial t}\psi(\mathbf{r},\mathbf{R},t) = \hat{H}\,\psi(\mathbf{r},\mathbf{R},t) \tag{2.1}$$

where $\mathbf{r} = \{\mathbf{r}_i\}$ and $\mathbf{R} = \{\mathbf{R}_I\}$ are shorthand notations for the sets of coordinates of the N_I ions and N_e electrons on which the many-body wavefunction $\psi(\mathbf{r},\mathbf{R},t)$ depends[1]. The Hamiltonian $\hat{H}$ has the form

$$\hat{H} = -\sum_I \frac{1}{2M_I}\nabla_I^2 - \sum_i \frac{1}{2}\nabla_i^2 + \sum_{I<J}\frac{Z_I Z_J}{|\mathbf{R}_I - \mathbf{R}_J|} + \sum_{I,i}\frac{-Z_I}{|\mathbf{R}_I - \mathbf{r}_i|} + \sum_{i<j}\frac{1}{|\mathbf{r}_i - \mathbf{r}_j|}. \tag{2.2}$$

$$= \hat{T}_I + \hat{H}_e \tag{2.3}$$

In this equation the derivatives ∇_I and ∇_i are with respect to the I-th ion coordinate $\mathbf{R}_I$ and the i-th electron coordinate $\mathbf{r}_i$ respectively and Z_I is the atomic number of the corresponding ion. As the mass of the electrons and the ions differs by orders of magnitude and thus the electrons follow the ions instantaneously it is tempting to solve Equation 2.1 in two distinct steps. First one has to find the solutions $\phi_{\mu,\mathbf{R}}(\mathbf{r})$ of the time independent SGE for N_e electrons in a stationary background potential caused by the ions:

$$\hat{H}_e\phi_{\mu,\mathbf{R}}(\mathbf{r}) = U_\mu\,(\mathbf{R})\,\phi_{\mu,\mathbf{R}}(\mathbf{r}), \tag{2.4}$$

[1] This is actually the only place in the Thesis where this convention is needed due to simplicity. Later on, when the system is simplified to single particle equations $\mathbf{r}$ and $\mathbf{R}$ denote the usual three dimensional spatial coordinates.

where $U_\mu(\mathbf{R})$ are the eigenvalues for a fixed set of positions $\mathbf{R}$ of the ions and μ is a state index with zero denoting the ground state. The electronic wavefunction depends parametric on the positions $\mathbf{R}$ of the ions. The set of solutions $\phi_{\mu,\mathbf{R}}(\mathbf{r})$ is complete and thus allows for expanding the full wavefunction $\psi(\mathbf{r},\mathbf{R})$ in terms of the electronic wavefunctions $\phi_{\mu,\mathbf{R}}(\mathbf{r})$ which results in $\psi(\mathbf{r},\mathbf{R}) = \sum_\nu \chi_\nu(\mathbf{R})\phi_{\nu,\mathbf{R}}(\mathbf{r})$. The expansion coefficients $\chi_\nu(\mathbf{R})$ which are the ionic wavefunctions can be obtained by inserting the expansion in Equation 2.1:

$$
\begin{aligned}
i\frac{\partial}{\partial t}\sum_\nu \chi_\nu(\mathbf{R},t)\phi_{\nu,\mathbf{R}}(\mathbf{r}) &= \hat{H}\sum_\nu \chi_\nu(\mathbf{R},t)\phi_{\nu,\mathbf{R}}(\mathbf{r}) && (2.5)\\
&= \left(\hat{T}_I + \hat{H}_e\right)\sum_\nu \chi_\nu(\mathbf{R},t)\phi_{\nu,\mathbf{R}}(\mathbf{r}) && (2.6)\\
&= \hat{T}_I\sum_\nu \chi_\nu(\mathbf{R},t)\phi_{\nu,\mathbf{R}}(\mathbf{r}) + \sum_\nu \chi_\nu(\mathbf{R},t)U_\nu(\mathbf{R})\,\phi_{\nu,\mathbf{R}}(\mathbf{r}) && (2.7)
\end{aligned}
$$

If we now multiply from the left with $\phi_{\mu,\mathbf{R}}(\mathbf{r})$ and integrate over the electron coordinate $\mathbf{r}$ we end up due to the orthogonality of the solutions of the electronic problem with a time dependent SGE for the ionic wavefunctions $\chi_\mu(\mathbf{R},t)$:

$$
i\frac{\partial}{\partial t}\chi_\mu(\mathbf{R},t) = \sum_\nu \int \mathrm{d}^3\mathbf{r}\,\phi_{\mu,\mathbf{R}}(\mathbf{r})\,\hat{T}_I\,\phi_{\nu,\mathbf{R}}(\mathbf{r})\,\chi_\nu(\mathbf{R},t) + U_\mu(\mathbf{R})\,\chi_\mu(\mathbf{R},t). \qquad (2.8)
$$

The integral term on the right hand side contains vibronic coupling between different states μ,ν. When solving this equation usually only the diagonal terms $\mu = \nu$ are considered as the second step after the solution of the electronic problem. This simplification is called the Born-Oppenheimer approximation [70]. By neglecting the vibronic coupling the system once in the ground state $\mu = 0$ will always stay in the ground state.

To proceed with the first step we first have to solve the electronic part of the problem. Unfortunately an exact analytic solution of Equation 2.4 is known only for a small set of simple special cases. For this reason a variety of computational methods to treat the problem numerically has been developed. In quantum chemistry full configuration interaction (CI) [71] is the state of the art technique to numerically solve the SGE. The many-body wavefunction is expanded in a basis of Slater determinants. The eigenvalues of the Hamiltonian can then be obtained by matrix diagonalization. Quantum Monte Carlo (QMC) is a complete class of computational methods where the desired physical quantity is expressed as a high dimensional integral of the many-body wavefunction which then can be approximately solved by Monte Carlo integration [72, 73]. The statistical error of these methods can be reduced just by increasing the simulation time without the need to infer higher order approximations. From many body perturbation theory the Green's function method can be derived [74]. The Green's function of a system introduced formally as the solution to the differential equation given by the SGE can be calculated in a perturbation series in order to predict physical quantities. All of

the just mentioned methods have in common that they are very demanding in terms of computation and are thus restricted to "smaller" systems even on modern computers. In this case "smaller" means a few atoms in the case of CI and maybe 10^2 for Green's function methods. When the adsorption of organic molecules adsorbed on metal surfaces is considered, for which system sizes reach easily a few 10^2 atoms, one has to look for a less demanding method.

One way to treat Equation 2.1 numerically for in the sense of the last paragraph large systems is the framework of density functional theory (DFT) based on the Nobel prize awarded theorems of Hohenberg and Kohn [75]. DFT is in quantum mechanics used in the formulation of Kohn and Sham [76] which maps the fully interacting many-body system on a set of non interacting spin half particles. By this the numerical effort will be reduced to the solution of a set of single particle equations. It will be shown how this works and which prize one has to pay for the simplification i.e. by choosing an appropriate approximated functional to describe exchange and correlation. The numerical solution of the Kohn-Sham equations will be done by using the VASP-code [77–79] for which basic concepts of its implementation will be provided.

2.1. Basics of DFT

There is a large number of numerical methods to calculate the electronic ground state of a system following the Ritz principle

$$E_0 = \min_{\langle\psi|\psi\rangle=1} \langle\psi| \hat{H} |\psi\rangle \leq \min_{\langle\psi_T|\psi_T\rangle=1} \langle\psi_T| \hat{H} |\psi_T\rangle . \tag{2.9}$$

This states that the ground state energy E_0 of a system equals the minimal expectation value of the Hamiltonian $\hat{H}$ when the minimization includes all possible wavefunctions ψ. Unfortunately in reality one is restricted to give only an upper limit for E_0 as only a confined set of trial wavefunctions ψ_T is available for evaluation.

Another point is that for the minimization the full many body wavefunction has to be used, which makes the process highly inefficient. Without even starting a calculation just providing the memory to store the information for the wavefunction of hundreds of electrons on a sufficiently dense grid in an appropriate simulation cell is already a demanding task[2]. If one is only interested in the ground state energy E_0 the many body wavefunction contains way too much information. A way to make the minimization problem Equation 2.9 more efficient is offered by density functional theory in the formulation of Hohenberg and Kohn [75]. It is formulated by the two famous Hohenberg-

[2] The storage space required to store the data of the many body wavefunction, which goes with the number of grid points to the power of the number of electrons, easily reaches astronomical dimensions even when considering a, in the prospect of this thesis, relatively small system of 10 electrons on a $100 \times 100 \times 100$ grid. With 16 Bytes required per entry of a double complex Fortran array and a storage density of ≈ 1 TB/cm^2 the required hard disk would not fit into the solar system.

Kohn-theorems which have been generalized under certain restrictions by Runge and Gross [80] to the time dependent case (TDDFT).

The ground state energy of a system with N_e electrons is according to the first Hohenberg-Kohn-theorem (HK I) a functional $E_0[n]$ of the density $n(\mathbf{r})$. In the accompanying proof [75] it is shown that there is a bijective mapping between ground state densities $n(\mathbf{r})$ and a, up to an additive constant, unique one body potential $v(\mathbf{r})$. This one body potential then defines a SGE from which, by solving it, the ground state energy can be obtained. This allows to define the so called Hohenberg-Kohn-functional

$$F_{HK}[n] := E_0[n] - \int \mathrm{d}^3\mathbf{r}\, v([n], \mathbf{r})\, n(\mathbf{r}) \tag{2.10}$$

where $v([n], \mathbf{r})$ is the one body external potential related to $n(\mathbf{r})$ via HK I. Let $|\Phi\rangle$ be the ground state wavefunction, then F_{HK} can be expressed as the ground state expectation value

$$F_\mathrm{HK} = \langle\Phi|\hat{T} + \hat{V} + \hat{W}|\Phi\rangle - \langle\Phi|\hat{V}|\Phi\rangle = \langle\Phi|\hat{T} + \hat{W}|\Phi\rangle \tag{2.11}$$

of the kinetic energy operator $\hat{T}$, the potential energy operator $\hat{V}$ and the coulomb interaction operator $\hat{W}$ between the electrons. Thus, F_HK is the sum of the expectation values of the kinetic energy and the coulomb interaction. By this one can define an additional functional:

$$E_v[n] := F_\mathrm{HK}[n] + \int \mathrm{d}^3\mathbf{r}\, v(\mathbf{r})\, n(\mathbf{r}) \tag{2.12}$$

This functional does in contrast to F_HK not only depend on the density $n(\mathbf{r})$ but also on a one body external potential $v(\mathbf{r})$, which is not necessarily the by HK I to $n(\mathbf{r})$ corresponding potential. We arrive now at the second theorem of Hohenberg and Kohn (HK II) which is basically a reformulation of Ritz principle in terms of density functionals:

$$E_{v_0}[n] \geq E_{v_0}[n_0] = E_0[n_0]\ , \tag{2.13}$$

where $n(\mathbf{r})$ is an arbitrary one particle density, n_0 is the ground state density and v_0 is the to n_0 corresponding external potential. The ground state energy is the minimum of a density dependent functional. The necessary minimization of the expectation value of the Hamiltonian to find the systems ground state with respect to all possible many body wavefunctions has been reformulated to a minimization of a functional with respect to one body densities which is a huge gain in terms of efficiency.

The minimization of $E_v[n]$ follows the idea proposed by Kohn and Sham [76] to map the fully interacting system onto a non interacting system with the same density $n(\mathbf{r})$. For both systems the considerations made up to now hold true such that one can write down the energy functional $E_{\tilde{v}}^\mathrm{KS}[n]$ for the non interacting system, the so called Kohn-Sham-system (KS):

$$E_{\tilde{v}}^\mathrm{KS}[n] = T_\mathrm{S}[n] + \int \mathrm{d}^3\mathbf{r}\, \tilde{v}(\mathbf{r})\, n(\mathbf{r}) \tag{2.14}$$

In this case T_S replaces F_HK, as in the Kohn-Sham-system the interaction vanishes by definition. The same can be done for the interacting system, where all contributions to the interaction, which can be calculated by available analytic terms are written down explicitly. The remaining part will be called or more precise be hidden in the exchange-correlation-functional $E_\mathrm{xc}[n]$, which is implicitly defined by the following equation for the energy functional $E_v[n]$ of the fully interacting system

$$E_v[n] = T_\mathrm{S}[n] + \int \mathrm{d}^3\mathbf{r}\, v(\mathbf{r})\, n(\mathbf{r}) + \int \mathrm{d}^3\mathbf{r}\, \mathrm{d}^3\mathbf{r}' \frac{n(\mathbf{r})\, n(\mathbf{r}')}{|\mathbf{r}-\mathbf{r}'|} + E_\mathrm{xc}[n] \tag{2.15}$$

The minimization of $E_v[n]$ with respect to $n(\mathbf{r})$ will be done under the constraint that an integration of the density $n(\mathbf{r})$ over the full space $\mathbf{r}$ conserves the total number of particles N, which will be ensured by a Lagrange multiplier μ. With this the variational problem has the form:

$$\frac{\delta}{\delta n(\mathbf{r})} \left\{ E_v[n] - \mu \int \mathrm{d}^3\mathbf{r}\, n(\mathbf{r}) \right\}\Bigg|_{n_0} = 0 \tag{2.16}$$

Inserting the expression for $E_v[n]$ leads to

$$\int \mathrm{d}^3\mathbf{r} \left(\frac{\delta T_S[n]}{\delta n(\mathbf{r})}\bigg|_{n_0} + v(\mathbf{r}) + v_H(\mathbf{r}) + v_{xc}(\mathbf{r}) - \mu \right) \delta n(\mathbf{r}) = 0, \tag{2.17}$$

if one uses the following definitions of the Hartree potential $v_\mathrm{H}(\mathbf{r})$ and the exchange correlation potential $v_\mathrm{xc}(\mathbf{r})$

$$v_\mathrm{H}(\mathbf{r}) = \int \mathrm{d}^3\mathbf{r}'\, \frac{n_0(\mathbf{r}')}{|\mathbf{r}-\mathbf{r}'|} \tag{2.18}$$

$$v_\mathrm{xc}(\mathbf{r}) = \frac{\delta E_\mathrm{xc}[n]}{\delta n(\mathbf{r})}\bigg|_{n_0} \tag{2.19}$$

The consideration that the variation of the density $\delta n(\mathbf{r})$ is arbitrary except for the conservation of the particle number, i.e. $\int \mathrm{d}^3\mathbf{r}\, \delta n(\mathbf{r}) = 0$ holds, leads to the equation:

$$\frac{\delta T_\mathrm{S}[n]}{\delta n(\mathbf{r})}\bigg|_{n_0} + v(\mathbf{r}) + v_\mathrm{H}(\mathbf{r}) + v_\mathrm{xc}(\mathbf{r}) = \mu \tag{2.20}$$

This calculus can be repeated for the non interacting KS system and one obtains:

$$\frac{\delta T_\mathrm{S}[n]}{\delta n(\mathbf{r})}\bigg|_{n_0} + \tilde{v}(\mathbf{r}) = \mu \tag{2.21}$$

Equations 2.20 and 2.21 are identical, when $\tilde{v}(\mathbf{r}) = v(\mathbf{r}) + v_H(\mathbf{r}) + v_\mathrm{xc}(\mathbf{r})$ is chosen. With this particular choice the potential $\tilde{v}(\mathbf{r})$ is usually referred to as the effective or the Kohn-Sham potential.

The ground state density $n_0(\mathbf{r})$ of an interacting many particle system can thus be determined by the self-consistent solution of the Kohn-Sham-equations

$$-\frac{1}{2}\nabla^2\,\phi_i(\mathbf{r}) + \tilde{v}(\mathbf{r})\phi_i(\mathbf{r}) = \epsilon_i\phi_i(\mathbf{r}), \tag{2.22}$$

where $\phi_i(\mathbf{r})$ with $n(\mathbf{r}) = \sum_i f_i\,|\phi_i(\mathbf{r})|^2$ are the eigen functions of a system of non interacting fermions in the potential $\tilde{v}(\mathbf{r}) = v(\mathbf{r}) + v_{\mathrm{H}}(\mathbf{r}) + v_{\mathrm{xc}}(\mathbf{r})$, ϵ_i are the corresponding eigen values, and f_i are their occupation numbers.

2.2. Extension to the spin-polarized case

Up to now the introduced theoretical framework does not consider spin. As the focus of the thesis is also on magnetic systems, an extension to the spin polarized density functional theory will be given.

In the extension to spin polarized systems by von Barth and Hedin [81] the scalar density $n(\mathbf{r})$ is replaced by a Hermitian 2×2 matrix $\mathbf{n}(\mathbf{r})$. The same happens to the external potential $v(\mathbf{r})$ which also becomes a 2×2 matrix

$$\mathbf{n}(\mathbf{r}) = \begin{pmatrix} n^{\uparrow\uparrow}(\mathbf{r}) & n^{\uparrow\downarrow}(\mathbf{r}) \\ n^{\downarrow\uparrow}(\mathbf{r}) & n^{\downarrow\downarrow}(\mathbf{r}) \end{pmatrix} \tag{2.23}$$

$$\mathbf{v}(\mathbf{r}) = \begin{pmatrix} v^{\uparrow\uparrow}(\mathbf{r}) & v^{\uparrow\downarrow}(\mathbf{r}) \\ v^{\downarrow\uparrow}(\mathbf{r}) & v^{\downarrow\downarrow}(\mathbf{r}) \end{pmatrix} \tag{2.24}$$

$$n^{\alpha\beta}(\mathbf{r}) = \langle\Psi|\,\psi^{+}_{\alpha}(\mathbf{r})\psi_{\beta}(\mathbf{r})\,|\Psi\rangle \tag{2.25}$$

where $n^{\alpha\beta}(\mathbf{r})$ are the components of the density matrix $\mathbf{n}(\mathbf{r})$ (α and β can take the values $\uparrow$ and $\downarrow$) and $\psi^{(+)}_{\alpha}(\mathbf{r})$ is the creation or annihilation operator of a spin α particle at $\mathbf{r}$ respectively. The density matrix $\mathbf{n}(\mathbf{r})$ can be rewritten in terms of a charge density $n(\mathbf{r})$ and a 3-component vector spin density $\mathbf{m}(\mathbf{r})$ by

$$\mathbf{n}(\mathbf{r}) = n(\mathbf{r}) \cdot \mathbf{1} + \mathbf{m}(\mathbf{r}) \cdot \boldsymbol{\sigma} \tag{2.26}$$

where $\mathbf{1}$ is the 2×2 unity matrix and $\boldsymbol{\sigma}$ is the 3-component vector of Pauli matrices

$$\sigma_x = \begin{pmatrix} 0 & 1 \\ 1 & 0 \end{pmatrix}, \quad \sigma_y = \begin{pmatrix} 0 & -i \\ i & 0 \end{pmatrix}, \quad \sigma_z = \begin{pmatrix} 1 & 0 \\ 0 & -1 \end{pmatrix} \tag{2.27}$$

The total energy of the system is now a functional of the density matrix $\mathbf{n}(\mathbf{r})$:

$$E\,[\mathbf{n}] = T_{\mathrm{S}}\,[\mathbf{n}] + \sum_{\alpha\beta}\int \mathrm{d}^3\mathbf{r}\, v^{\alpha\beta}(\mathbf{r})\, n^{\alpha\beta}(\mathbf{r}) + \int \mathrm{d}^3\mathbf{r}\,\mathrm{d}^3\mathbf{r}'\frac{n(\mathbf{r})\,n(\mathbf{r}')}{|\mathbf{r}-\mathbf{r}'|} + E_{\mathrm{xc}}\,[\mathbf{n}] \tag{2.28}$$

As before in the unpolarized case of Equation 2.22 the variational principle leads us to the KS-equations which including spin have the form

$$\left[\left(-\frac{1}{2}\nabla^2 + \sum_\alpha \int \mathrm{d}^3\mathbf{r}' \frac{n^{\alpha\alpha}(\mathbf{r}')}{|\mathbf{r}-\mathbf{r}'|}\right)\mathbf{1} + \mathbf{v}(\mathbf{r}) + \frac{\delta E_{\mathrm{xc}}}{\delta \mathbf{n}(\mathbf{r})}\right]\begin{pmatrix}\phi_i^\uparrow(\mathbf{r})\\ \phi_i^\downarrow(\mathbf{r})\end{pmatrix} = \epsilon_i \begin{pmatrix}\phi_i^\uparrow(\mathbf{r})\\ \phi_i^\downarrow(\mathbf{r})\end{pmatrix}. \tag{2.29}$$

By construction the density of the real system equals the density of the KS-system. Thus, we can calculate the density matrix from the KS-orbitals $\phi_i^\alpha(\mathbf{r})$ by summing over all occupied states

$$n^{\alpha\beta}(\mathbf{r}) = \sum_{\substack{i \\ \epsilon_{i\alpha},\epsilon_{i\beta}\leq E_\mathrm{F}}} \phi_i^{\alpha\,*}(\mathbf{r})\phi_i^\beta(\mathbf{r}) \qquad \alpha,\beta = \uparrow,\downarrow \tag{2.30}$$

Like the density matrix in Equation 2.26 we can split the two potentials $v(\mathbf{r})$ and $v_{\mathrm{xc}}(\mathbf{r})$ into a scalar part and a three component vector which in case of the external potential is simply the applied external magnetic field $\mathbf{B}(\mathbf{r})$. For the xc-potential we obtain an xc-magnetic field $\mathbf{B}_{\mathrm{xc}}(\mathbf{r})$ in the following way:

$$v_{\mathrm{xc}}^{\alpha\beta} = \frac{\delta E_{\mathrm{xc}}}{\delta n^{\alpha\beta}(\mathbf{r})} = \frac{\delta E_{\mathrm{xc}}}{\delta n(\mathbf{r})}\frac{\delta n(\mathbf{r})}{\delta n^{\alpha\beta}(\mathbf{r})} + \frac{\delta E_{\mathrm{xc}}}{\delta \mathbf{m}(\mathbf{r})}\cdot\frac{\delta \mathbf{m}(\mathbf{r})}{\delta n^{\alpha\beta}(\mathbf{r})} = \frac{\delta E_{\mathrm{xc}}}{\delta n(\mathbf{r})}\delta^{\alpha\beta} + \frac{\delta E_{\mathrm{xc}}}{\delta \mathbf{m}(\mathbf{r})}\cdot\boldsymbol{\sigma}^{\alpha\beta}, \tag{2.31}$$

where we have used that the derivative of the charge density $n(\mathbf{r})$ with respect to the density matrix elements $n^{\alpha\beta}(\mathbf{r})$ is $\delta^{\alpha\beta}$ and the derivative of the magnetization density $\mathbf{m}(\mathbf{r})$ is $\boldsymbol{\sigma}^{\alpha\beta}$.

$$\mathbf{v}(\mathbf{r}) = v(\mathbf{r})\,\mathbf{1} + \mu_B\,\boldsymbol{\sigma}\cdot\mathbf{B}(\mathbf{r}) \qquad \mathbf{v}_{xc}(\mathbf{r}) = v_{xc}(\mathbf{r})\,\mathbf{1} + \mu_B\,\boldsymbol{\sigma}\cdot\mathbf{B}_{xc}(\mathbf{r}) \tag{2.32}$$

Equation 2.29 is capable of describing the general case of a non collinear arrangement of spins within DFT. In the case of collinear arranged magnetic moments the occurring matrices become diagonal and Equation 2.29 decouples into two separate equations

$$\begin{aligned}\left(-\frac{1}{2}\nabla^2 + v_H(\mathbf{r}) + v^\uparrow(\mathbf{r}) + v_{xc}^\uparrow(\mathbf{r})\phi_i^\uparrow(\mathbf{r})\right) &= \epsilon_i^\uparrow\phi_i^\uparrow(\mathbf{r})\\ \left(-\frac{1}{2}\nabla^2 + v_H(\mathbf{r}) + v^\downarrow(\mathbf{r}) + v_{xc}^\downarrow(\mathbf{r})\phi_i^\downarrow(\mathbf{r})\right) &= \epsilon_i^\downarrow\phi_i^\downarrow(\mathbf{r})\end{aligned} \tag{2.33}$$

for the spin-↑- and the spin-↓-component. The xc-potentials $v_{xc}^\uparrow, v_{xc}^\downarrow$ are in this case the derivatives of the xc-functional with respect to the spin-↑- and spin-↓-density. Both equations can be solved independently, thus the computational cost of spin polarized calculations compared to non polarized calculations grows only by a factor of two.

2.3. Spin-Orbit-Coupling

Up to this point the presented formalism will yield no energy difference depending on the orientation of the spins in the case of all spins aligned collinear due to the choice of the quantization axis being arbitrary. In order to calculate MAE we have to include spin orbit coupling into the formalism of DFT to add an orientation of spins dependence to the total energy. In order to do so it would be necessary to use fully relativistic DFT [82] which generalizes the above derived theorems to functionals of four-currents j^μ and 4 component vector potentials. It is however possible to derive single particle Dirac equations which otherwise adopt the form of Equation 2.29 [83]. To achieve this a spin orbit coupling Hamiltonian

$$H_{\mathrm{SOC}} = \frac{1}{r}\frac{\partial V(r)}{\partial r}\,\boldsymbol{\sigma}\cdot\mathbf{L} \tag{2.34}$$

has to be added, where $\mathbf{L} = \mathbf{r}\times\mathbf{v}$ is the angular momentum of the electrons and $V(r)$ the radial potential of the ions in which the electrons are moving. This radial potential of the ions acts like a magnetic field on the moving electrons which couples to their magnetic moment and thus a certain orientation of the electrons magnetic moments gets energetically favored. The inclusion of the spin orbit coupling term H_{SOC} prevents the before mentioned decoupling of spin up and spin down equations [84] which was possible in the case of collinear DFT. Thus, the computational costs are increased significantly.

2.4. Exchange and correlation functionals

During the derivation of the DFT formalism we have assumed that the exchange correlation potential defined by Equation 2.19 and the corresponding functional E_{xc} are known. Then we can compute the exact ground state energy of the KS system which by construction corresponds to the ground state energy of the real system. Strictly speaking we have just shifted the complications of evaluating the fully interacting system to the evaluation of an existing but in general unknown exchange correlation functional for the ground state density. As the exact form of the xc-energy functional is currently unknown approximations have to be done in order to carry out numerical calculations. In the last decades the *ab initio* community invested a lot of effort in developing and testing approximated xc-functionals and this section shall give a short overview of what has been done.

The first approximation to the xc-functional which already has been proposed in the original paper by Kohn and Sham [76] was the local density approximation (LDA), which despite of its simple form has been quite successful. For a given density one obtains the xc energy as an integral of the xc-energy density of the homogeneous electron gas times the density. The xc-energy density $\epsilon_{\mathrm{xc}}^{\mathrm{hom}}(n(\mathbf{r}))$ has been calculated by Monte Carlo simulations by Ceperley and Alder [85] and afterwards has been parameterized by Perdew and Zunger [86]. We will refer to this functional as being local in the sense that

the xc-energy density $\epsilon_{\mathrm{xc}}^{\mathrm{hom}}(n(\mathbf{r}))$ at a given point $\mathbf{r}$ is determined by the charge density evaluated at that specific point and not by the charge density in the whole space. The xc-energy in LDA takes the form:

$$E_{\mathrm{xc}}^{\mathrm{LDA}}[n] = \int \mathrm{d}^3\mathbf{r}\epsilon_{\mathrm{xc}}^{\mathrm{hom}}(n(\mathbf{r}))\, n(\mathbf{r}). \tag{2.35}$$

As for all functionals there is no general assessment of accuracy available for LDA for all possible systems. It has to be applied to a large number of different systems and its performance has to be checked carefully. LDA however is known to reproduce experimental lattice constants within a few percents of error [87] where the lattice constant is usually predicted to be smaller than the experimental value. For bulk moduli the error can be between $10-20\%$. But these deviations as pointed out in [87] also include errors because of evaluating the bulk modulus at the theoretical lattice constant, which was already wrong by a few percent. The error of the lattice constant increases the error of the bulk moduli due to an insufficient description of core-valence interactions in the equation of state from which the bulk moduli are extracted [87]. After correcting for this deficiency by adding an appropriate correction term to the equation of state the authors obtain a mean relative error of around 5% [87]. One famous deficiency of LDA is its failure to predict a nonmagnetic instead of a ferromagnetic ground state for bcc Fe [88].

The first way for improvements over the LDA is the generalized gradient approximation (GGA). In the GGA one additionally takes into account the gradient of the charge density. The GGA is often termed a semi-local approximation as it relates a given point in space with its infinitesimal surrounding via the gradient. In its functional form the GGA is written as

$$E_{\mathrm{xc}}^{\mathrm{GGA}}[n] = \int \mathrm{d}^3\mathbf{r}\epsilon_{\mathrm{xc}}^{\mathrm{GGA}}(n(\mathbf{r}), \nabla n(\mathbf{r}))\, n(\mathbf{r}) \tag{2.36}$$

As there is no unique way to define the gradient dependence of the functional there is a number of different flavors of GGA available on the market. Some of them are semi-empirical e.g. BLYP which means that the parameters of the functional are fitted to best reproduce the properties of a special set of systems. The functional by Perdew and Wang [89] (PW91) is a non empirical GGA. It usually gives very similar results to the simpler version proposed by Perdew, Burke and Ernzerhof [90] (PBE) which will be used within this thesis. PBE contains one parameter which is often used to claim that it is also a semi-empirical functional. But as pointed out by Perdew *et al.* [91] the difference is that in this case the parameter has been chosen such that the PBE functional fulfills as many constraints as possible posed by theoretical knowledge about the exact xc-functional. The advantage of the PBE functional is its higher generality, which should lead to a better performance than semi-empirical functionals for systems for which the latter have not been designed for. The exact value of the parameter left in the PBE functional has been the topic of further readjustments e.g. by Y. Zhang and W. Yang [92] who proposed the so called revised PBE (revPBE) which improves the results of PBE on

total energies of atoms and atomization energies of molecules. The variation of the PBE results with respect to experimental values for lattice constants and bulk moduli is of the same order as the variation of the results obtained with the LDA [87]. As a trend PBE overestimates lattice constants by roughly the same amount as LDA underestimates them. For atomization energies of small molecules [93], magnetic properties [88], and cohesive energies of surfaces [87] PBE performs significantly better than LDA. There has also been some effort in adjusting the PBE functional for special cases e.g. for solids PBEsol [94]. In PBEsol the parameter left in the exchange expressions of PBE has been readjusted together with a compensating change in the correlation part such that the correct gradient expansion of the exchange energy over a large range of density gradients is fulfilled, which otherwise had to be violated in order to calculate accurate atomic exchange energies in the slowly varying density limit [94]. In consequence as pointed out in [95] PBEsol improves upon lattice constants but worsens the results for surface energies and atomization energies. Another way to refine the results of the GGA proposed by Becke [96] is to mix in some part of exact exchange. This leads to hybrid functionals like B3LYP [97] the workhorse in quantum chemistry, HSE [98] and PBE0 [99]. Due to the admixture of the orbital dependent exact exchange the computational cost for calculations employing hybrid functionals increases significantly. A prominent failure of GGA type of functionals is the so called CO-puzzle [100]. For a number of $4d$ and $5d$ transition metal (111) surfaces PBE is unable to predict the correct, experimentally measured adsorption site of CO. E.g. on Cu(111) PBE favors the fcc hollow site of the surface while in experiments the Molecule adsorbs on top of a Cu atom. The authors attribute this to the incorrect description of long range vdW interactions [100].

As a next step meta-GGAs are now ready for applications. These functionals incorporate additionally the kinetic energy density $\tau(\mathbf{r})$ and the Laplacian of the charge density.

$$E_{\mathrm{xc}}^{\text{meta-GGA}}[n] = \int \mathrm{d}^3\mathbf{r}\epsilon_{\mathrm{xc}}^{\text{meta-GGA}}\left(n(\mathbf{r}), \nabla n(\mathbf{r}), \nabla^2 n(\mathbf{r}), \tau(\mathbf{r})\right) n(\mathbf{r}) \tag{2.37}$$

$$\tau(\mathbf{r}) = \frac{1}{2}\sum_{\mathrm{occ}} |\nabla\varphi(\mathbf{r})|^2 \tag{2.38}$$

This improves the reproducibility of gradient expansions in the slowly varying density case. The functional by Tao, Perdew, Staroverov and Scuseria (TPSS) [101] in fact does not depend on the laplacian of the density in order to fulfill known constraints of the exact xc-functional [91]. TPSS performed quite well for atomization and cohesive energies but stayed behind the expectations for lattice constants [95]. For that reason a revised version termed revTPSS [95] was developed following the same idea as the solid state specialized PBEsol functional. The increase of accuracy of the results obtained with meta-GGA functionals goes in hand with a roughly 30% increase in computational cost compared to usual GGAs [95]. Although meta-GGAs might perform well and give

a significant improvement over GGA, for the adsorption of small molecules on noble metal surfaces as it has been shown in [102] for the M06-L [103] functional, which has been fitted to molecular data, meta-GGAs are intrinsically not able to correctly account for vdW interactions as their correlation part is still semi-local. In this case two distant charge density distributions interact with each other only in their overlap region, which leads to a strongly underestimated effect on the first density due to the presence of the second one.

The just mentioned functionals are the first three rungs on the five rung Jacobs ladder to functional heaven [104] or chemical accuracy. Each rung takes one more ingredient into account which makes the computation of the functional more expensive. On the fourth rung exchange is treated exact and has to be combined with a proper correlation functional which leads to the so called hyper-GGA [105]. The ingredient added in this case is the orbital dependence by the exchange energy density. On the fifth rung both the exchange and parts of the correlation are treated in an exact way, which results in generalized random phase approximations [105]. The ladder is also not strictly discrete as e.g. the mentioned hybrid functionals are somewhat "in between" the rungs.

Insight in the structure of the exact xc-functional and constraints for the derived approximations to it can be obtained from the adiabatic connection fluctuation dissipation theorem (ACFDT) [106–108]. Herein one varies the interaction strength between the fully interacting system and the non interacting KS system along an adiabatic connection. Within this framework an analytic expression for the xc-energy in terms of the response function χ_λ of the system can be given, which then allows to derive functionals by approximating the response function χ_λ. When the exact exchange energy as a functional of the KS orbitals is subtracted from the ACFD expression for the xc-functional the correlation energy can be written as:

$$E_\mathrm{c} = -\frac{1}{2}\int_0^\infty \frac{\mathrm{d}u}{\pi} \int \mathrm{d}^3\mathbf{r}\mathrm{d}^3\mathbf{r}'\; v\left(\mathbf{r}-\mathbf{r}'\right)\left[\int_0^1 \mathrm{d}\lambda\; \chi_\lambda(\mathbf{r},\mathbf{r}',iu) - \chi_{KS}(\mathbf{r},\mathbf{r}',iu)\right] \tag{2.39}$$

where λ is the coupling constant of the adiabatic connection. One corresponds to the real system while zero denotes the KS system. χ_λ is the response of the λ-interacting system and χ_{KS} the response of the KS system respectively[3]. The response function of the λ-interacting system can be obtained from a Dyson-like equation:

$$\chi_\lambda = \chi_\mathrm{KS} + \chi_\mathrm{KS}\left(\lambda v + f_{\mathrm{xc},\lambda}\right)\chi_\lambda \tag{2.40}$$

where $f_{\mathrm{xc},\lambda}$ is the λ dependent second functional derivative of the xc-functional with respect to the charge density $n(\mathbf{r})$. Usually the λ-interacting response function is calculated within the random phase approximation (RPA), which implies neglecting the $f_{\mathrm{xc},\lambda}$. H. Nguyen *et al.* have studied noble gas and alkali earth dimers by combining EXX with RPA correlation [109]. They found a significant improvement of binding energy curves

[3] Definitions of the different response functions in particular to which potentials they correspond are given in Appendix A

when compared to semi-local DFT calculations. Nevertheless, the authors remark that this functional leads to an unphysical maximum in the binding energy curve for large separations of Be_2, which they attribute to the present lack of self-consistency of the EXX/RPA method applied in their study [109]. J. Harl *et al.* [110] reported for solids of noble gases an improvement over PBE results for lattice constants and cohesive energies when compared to the experiment. In a second study the authors addressed solids, small molecules and adsorbates on surfaces [111]. For Graphite the correct $1/d^4$ dependence of the interlayer interaction energy on the interlayer distance d is recovered. In addition the graphite phase and the diamond phase of C are predicted to be degenerate in energy which is an improvement over PBE and LDA. Both of them in contrast to the experiment predict the graphite phase to be more stable [111]. As an example for surface science applications J. Harl *et al.* chose to study the already mentioned CO puzzle of the adsorption of CO on a Cu(111) surface. EXX/RPA is able to reproduce the correct adsorption site order and to give a fairly accurate adsorption energy [111]. J. Paier *et al.* [112] investigated atomization energies and reaction barrier heights for small molecules and solids with EXX/RPA.

2.5. DFT in practice

To implement the introduced concepts a number of efficient codes have been written. The results presented in this thesis have been obtained with the VASP code for the density functional theory calculations and JuNoLo for the non local xc-functional in case of vdW corrections. For VASP we want to shortly describe the scheme of a self consistency cycle. An overview of all implemented algorithms can be found in [113]. The original version of JuNoLo has been described in [114]. We will focus in Section 3.3 on the changes introduced by the update with the efficient Soler scheme for vdW-DF [115] and rVV10 [116]. A detailed description of the theoretical formalism is given in Appendix A.

In general, VASP minimizes the total energy of a system as a functional of the one particle density by iteratively solving the KS-equations. As input it needs atomic positions from which an initial density is set up for the first step based on atomic orbitals. The wavefunctions are initialized with random numbers and thus in the first few steps of a selfconsistency cycle the charge density is kept fixed until the wavefunctions are reasonable. From this initial charge density a potential is constructed which allows to obtain the eigenvalues and the refined wavefunctions by a residual minimization scheme with direct-inversion-in-iterative-subspace (RMM-DIIS). From the wavefunctions partial occupancies, the total energy and a new charge density will be calculated which serves as input for the next iteration. This procedure is repeated until a given threshold for the energy difference of two consecutive iterations is reached. In order to reach selfconsistency the norm of the residual vector of the charge density has to be decreased until it becomes minimal. To achieve this a certain amount of the residual vector is added to

the charge density between two consecutive steps by a Pulay mixing scheme.

After the electronic self consistency has been reached as described in the previous paragraph the Hellmann-Feynman-forces on the atoms can be evaluated and used to update the atomic positions. The limit below which forces are considered as being relaxed is 0.003 eV/Å, if not stated differently in the corresponding chapters. In order to obtain accurate forces a strict criterion for the electronic self consistency has to be chosen. At this step also the semi-empirical vdW corrections are evaluated and added to the DFT result.

The KS-wavefunctions $\phi_{i,\mathbf{k}}(\mathbf{r})$ are expanded in a plane wave basis

$$\phi_{j,\mathbf{k}}(\mathbf{r}) = \sum_{\mathbf{G}} c_j(\mathbf{k}+\mathbf{G}) e^{i(\mathbf{k}+\mathbf{G})\mathbf{r}}, \tag{2.41}$$

where j is the band index, $\mathbf{k}$ is a vector from the first Brillouin zone (BZ) and $\mathbf{G}$ is a reciprocal lattice vector. This allows to treat the system efficiently in a supercell approach. The positions of the ions and the lattice vectors of the supercell which is periodically repeated in all three spatial directions have to be provided as input. The charge density can then be obtained by Fourier transforming the wavefunctions and integrating over the first BZ in reciprocal space. The first BZ is sampled on a discrete grid by a set of $\mathbf{k}$ points which is generated by the scheme of Monkhorst and Pack [117]. The choice of this special $\mathbf{k}$ point grid i.e. the number of $\mathbf{k}$-points left after symmetrization in the irreducible BZ is a parameter which determines the accuracy of the calculations. To correctly describe electrons close to the core, high values of $(\mathbf{k}+\mathbf{G})$ are necessary. Hence, one has to include a large number of plane waves into the basis set. Due to this reason pseudopotentials are used, which exclude the for chemical properties usually unimportant core electrons from the calculations. By only considering the valence electrons the total cost of the calculations due to the number of involved electrons is decreased and the cut-off energy E_{cut}, which satisfies

$$|\mathbf{k}+\mathbf{G}| \leq E_{\text{cut}} \tag{2.42}$$

and determines the maximal amount of plane waves in the basis set, can be chosen smaller. The number or plane waves included in the basis set is another parameter which can be systematically increased in order to improve the accuracy of the calculations. The plane wave cut-off energy E_{cut} does not only affect the electronic structure but also has an impact on the accuracy of the Hellmann-Feynman forces.

To describe the interaction of the electrons with the ions of the system pseudopotentials either ultrasoft or constructed in the PAW approach developed by Blöchl [118] are available for a large part of the periodic table. In this work we will rely on the latter ones. Within the PAW method the all-electron wavefunction is split with the help of projectors into a smooth part for the valence electrons, which can be treated by the usual pseudopotential methods, and a core part localized around the ions, which is expanded

into spherical harmonics and treated on a radial grid. From these two components the all electron wavefunction can be reconstructed by the linear transformation

$$| \psi_n \rangle = | \tilde{\psi}_n \rangle + \sum_i \left(| \phi_i \rangle - | \tilde{\phi}_i \rangle \right) \langle \tilde{p}_i \mid \tilde{\psi}_n \rangle , \tag{2.43}$$

where ψ_n is the all electron wavefunction, $\tilde{\psi}_n$ is the smooth pseudo wavefunction, i is a multiindex over the atomic site, the angular momentum and the energy index, ϕ_i are the all electron partial waves obtained for a reference atom, $\tilde{\phi}_i$ the corresponding pseudo partial waves and the projector functions $\tilde{p}_i$ are dual to the pseudo partial waves i.e. $\langle \tilde{p}_i \mid \tilde{\phi}_j \rangle = \delta_{ij}$ [118, 119]. The PAW pseudopotentials leads to smoother pseudo wavefunctions when compared to norm conserving pseudopotentials which allows the use of much smaller cut-off energies for PAW pseudopotentials than their norm conserving representatives.

3 Van der Waals interactions

Besides ionic and covalent binding, the interaction of particles at the nano to micrometer scale can be ascribed to the so called van der Waals (vdW) interactions. Starting from the binding of dimers of noble gas atoms, over the interactions in an ensemble of organic molecules, reaching up to the self-organization of viruses and even the ability of Geckos to climb on flat surfaces, the vdW interactions are present and of importance in a vast range of systems. The focus of this thesis is on the interaction of organic molecules with metal surfaces, which are as discussed in the first chapter candidates for the development of new electronic or spintronic devices or new functional materials. Thus, this chapter will give an introduction on van der Waals interactions.

First of all there is a distinction to be made between vdW- and dispersion interactions [120]. Both terms are used sometimes erroneously synonymous and sometimes for different meanings depending on the community using them. Thus, the way how the terms vdW interactions and dispersion interactions are used throughout this thesis should be clarified. The actual vdW-interactions have been named after Johannes Diderik van der Waals, who brought up the idea of a new type of binding besides ionic binding and covalent binding while developing a new equation of state for gases and liquids, which also governs the gas liquid phase transition. He modified the equation of state of the ideal gas by introducing an attractive interaction between the molecules in the gas proportional to the squared inverse volume of the gas. This leads to an attractive force between the molecules considered, which at large distances R scales as $1/R^6$ [121, 122]. This force is referred to as the vdW force and whenever attempting to develop a microscopic description of the interaction between neutral organic molecules this is the limit which the theory has to fulfill. However, there are a number of effects which lead to a deviation from the $1/R^6$ of law. Just to name one of them retardation due to the finite speed of light will lead rather to a $1/R^7$ dependence as photons mediate the vdW-interactions [123]. A first definition of vdW interactions is interactions which are not due to ionic or covalent binding. These interactions include mainly elec-

trostatic interactions between permanent multipole moments, induction of a multipole moment by a permanently polarized molecule to an otherwise unpolarized molecule and the interaction of instantaneous multipole moments.

One microscopic model to explain the occurrence of an attractive force between neutral particles are charge fluctuations. Random fluctuations of the charge density induce instantaneous and varying dipole and higher order multipole moments in otherwise neutral and unpolarized molecules. The interaction of these induced multipole moments leads to an attractive force between the molecules. The lowest order would be the interaction of two induced dipole moments which scales as $1/R^6$ [121, 122]. The next higher order would be the interaction of an induced dipole with an induced quadrupole which scales like $1/R^8$. This in principal infinite series of interaction terms is referred to as dispersion interactions. In the case where the interacting particles do not have a permanent multipole moment and thus electrostatic and induced dipole interactions are excluded the dominant part of the vdW-interactions would be dispersion. In the sense of the definition of vdW interactions given here also repulsive contributions like e.g. Pauli repulsion are included in vdW interactions. Sometimes the term vdW interaction is used exclusively for attractive interactions which can lead to a confusion of vdW interactions and dispersion interactions.

After establishing the nomenclature and drawing a line between vdW- and dispersion interactions this chapter will provide a few simple models related to dispersion interaction. The appropriate theoretical footing to deal with charge fluctuations due to virtual excitations would be quantum electrodynamics [124], which is beyond the scope of this thesis. Thus, an illustrative model for London dispersion and one famous example of two vdW interacting hydrogen atoms will be given in the following section. The correct treatment of vdW interactions within DFT is a topic of current research [125, 126]. Thus, we will provide an overview about methods developed to include vdW interactions in DFT calculations.

3.1. London dispersion

The interaction energy of two instantaneously polarizable spherical particles at a distance R from each other, large enough that no overlap of their charge distributions occurs, follows the $1/R^6$ law derived by F. London [121, 122]. This part of the dispersion interactions has thus been termed London dispersion. We will begin with a simple example following the derivation in [127]. The system will be modeled by two identical harmonic oscillators at a distance R, which are allowed to oscillate along the x axis connecting both oscillators with amplitudes x_1 and x_2. The amplitudes describe the separation distances of the two charges $\pm e$ in the spontaneously appearing dipoles due to charge fluctuations on both oscillators. The force constant is C and the Hamiltonian

in atomic units ($\hbar = m_e = e = 1$) describing both oscillators without interaction is

$$H_0 = \frac{1}{2}p_1^2 + \frac{1}{2}Cx_1^2 + \frac{1}{2}p_2^2 + \frac{1}{2}Cx_2^2 \tag{3.1}$$

It is assumed that the frequency ω_0 of each oscillator, related to the force constant by $C = w_0^2$ is the frequency of the strongest optical adsorption line. For a certain displacement x_1, x_2 of the charges the Coulomb interaction of the system is

$$H_1 = \frac{1}{R} + \frac{1}{R + x_1 - x_2} - \frac{1}{R + x_1} - \frac{1}{R - x_2} \tag{3.2}$$

The separation R is assumed to be much larger than both amplitudes $R \gg |x_1|, |x_2|$ which allows us to expand H_1 to lowest order

$$H_1 \approx \frac{2x_1x_2}{R^3} \tag{3.3}$$

The total Hamiltonian $H_0 + H_1$ represents now two coupled harmonic oscillators. The coupled equation can be diagonalized by the normal mode transformations

$$x_1 = \frac{1}{\sqrt{2}}(x_+ + x_-), \quad x_2 = \frac{1}{\sqrt{2}}(x_+ - x_-) \tag{3.4}$$

$$p_1 = \frac{1}{\sqrt{2}}(p_+ + p_-), \quad p_2 = \frac{1}{\sqrt{2}}(p_+ - p_-) \tag{3.5}$$

With this transformation the total Hamiltonian $H = H_0 + H_1$ reads:

$$H = \frac{1}{2}p_+^2 + \frac{1}{2}\left(C - \frac{2}{R^3}\right)x_+^2 + \frac{1}{2}p_-^2 + \frac{1}{2}\left(C + \frac{2}{R^3}\right)x_-^2 \tag{3.6}$$

By comparing the oscillation terms containing $x_\pm^2$ in the last equation with the usual form ω^2x^2 for a harmonic oscillator we can identify the frequencies $\omega_\pm$ of the coupled system:

$$\omega_\pm = \sqrt{C \pm \frac{2}{R^3}} \approx \omega_0\left[1 \pm \frac{1}{2}\left(\frac{2}{CR^3}\right) - \frac{1}{8}\left(\frac{2}{CR^3}\right)^2 + \cdots\right] \tag{3.7}$$

where in the second step the square root has been expanded in a Taylor series. The uncoupled system of two harmonic oscillators would have a zero point energy $U = 2 \cdot \frac{1}{2}\omega_0$. For the coupled oscillators the energy will be $U = \frac{1}{2}(\omega_+ + \omega_-)$:

$$U = \omega_0\left[1 - \frac{1}{8}\left(\frac{2}{CR^3}\right)^2\right] = \omega_0 - \frac{C_6}{R^6} \tag{3.8}$$

The energy of the coupled harmonic oscillators is reduced with respect to the uncoupled case by the famous C_6/R^6 term. A simple approximation for the C_6 coefficient of two identical atoms would be $C_6 = \omega_0\alpha^2$ with the electronic polarizability α.

For a three dimensional system modeling two spherical polarizable hydrogen atoms F. London applied a perturbation theory approach to obtain a similar result [122]. We will outline his derivation. The small perturbation required for the perturbation theory in this case is the dipole dipole interaction $V = (1/R^3)(\mathbf{r_1} \cdot \mathbf{r_2} - 3\mathbf{r_1} \cdot \hat{R}\, \mathbf{r_2} \cdot \hat{R})$ with the distance R between the atoms, $\mathbf{r_1}, \mathbf{r_2}$ the position vectors of the two atoms and $\hat{R}$ the direction vector connecting both atoms. While the first order perturbation vanishes due to $< \mathbf{r_1} >=< \mathbf{r_2} >= 0$, the second order contribution for an atom in the state i interacting with an atom in the state j, when the coordinate system is chosen such that $\hat{R}$ points into z direction, is

$$E^{(2)} = -\frac{1}{R^6} \sum_{ij} \frac{\left| \left\langle \psi_i^{(1)} \psi_j^{(2)} \right| x_1 x_2 + y_1 y_2 - 2 z_1 z_2 \left| \psi_0^{(1)} \psi_0^{(2)} \right\rangle \right|^2}{\omega_{i0} + \omega_{j0}} \tag{3.9}$$

where $\omega_{i0} = E_i - E_0$ is the energy difference between the ith excited state and the ground state. By averaging over all orientations of the dipoles F. London [122] separated the square of the expectation value of the sum over all three spatial components of the dipole moments and arrived at

$$E^{(2)} = -\frac{6}{R^6} \sum_{ij} \frac{\left| Z_{i0}^1 \right|^2 \left| Z_{j0}^2 \right|^2}{\omega_{i0} + \omega_{j0}} \tag{3.10}$$

where $Z_{i0}^1 =< \psi_i | z_1 | \psi_0 >$. With the integral identity

$$\frac{1}{a+b} = \int_0^\infty \frac{\mathrm{d}u}{2\pi} \frac{4ab}{(a^2+u^2)(b^2+u^2)} \tag{3.11}$$

and a simple model for the dynamic polarizability $\alpha(\omega) = \sum_i 2\omega_{i0} |Z_{i0}|^2 / (\omega_{i0}^2 - \omega^2)$ of the hydrogen atom inserted into Equation 3.9 we arrive at the final form

$$E^{(2)} = -\frac{6}{R^6} \int_0^\infty \frac{\mathrm{d}u}{2\pi} \alpha_1(iu) \alpha_2(iu) \tag{3.12}$$

Hence, the dispersion interaction of the two hydrogen atoms in second order perturbation theory is proportional to the product of their dynamic polarizabilities $\alpha(\omega)$. This result is similar to what has been derived including interactions of the electromagnetic fields with the electrons by C. Mavroyannis and M. J. Stephen [128] for more general polarizable objects in the limit of R much smaller than the wavelengths appearing in the atomic adsorption spectrum. For larger distances the finite speed of light leads rather to a $1/R^7$ decay as shown by H. Casimir and D. Polder [123]. They found that retardation leads to a correcting factor for the interaction energy equal to one for small distances and monotonically decreasing with $1/R$ for large distances.

Another unconventional aspect of dispersion interactions is their nonadditivity. If we repeat the above derivations with more than two multipoles, the perturbation theory will lead to terms which cannot be obtained by simply adding the pair interactions of every

pair of multipoles in the system. The dispersion interaction of a three body system has been derived by B. M. Axilrod and E. Teller [129]. The geometric configuration which the three atoms adopt determines whether the dispersion interactions in this case are attractive e.g. in the case of all three dipoles in a row or repulsive when e.g. the three dipoles are on an equilateral triangle [129].

For the vdW interaction of a electrical polarizable and a magnetically polarizable atom C. Farina *et al.* [130] reported a deviation from the $1/R^6$ dependence. The authors followed a way similar to the first simple model presented in this section and arrived at a $1/R^4$ dependence of the interaction energy without retardation. This effect has been proposed earlier in general approach by G. Feinberg and J. Sucher [131].

3.2. Van der Waals interactions in DFT

It is stated [132] that except for the fifth rung all rungs of the Jacobs ladder are not correctly describing the vdW interactions which are of particular interest for this thesis. One reason for this is the fact that up to the fourth rung all functionals treat correlation in a local or semi-local way. Due to this the interaction of two distant charge densities is accounted for only in their region of overlap. The fourth and the fifth rung as well as functionals derived from the ACFDT are orbital dependent functionals due to the inclusion of exact exchange, exact parts of correlation or the response function, which are functionals of the orbitals. This leads to high computational costs even on up to date computers. And as systems where vdW interactions are relevant are usually of considerable size it would be preferable to have a functional or correction scheme which - of course trading for accuracy - is at most density dependent. In this section an overview of current approaches how to deal with vdW interactions within DFT calculations will be given. Also a look at the performance of the discussed methods will be taken. To assess the performance of dispersion corrections schemes is quite involved as to obtain appropriate reference data e.g. from higher order quantum chemistry calculations or experimental studies is non trivial. While calculations are restricted to very small systems experiments are often difficult to compare with the computational results [133].

To correct for the deficiencies in correctly describing vdW interactions of common local and semi-local xc-functionals has been and still is an active field of research [125, 126]. The methods developed can be roughly distinguished in semi-empirical and *ab initio* approaches. In historical order we will start with the semi-empirical methods. In this case one assumes that the total energy of the system can strictly be divided into the total energy E^{DFT} obtained by the DFT calculation and the vdW energy E^{vdW}.

$$E^{\mathrm{tot}} = E^{\mathrm{DFT}} + E^{\mathrm{vdW}} \tag{3.13}$$

The latter can be calculated following the London dispersion formula. The vdW interaction energy of two atoms A and B is their interatomic C_6 coefficient divided by the distance to the sixth power, which is the leading order of an interacting spontaneous

multipole expansion. Higher order terms like C_8/r^8, C_{10}/r^{10}, and so on as well as many body interactions with more than two interacting bodies are neglected. Following the notation of S. Grimme [18] the total vdW interaction energy is then given by

$$E^{\mathrm{vdW}} = -s_6 \sum_{A<B} f(R_A^0, R_B^0, R_{AB}) \frac{C_{6,AB}}{R_{AB}^6}, \tag{3.14}$$

the sum over all interacting atom pairs A, B times a damping function $f(R_A^0, R_B^0, R_{AB})$ depending on the van der Waals radii R_A^0 of the interacting atoms, which ensures that for small distances the corrections will be cut off and thus will not affect the results of the DFT calculations in the short range regime. More importantly the damping function prevents the divergence of the correction term for small distances. As the damping function is not uniquely defined there is a number of different proposals for it [18, 134–136], but it has been reported in the literature that the influence of the exact form of the damping function in a DFT-D method is small compared to the total dispersion correction [137]. The parameter s_6 which determines the overall strength of the correction has to be adjusted to the underlying xc-functional, which has been used for the calculation of E^{DFT} as it has been done in [18] by least square fitting to interaction energies of a set of small molecules. In addition the atomic C_6 coefficients have to be chosen. They can be directly calculated by time dependent density functional theory (TDDFT) or, as it has been done by F. Ortmann and F. Bechstedt [134], via the London dispersion formula

$$C_{6,AB} \approx \frac{3}{2} \alpha_A \alpha_B \frac{I_A I_B}{I_A + I_B} \tag{3.15}$$

from experimentally obtained ionization energies I_A and polarizabilities α_A. A similar approach has also been used by S. Grimme for the DFT-D2 method [18]. Instead of experimental values for the ionization potentials and static polarizabilities the author utilized values obtained from PBE0 calculations. Some of the C_6 coefficients, i.e. those for alkali and alkali earth elements as well as transition metals have been obtained as an average value over the C_6 coefficients of the preceding noble gas and the following group III element due to the fact that for those elements the difference between the free atom and a bound atom would be too large to justify the proposed approach of calculating C_6 coefficients from atomic properties [18]. A. Tkatchenko *et al.* calculated the C_6 from the ratio of effective volumes which were obtained from the density of a free atom and an atom which is bound to other atoms [136]. P. L. Silvestrelli *et al.* did something conceptually similar by expressing the C_6 coefficients in terms of maximally localized Wannier functions [138–140]. If the C_6 are calculated by *ab initio* methods one has to obtain the pair coefficient $C_{6,AB}$ from those. This can be done by a geometrical average as it has been done in the method introduced by S. Grimme (DFT-D2) [18]. It has been argued that choosing the C_6 coefficients for the atoms once and for all is inaccurate as the polarizability of an atom depends on its environment e.g. if the atom is part of a surface and thus experiences screening effects or part of a molecule where those electrons involved

in chemical bonds contribute less to the overall polarizability. This problem has been addressed in more recent versions of the DFT-D approach [135], where the C_6 coefficients depend on fractional coordination numbers and by this on their chemical environment and in addition on the distance between the interacting atoms A and B. The performance of the so termed DFT-D3 method has been tested for hydrogen bonded systems [141] and the authors suggested in order to obtain both accurate equilibrium separations and binding energies one should do geometry optimization with the comparably cheap DFT-D3 method and afterwards calculate the binding energy with a single shot calculation on a higher level of theory. The approach of A. Tkatchenko and M. Scheffler [136] (TS-vdW) has the same goal i.e. to adapt the C_6 coefficients of the atoms to their environment. In earlier versions of that method the C_6 coefficients are calculated as a functional of the density with respect to the density of a free atom. More recently also screening effects and three body interactions are considered by employing the self consistent screening equation of classical electrodynamics to calculate the polarizability tensor [142, 143]. K. Tonigold and A. Groß [144] have deduced the C_6 coefficients of metal atoms in clusters by means of a hybrid quantum Monte Carlo method in order to obtain coefficients which are appropriate to describe metal atoms in a surface. All of the just discussed schemes have the major advantage that they are of relatively low computational cost compared to the electronic structure calculations. Thus, within this thesis in particular DFT-D2 and to a larger extent DFT-D3 will be applied.

Semi-empirical approaches to account for vdW interactions have been applied in a large number of studies [18, 126, 134–136, 143, 145, 146] assessing the accuracy of the just introduced methods for molecules and complexes contained in the S22 [147] or S66 [148] test sets. For these systems, which most of the methods are designed for or fitted to, they are capable of decreasing the mean absolute percentage deviation (MAPD) in binding energies and geometries with respect to high level calculations or experimental results of 30% obtained with the PBE functional to about 5% [126], but no general prediction on the accuracy of a given semi-empirical method can be made [149] as in particular the performance of a semi-empirical method depends on the underlying GGA functional [18, 135, 149]. Attempts to refit the GGA to better support the DFT-D approach led to improvements for a certain subset of the studied systems while decreasing the accuracy for others [149]. T. Björkman *et al.* [125] have studied equilibrium geometries and binding energies for several weakly bound layered solids with different approaches to deal with vdW interactions including DFT-D2. As benchmark they used RPA calculations and where available experimental results for the interlayer distances. For the c-axis length which combines the results for the covalent binding dominated intralayer thickness and the vdW driven interlayer distance DFT-D2 yields on average good geometries but has a wider spread of the values with sometimes unexplainable far off exceptions [125]. Regarding the binding energies DFT-D2 strongly overestimates the RPA numbers and at the same time does not reproduce trends [125].

Despite of the just discussed tests of semi-empirical correction schemes for molecules and solids in the context of this thesis it is important to see how these methods deal

with the adsorption of organic molecules on surfaces. E. R. McNellis *et al.* [150] compared different DFT-D approaches including DFT-D2 and TS-vdW to correct for vdW interactions in the case of benzene and azobenzene adsorbed on the noble metal surfaces Cu(111), Ag(111) and Au(111) and critically discuss the obtained adsorption energies with respect to experimentally measured values. While the adsorption energy of Benzene on all three metal surfaces calculated with the PBE functional has been between about -0.06 eV for Cu(111) and -0.08 eV for Au(111) the tested semi-empirical vdW corrections led to adsorption energies between -0.5 eV up to -1.05 eV. Compared to an experimentally obtained adsorption energy of approximately -0.6 eV, which is one order of magnitude larger than the PBE value, all the different vdW schemes improve upon PBE but still do not yield very good numbers [150]. The increase in adsorption energy goes in hand with a decrease of the molecule surface distance by 0.3 Å up to 1.0 Å with a rather large spread among the different semi-empirical methods [150]. This led the authors to the careful conclusion that the account of dispersive interactions at the metal surfaces provided by the various schemes could be in the right ballpark but likely overbind [150]. In a related study of azobenzene on Ag(111) G. Mercurio *et al.* [151] measured the adsorption energy and structural parameters and compared them to their DFT calculations accounting for vdW interactions by using DFT-D2 and TS-vdW. The adsorption energy determined by TPD was -1.00 ± 0.1 eV and the distance between the N atom of the molecule and a Ag atom was 3.07 Å [151]. While PBE calculations resulted in a distance of 3.64 Å, both DFT-D schemes led to a value much closer to the experiment of 2.75 Å for DFT-D2 and 2.98 Å for TS-vdW respectively [151]. Both DFT-D schemes over corrected the by PBE underestimated adsorption energy to -2.16 eV for DFT-D2 and -1.71 eV for TS-vdW respectively [151]. As a consequence the authors suggested to take into account only the topmost layer of the metal surface when calculating the dispersion corrections in order to mimic the screening effect of the surface and by this to reduce the overbinding of the semi-empirical vdW corrections [151].

K. Toyoda *et al.* [152] compared adsorption energies and equilibrium distances of pentacene adsorbed on Cu(111), Ag(111) and Au(111) obtained with DFT-D2 to experimentally obtained values. While for Cu the adsorption energy calculated with DFT-D2 of -1.61 eV agreed well with the experimental result of -1.6 eV in both cases, Ag and Au, the calculated adsorption energies -2.28 eV and -2.58 eV strongly overestimated the experimental values of -1.5 eV and -1.1 eV and even failed to reproduce the trend of increasing binding strength from Au to Cu [152]. The equilibrium distance between pentacene and the metal surface had been measured only for Cu(111) and for this case the authors reported a calculated molecule-surface distance using DFT-D2 of 2.4 Å which agrees well with the experimental value of 2.34 Å while PBE overestimated the distance with 4.2 Å.

K. Lee *et al.* [153] have compared calculations of potential energy curves (PECs) using different methods to account for vdW interactions including DFT-D3 and vdW-TS for physisorbed H_2 molecules on the low index surfaces of Cu with results extracted from selective-adsorption bound-state measurements. For H_2 adsorbed on the atop site of the

Cu(111) an equilibrium distance of 3.5 Å and a potential well depth of −29 meV has been extracted. Both semi-empirical schemes DFT-D3 with 2.8 Å and −98 meV as well as TS-vdW with 3.2 Å and −66 meV led to over corrections with TS-vdW being closer to the experimental values [153]. The authors attributed this discrepancy to the nature of the semi-empirical methods, which despite of putting effort in correctly describing the real electron distribution due to polarization around each single atom by including the atomic C_6 coefficient, lack the ability to mimic the global charge redistribution of the entire adsorbate on the surface [153].

A member of the second class of approaches to correct for vdW interactions which are the *ab initio* methods arises from the usage of non local correlation functionals as the one developed by Langreth and Lundqvist [19, 154–156] over a long period of time. Starting from the ACFDT the authors, in its final version for general geometries by Dion *et al.* [19] (vdW-DF1), have derived a non local functional for correlation, which depends on the density only. The purpose of this functional was to replace the correlation part of a given GGA by a non local term and by this not only to address the open issue of vdW interactions but also to allow for general improvements of the GGA functional. The non local part of that replacement has the form

$$E_{\mathrm{c}}^{\mathrm{nl}} = \frac{1}{2} \iint \mathrm{d}^3\mathbf{r}\mathrm{d}^3\mathbf{r}'\, n(\mathbf{r}) n(\mathbf{r}') \phi\left(q, q', |r - r'|\right) \tag{3.16}$$

where $\phi\left(q, q', |r - r'|\right)$ is an interaction kernel basically containing information about the dielectric function of the system. It depends on the charge density and its gradient by the variables q, q' as well as on the distance between two points in space. A detailed derivation of the vdW-DF functional is given in Appendix A. To this non local part of the correlation functional a proper local part has to be chosen as the local part is explicitly subtracted during the derivation. In their original work Dion *et al.* used LDA correlation but later on also full GGA correlation has been assessed [157]. The second ingredient which has to be chosen properly is the exchange part of the functional. In the original proposal revPBE [92] has been used, which among the tested exchange functionals best mimicked Hartree-Fock exchange and more importantly did exhibit less spurious binding of vdW systems by exchange only. A later revision of the functional by K. Lee *et al.* [158] employed rPW86 exchange which has been especially refitted. They also reparameterized the non local part, which then led to the improved version called vdW-DF2. Which exchange performs best is still under discussion [159–162]. Cooper *et al.* [160] pointed out that the present underbinding of vdW-DF is due to the overestimation of exchange repulsion by the at that time used exchange functionals and suggested the use of C09x exchange in combination with vdW-DF instead. Recently the functional proposed by Vydrov and van Voorhis VV10 [163] which is based on the same idea as vdW-DF but contains a different and simpler kernel function has attracted a lot of attention due to its promising results [145, 164]. Earlier versions of that functional [165] have been criticized due to the violation of some general constraints on the exact xc-functional [166].

When the vdW-DF functional appeared its evaluation has been quite expensive due to the double spatial integral. Thus, first studies were restricted to rather small systems like noble gas dimers and only post processing, which means evaluating the non local correlation term after a normal DFT calculation, had been done [46, 167, 168]. As self-consistent calculations were already close to being impossible one was not even thinking of structural relaxations which would involve multiple self consistent evaluations of the total energy. In time a number of new approaches to calculate the non local correlation energy more efficiently have occurred. P. Lazic *et al.* [114] relied on a massively parallel implementation in the JuNoLo code, Gulans *et al.* used a linear scaling self consistent implementation [169] and in the group of C. Ambrosch-Draxl the six dimensional integral has been solved by means of Monte Carlo integration [170]. G. Roman-Perez and J. M. Soler [115] have proposed a scheme which, via interpolation of the kernel, leads to a single spatial integral in reciprocal space, which makes vdW-DF available at the expense of a normal GGA calculation. The latter approach is nowadays available in a number of DFT codes and has also been added to the functionalities of JuNoLo. A more detailed description of the Soler-scheme is given in Appendix A. Thus, from this point on the non local vdW-DF can also efficiently be used for structural relaxations. Due to its particular functional form the Soler scheme is not directly applicable to the VV10 functional. Additional approximations had to be done by R. Sabatini *et al.* [116] in order to implement an efficient version of that functional which is then termed rVV10. The new functional rVV10 can easily be calculated with the already existing implementation of the Soler scheme in JuNoLo.

The number of theoretical studies investigating the predictive capabilities of the different non local vdW functionals is increasing [126]. In particular surface science applications regarding the adsorption of small organic molecules on metal or semiconductor surfaces [133, 152, 153, 162, 171–174] can be tested. In the already discussed study of weakly bound layered solids by T. Björkman *et al.* [125] also non local xc-functionals have been applied. The prediction of equilibrium geometries was the worst among the studied functionals when applying vdW-DF1 and vdW-DF2 which both predict too large interlayer distances [125]. Although vdW-DF paired with PBE exchange performed better it could not compete with VV10, with which results even close to the benchmark RPA results could be obtained [125]. For the binding energies vdW-DF1 and vdW-DF2 underestimated the RPA values with the newer vdW-DF2 been closer to the benchmark [125]. VV10 overestimated the binding energy to a larger extent than vdW-DF1 underestimated it [125]. J. Klimeš *et al.* [161] found in their study on lattice constants, bulk moduli and atomization energies for solids an overall worse performance of vdW-DF1 and vdW-DF2 for lattice constants and bulk moduli respectively, mostly due to the underestimation of the lattice constants for alkali metals, while atomization energies are slightly improved when compared to the PBE functional. The authors assigned this to the too repulsive exchange part of the functionals as it also has been reported by Cooper *et al.* [160].

Regarding the role of vdW interactions in the case of molecule surface interfaces P.

Sony *et al.* [171] investigated the adsorption of thiophene on the Cu(110) surface employing vdW-DF to correct for vdW interactions. For the PBE functional a molecule-surface distance of 2.4 Å and an adsorption energy of −0.26 eV is reported where comparison to revPBE calculations which did not yield any binding at all showed that the present binding in PBE is due to exchange [171]. The authors found that the vdW-DF functional increases the distance between the molecule and the surface by 0.4 Å and almost doubles the adsorption energy to −0.5 eV [171]. Unfortunately experimental benchmark data is available only for the Cu(111) and Cu(100) surface thus P. Sony *et al.* concluded based on those results that vdW-DF suggests a behavior which is in accordance with the experiment [171].

The adsorption of three small molecules, namely melamine, NTCDA and PTCDA, which bind to each other by hydrogen bonds, on Au(111) was studied by M. Mura *et al.* [133]. While the PBE functional calculations resulted in adsorption energies between −0.1 eV and −0.25 eV with no trend for increasing adsorption energy with increasing molecule size the self consistent vdW-DF calculations yield −0.88 eV for melanine, −1.31 eV for NTCDA and −1.88 eV for PTCDA [133]. These values not only reproduced the expected trend in adsorption energy due to the additivity of the vdW interactions, but in addition were close to the reported experimentally obtained values of −1.5 eV and −2.0 eV for NTCDA and PTCDA respectively adsorbed on Au(111) [133]. The distance between the molecules and the surface was in this case reduced with respect to the PBE values, which were between 3.5 Å and 3.6 Å, to 3.1 Å for melanine 3.5 Å for NTCDA and 3.3 Å for PTCDA of which the latter one got closer to the reported experimental value of 3.27 Å [133]. The authors stressed the importance of self consistent calculation with vdW-DF as the results may be off by 20% for some cases when non selfconsistent calculations are performed [133].

F. Hanke *et al.* [162] examined the behavior of different xc-functionals including vdW interactions and in particular combinations of different exchange functionals with vdW-DF for the adsorption of ethene on the low index surfaces of Cu. On Cu(111) no prediction of the preferred adsorption site by the experiment was available, but the calculated molecule surface distance and the C-C bond length corresponding to physisorption agreed well with the measured values for all tested functionals [162]. On both surfaces Cu(100) and Cu(110) an adsorption on the on top site and equilibrium distances as well as C-C bond lengths corresponding to a chemisorption are observed [162]. While the adsorption site has been in agreement with the experiment for the (110) surface, it varied from the observed cross-hollow site on the (100) surface. In addition only vdW-DF combined with PBE or revPBE exchange were able to at least predict heights and C-C bond lengths corresponding to chemisorption but both still overestimated the experiment for this particular adsorption site [162]. Regarding these results the authors could not recommend a particular density functional and pointed out that while there is evidence for vdW density functionals performing quite well in the case of physisorbed molecules the ability to reliably predict geometries in the case of mixed metal-molecule bonding states remains an open issue for future work [162]. The ad-

`216 224 432`	N_x, N_y, N_z
`1400.0 0.0 0.0`	G_{cut}
`27.90065 0.00000 0.00000`	a_1
`0.00000 28.99521 0.00000`	a_2
`0.00000 0.00000 54.67389`	a_3
`0.725405611557`	$n(x, y, z)$
⋮	

Figure 3.1.: Header of an example inputfile for JuNoLo. N_x, N_y, N_z are the number of grid points for the three spatial directions, a_1, a_2, a_3 are the lattice vectors on units of bohr and $n(x, y, z)$ is the charge density with the z coordinate as the fastest running index.

sorption energies were increased by the vdW functionals especially for the physisorbed adsorption site with respect to those obtained by the PBE functional [162].

For the physisorption of H_2 on the atop site of Cu(111) K. Lee *et al.* calculated and compared to experimental results PECs using vdW-DF1 and vdW-DF2 [153]. The equilibrium distances and potential well depths of 3.8 Å and −53 meV with vdW-DF1 and 3.6 Å and −39 meV with vdW-DF2 compared better with the experimental results 3.5 Å and −29 meV than the previously discussed semi-empirical approaches DFT-D3 and TS-vdW [153]. In contrast to the semi-empirical approaches both vdW-DF1 and vdW-DF2, which gave an improvement upon its older version for both the equilibrium distance and the well depth, were able to account for charge redistributions at the surface [153].

It seams to be a common message of the just discussed literature that first of all at the moment there is no final solution to correctly account for vdW interactions without sacrificing the speed of DFT in the GGA and second the performance of a given correction scheme is like for all xc-functionals strongly system dependent. Semi-empirical methods in their most recent versions give promising geometries but tend to overbind and *ab initio* methods of the vdW-DF type are able to give reasonable adsorption energies but tend to yield too large molecule surface distances. Up to now there is only a small number of studies on organic molecules adsorbed on metal surfaces utilizing the most recent versions of vdW-schemes and thus it is not clear how these two statements transfer to DFT-D3 or rVV10. The study presented in Chapter 4 and [16] will contribute to a clarification of this issue. The accuracy of the different approaches to deal with vdW interactions in DFT is improving with every generation. A general assessment of the methods is not available and thus we have to do careful checks on the accuracy of the correction schemes applied in this thesis as it will be done in Chapter 4. Another open question is the behavior of vdW-interactions for magnetic systems. While higher level methods include spin in a natural way the here discussed schemes do not include spin explicitly. VdW interactions are considered to be due to spontaneous virtual dipole excitations and as in a magnetic system the energy difference to the excited states de-

pends on the spin, dipole excitations with the smaller energy gap to overcome occur statistically more often. From a theoretical point of view the issue of spin in vdW is addressed in Appendix A where a spin dependent formalism for vdW-DF is given. Only very recently M. Obota *et al.* [175] have published a study applying a spin dependent approximate version of vdW-DF.

3.3. vdW-DF in JuNoLo

The original JuNoLo code calculates the non local part of the correlation energy by massively parallelized direct integration of Equation 3.16. This approach has the disadvantage that its computational cost makes self-consistent implementations of vdW-DF not impossible as the potential can be calculated [176] but very expensive. The Soler approach [115] allows for selfconsistent calculations on the cost only slightly larger than a normal GGA calculation. Within the Soler approach Equation 3.16 is brought by expanding the kernel $\phi(q, q', |\mathbf{r} - \mathbf{r}'|)$ in q and q' to the form

$$E_c^{\mathrm{NL}}[n] = \frac{1}{2} \sum_{\alpha,\beta} \int \Theta_\alpha^*(\mathbf{k})\, \Theta_\beta(\mathbf{k})\, \phi_{\alpha\beta}(k)\, \mathrm{d}^3\mathbf{k}, \tag{3.17}$$

where the sum runs over all interpolation points α, β, the integration runs over the first BZ and $\Theta_\alpha(\mathbf{k})$ is the Fourier transform of $\Theta_\alpha(\mathbf{r}) = n(\mathbf{r}) p_\alpha(q(\mathbf{r}))$ with $p_\alpha(q(\mathbf{r}))$ being the expansion polynomials. The intention of upgrading JuNoLo with the Soler scheme was to provide a set of subroutines which can be called from an arbitrary DFT code in order to implement vdW-DF selfconsistently. The difference in the parallelization between the original JuNoLo and the updated version then led to an independent program which inherited the format of the original JuNoLo inputfile. An example for an inputfile is shown in Figure 3.1. The first line of the inputfile holds the number of grid points N_x, N_y, N_z in all three spatial dimensions. The second line is in the original JuNoLo code used to shift the origin of the simulation cell. This option is not available in the updated version and thus the first entry of the second line will be used to enter the cutoff for the reciprocal space integration G_{cut}. If the code is used to calculate the non local correlation energy based on a charge density obtained with the VASP code the value of ENAUG from the OUTCAR file would be the appropriate number to have consistent cut-off energies. In the next lines the lattice vectors in bohr and the charge density in units of $(1/\mathrm{bohr})^3$ have to be provided. These are also the required quantities which have to be provided when the subroutines are called by another DFT code.

The Soler approach relies on Fourier transforms. In this specific implementation FTs are needed in two different places: for the calculation of the gradient of the charge density and to Fourier transform the θ_α occurring in Equation 3.17. At compilation either FFTW [177] or the FFT of the intel MKL library both in serial or parallel can be chosen. If other versions of FFT need to be used the subroutine taking the direction

of the transform and the array to be transformed as input has to be modified. The FT is also the point which determines the efficiency of the parallelization and leads to the different strategy as compared to the original JuNoLo. First of all each process taking part in the FT needs at least one complete two dimensional slice of the three dimensional array. This limits the total number of processes over which the FT is parallelized to the number of grid points in the third spatial direction. Second the parallel FT is most efficient in the case that the number of grid points in the third spatial dimension is an integer multiple of the number of processes involved in the FT. Otherwise the workload over the processes will be unbalanced.

4 Semi-empirical dispersion versus *ab initio* correlation effects

4.1. Thiophene on Cu(111)

One goal of molecular based nano electronics is to build electronic devices by adsorbing organic molecules on a substrate which can be combined to integrated circuits. This has been achieved by Smits *et al.* for SAMFETs[1] made of oligothiophene on SiO_2 [178]. Oligothiophene was chosen because of its well known conducting properties. As spacer they used an aliphatic chain which helped forming the SAM. The molecules were then connected to a lithographically established Au contact on a SiO_2 wafer. From these SAMFETs it was possible to build an integrated circuit. Molecular wires made of oligothiophenes adsorbed on an insulating NaCl bilayer on Cu(111) have been studied by Repp *et al.* [179] by STM and STS. The authors have shown that in these wires the small distance between electronic energy levels leads to a coherent coupling of the electronic and nuclear motions. For this kind of coupling the Born-Oppenheimer-Approximation does not hold anymore. This beyond Born-Oppenheimer regime might be useful for future applications in molecular electronics e.g. for the mechanical control of electron transport in molecular wires. Sändig *et al.* [180] have studied the adsorption of 6-thiophene and its rotamers on Au(111) by the so called "glue model" [181] which is a formulation of the embedded atom method. In contrast to the free 6-thiophene molecule in the gas phase, where the all trans configuration[2] is the most stable one, the study by Sändig *et al.* [180] shows that the molecules adsorb in the all cis banana shape[3]. The adsorption is driven

[1] self assembled monolayer field effect transistor

[2] In the all trans configuration the S atoms of two neighboring thiophene molecules within the 6-thiophene molecule point in opposite directions.

[3] In the all cis shape the S atoms of two neighboring thiophene molecules within the 6 thiophene molecule point in the same direction, which leads to a curved, banana like shape.

by the interaction of the induced molecular dipole and the metal. The single thiophene molecule adsorbed on Ni(110) [48], Ni(100), Cu(100) and Pd(100) [182], Cu(110) [171] and Cu(111) [144] has been studied theoretically by means of DFT calculations. The first article [48] focusses on the desulfurization reaction of thiophene which occurs on the strongly interacting Ni(110) surface. The authors identify adsorption configurations with dissociated thiophene molecules and propose reaction paths having a rather small activation barrier. Orita and Itoh also find stable dissociated adsorption configurations for single thiophene on Ni(100) but not for the less reactive Cu(100) and Pd(100) [182]. The article by P. Sony *et al.* [171] is usually cited in the context of corrections to DFT with respect to dispersion interactions. They studied the adsorption of single thiophene molecules adsorbed on Cu(110) with the help of the non local vdW-DF functional and concluded that the binding of thiophene to the Cu(110) surface is only due to vdW interactions. K. Tonigold and A. Gross came to a similar conclusion in their study on the adsorption of small aromatic molecules on Cu(111) and Au(111) [144] with the semi empirical DFT-D2 method to account for vdW-interactions.

An experimental study directly corresponding to the calculations reported in this work has been performed by Kakudate *et al.* [183]. They have investigated by means of STM measurements the adsorption of 8-thiophene on the Cu(111) surface at room temperature. The 8-thiophene molecules adsorb in chainlike structures on the surface. For low coverages the chains are oriented in the $\langle 11\bar{2} \rangle$ surface direction. When the coverage of 8-thiophene molecules was increased, which leads to a decrease of the number of possible adsorption sites for molecules oriented along the $\langle 11\bar{2} \rangle$ direction, also molecules oriented in the $\langle 110 \rangle$ direction connecting two chains can be observed. The proportions of the 8-thiophene molecule and the Cu(111) surface are such that in the case of the 8-thiophene molecule oriented in the $\langle 110 \rangle$ direction every S atom would be located directly above a Cu atom. For a 8-thiophene molecule oriented in the $\langle 11\bar{2} \rangle$ direction this is not the case. Thus, the authors emphasized that for the molecules oriented in the $\langle 11\bar{2} \rangle$ direction the distance between two single thiophene units was 4.4 Å which is roughly 10% larger than the normal distance of 3.9 Å [183]. With these elongated molecules the match between the geometric structures of the molecules and the surface will be reversed with respect to the orientation of the 8-thiophene molecules.

Experimental results investigating the adsorption of single thiophene molecules on the Cu(111) surface can be found in [184–187]. These are NIXSW and NEXAFS measurements by which the authors were able to determine the adsorption site, the molecule surface distance and the tilt angle of the single thiophene molecules for different coverages. As it can be seen from Table 4.1, where the main results of the just mentioned studies have been gathered, there are some differences between the results. Thus, there is no definite picture how the single thiophene molecule adsorbs on Cu(111) from the experimental side. The temperature programmed desorption (TPD) experiment done by P. K. Milligan *et al.* provides an adsorption energy of -0.590 eV [185].

The motivation for the oligothiophene adsorbed on the Cu(111) surface is to use them as molecular wires and by this to further reduce the dimensions of electronic devices to

Table 4.1.: Experimental results for the tilt angle of the molecule with respect to the surface, the adsorption site, and the molecule surface distance $d_{\text{S-Cu}}$ for the adsorption of thiophene on Cu(111) obtained from NIXSW and NEXAFS for different coverages.

Reference	Method	Coverage	Orientation	Adsorption Site	$d_{\text{S-Cu}}$/Å
[184]	NIXSW NEXAFS	0.06 ± 0.01 ML *0.13 ML = 1ML	(roughly) flat	top	2.6 ± 0.05
[185]	NIXSW	Defect site	0-7	uncertain	< 2.62 ± 0.03
	NEXAFS	Terrace	26	top	2.62 ± 0.03
		0.03 ML	12 ± 2		
		0.05 ML	20 ± 3		2.62 ± 0.03
		0.1 ML	25 ± 4		
		0.12 ML	41 ± 6	top	2.83 ± 0.05
		0.14 ML	45 ± 6	top	2.83 ± 0.05
		0.18 ML (multilayer)	55 ± 8		
		0.23 ML (multilayer)	54 ± 8		
[186]	NIXSW NEXAFS		(roughly) flat	top	2.7 ± 0.05
[187]	NEXAFS SEXAFS	0.07 ML *0.11 ML = 1ML	flat		2.5 ± 0.02

the scale of several or even single molecules e.g. by contacting one oligothiophene on both ends with the tips of a STM and using the molecule as a wire. In this section we are going to study the adsorption behavior of single thiophene molecules, their dimers, 4-thiophene as a representative of oligothiophenes and dimers of 4-thiophene on the Cu(111) surface. The section is organized as follows: First we will discuss the single thiophene and its dimer as well as 4-thiophene and its dimer in the gas phase. Then we will give the parameters of the calculations, discuss the geometric and the electronic structures and also compare our results with recent experiments where available. Most of the results presented in this section have been already published in [16].

We optimized the geometry of a single thiophene molecule in a 15 Å × 15 Å × 15 Å and 4T in a 25 Å × 15 Å × 15 Å large, empty box. We used the hard PAW pseudopotentials for C, H and S from the VASP database. The cutoff energy was chosen to be 700 eV in order to obtain bond lengths and bond angles which are within deviation from the experiment and from recent DFT calculations [144]. The calculated dipole moment of the single thiophene molecule is 0.41 D which is close to the value obtained in [144]. The 4T molecule has been calculated in the all trans configuration which is the proposed

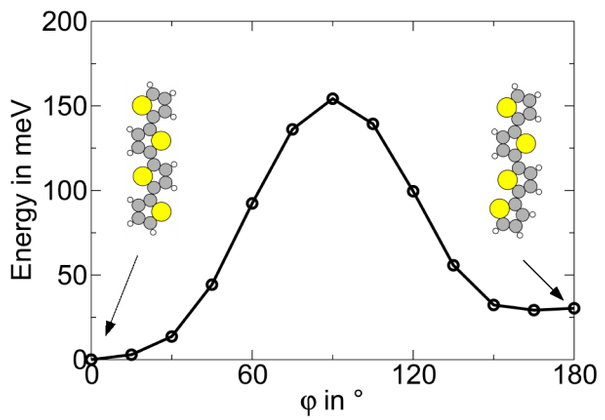

Figure 4.1.: Energy difference with respect to the optimized geometry of the 4T molecule upon rigid rotation along the 2,2' C-bond. The barrier height for rotating one part of the 4-thiophene molecule is only 160 meV.

configuration of [183], thus the total dipole moment of the molecule vanishes. The energy cost to rotate one thiophene unit of the 4T molecule from the trans to the cis configuration has been calculated by successively rotating one thiophene unit around the 2,2' C-C bond to the next thiophene unit. The resulting curve of the energy as a function of the rotation angle is depicted in Figure 4.1. The barrier height for the rotation of one thiophene unit from the trans to the cis configuration is 160 meV. Previously published results regarding the change of bithiophene from the cis to the trans conformation show similar values [188, 189]. Because of this low barrier we have to expect upright standing molecules with rotated parts as it has been studied for terpyridine on Cu(111) by Shi *et al.* [190] although in their study the authors have found that flat physisorption is favored with respect to chemisorption.

To prepare for the later calculations of dimers of thiophene and 4T adsorbed on the Cu(111) surface, we also studied the molecules in the gas phase. The 1T dimers have been calculated in a large empty box in four different configurations, which are shown adsorbed on the Cu(111) surface in Figure 4.4. Except for configuration (d) all configurations are within computational accuracy equal in energy and are only weakly bound. The distance between the geometric centers of the two molecules is 6.81 Å, 6.61 Å, 6.57 Å and 4.61 Å for configuration a, b, c and d. This picture is not changed by adding vdW corrections, neither by DFT-D2 nor DFT-D3. The absolute values of the binding energies are increased by the inclusion of vdW corrections but they are still within error bars equal and the distance between the two molecules is changed by

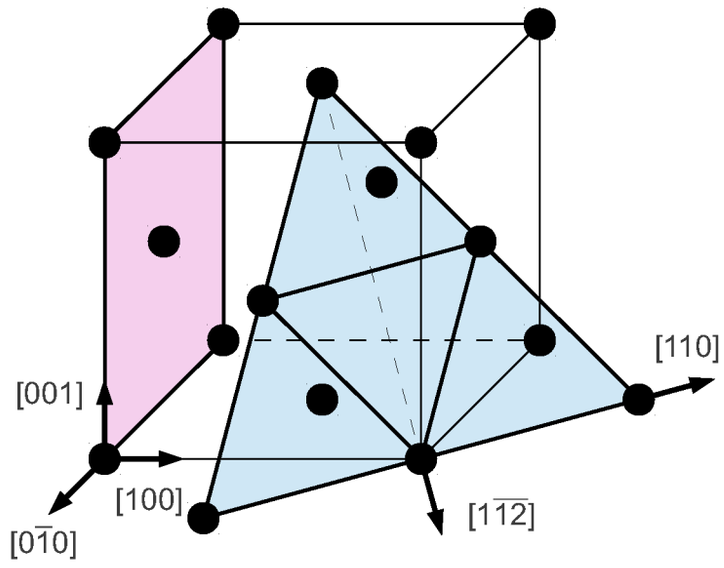

Figure 4.2.: Schematic of the fcc cell to visualize the crystallographic directions needed throughout the discussion in this chapter. The blue area represents the hexagonal (111) surface plane of the fcc lattice and the red area the (100) surface plane. The [110] direction along the nearest neighbor atoms and the $[1\bar{1}\bar{2}]$ along the diagonal of the diamond spanning the hexagon of the (111) surface are depicted.

less than 0.01 Å. The same holds true for 4T dimers, where we checked whether the molecules like to stack either by completely overlapping or by overlapping at only one thiophene part. The latter case is slightly preferred but the energy differences are with at most 12 meV small.

As an initial step we studied the adsorption geometry of single thiophene molecules on the Cu(111) surface. By this we can get a first guess how the oligothiophene chains would adsorb on the surface e.g. where the S atoms of the molecule like to adsorb and in which direction the rest of the molecule is oriented. For the single thiophene molecule we used a $5 \times 3\sqrt{3}$ supercell with respect to the unit cell of the (111)-surface. This choice leads to a 12.86 Å distance between periodically repeated images of the thiophene molecule in x direction and 13.37 Å in y direction. The in our method intrinsic interaction between periodic images should by this be reduced to a minimum which means we are really dealing with a single thiophene molecule adsorbed on Cu(111). For the study of single thiophene dimers adsorbed on the Cu(111) surface we took the relaxed geometries of the dimers from the gas phase and adsorbed them on the surface such that one of

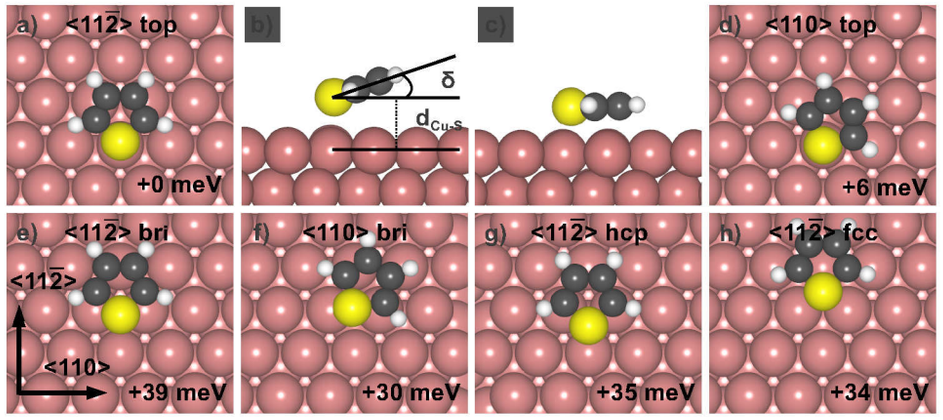

Figure 4.3.: (a) single thiophene molecule in the relaxed configuration. The molecule adsorbs on the top position with the molecular c_2-axis oriented along the $\langle 11\bar{2}\rangle$ surface direction. (b) side view of the single thiophene molecule. The tilt angle $\delta = 18°$ goes to zero when vdW corrections are included (c). (d) - (h) other adsorption configurations with the S atom occupying the high symmetry adsorption positions top, bridge, fcc- and hcp-hollow of the (111) surface with the molecule oriented in $\langle 11\bar{2}\rangle$ or $\langle 110\rangle$. The directions on the (111) surface are indicated in (e). Energy differences are given with respect to the lowest energy configuration depicted in (a) which defines the zero.

the two molecules lies in the most stable geometry of a single thiophene molecule on the surface. In order to minimize the interaction with periodically repeated images of the molecules we used a $6 \times 4\sqrt{3}$ supercell. For the 4-thiophene (4T) molecule we extended the supercell used for a single thiophene molecule to a rectangular $9 \times 3\sqrt{3}$ supercell. The distance between the 4T molecules in neighboring unit cells is at least 6.84 Å. For dimers of 4-thiophene we chose a $14 \times 4\sqrt{3}$ supercell. Except for the calculations regarding the dimers of 4-thiophene the Cu(111) surface was represented by a slab consisting of six layers with the computationally obtained lattice constant of Cu $a_0 = 3.63$ Å. Due to computational costs the number of Cu layers had to be reduced to three for the calculations of the 4-thiophene dimers. While the adsorption geometry is not very sensitive to the number of metal layers greater than three, the electronic structure might be influenced as the correct description of the Cu(111) surface requires a greater number of layers. The Cu(111) slab was separated from its mirror image in z direction by 13 Å of vacuum. As cutoff energy for the calculations 500 eV has been chosen. For the Brillouin-Zone integration we used the $\mathbf{\Gamma}$-point during relaxations. The molecules and the uppermost three layers of the surface were allowed to relax until the forces acting on each atom became smaller than 0.003 eV/Å. In the case of 4T dimers only the uppermost Cu layer was free to relax.

As possible adsorption sites we calculated configurations with the S atom occupying the top position, the bridge site and the fcc or hcp hollow sites of the Cu(111) surface, which are the positions of high symmetry for the (111) surface. The top site is directly on top of a Cu atom of the first surface layer. The hcp and fcc hollow sites are on top of Cu atoms in the second and third layer respectively. The bridge site is on the center between two surface atoms. The top and the two hollow sites fcc and hcp have a threefold symmetry while the bridge position is only twofold symmetric. As starting orientation the molecule was oriented in $\langle 110 \rangle$ or in $\langle 11\bar{2} \rangle$ direction of the surface or perpendicular to the surface. We also calculated one orientation rotated by 15 ° with respect to the $\langle 11\bar{2} \rangle$ direction in order to get a better understanding of the structure of the potential energy surface but this configuration was not stable and the molecule rotated back to the $\langle 11\bar{2} \rangle$ direction. Within DFT the most stable adsorption position turned out to be with the S atom adsorbed almost on top of a Cu atom with the molecule oriented in $\langle 11\bar{2} \rangle$ direction. The S is 0.18 Å in $\langle 11\bar{2} \rangle$ direction away from the exact on top position. The distance between the S atom and the Cu atom underneath is 2.67 Å. A change of the orientation to the $\langle 110 \rangle$ direction leads to an energy difference of 6 meV which is rather small and roughly represents the accuracy limit of our calculations. The energy difference when moving the S atom from the top to the bridge position while keeping the orientation of the molecule fixed is with 39 meV more significant. Thus, for the adsorption of single thiophene molecules on the Cu(111) surface it is more important where the S atom is located than how the molecule is oriented. Experiments for thiophene on Au(111) show that the molecule adsorbs in an upright standing configuration for densely packed structures [191, 192]. Although Tonigold *et al.* in their calculations did not find stable configurations with upright standing thiophene molecules on Au(111) we also checked this case for Cu(111) because when we study later dimers of thiophene adsorbed on the surface a $\pi-\pi$ stacked chain of thiophene molecules could be a stable solution. Except for the configuration with S over the bridge position, which is 116 meV and thus significantly higher in energy than the most stable configuration, the perpendicular configurations were not stable and relaxed to the already known flat geometries. The relaxation of the surface will be shortly discussed now as the adsorption of S containing species on the Cu(111) surface has been shown to induce significant distortions of surfaces. For the adsorption of single S atoms on the Cu(111) surface a coverage dependent displacement of nearest neighbor atoms up to 0.1 Å for the lowest coverage has been reported [193] due to the strong interaction of the S atom with the Cu surface atoms. In the case of a single thiophene molecule adsorbed on the Cu(111) surface the maximum displacement of nearest neighbor atoms of the uppermost surface layer is 0.03 Å and thus much less pronounced than for the single S atom. The largest distortion in our case is that the Cu atom underneath the S atom is pulled out of the surface plane by 0.1 Å.

In Figure 4.3 (b) the side view of the thiophene molecule adsorbed on the Cu(111) surface shows that the molecule is not adsorbed flat but tilted with respect to the plane of the surface by an angle $\delta = 18\,^{\circ}$. As the tilt angle as well as the molecule surface distance depend crucially on the correct description of dispersion interaction, we also did

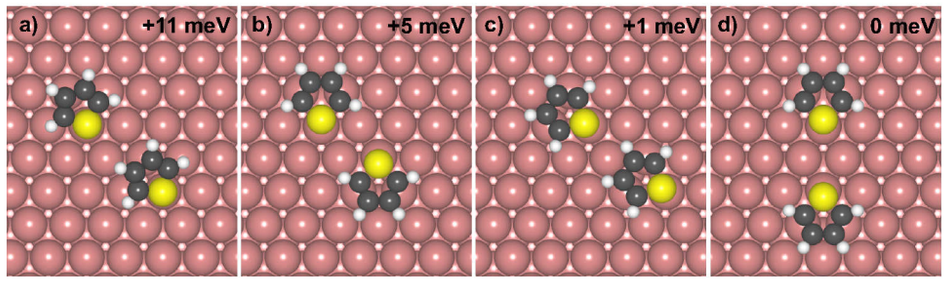

Figure 4.4.: Relaxed adsorption configurations of dimers of single thiophene molecules adsorbed on the Cu(111) surface. The energies given are with respect to the state of lowest energy (a).

Table 4.2.: Adsorption energies in eV, molecule surface distances in Å and tilt angles in ° for the single thiophene molecule adsorbed on the Cu(111) surface self consistently calculated with the PBE functional, the DFT-D2 and the DFT-D3 method for comparison with the experiment [185]. The vdW-DF1 adsorption energy evaluated at each particular geometry is given in brackets.

Method	Exp. [185]	PBE	DFT-D2	DFT-D3
E_{ads} (eV)	-0.590	-0.137 (-0.722)	-1.018 (-0.373)	-0.605 (-0.575)
$d_{\mathrm{Cu\text{-}S}}$ (Å)	2.62 ± 0.03	2.67	2.41	2.66
δ (°)	26 ± 5	18	0	9

relaxations for the described configurations using the semi-empirical DFT-D2 and DFT-D3 methods as well as the non-local vdW-DF functional as an attempt to correct for long range dispersion interaction within DFT. When using the DFT-D2 method for the flat lying molecule all starting configurations relaxed towards the already discussed most stable configuration with S on top of Cu and the molecule oriented in $\langle 11\overline{2} \rangle$ direction. The tilt angle δ is decreased to zero and the distance between S and the Cu atom directly underneath is reduced to 2.41 Å. The tilt angle obtained with DFT-D3 is $\delta = 9\,^{\circ}$ and the distance between the molecule and the surface is 2.66 Å which is very close to the PBE result. With the non local vdW-DF2 functional the tilt angle vanishes and the molecule surface distance increases to 3.38 Å.

This can be compared to the results for the adsorption site, the tilt angle and the molecule surface distance of the already mentioned NIXSW and NEXAFS measurements. These experiments have been done by P. K. Milligan *et al.* [184, 185], Imanishi *et al.* [187] and Rousseau *et al.* [186]. Some data from their studies has been gathered in Table 4.1 and the relevant data for the comparison of our calculations is given in Table 4.2. In their extensive study [185] on single thiophene adsorbed on Cu(111) for a set of different

coverages P. K. Milligan *et al.* concluded that thiophene adsorbs in the top position with a tilt angle of $26 \pm 5\,^{\circ}$ and a distance between the S atom and the Cu atom underneath of 2.62 ± 0.03 Å for a coverage of 0.03 ML. 1 ML corresponds to one thiophene molecule per surface atom in their definition. Applying this definition to our system leads to a coverage of 0.033 ML. Thus, our coverage is comparable to the experiment. When comparing the adsorption geometry all applied methods PBE, DFT-D2, DFT-D3 and vdW-DF yield the correct adsorption site. While the distance between the S atom and the Cu atom predicted by PBE and DFT-D3 is in agreement with the experiment the DFT-D2 methods underestimates the molecule surface distance and vdW-DF yields a way too large distance. In addition, at variance with the experiment, both DFT-D2 and vdW-DF predict a flat lying thiophene molecule. Thus, from this comparison we can conclude that the PBE functional describes the adsorption geometry of thiophene adsorbed on Cu(111) well and among the tested methods to account for long range dispersion interactions DFT-D3 is closest to the experiment.

In the following we will address how dimers of single thiophene adsorb on the Cu(111) surface. In all relaxed configurations depicted in Figure 4.4 both S atoms occupy a top position of the Cu(111) surface and in most of them both molecules are oriented in the $\langle 11\overline{2} \rangle$ direction. The tilt angle is the same for both molecules as for a single thiophene molecule. In the most stable configuration both S atoms are facing each other being adsorbed on nearest neighbor Cu atoms in $\langle 11\overline{2} \rangle$ direction. The molecules are separated by a distance of 8.8 Å between their geometric centers. The distance between the S atoms and the Cu atoms underneath is 2.58 Å calculated with the PBE functional and 2.40 Å with DFT-D2, which is slightly shorter than for a single thiophene molecule. The energy differences between the relaxed adsorption configurations calculated with the PBE functional are with at most 11 meV similarly small as in the single thiophene case. This suggests that a larger number of different geometrical configurations can be observed experimentally. However, when accounting for dispersion interactions via the DFT-D2 scheme the energy difference between the most stable configuration and the least stable configuration increases to 103 meV.

Kakudate *et al.* [183] observed in their STM study of 8-thiophene adsorbed on Cu(111) done at room temperature chain like structures oriented in $\langle 11\overline{2} \rangle$ for low coverages. When increasing the coverage and thus the available space for molecules oriented in $\langle 11\overline{2} \rangle$ gets filled, 8-thiophene molecules also adsorb oriented in the $\langle 110 \rangle$ direction. We investigated the already computational demanding adsorption of 4-thiophene on the Cu(111) surface as a model for the larger system studied in the experiment. Besides the configurations having the two different orientations in $\langle 11\overline{2} \rangle$ and in $\langle 110 \rangle$ direction we also examined a configuration with the short axis of the molecule perpendicular to the surface, but this configuration has not been stable i.e. it relaxed back to the flat adsorption geometries. For the single thiophene molecule the S atom adsorbed directly on top of a Cu atom in the most stable geometry. This fact favors the 4-thiophene molecule oriented in the $\langle 110 \rangle$ direction because in this case the match between the size of the molecule and the distance between the Cu atoms of the surface is perfect and every

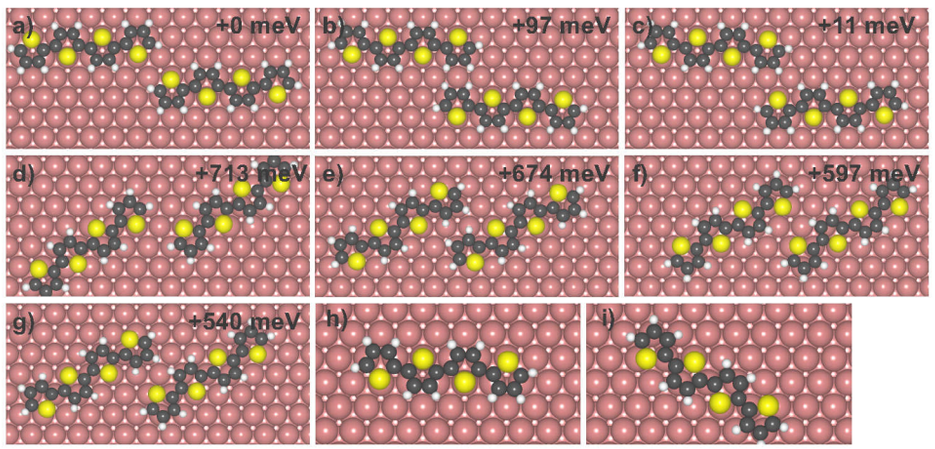

Figure 4.5.: (a-g) relaxed geometries of 4-thiophene dimers adsorbed on Cu(111) with different orientations. Energy differences are given with respect to the lowest energy configuration depicted in (a) which defines the zero. (g)-(i) relaxed configuration of single 4-thiophene molecules adsorbed on Cu(111) oriented in $\langle 110 \rangle$ and $\langle 11\bar{2} \rangle$ direction.

S atom of 4-thiophene is able to occupy a top position. This reasoning is reflected by the results of our calculations. With the PBE functional the configuration with 4-thiophene oriented in the $\langle 110 \rangle$ direction is more stable and the energy difference is 58 meV. The calculations with the DFT-D2 method yields an energy difference of 251 meV in favor for the molecule oriented in $\langle 110 \rangle$. Also computing an energy difference of 107 meV with the post-processing method of vdW-DF1 based on the PBE geometry and charge density does not change this energetic order. Thus, our calculations predict for the adsorption of 4-thiophene on the Cu(111) an orientation of the molecule which is opposite to the orientation observed in the experiment. The 4-thiophene molecule adsorbed on the Cu(111) surface is slightly bent. The distance between the S atoms of the outer two thiophene units and the Cu atoms directly underneath them obtained with the PBE functional is with a value of 3.02 Å shorter than the molecule surface distance of the central two thiophene units, which is 3.10 Å. But both distances are significantly larger than the molecule surface distance of the single thiophene molecule. DFT-D2 results in a less bent geometry with again much shorter distances between S and Cu of 2.41 Å and 2.49 Å for both the outer and the central two thiophene units.

The adsorption of a second 4-thiophene molecule on Cu(111) to form a dimer is our model for the molecular chains observed in the experiment. However, the preferences for the $\langle 110 \rangle$ direction which has been shown in the last paragraph is conserved. The most stable configuration of a 4-thiophene dimer oriented in the $\langle 11\bar{2} \rangle$ is still 0.5 eV with DFT-D2 higher in energy than the least stable configuration oriented in the $\langle 110 \rangle$ direction.

Table 4.3.: Adsorption energies per molecule of single thiophene, a dimer of single thiophene, 4-thiophene and a dimer of 4-thiophene adsorbed on Cu(111) calculated with the PBE functional and the DFT-D2 method in eV.

Molecule	Configuration	PBE	DFT-D2
Thiophene	Fig. 4.3 (a)	-0.137	-1.018
Thiophene dimer	Fig. 4.4 (d)	-0.148	-1.112
4-thiophene	Fig. 4.5 (h)	-0.344	-3.554
4-thiophene dimer	Fig. 4.5 (a)	-0.392	-3.636

Kakudate *et al.* [183] observed in their experiment a distance of 4.4 Å between two bright lobes which have been assigned to single thiophene units of the 8-thiophene molecule. This distance is larger than the 3.9 Å which an 8-thiophene molecule would have in the gas phase. These elongated 8-thiophene molecules would reverse the energetic order of the two different orientations due to the perfect match between the geometric structures of the molecule and the surface as the distance between two single thiophene units in the elongated 8-thiophene molecule would be very similar to the distance between two Cu atoms in the $\langle 11\overline{2} \rangle$ direction. Thus, we repeated the calculations of 4-thiophene dimers on the Cu(111) surface with elongated molecules in order to check the validity of the just described scenario. When the elongated 4-thiophene molecules are allowed to freely relax on the Cu(111) they immediately return to their not stretched state due to the large amount of energy required to elongate the intramolecular bonds. If we fix the position of the S atoms above the Cu atoms and by this force the molecules to stay in their elongated shape the final configuration is 5.56 eV higher in energy than the corresponding configuration with not stretched molecules. In consequence our calculations have shown that the scenario of elongated 4-thiophene molecules oriented in $\langle 11\overline{2} \rangle$ direction is energetically not stable.

The adsorption energy of single thiophene molecules on the Cu(111) surface has been measured experimentally by P. K. Milligan *et al.* [185]. Its value -0.59 eV suggests that thiophene is weakly chemisorbed on the Cu(111) surface. Calculated with the PBE functional the adsorption energy is -0.137 eV where negative values mean that the molecule is bound to the surface and the adsorption energy has been obtained as the difference of total energies of the combined system and the sum of the clean surface and the molecule in the gas phase:

$$E_{\text{ads}} = E_{\text{1T/Cu(111)}} - E_{\text{Cu(111)}} - E_{\text{1T}} \tag{4.1}$$

Previous calculations [144] resulted in a less strong adsorption energy of -0.070 eV. One reason for this difference is the smaller supercell in their case, which corresponds to a higher coverage. They also used different parameters for their calculations: a lower cutoff energy of 400 eV, five layers of Cu to model the surface slab and consistently with their smaller supercell a $4 \times 4 \times 1$ **k**-point mesh. Unlike the molecule surface distance,

which was already reasonably predicted by the PBE functional, the adsorption energy is underestimated by our PBE calculations when compared to the experimental value of -0.590 eV [185]. When we compute the adsorption energy at the PBE geometry with the vdW-DF1 functional we obtain -0.722 eV as given in Table 4.2 which indicates a much stronger binding of the molecule to the surface and is closer to the experimental value.

We have also calculated the adsorption energy self consistently with the DFT-D2 and the DFT-D3 approach to correct for long range dispersion interactions within DFT. Applying the DFT-D2 approach leads to an adsorption energy of -1.018 eV. One can observe that DFT-D2 results in a strong binding of the molecule to the surface and overestimates the adsorption energy with respect to the experimental value at a similar order of magnitude as the PBE functional underestimated it. This is mainly due to the fact that DFT-D2 is not sensitive to the chemical environment of the atoms. It treats every atom of a species with the same C_6 coefficient. But in reality the polarizability and thus the C_6 coefficient of the metal atoms further away from the surface should decrease as a function of the distance to their interacting partners due to screening effects of the metal. Mercurio *et al.* proposed in their study [151] a way to achieve an effect similar to the screening of the metal. When calculating the vdW corrections via DFT-D2 they took into account a smaller number of metal layers than have been present in their original calculations. By this they obtain a much better agreement of the adsorption energy with their experimentally obtained value. We followed this proposal for our case of thiophene adsorbed on Cu(111) by subsequently neglecting all Cu layers except for the uppermost one when calculating the dispersion corrections. The adsorption energy using DFT-D2 with only one surface layer taken into account is -806 meV which is closer to the experiment than the original DFT adsorption energy but still not perfect. The main contribution to the difference of 212 eV between the DFT-D2 adsorption energy calculated with all six layers and with only one layer is provided by the first two layers. DFT-D3 which includes the bonding situation of the atoms by distance and coordination number dependent C_6-coefficients leads to a significantly smaller correction of the adsorption energy to -0.605 eV which again is close to and in remarkably good agreement with the experimental value. In fact for all three quantities tilt angle, molecule surface distance and adsorption energy, which are listed for comparison of our calculations with the experiment in Table 4.2, DFT-D2 gives too strong corrections while the DFT-D3 results are more moderate and comparable to the experiment. While the self consistent calculation using the vdW-DF2 functional lead to a way too large molecule surface distance and a vanishing tilt angle the adsorption energy of -0.478 eV is not so far from the experimental adsorption energy.

The adsorption energies per molecule for the single thiophene dimer, the 4 thiophene molecule and the dimer of 4 thiophene molecules which have been calculated with the PBE functional and the DFT-D2 method are listed in Table 4.3. In the last two paragraphs we have shown that PBE and DFT-D2 yield the two extreme cases for the adsorption energy of weak binding in the case of PBE and strong binding in the case

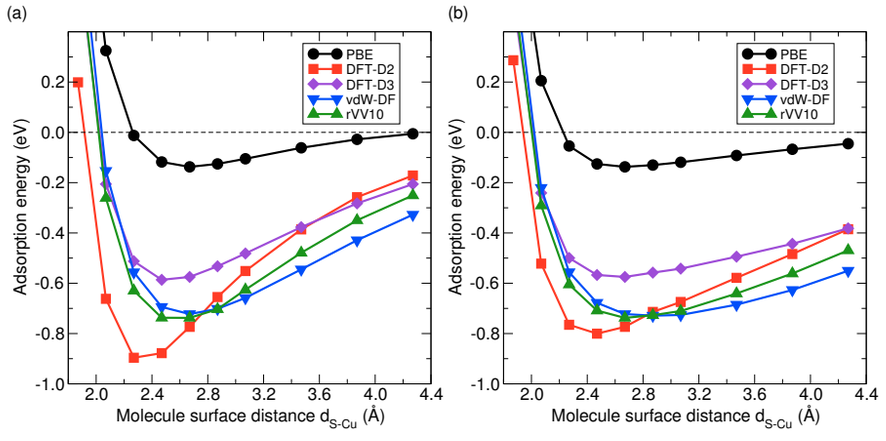

Figure 4.6.: Adsorption energy of a single thiophene molecule adsorbed on Cu(111) as a function of the molecule surface distance calculated with PBE, DFT-D2, DFT-D3, vdW-DF and rVV10. Starting from the PBE geometry the molecule has been rigidly shifted closer or further away from the surface (a) or the Cu-S distance has been fixed while the rest of the molecule was allowed to relax (b).

of DFT-D2. The adsorption energy per molecule of a single thiophene dimer calculated with the PBE functional is -0.148 eV and with the DFT-D2 method -1.112 eV. Both methods yield a slightly stronger binding per molecule for a dimer than for a single thiophene molecule. Thus, the formation of dimers is favored over the adsorption of single molecules on the Cu(111) surface. For the 4-thiophene molecule we obtain an adsorption energy of -0.344 eV with the PBE functional and -3.554 eV with the DFT-D2 method. Overall the 4-thiophene molecule is bound more strongly to the surface than a single thiophene molecule but the adsorption energy of a 4-thiophene molecule is less than four times the adsorption energy of a single thiophene molecule. This is due to the fact that first of all we have six C-H groups less than four single thiophene molecules would have and second the molecule surface distance of the central two thiophene units is larger than it would be for a single thiophene molecule which is an indicator for a less strong binding. Also for 4-thiophene molecules the formation of dimers is favored over the adsorption of single molecules.

Up to now we discussed regarding the correction for dispersion interactions the results from our self consistent calculations which means we computed the forces on the atoms from the dispersion energy and added these forces to the DFT forces. By this procedure we obtained self consistent relaxed coordinates. One can also calculate the adsorption energy as a function of the molecule surface distance by rigidly shifting the molecule

closer to or further away from the surface without further relaxations. The position of the minimum of the curve gives the equilibrium distance between the molecule and the surface and its depth the adsorption energy. An important issue when calculating molecule surface distances and adsorption energies with this procedure is the choice of the geometry and the relevance of structural relaxations for the evaluation of the total energies with the different methods to account for dispersion interactions. The numbers calculated in this way will differ from the self consistently obtained values due to the fact that the geometry assumed for the calculation might not and in most cases will not be the equilibrium geometry belonging to the method under consideration. In Figure 4.6 the adsorption energy of a single thiophene molecule adsorbed on the Cu(111) surface as a function of the molecule surface distance has been plotted for different methods to account for dispersion interactions and different approaches how to treat structural relaxations. First we took the relaxed PBE coordinates, shifted the molecule without further relaxations and calculated the total energy with the different functionals and semi-empirical methods which are depicted in Figure 4.6. The according curves in Figure 4.6 (b) include additional relaxations of the molecule only. To obtain this we fixed the distance between the S atom and the Cu atom and allowed the rest of the molecule to relax. By this procedure we obtain an equilibrium configuration for each particular molecule surface distance. While the equilibrium distance of the self-consistent DFT-D2 calculations is reproduced quite well when additional relaxations of the thiophene molecule are allowed, the unrelaxed curve predicts an even 0.2 Å shorter molecule surface distance. The DFT-D2 adsorption energies extracted from Figure 4.6 (a) and (b) -0.896 eV and -0.801 both underestimate the self-consistent DFT-D2 adsorption energy due to the fact that both geometries used to calculate the adsorption energy are not the equilibrium geometry of the DFT-D2 method. The same conclusions can be drawn for the DFT-D3 results which emphasizes the importance of structural relaxations for an appropriate description of the adsorption energy and the molecule surface distance. For the rVV10 functional up to now unfortunately no self consistent implementation is available in the VASP code. Thus using the post processing approach is the only way to evaluate its performance. The predicted molecule surface distance agrees with the PBE and the DFT-D3 value and thus also with the experiment when relaxations of the molecule are taken into account. Without the additional relaxations the curvature of the binding energy curve obtained with the rVV10 functional shows a tendency towards a slightly shorter molecule surface distance but both the relaxed and the unrelaxed curve have their minimum at 2.67 Å. The adsorption energy without and with relaxations is identical -0.738 meV because both the relaxed and the unrelaxed curve have their minimum at the PBE equilibrium distance. In this case both geometries coincide.

An adsorption energy of -0.137 eV for the single thiophene molecule adsorbed on the Cu(111) surface would suggest that the molecule is physisorbed. The second quantity to look at in order to make this statement definite is the charge transfer. In Figure 4.7 the charge density difference integrated over the plane perpendicular to the [111] direction for both the PBE and the DFT-D2 calculation is plotted which allows us to discuss the

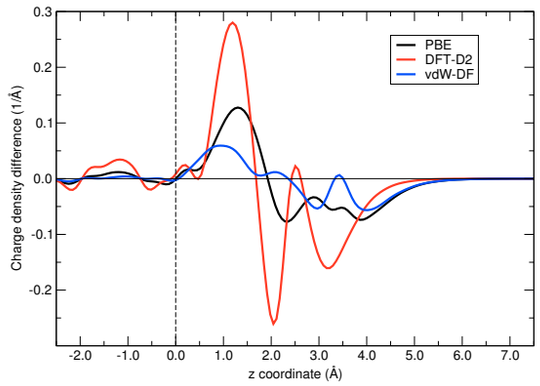

Figure 4.7.: Charge density difference upon adsorption of a single thiophene molecule on the Cu(111) surface integrated over the plane perpendicular to the [111] direction. The position of the uppermost surface layer is at $z = 0$. Overall charge is been transferred from the molecule to the surface. Also a small dipole forms between the molecule and the surface.

charge transfer occurring at the interface. To obtain this image we subtracted the charge density of a single thiophene molecule in the gas phase and the charge density of the clean surface from the total charge density of the molecule adsorbed on the surface and integrated over the surface plane. In order to give a number for the amount of charge transferred from the molecule to the surface one has to define a surface separating the thiophene molecule and the Cu(111) surface. This will lead to a rather rough estimate of the charge transfer, which gives a hint of the order of magnitude of the effect. These kind of estimation for the transferred charge has also been done by Rusu et al. [194] for PTCDA[4] adsorbed on different metal surfaces. The amount of charge transferred can be estimated by

$$q = -\int_{z_0} \Delta n(z) \mathrm{d}z, \tag{4.2}$$

where z_0 is the point where the charge density difference integrated over the surface direction $\Delta n(z)$ depicted in Figure 4.7 equals zero in the region between the molecule and the surface. This point z_0 defines the aforementioned surface separating the thiophene molecule and the Cu(111) surface. By following this procedure we obtain ≈ 0.1 electrons transferred from the molecule to the interface for the PBE calculation and ≈ 0.2 for the DFT-D2 calculation. With the non local vdW-DF2 functional the charge transferred from the molecule to the interface amounts to ≈ 0.06 electrons. These numbers show

[4] 3,4,9,10-perylene-tetra-carboxylic-di-anihydride

us that the charge transfer for thiophene adsorbed on Cu(111) is small compared to the charge transfer obtained for PTCDA [194]. Kiguchi et al. observed in their XPS[5] experiments [195] for 6-thiophene films on Cu(111) that the position of the principal peak in the spectrum did not change as a function of the substrate temperature and the film thickness. From this they conclude that the interaction of 6-thiophene with the surface is weak and the charge transfer must be very small. Keeping in mind that we have investigated single thiophene molecules instead of 6-thiophene and used a much lower coverage this can only be seen as a small hint not to expect very large charge transfer and thus support our very small numbers. In Figure 4.8 (a) a section of the three dimensional charge density difference with a plane cutting through the center of the thiophene molecule is shown, from which we can see that charge rearranges at the molecular side. In addition charge accumulates at the interface between the S and the Cu atom which is due to the formation of weak chemical bond. The charge rearrangement at the molecular side shows that not only the S lone pair contributes to the chemical bond but also the π electron system. Thus, regarding the small adsorption energy we are dealing in this case with weak chemisorption.

Because of the large difference between the PBE adsorption energy -0.137 eV and the adsorption energy calculated with the vdW-DF functional -0.722 eV at the PBE geometry and with the PBE charge density, it is worth to have a closer look at the correlation energy term of the total energy. When in both calculations the same exchange functional is used the difference in the adsorption energies $\Delta E_{\mathrm{ads}} = E_{\mathrm{ads}}^{\mathrm{PBE}} - E_{\mathrm{ads}}^{\mathrm{vdW\text{-}DF}}$ equals the difference of the correlation binding energies of both functionals. In particular both functionals include the LDA correlation thus the difference arises only from the semi-local correction to LDA in the case of the PBE functional and from the non-local correction to LDA in case of the vdW-DF functional: $\Delta E_{\mathrm{ads}} = \Delta E_{\mathrm{c}}^{\mathrm{SL}} - \Delta E_{\mathrm{c}}^{\mathrm{NL}}$. The real space correlation binding energy densities, which are according to the charge density difference defined as the difference of the correlation energy density of the total system and the sum of the correlation energy densities of the clean Cu(111) surface and the single thiophene molecule in the gas phase, are shown in Figure 4.8 for the PBE, the DFT-D2 and the vdW-DF2 relaxed geometry. The LDA correlation binding energy density depicted in Figure 4.8 (b) follows closely the charge density difference due to the functional form of the LDA. The largest negative contribution comes from the area at the interface between the Cu atom and the S atom where the weak chemical bond is formed. The semi-local correlation binding energy density is the semi-local correction to the LDA correlation used in the PBE functional. It is spatially confined to a similar region as the LDA correlation binding energy density. The main difference is the slightly larger spatial extension due to the additional information about the surrounding of each charge density point from the charge density gradient entering the correlation energy density. In contrast to the semi local correction to the correlation binding energy density the non local correlation relates not only points from the direct neighborhood to each

[5] x-ray photoelectron spectroscopy

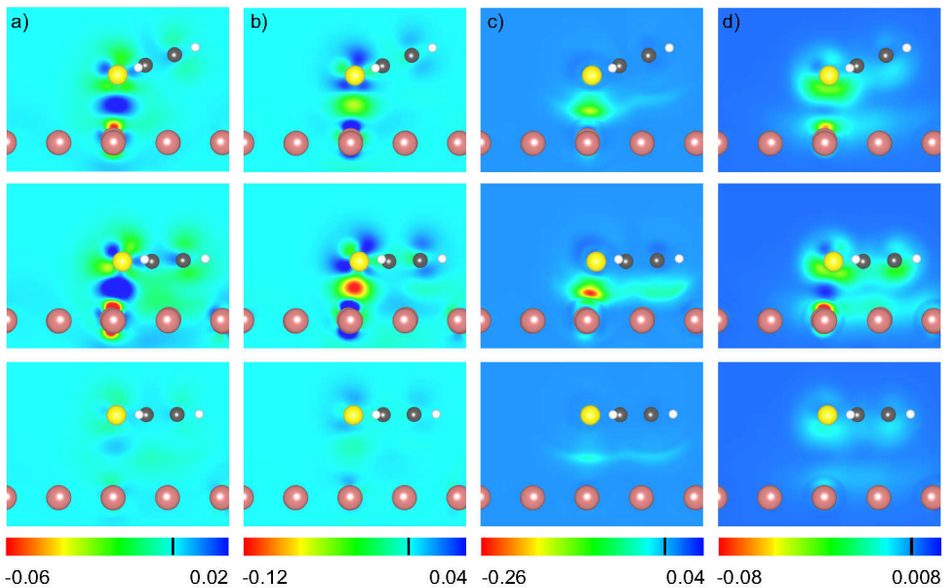

Figure 4.8.: The columns show from left to right the charge density difference (a), the LDA correlation binding energy density (b), the semi local correction (c) and the non local correction (d) to the correlation binding energy density on a plane cutting through the center of the thiophene molecule adsorbed on Cu(111) in the from top to bottom relaxed PBE, DFT-D2 and vdW-DF2 geometry. The same color scale has been used for each particular set of densities. The black line in the color bar indicates the position of the zero.

other but basically the whole unit cell in real space. Thus, also regions can contribute to the correlation binding energy density which did not have an impact in the LDA or the semi local case. In the right hand column of Figure 4.8 (d) the non local correlation is mainly localized around the S atom and the Cu atoms of the first surface layer while LDA and the semi local correction have been localized in the area between those atoms where the weak chemical bond is formed. The overall behavior does not change when we perform the same analysis for the other two geometries shown in Figure 4.8. The change of the strength of the depicted quantity corresponds to the change of the interaction strength when going from weakest to strongest vdW-DF2 over PBE to DFT-D2.

In Figure 4.9 the PDOS for the single thiophene molecule adsorbed on Cu(111) is shown for the equilibrium geometries obtained with and without vdW corrections. The upper panel shows projections onto s and p states of the thiophene molecule obtained from the PBE, the DFT-D2 and the self-consistent vdW-DF2 calculation which would correspond to σ and π type orbitals in the case of the thiophene molecule in the gas phase.

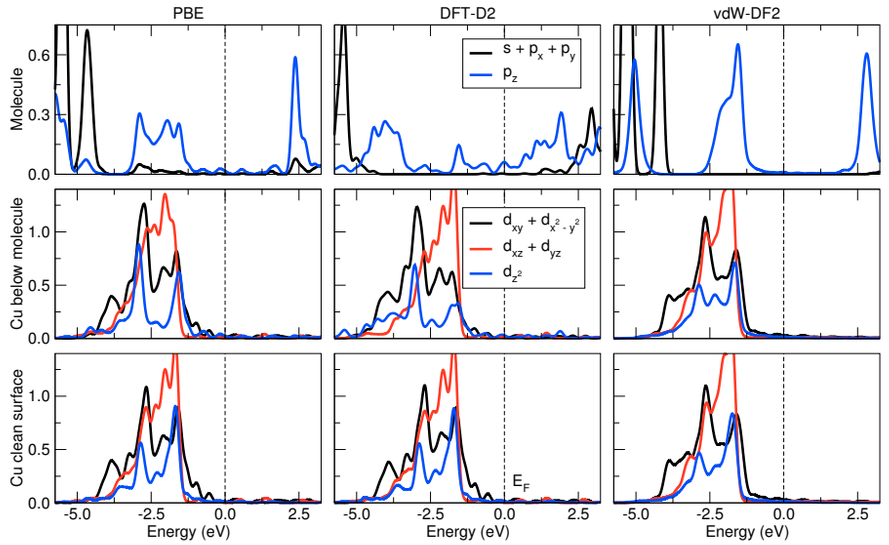

Figure 4.9.: Projected density of states on specific atomic orbitals for a single thiophene molecule adsorbed on Cu(111), the Cu atom directly underneath the S atom and a Cu atom of the clean Cu(111) surface calculated with the PBE functional (left), with the DFT-D2 method (middle) and with the non local vdW-DF2 (right). The PDOS has been broadened by a 0.1 eV Gaussian.

The PDOS calculated with the PBE functional shows that the interaction between the p_z states of the molecule with the d states of the Cu(111) surface leads to the formation of hybrid molecule surface interface states in the energy interval between -3.2 eV and -1.25 eV. The energetic position of these interface states changes when the DFT-D2 method is applied. The distance between the thiophene molecule and the Cu(111) surface is decreased which results in a stronger interaction and therefore a shift of the interface states to lower energies. In addition the sharp peak present at 2.1 eV above the Fermi level is broadened and shifted to lower energies. The opposite is the case when the vdW-DF2 functional is used for the calculations. The hybrid molecule surface interface states are more sharp at the molecular site compared to the calculation with the PBE functional. The interaction between the molecule and the surface is reduced because of the much larger molecule surface distance. The middle and the lower row in Figure 4.9 show the PDOS on the d states of the Cu atom directly underneath the S atom and of a Cu atom on the clean Cu(111) surface. The shape of the PDOS for the in-plane orbitals d_{xy} and $d_{\mathrm{x^2-y^2}}$ is practically unaffected by the adsorption of the single thiophene molecule on the Cu(111) surface. The shape of the PDOS for the out of plane

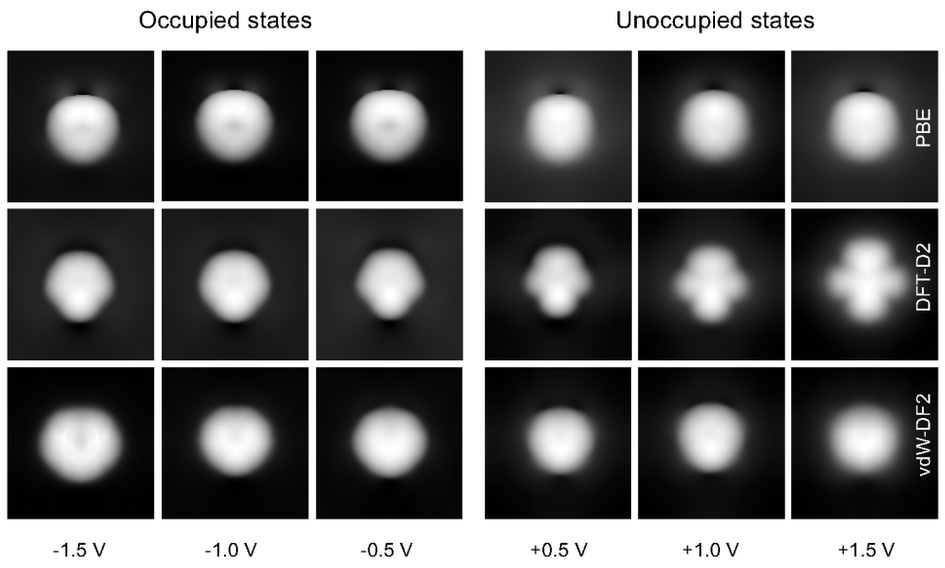

Figure 4.10.: Simulated STM images of the single thiophene molecule adsorbed on Cu(111) calculated with the PBE, the DFT-D2 and the vdW-DF2 geometry in order to show all extreme cases for a number of bias voltages between -1.5 V and $+1.5$ V. Negative bias voltages correspond to tunneling from occupied sample states to empty tip states.

d orbitals d_{xz}, d_{yz} and d_{z^2} is changed due to the strong molecule metal hybridization in the case of the PBE functional and the DFT-D2 method. For the latter the out-of-plane $d-$states are pushed to lower energies compared to the PBE calculation. With vdW-DF2 only the d_{z^2} PDOS changes due to the adsorption of the thiophene molecule. The same observations can be made for the densities of states of the dimers of single thiophene, the 4T molecule and dimers of 4T adsorbed on the Cu(111) surface.

The differences in the electronic structure for the three different geometries obtained with the PBE functional, the semi-empirical DFT-D2 approach and the vdW-DF2 functional are also visible in the simulated STM images depicted in Figure 4.10. These STM images have been simulated within the framework of the Tersoff-Hamann-model [196] by calculating an isosurface of the charge density as a function of energy integrated from the Fermi level to the applied bias voltage. These surfaces of equal charge density correspond to surfaces of equal current within the Tersoff-Hamann model of the STM and thus offer a way to simulate STM images in the constant current mode. The simulated STM images obtained with the PBE functional shown in Figure 4.10 do not vary a lot as a function of the bias voltage. For negative voltages they show a round shape which becomes slightly more rectangular for positive bias voltages. The non zero tilt

angle of thiophene adsorbed on the Cu(111) surface calculated with the PBE functional shows up as a variation of contrast from bright to dark when going from the top to the bottom of the image. This contrast vanishes together with the tilt angle when using the DFT-D2 method instead of the PBE functional. In addition the thiophene molecule has a pentagonal shape for negative bias voltages which is enhanced to a crosslike shape for positive bias voltages. The different shape of the thiophene molecule between the images obtained with the PBE functional and the DFT-D2 method are due to stronger hybridization between the molecule and the surface in the second case. In the simulated STM images obtained with the vdW-DF2 functional we can see the third case in terms of molecule surface interaction. The thiophene molecule does not show the brightness asymmetry because also with vdW-DF2 the tilt angle vanishes. The thiophene molecule is round shaped due to the large molecule surface distance and the corresponding weaker hybridization between the molecule and the surface. These differences in the simulated STM images for the three different geometries should be identifiable also in a real STM experiment.

4.2. From weak to strong coupling - COT on Au(111), Au(100), Ag(100) and Cu(100)

The cyclooctatetraene (COT, C_8H_8) molecule in its neutral charge state is a non aromatic molecule. It does not fulfill Hückel's rule of aromaticity because it has only eight π electrons which cannot be expressed by $4n + 2$ where n is an integer. If COT in the charge neutral state would adopt a flat shape there would be a HOMO consisting of two degenerate half occupied π states which is a textbook example of the first order Jahn-Teller effect. If a molecule has a half filled double degenerate HOMO it can lower its energy by completely filling one of the two degenerate states. The now empty state will rise in energy. The asymmetric change in the charge density of the now completely filled orbital leads to a symmetry breaking of the molecule. Thus, the most stable conformation of COT in its charge neutral state breaks the D_{8h} symmetry which a planar structure of the molecule would suggest. It is not flat but has a tub like shape which has D_{2v} symmetry [197]. When the molecule gets charged or ionized twice it can become aromatic as in this case Hückel's rule is fulfilled and the molecule in addition undergoes a conformational change and becomes flat [198, 199]. With the first electron added or withdrawn from the molecule COT adopts a flat shape with D_{4h} symmetry [199] while the second charging leads to a flat shape with D_{8h} symmetry [198]. If this mechanism could be exploited to change the conformation of COT when it is adsorbed on a surface the system could be considered as a conformational switch.

C. Nacci *et al.* [200, 201] used cyclooctadiene (COD, C_8H_{16}), which is closely related to COT, adsorbed on Si(100) as a conformational switch. The difference between both molecules is the number of hydrogen atoms attached to each C. While it is one H atom

for COT there are two in the case of COD. For the COD molecule adsorbed on the Si(100) surface there are two equivalent conformers: left- and right-handed dimer bound. By applying a bias voltage vibrational modes of the molecule can be excited in order to overcome the potential barrier between the two states. This switching has been observed in the experiment where the conductance as a function of time showed switching between two distinct states of conduction. These two states of different conductance have been ascribed to the two possible conformational geometries.

In the preceding section we have investigated a weakly chemisorbed molecule on the Cu(111) surface. In this section we will gain further knowledge about the two generic cases of binding, physisorption and chemisorption, and in addition explore theoretically if COT can be considered as a conformational switch when it is adsorbed on a particular surface. For this we will study COT adsorbed on the (100) surfaces of Cu, Ag and Au as well as on the Au(111) surface. The content of this chapter has been published in [17]. In particular the geometry and the binding of COT to the Au(111), Ag(100) and Cu(100) surfaces have been discussed in addition to the questions of aromaticity and the change of conformation together with the corresponding STM experiments in [17].

The supercells have been set up with the computational lattice constants of 4.176 Å for Au, 4.165 Å for Ag and 3.63 Å for Cu obtained with the PBE functional. In order to calculate a single COT molecule adsorbed on the surface for the (100) surfaces a (4×4) supercell has been used which leads to a distance of 16.7 Å in the case of Au and Ag and 14.5 Å in the case of Cu between two periodically repeated images. For the Au(111) surface a $(5 \times 3\sqrt{3})$ supercell has been chosen which leads to distance of 14.8 Å in [110] direction and 15.3 Å in $[11\overline{2}]$ direction. All surfaces in this study have been modeled by a slab consisting of six metal layers and the distance between periodic images in z direction has been chosen to be 16.8 Å for Au(111), 14.6 Å for Au(100) and Ag(100), and 12.8 Å for Cu(100). The cutoff energy was set to 500 eV. The forces have been minimized until they were smaller than 0.003 eV / Å and the Γ-point has been used for **k**-space sampling during the relaxations. For calculations of molecules on the Au(111) surface one should always be aware of the prominent herringbone reconstruction [202] of this surface. This is a reconstruction containing one additional Au atom in a row of 22 Au atoms which leads to a $22 \times \sqrt{3}$ supercell. The surface is separated in so called fcc and hcp regions with continuous transitions between them. In this regions the structure of the surface layer is very close to normal fcc or hcp stacking. In the transition region the atoms of the uppermost layer sit almost on bridge positions. These atoms are pushed a bit further away from the surface and can be seen as bright stripes in STM experiments which look like herringbones. While a computational study regarding the reconstruction of the Au(111) surface using the VASP code has been done in a $22 \times \sqrt{3}$ including three layers of Au and seven layers of vacuum [203], the investigation of the adsorption of COT on the Au(111) surface requires a $22 \times 3\sqrt{3}$ supercell. Thus, due to the size of the supercell of this reconstruction calculations have to be done on an ideal Au(111) surface. In the case of COT this is not a too crude approximation due to the relatively small size of the molecule.

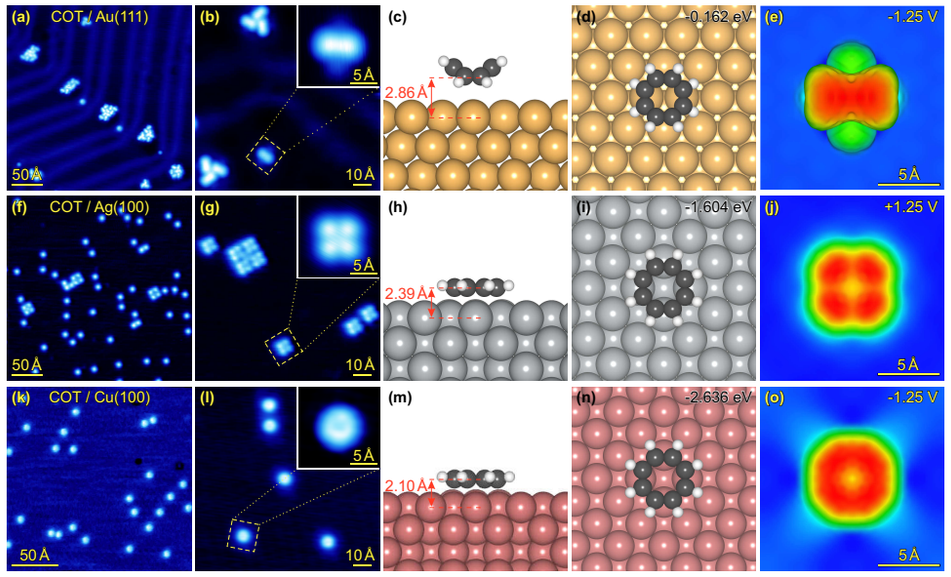

Figure 4.11.: STM images and DFT results for the adsorption of COT on Au(111) (top row), Ag(100) (middle row) and Cu(100) (bottom row). From left to right there are overview and close up STM images, side- and topviews of the most stable adsorption geometry calculated with the PBE functional, and simulated STM images. The change of structural symmetry of the COT molecule goes in hand with an increasing interaction strength shown by the adsorption energies.

The (100) surface of a fcc crystal depicted as red area in Figure 4.2 has three high symmetry positions which have to be considered as possible adsorption sites. The on top position, the bridge position at the center on the connection between nearest neighbor surface atoms and the hollow site in the center between four surface atoms. On all (100) surfaces Au, Ag and Cu we placed the COT molecule in its tub shape as well as in its flat shape on those high symmetry positions as starting configurations for the relaxations. On the Au(111) surface the COT molecule was placed on the top, bridge, fcc- and hcp-hollow site for both the tub and the flat shape. The relaxed configurations on the Au(111), Ag(100) and Cu(100) surface are depicted in the fourth column of Figure 4.11. On the (100) surfaces using the PBE functional the most stable relaxed configuration is COT adsorbed flat occupying the hollow site. In the case of Cu and Ag also the flat molecule placed on the top and bridge site lead to local minima but as it can be seen from the energies given in Table 4.4 the bridge site is already 294 meV in the case of Cu and 273 meV in the case of Ag higher in energy and the top site 784 meV and 802 meV respectively. On Au(100) the relaxation of COT adsorbed on both top

Table 4.4.: Adsorption energies in eV of flat COT adsorbed on the bridge, top and hollow positions of the Cu(100), Ag(100) and Au(100) as well as tub shaped COT on the bridge, top, fcc- and hcp-hollow site of the Au(111) surface obtained with different methods to account for vdW interactions. The PBE, DFT-D2 and DFT-D3 adsorption energies have been calculated self consistently for all adsorption sites. The vdW-DF1, vdW-DF2 and rVV10 values have been obtained via single shot post processing calculations at the PBE geometry. Empty fields in the table represent configurations which did not relax to a local minimum.

	Cu(100) E_{ads} (eV)			Ag(100) E_{ads} (eV)			Au(100) E_{ads} (eV)		
	bri	hol	top	bri	hol	top	bri	hol	top
PBE	-2.342	-2.636	-1.852	-1.331	-1.604	-0.802	-	-1.356	-
DFT-D2	-3.535	-3.837	-3.120	-	-	-	-	-3.561	-
DFT-D3	-3.114	-3.389	-2.638	-1.913	-2.174	-1.400	-	-2.015	-
vdW-DF1	-1.547	-1.931	-1.124	-0.793	-0.964	-0.434	-	-0.616	-
vdW-DF2	-0.971	-1.425	-0.551	-0.465	-0.549	-0.207	-	0.256	-
rVV10	-2.617	-2.942	-2.150	-1.700	-1.879	-1.265	-	-1.781	-

	Au(111) E_{ads} (eV)			
	bri	top	fcc	hcp
PBE	-0.162	-0.136	-0.154	-0.152
DFT-D2	-2.310	-2.427	-2.424	-2.426
DFT-D3	-0.679	-0.645	-0.664	-
vdW-DF1	-0.731	-0.696	-0.716	-0.714
vdW-DF2	-0.727	-0.683	-0.704	-0.701
rVV10	-0.980	-0.882	-0.940	-0.934

and bridge site did end up with the molecule in the hollow position. The inclusion of vdW-interactions with the DFT-D2, DFT-D3, vdW-DF, vdW-DF2 and rVV10 did not change the energetic order of the adsorption configurations for COT adsorbed on the (100) surfaces.

Of particular interest are the configurations with COT adapting its tub shape on the (100) surfaces. If those are stable and separated from the corresponding flat configurations by a sufficiently large energy barrier then the COT molecule on these surfaces is stable in both of its conformations known from the gas phase and could be considered as a conformational switch. On all three (100) surfaces the tub shaped configurations, rotated such that the lower two C double bonds are not on top of Cu surface atoms, on the top position and on the bridge position were stable. The top position is 2.051 eV on Cu(100), 1.033 eV on Ag(100) and 1.069 eV on Au(100) higher in energy than the most stable flat adsorption configuration. For the bridge position the energy differences are 2.069 eV, 1.012 eV and 0.968 eV for Cu, Ag, and Au respectively. On Au(100) and

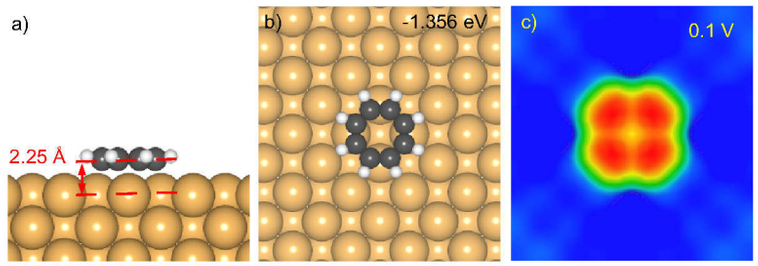

Figure 4.12.: The most stable adsorption configuration of flat COT on Au(100) is shown. The Au(100) surface was not available in the STM experiment due to reconstruction of the Au(100) surface.

Ag(100) in addition the configuration of tub shaped COT adsorbed on the hollow side was stable but 0.707 eV and 1.044 eV respectively higher in energy. Thus, we could find both conformations of COT stable on all three (100) surfaces but on Cu(100) to switch them from one conformation to the other one it would first be necessary to force the COT molecule away from its equilibrium position at the hollow site, which did not have a stable tub shaped partner, and then change its shape to the tub configuration. On Ag(100) as well as on Au(100) there is also a local minimum at the hollow site. On the Ag(100) surface the energy needed to change the molecule adsorbed on the hollow site to the tub shaped conformation is of the order of magnitude but slightly smaller then the energy required to shift the molecule to the less stable bridge position. On Au(100) the energy needed for the change is slightly smaller compared to Ag(100) but the other adsorption sites did not lead to stable local minima thus there is no energy to compare with. Au(100) would be the most promising surface for conformational switching as the number of additional states to which the COT could be driven when trying to switch the molecule is lower than on Cu(100) and Ag(100). The tub shaped configurations on the (100) surfaces have however not been observed in the STM experiment and especially the Au(100) surface was not accessible due to strong reconstructions of the surface.

On Au(111) non of the flat configurations lead to a stable solution. They all relaxed towards the corresponding tub shaped configurations. The most stable adsorption site was the bridge position with the tub shaped COT molecule oriented such that the lower C double bonds were on top of Au atoms. But in this case the energetic order is not as clearly distinguished as on the (100) surfaces. The fcc and the hcp hollow sites are only 8 meV and 10 meV less stable than the bridge site and the least stable configuration on top is only 26 meV higher in energy. These energy differences are about the convergence error of our calculations not even speaking about errors introduced by the use of an inappropriate xc-functional. And thus the inclusion of vdW-interactions also changed the energetic order in this case. DFT-D2 yields the top and both hollow sites almost degenerate and 110 meV lower in energy than the bridge site. DFT-D3, vdW-DF and

rVV10 all result in the bridge position being the lowest in energy but in the case of vdW-DF the energetic order of the other three positions is interchanged. All applied vdW schemes lead to larger energy differences between the most stable and the least stable configuration.

While stable configurations both with tub and flat shaped COT are predicted for the adsorption of COT on the (100) surfaces which have not been observed in the experiment, the opposite is the case on Au(111). Starting from a flat adsorption configuration the COT molecule relaxed to a tub shape on all examined adsorption sites. Thus, on Au(111) our calculations did not lead to stable flat adsorption configurations. In the experiment both configurations could be observed on the Au(111) surface. COT changed its shape from tub to flat after moving the molecule from the fcc region of the herringbone reconstruction to an elbow dislocation site via STM manipulation. The elbow dislocation occurs when two facets of the sixfold symmetric herringbone reconstructed Au(111) intersect, which are rotated by 30° with respect to each other. Hence, the dislocation site is due to the system size unavailable for DFT calculations at present.

The shape of COT in its most stable adsorption geometry directly translates into the shape depicted in the simulated STM images in the fifth column of Figure 4.11. The simulated STM images have been generated within the Tersoff-Hamann model [196] as described in the previous Section 4.1. In order to obtain those images especially with the for simulated STM images small bias voltage of 0.1 V we had to increase the density of the **k**-point grid to a $6 \times 6 \times 1$ Monkhorst-Pack-grid in order to have a reasonable number of states inside the energy interval. On Au(111) an ellipsoidal shape with two small protrusions on its top and bottom side can be observed. The high ellipsoidal shape corresponds to the four C-H groups pointing away from the surface while the faint protrusions correspond to those pointing towards the surface. On Ag(100) as well as on Au(100) the simulated STM image shows a flat four fold symmetric structure while on Cu(100) the symmetry appears to be higher and the image shows more a ring like shape. This difference in the symmetry of the COT molecule when adsorbed on Cu(100) and on Ag(100) is also visible in the experimentally obtained images depicted in the second column of Figure 4.11. To investigate if this change of the symmetry is connected to the geometric structure or purely an effect of the electronic orbitals depicted by the STM the C single and double bond distances of COT adsorbed on the surfaces are given in Table 4.5. If on Cu(100) the structural symmetry was higher in explicit D_{8h} than D_{4h} which would be the symmetry associated with the simulated STM images of COT adsorbed on Ag(100) and on Au(100) the length of all the carbon bonds should be equal. As it can be seen from Table 4.5 the lengths of the C single and double bonds for COT adsorbed on Cu(100) do differ and they are comparable to those of COT adsorbed on Ag(100) and Au(100). The structural symmetry of the configuration of COT adsorbed on Cu(100), Ag(100) and Au(100) is the same. Thus, we are dealing here with a purely electronic effect.

The relaxed molecule surface distances obtained with the PBE functional are listed in Table 4.5. The molecule is closest to the surface with a distance of 2.10 Å on Cu(100).

Table 4.5.: C − C bond lengths in Å to identify the symmetry and equilibrium distances d_{eq} in Å obtained with different methods to account for vdW interactions of tub shaped COT adsorbed on Au(111) as well as flat COT adsorbed on Au(100), Ag(100) and Cu(100). The empty field in the table corresponds to a configuration where no stable local minimum has been found.

Surface	C − C (Å)	C = C (Å)	d_{eq} (Å)			
			PBE	DFT-D2	DFT-D3	vdW-DF2
Au(111)	1.474	1.349	2.86	2.23	2.71	3.26
Au(100)	1.443	1.418	2.25	2.19	2.25	2.98
Ag(100)	1.436	1.416	2.39	-	2.39	2.58
Cu(100)	1.443	1.418	2.10	2.08	2.10	2.26

On the other two (100) surfaces the equilibrium distances between the molecule and the surface are 2.39 Å in the case of Ag and 2.25 Å on Au. On Au(111) the molecule surface distance is 2.86 Å. As a trend the molecule surface distance is connected to the energetic distance between the center of the d band of the surface and the position of the LUMO of the molecule [152, 204]. By this relationship the ascending order in terms of molecule surface distance from the Cu(100) to Au(111) from the most reactive to the least reactive surface can be explained together with the exception of COT having a slightly smaller molecule surface distance on Au(100) than on Ag(100). This point will be addressed in the corresponding paragraph about the electronic structure. In the case of the (100) surfaces the COT molecule adsorbs close to the surface and the energy differences to the less stable adsorption sites are high. These are hints for a strong interaction of the molecule with the surface already when using the PBE functional. Thus, in these cases vdW interactions should be of minor importance. The opposite is the case for COT adsorbed on the weakly interacting Au(111) surface. Here vdW interactions are expected to play a crucial role. We have applied the different schemes to account for vdW interactions for COT adsorbed on all the studied surfaces which will give us information on how to judge the results of those schemes in cases where vdW interactions are of minor importance. On the (100) surfaces the semi empirical DFT-D3 approach did not change the adsorption geometry at all. As it can be seen from Table 4.5 the molecule surface distances are equal to those obtained with the PBE functional. With the non local vdW-DF2 the molecule surface distances on the (100) surfaces are increased to 2.26 Å, 2.58 Å and 2.98 Å for Cu, Ag and Au respectively. As already discussed in Section 3.2 the functionals of the vdW-DF type tend to overestimate the binding distances. Thus, the increase of the molecule surface distance in the case of COT adsorbed on the strongly interacting (100) is not unexpected. On Au(111) the semi-empirical schemes decrease the molecule surface distance to 2.23 Å with DFT-D2 and 2.71 Å with DFT-D3. In the case of DFT-D3 the molecule besides of a slightly changed dihedral angle still remains in its tub shape while DFT-D2 leads to an almost

flat configuration. DFT-D2 probably overcorrects the vdW interactions also in this case as the obtained geometry is in contradiction with the experimentally observed tub shaped geometry. Unfortunately there is no direct measurement of the molecule surface distance of COT adsorbed on the Au(111) surface available. Similar as for the (100) surfaces the non local vdW-DF increases the equilibrium distance to 3.26 Å for COT adsorbed on Au(111). The vdW-DF does not only change the molecule surface distance. Also the interlayer distance of the metal surface is increased for those three layers which are allowed to relax. This can be correlated to the tendency of vdW-DF to overestimate the lattice constants of Cu, Ag, and Au. In [161] J. Klimeš *et al.* reported lattice constants of Cu and Ag calculated with vdW-DF which are by 2% and 2.4% larger than the PBE lattice constants. The PBE lattice constants already overestimate the experimental lattice constants thus the vdW-DFs predict even worse lattice constants. The increase of the interlayer distance due to an increased lattice constant adds to the overestimation of the molecule surface distance. In addition to the overestimated molecule surface distance relaxations using vdW-DF2 also result in a flat shaped COT molecule which is in disagreement with the experimentally observed STM images of COT adsorbed on Au(111).

The adsorption energies of COT adsorbed on the different noble metal surfaces are summarized in Table 4.4. On the (100) surfaces starting with the results obtained with the PBE functional the COT molecule is strongly bound to the surface. The adsorption energies are -2.636 eV for Cu(100), -1.604 eV for Ag(100) and -1.356 eV for Au(100). These adsorption energies suggest that we deal in this case already with the regime of chemisorption. The order of the three noble metal (100) surfaces induced by the adsorption energy is from weakest interaction on Au to strongest interaction on Cu. This order differs from what we have obtained in terms of the molecule surface distance by an interchange of Ag and Au. Thus, the molecule surface distance is not strictly connected to the interaction strength. As already mentioned for the equilibrium distances we also investigated the adsorption energy with the help of different schemes to account for vdW interactions in order to investigate their performance in the case where vdW interactions are of minor importance. For both semi-empirical schemes DFT-D2 and DFT-D3 we obtain a large correction with respect to the PBE adsorption energy. This is due to the nature of those semi-empirical methods. Their contribution to the adsorption energy is always different from zero and always has the same sign. Hence, there will always be a correction to the PBE values of the adsorption energy even in cases where the PBE adsorption energy would be already accurate. For a system where it is at the beginning of the calculations not clear if vdW interactions are of importance or not and thus the PBE results are unreliable or not, one should be careful to trust in adsorption energies obtained with a semi-empirical approach. For COT adsorbed on Cu(100) the *ab initio* vdW-DF2 yields selfconsistently applied -1.875 eV in contrast to the -1.425 eV as reported in Table 4.4 for the single shot calculation at the PBE geometry. The same occurs on the Ag(100) and the Au(100) surface with self consistent vdW-DF2 adsorption energies of -1.140 eV and -1.401 eV which have to be compared to the single

shot quantities −0.549 eV and 0.256 eV. In all three cases the single shot calculation underestimates the selfconsistent adsorption energy. The most severe underestimation occurs for Au(100) where the molecule is not even bound to the surface according to the single shot calculation. Here we encounter another problem with the single shot post processing calculations. The absolute value of the true selfconsistently obtained adsorption energy is always greater or equals the absolute value from a single shot calculation as the assumed geometry is either the equilibrium geometry corresponding to the particular xc-functional considered or not. Now depending on how steep the potential energy curve in the direction of the minimum is, the adsorption energy at the non equilibrium geometry will more or less dramatically underestimate the selfconsistent adsorption energy. While for weakly bound systems the error reported in [133] was up to 20% in our case of the adsorption of COT on the (100) noble metal surfaces it reaches 66%. In order to test if this underestimation of the adsorption energy is only due to the wrong geometry we in addition did a single shot calculation at the relaxed vdW-DF2 geometry with the charge density obtained with the PBE functional. Also for this setup the estimated adsorption energy is only −1.419 eV. This means that the change of the charge density due to the potential arising from the non local correlation functional has a strong impact on the calculated adsorption energy. Also the contribution of the potential arising from the non local correlation energy is not considered in a post processing calculation. From what we have just seen this effect is more important in a case where the molecule interacts strongly with the surface as it is the case on the (100) noble metal surfaces. If one uses the PBE densities as input for the post processing the minimum energy configuration can be reached at a geometry which does not in general coincide with the geometry self consistently calculated with the vdW-DF functional. In addition the adsorption energy tends to be underestimated due to the inconsistent charge density used as input and the neglect of the potential in the single shot calculations. Despite of the just mentioned issues it is worth to have a look at the adsorption energies of COT on the (100) noble metal surfaces with vdW-DF1, vdW-DF2 and rVV10 obtained by single shot calculations listed in Table 4.4 as for the latter functional at the moment no selfconsistent implementation is available in VASP. With vdW-DF2 the COT molecule is bound less strongly by between 300 meV and 500 meV than with vdW-DF1. The rVV10 functional binds stronger than both vdW-DFs and even the PBE functional.

On Au(111) the adsorption energy obtained with the PBE functional is −0.162 eV which is an order of magnitude smaller than for the just discussed (100) surfaces. It in addition indicates a physisorption type of bonding. As the molecule is so weakly bound to the surface in this case vdW interactions will be of importance. The DFT-D2 scheme increases the binding strength and leads to an adsorption energy of −2.427 eV for the most stable configuration with DFT-D2 where COT is adsorbed on a top site. For COT adsorbed on Au(111) we additionally applied the screening method introduced by G. Mercurio *et al.* to see if this can reduce the large correction of the adsorption energy introduced by the DFT-D2 method. When we consecutively reduce the number of Au layers which are taken into account to compute the dispersion energy we obtain

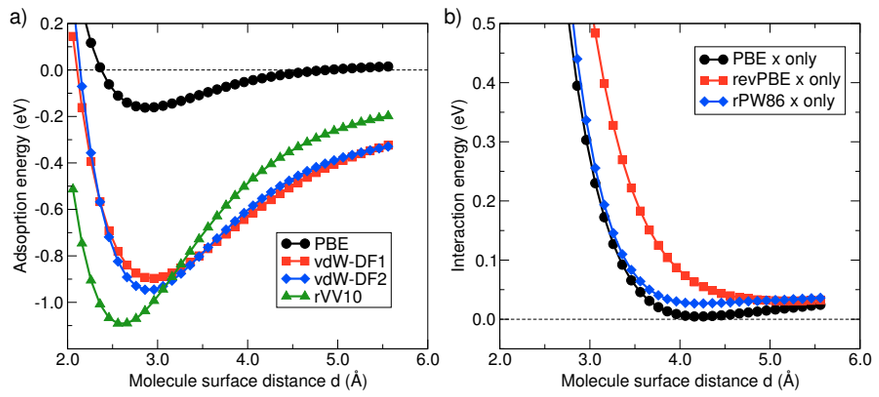

Figure 4.13.: Potential energy curves for COT adsorbed on the bridge site of Au(111) calculated with the PBE, vdW-DF1, vdW-DF2 and rVV10 (a). While the estimated equilibrium distance between the molecule and the surface is increased by both vdW density functionals, rVV10 predicts a smaller molecule surface distance with respect to PBE. The exchange only interaction energy (b) plotted with PBE, revPBE and rPW86 exchange does not show spurious binding. The energies have been calculated based on the PBE charge density.

an adsorption energy of −2.138 eV when only one layer is considered. The adsorption energy as a function of layers allowed to interact with the COT molecule converges relatively fast. Already when two layers only are used to compute the dispersion energy the adsorption energy differs only by 58 meV from the value with six layers. DFT-D3 more moderately corrects the adsorption energy to −0.679 eV for the in this case most stable bridge site. With the non local vdW-DF1 we obtained an adsorption energy of −0.731 eV. While on the (100) surface the VdW-DF2 result was about half of the vdW-DF1 result in this case vdW-DF2 yields almost the same value as vdW-DF1 does. Also for the adsorption of COT on Au(111) the single shot calculations of the vdW-DF2 adsorption energy reported in Table 4.4 underestimates the selfconsistently obtained value of −1.195 eV. With the rVV10 functional the adsorption energy is −0.980 which follows the trend observed on the (100) surfaces where the rVV10 was always binding more strongly than both vdW-DF functionals. Unfortunately unlike for the thiophene system no experimental value for the adsorption energy is available.

In Figure 4.13 (a) potential energy curves for tub shaped COT adsorbed on the bridge site of Au(111) are shown for LDA, PBE, vdW-DF1, vdW-DF2 and rVV10. The PECs have been obtained by rigidly shifting the COT molecule along an axis perpendicular to the surface. The PBE curve is as expected for a weakly bound system rather flat

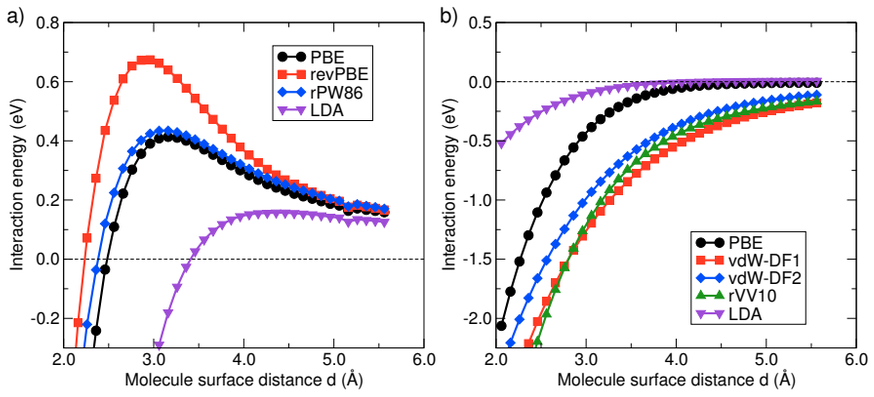

Figure 4.14.: Exchange (a) and correlation (b) contribution to the interaction energy in eV of COT adsorbed on Au(111) as a function of the molecule surface distance in Å for different approximations to the xc-functional. All the energies have been calculated based on the PBE density.

with a molecule surface distance and adsorption energy equal to the already discussed selfconsistently obtained values. Both vdW-DF curves are despite of the different applied exchange functionals very close to each other. In particular their predicted adsorption energies differ only by 49 meV and the predicted equilibrium distances agree within 0.1 Å. The absolute values deviate from the discussed selfconsistently calculated values. The predicted molecule surface distance is shorter than that obtained selfconsistently and the molecule is less strongly bound to the surface. In total this effect is less pronounced than on the already discussed (100) surfaces. The rVV10 PEC shows a much stronger binding of COT to the Au(111) surface by both the adsorption energy of -1.091 eV as well as the molecule surface distance of 2.56 Å. The exchange only contribution defined as

$$E^{\mathrm{x,only}} = E^{\mathrm{DFT}} - E_{\mathrm{c}} \tag{4.3}$$

to the interaction energy, which is the interaction energy without correlation, is plotted in Figure 4.13 (b) for the three different exchange functionals PBE, revPBE, and rPW86 used for the calculation of the vdW density functionals. None of the three exchange only functionals shows spurious binding of the COT molecule to the Au(111) surface. For a benzene dimer however the PBE functional showed a binding by the exchange only functional [19]. The exchange only functional which shows the strongest repulsion in our case is the revPBE.

In Figure 4.14 the contribution to the interaction energy of COT adsorbed on Au(111)

is resolved for the exchange and correlation functionals used to obtain the PECs discussed in the last paragraph. The total change of the adsorption energy as a function of the molecule surface distance cannot be reproduced by adding both contributions as the contribution of relaxations of both the molecule in the gas phase and the clean surface has been excluded. The exchange contributions of the three GGA type functionals under consideration do not show binding due to exchange for molecule surface distances greater than 2.5 Å. In the region of molecule surface distances around the respective equilibrium distances the exchange part of the GGA contribution to the interaction energy is repulsive. This repulsion is the strongest for revPBE which is the exchange used in vdW-DF1 which might contribute to the more drastic increase of the molecule surface distance by this particular functional when comparing to the other *ab initio* vdW functionals. The exchange contributions to the interaction energy of PBE and the refitted PW86 functional are quite similar with rPW86 being slightly more repulsive. In contrast for LDA in the region of molecule surface distances around the estimated equilibrium distance there is binding due to the exchange contribution. Except for the case of LDA in combination with the discussion from the last paragraph about the exchange only binding the general statement about erroneous exchange binding should be reformulated with care. The erroneous binding is not due to exchange which can be repulsive as it has been just shown. The formulation for vdW systems should be binding erroneously not due to correlation. The relation between the different correlation contributions to the interaction energy can be seen from Figure 4.14. For both vdW-DF functionals a non local correction is added to the LDA correlation energy. This has an effect on the curvature of the corresponding curves. In the case of rVV10 a non local correction is added to the PBE correlation energy. Both curves show a similar behavior with the rVV10 curve having a slightly higher curvature. The difference between those two curves does not arise from the β-integral in the defining Equation A.94 of the non local correction of rVV10, as this contribution cancels when calculating the interaction energy. Thus, the change of curvature is only due to the non local kernel.

As discussed in the introduction to this chapter COT changes its conformation in the gas phase due to its charge state. The neutral COT molecule is tub shaped [197] while the charged anions and cations become flat [198, 199]. An idea why the difference of shape occurs when COT adsorbs on the (100) surfaces of Cu, Ag and Au compared to the adsorption on Au(111) was that the molecule gets charged on the (100) surfaces while it remains in its neutral charge state on the Au(111) surface. Thus, we have investigated the charge transfer to see if this simple explanation is valid. As in the previous section an estimate for the charge transferred from or to the molecule is the integration of the charge density difference between the adsorbed system and its two constituents, the clean surface and the molecule in the gas phase, as a function of z from the point between the interface and the molecule where the curve crosses zero to infinity. The charge density difference integrated over the xy plane as a function of z is depicted in Figure 4.15 for all the discussed systems. For the (100) surfaces the picture is similar to what we have obtained for thiophene in the last section. There is charge depletion at

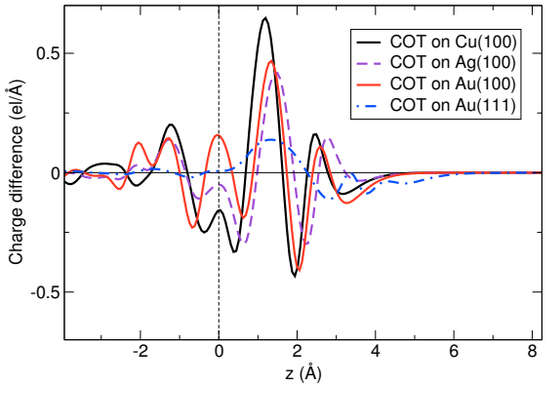

Figure 4.15.: Charge density difference in el/Å^3 integrated over the surface plane for COT adsorbed on Au(111), Au(100), Ag(100) and Cu(100) at the PBE geometry. Zero denotes the position of the respective uppermost surface layer. The charge transferred from the molecule to the interface is in all cases significantly smaller than one electron. Thus, when COT adsorbs on those surfaces it is not in a charged state.

the uppermost surface layer, charge accumulation between the molecule and the surface, which corresponds to the chemical bond formed between the molecule and the substrate, and charge rearrangement at the molecular site. Also for Au(111) the charge density difference curve shows a peak at the interface, but its height is much lower than for the (100) surfaces. This means that also for COT adsorbed on Au(111) a weak chemical bond is formed. Due to the significantly different size of the molecules these curves should not be directly compared to the thiophene charge density difference. In contrast to the (100) surfaces in the case of Au(111) there is almost no charge depletion at the surface and at the molecular site we do not observe charge rearrangement anymore but only charge depletion. When integrating the curves as described above on all surfaces in total a small amount of charge is transferred from the molecule to the interface. The values are between 0.1 electrons for Au(111) and 0.2 electrons for Cu(100). Despite of all the ambiguity with the definition of the starting point for the integration it is safe to say that no complete electron is transferred from or to the molecule and thus the change of the shape cannot be due to the charge state of the molecule. On the (100) surfaces it even appears difficult to still speak of the molecule as a single entity which could be charged as in these cases the molecule is strongly interacting with the surface and forms a new hybrid material. In [17] we arrived at the conclusion that the change of the strength of the molecule surface interaction by varying the substrate material should

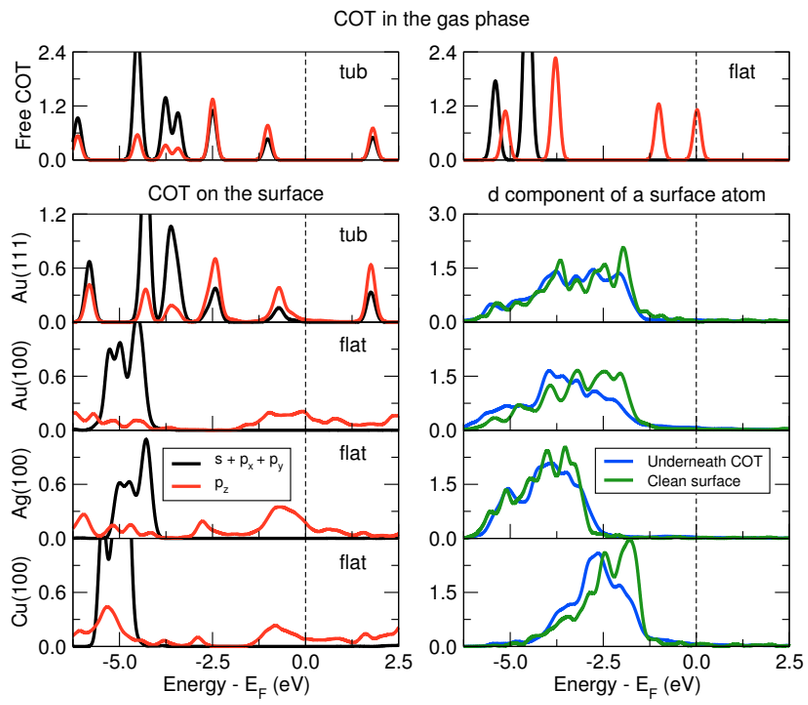

Figure 4.16.: Projected density of states of COT in the gas phase (top panel) for the tub shaped ground state geometry and for an enforced flat geometry and adsorbed (bottom panel) on Au(111), Au(100), Ag(100) and Cu(100). The PDOS has been broadened by a 0.1 eV Gaussian.

be considered as a different hybridization driven mechanism which can have the same effect as charging the molecule in the gas phase.

This statement can be further clarified by investigating the electronic structure of the system. The PDOS for COT adsorbed on the (100) noble metal surfaces and the Au(111) surface is depicted in Figure 4.16. To calculate the PDOS we have increased the density of the **k**-point grid to a $6 \times 6 \times 1$ Monkhorst-pack-grid. The top panel shows the PDOS of the tub shaped and flat shaped COT in the gas phase. In order to obtain the PDOS of the flat molecule we enforced a flat geometry without adding additional charges. As we did not observe significant charge transfer and also argued that the charged state is not very well defined when COT is adsorbed on a strongly interacting surface, the neutral molecule forced into a flat geometry has the appropriate electronic

structure to compare with. The difference in structural symmetry between the flat and the tub shaped molecule leads to different positions of the peaks, which can be seen e.g. at the significantly smaller HOMO-LUMO gap of the flat molecule. When COT adsorbs in its tub shape on Au(111) the molecule is only weakly interacting with the surface and thus little to no hybridization of the surface states with the p states of the molecule takes place. The peaks corresponding to the p states of COT align with the Fermi energy of the surface and are only slightly broadened. This is a clear signature of physisorption which fits with the small adsorption energy of COT on Au(111). On the (100) surfaces the situation is different. In these cases the states of the molecule strongly hybridize with the states of the surface and the peak structure of the gas phase molecule cannot be recognized anymore. This confirms that COT chemisorbs on the (100) noble metal surfaces which again corresponds to the adsorption energies calculated in these cases. As mentioned earlier the position of the center of the metal d-band is one determining factor for the equilibrium molecule surface distance. More precisely the molecule surface distance shows a trend to be inverse proportional to the energetic distance of the center of the metal d band and the LUMO of the molecule for PTCDA [204] and pentacene [152] adsorbed on noble metals. This also explains the order of the molecule surface distances from shortest on Cu(100) to largest on Au(111). The centers of the metal d band extracted from this calculations for Au(111), Au(100), Ag(100) and Cu(100) are at -3.130 eV, -3.166 eV, -4.074 eV and -2.426 eV. Although the center of the metal d band of Ag(100) lies lower in energy than that of Au(111) the molecule surface distance is larger due to the fact that on Au(111) COT adopts its tub shape. The tub shaped COT molecule has a larger HOMO-LUMO gap of 2.825 eV than the 1.033 eV of the flat shaped COT as can be seen from Figure 4.16 and thus the distance between the LUMO energy and the metal d band center is larger. For the order in molecule surface distances of the (100) surfaces only the position of the metal d band center is of importance because the COT molecule adopts its flat shape on all three substrates. Thus, the energy of the LUMO is the same on all three investigated (100) noble metal surfaces. The trend observed in [152, 204] predicts a shorter molecule surface distance on Au(100) than on Ag(100) because the center of the metal d band lies lower in energy for Ag than for Au. The adsorption of COT on Au(111), Au(100), Ag(100) and Cu(100) follows the rule that a lower lying metal d band center leads to a larger molecule surface distance.

In Figure 4.17 correlation binding energy densities as defined in the previous section are shown for COT adsorbed on Au(111) and the (100) surfaces of Au, Ag and Cu calculated with the PBE geometries. The normal vector of the cutting plane is the [010] direction and it cuts through the center of a C-C double bond. For each particular binding energy density the same color scale has been chosen in order to slightly simplify the comparison among the different metal substrates. The overall picture is similar to what has been already shown for thiophene adsorbed on Cu(111). In the charge density difference the small amount of charge density transferred to the interface to form a chemical bond shows up as charge accumulation for all studied surfaces. It is the least

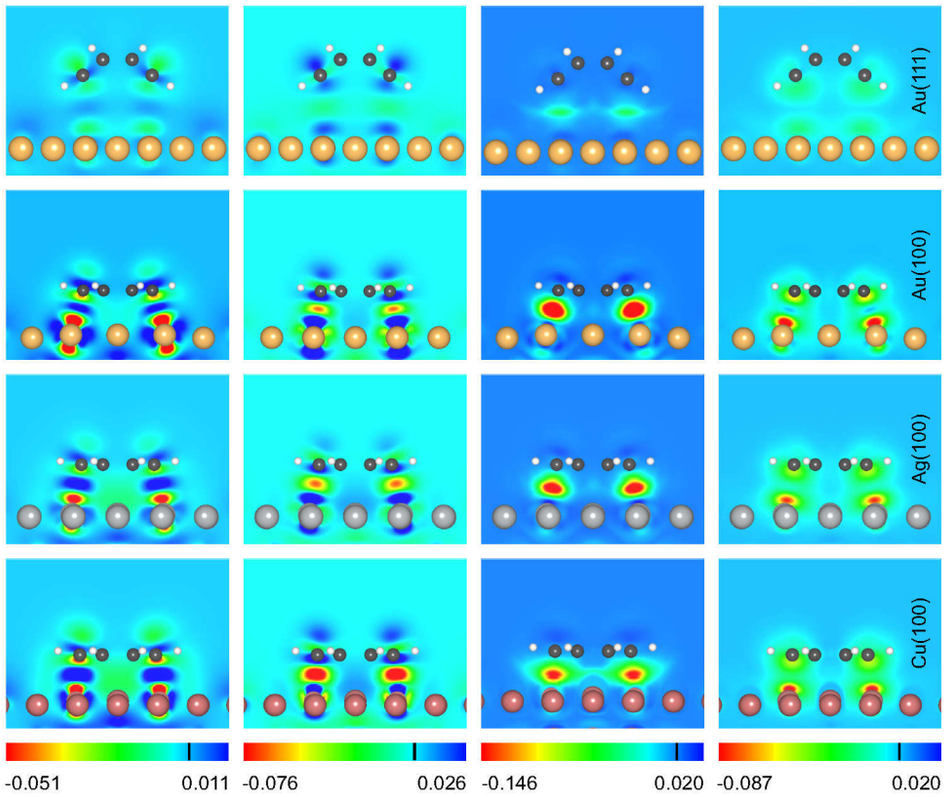

Figure 4.17.: The columns show from left to right the charge density difference, the LDA correlation binding energy density, the semi local correction to the correlation binding energy density and the non local correction to the correlation binding energy density on a plane cutting through a C double bond of the COT molecule adsorbed on Au(111), Au(100), Ag(100) and Cu(100) with the PBE geometries. The same color scale has been used for each particular set of densities. The black line in the color bar indicates the position of the zero.

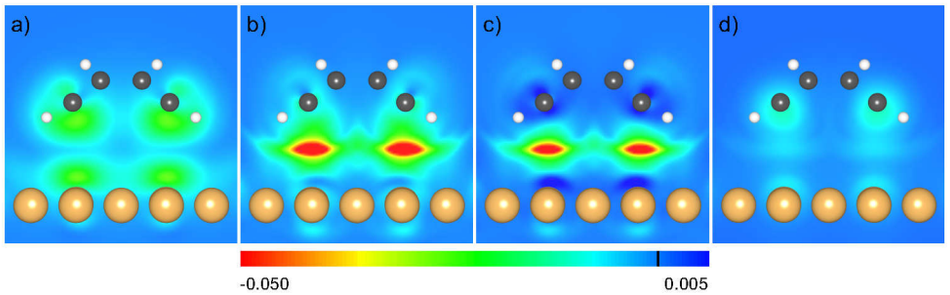

Figure 4.18.: Correlation binding energy densities for the correction to LDA of the vdW-DF, the rVV10 and the PBE functional. (d) Correlation binding energy density of the non local part of the rVV10 functional which is added to (c) in order to obtain (b).

pronounced on Au(111) and increases when going to the (100) surfaces from Au over Ag to Cu. Also the charge rearrangement at the molecular site can be seen. Charge is depleted from the molecular site and to a larger extent from the metal surface. The LDA correlation energy density shows the same overall structure as the charge density difference just with an opposite sign due to the functional form of the LDA. The semi-local correction has contributions at the same region as LDA with slight extension to its surrounding due to the additional information from the charge density gradient entering the correlation energy density of the PBE GGA. When comparing the plots for the different (100) surfaces one sees that the semi local correlation binding energy density shows the opposite trend than the LDA by becoming less pronounced when going from Au to Cu. In the case of the non local correction the contributions arise from regions closer to the molecule and to the surface than for both LDA and semi local correlation binding energy density. While we concluded in the case of thiophene that the difference in the spatial distribution of the semi local and the non local correction is responsible for the significant difference in the adsorption energy we have to refine this statement here. For Au(111) this observation still holds true as the adsorption energy of COT on this surface is also increased a lot by vdW-DF when compared to the PBE value. On the (100) surfaces however the self consistent adsorption energy obtained with vdW-DF has not been changed dramatically.

The correlation binding energy densities for the correction to LDA correlation of the vdW-DF2, rVV10, and PBE functionals as well as the non local contribution to the correlation binding energy density of the rVV10 functional are depicted in Figure 4.18. The non local contributions to vdW-DF2 and rVV10 are shown in (a) and (d). Close to the molecule and to the surface the non local part of vdW-DF2 is stronger than rVV10 but the latter one has in addition also contributions from the area between the molecule and the surface. In fact the semi local correction to the correlation binding

energy density is positive close to the molecule and to the surface exactly in those areas where the non local correction to the correlation binding energy density of rVV10 is negative. Combined with the semi local correction this leads to the rVV10 correlation binding energy density depicted in (b) which in addition to the semi local correction is more negative in the interface region and shows polarization around the molecule and the surface, which leads to the stronger binding of the rVV10 functional when compared with the PBE functional.

5 Molecular spintronics

In molecular electronics single molecules are already integrated in technologically relevant electronic devices like single molecule diodes [27, 207, 208] or organic field-effect transistors [33, 34, 209, 210]. The main intention for the use of molecules in conventional electronic devices is the miniaturization of already existing technology. Such electronic devices rely on the manipulation of the molecules electronic structure due to the molecule-surface interaction i.e. it involves the tuning of the hybrid molecule-surface electronic properties related to the conductance of an electron charge current. The usage of the electron charge current suffers like in larger scaled electronic devices from the production of heat and the corresponding necessity of cooling the device. The dramatically increasing power consumption together with the technological challenge of cooling and continuously shrinking the size of electronic devices initiates the search for an alternative to conventional electronics.

A popular approach is to replace the charge current by a spin current which requires hybrid electronic structures specifically tailored to exploit magnetic properties. One of the highlights introduced recently in the emerging field of molecular spintronics is the integration of a single molecule magnet in a supramolecular spin valve device [211, 212]. Also the transport through a single molecule magnet in a molecular junction has been investigated [212, 213]. Besides of directly implementing spintronic devices in molecular adsorption structures, organic molecules can be used to adjust the electronic and magnetic properties of the materials used within spintronic devices to fit specific requirements. E.g. it has been suggested that in the case of the adsorption of a double-decker molecule ($YbPc_2$) on a ferromagnetic substrate the magnetic exchange coupling constant describing the magnetic interaction between the molecule and the surface can vary depending on the amount of charge transferred at the molecule surface interface [214]. If the molecule possesses the correct electronic structure the system can in addition be used as a spin filter device, as it has been shown in the experiment and by calculations [212].

In this chapter we will investigate two promising approaches to realize the spin filter functionality by adsorbing COT on magnetic transition metal adatoms on Au(111) and PCP on the ferromagnetic Fe/W(110) surface as well as on the antiferromagnetic Fe/W(100) surface. The adsorption of PCP on the Fe coated W surfaces in addition allows to study the change of magnetic properties i.e. the magnetic exchange coupling between the Fe atoms of the substrate by the interaction with nonmagnetic molecules.

5.1. Cyclooctatetraene on magnetic and nonmagnetic adatoms on Au(111)

In addition to the properties analyzed in the last chapter COT can be used to synthesize molecular magnets by inserting magnetic adatoms between two COT molecules. In particular the 4f metals like Eu have been used for this purpose [215–217]. These sandwich structures could be adsorbed on a non magnetic surface for functionalization in the direction of spintronics applications. In a spintronic device there are two ferromagnets, a spin injector and a spin detector, separated by a nonmagnetic spacer [7]. In order to obtain a spin polarized current the injector has to act as a spin filter. The resistance of the device depends on the relative magnetization orientation of the injector and the detector which can be varied e.g. by an applied magnetic field. To further miniaturize such devices magnetic molecules adsorbed on non magnetic surfaces could be promising candidates. If there are well separated, sharp molecular states which are significantly spin split, different spin polarizations could be accessed in a STM experiment. The junction made of an organic molecule adsorbed on a magnetic adatom on a metal surface could be used as a spin filter like it has been proposed by Tao *et al.* [218]. In the last chapter we have seen that sharp molecular features occur in the case of physisorption of COT on Au(111) while strong molecule surface interaction between the COT molecule and the (100) noble metal surfaces led to the formation of broad hybrid bands. The latter observation makes the search for a molecular spin filter difficult because in order to induce a considerable spin splitting to the molecular orbitals a strong interaction with a magnetic surface would be required. Thus, in this chapter we will study the adsorption of COT on Au and $3d$ magnetic adatoms on the Au(111) surface which has also been generated in an experimental setup [219]. The spin splitting of the molecular orbitals of the nonmagnetic COT molecule will be induced by the magnetic adatoms adsorbed between the Au(111) surface and COT.

The unit cell and the parameters of the calculations are unchanged with respect to those given in the last chapter for the adsorption of COT on the bare Au(111) surface. In addition to the COT molecule an extra Au, Co, Fe or Mn adatom is adsorbed on the fcc site of the surface. The COT molecule is supposed to adsorb on top of this adatom. We started our investigation with a nonmagnetic Au adatom which has been exchanged in a systematic way with $3d$ magnetic atoms i.e. Co, Fe and Mn. The results regarding

Table 5.1.: Adsorption energy in eV, distance of the adatom to the Au(111) surface d_{Ad} in Å, the distance between the adatom and the COT molecule d_{COT} in Å, and the magnetic moment in μ_{B} for a Au, Co, Fe, and Mn adatom on Au(111) and for a COT molecule adsorbed on top of the adatom.

	without COT			with COT			
Adatom	E_{ads} (eV)	d_{Ad} (Å)	m (μ_{B})	E_{ads} (eV)	d_{Ad} (Å)	d_{COT} (Å)	m (μ_{B})
Au	-2.440	1.91	0.00	-0.901	2.10	1.88	0.00
Co	-3.649	1.59	2.09	-1.850	2.02	1.36	1.51
Fe	-3.528	1.60	3.26	-1.697	2.11	1.24	2.49
Mn	-2.996	1.72	4.27	-1.465	1.94	1.63	3.53

the adsorption energy, the distance to the surface and the magnetic moment from the calculations of the adatoms adsorbed on the Au(111) surface without the COT molecule are given in Table 5.1. The distance between the Au adatom and the Au(111) surface is 1.94 Å. This is significantly smaller than the interlayer distance of 2.44 Å of the Au(111) surface with the theoretical lattice constant. The distances for the 3*d* adatoms are even shorter. The Au adatom does not show any magnetic moment. For the 3*d* adatoms on Au(111) we obtain magnetic moments of 2.09 μ_{B} for Co, 3.26 μ_{B} for Fe and 4.27 μ_{B} for Mn. Our calculated magnetic moments of the Co and Fe adatom differ from the values reported by S. Bornemann *et al.* [206] by $\approx 10\%$. This is due to the different approach used in that calculations. S. Bornemann *et al.* used a cluster geometry with the magnetic adatoms placed at the ideal Au fcc site without further relaxations [206]. As we have just observed the distance between the adatoms and the Au(111) surface differs from the equilibrium interlayer distance of Au(111), which leads to different magnetic moments. For the Mn adatom the adsorption site is in agreement with previous calculations done by F. Muñoz *et al.* [205]. However, their calculated equilibrium distance 2.58 Å differs from our distance 1.72 Å, which leads to a higher magnetic moment of 4.82 μ_{B}. The origin of the different adsorption geometry of the adatom are the higher coverage considered and different computational parameters. The authors calculated a (3×3) supercell with a cutoff energy of 260 eV and a convergence criterion for the forces of 0.03 eV/Å [205]. The main contribution to the difference of our calculations stems from the different coverage. We did a test calculation in a $(3 \times \sqrt{3})$ supercell with our computational parameters and a consistently increased $12 \times 12 \times 1$ **k**-point grid and obtained a geometry which is closer to that published in [205]. In our calculations the difference in the magnetic moments of the adsorbed adatoms with respect to those of the free atoms is between 0.7 μ_{B} and 0.9 μ_{B}. Due to the hybridization of the states of the adatom with those of the Au(111) surface the electrons in the spin up and the spin down channel rearrange and in consequence the magnetic moments are reduced. Under this consideration also the Au adatom, which does not show a magnetization when it is adsorbed on the Au(111) surface, follows the trend of reducing its free atom magnetic moment by roughly one.

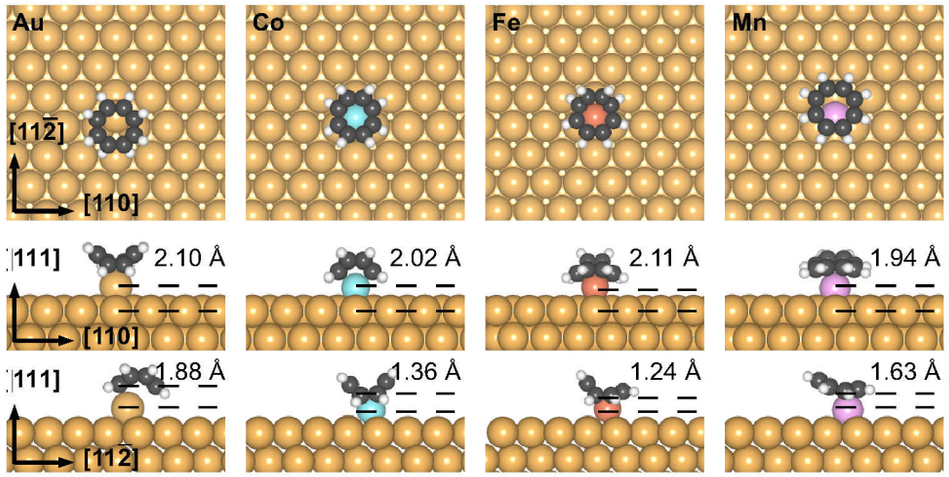

Figure 5.1.: Relaxed configurations of COT adsorbed on a Au, Co, Fe and Mn adatom on Au(111). Adsorbed on Au and Co the COT molecule adopts its tub shape while on Fe and Mn the molecule shows a new shape which in case of Mn is already rather close to a flat shape.

The COT molecule was placed in its tub shape with its center on top of the adatom. The relaxed configurations are shown in Figure 5.1. Apart from the flat and the tub shape conformations discussed in the previous chapter we additionally observe in this case an L like shape for COT adsorbed on Fe and Mn. Although in the latter case the molecule is very close to the flat shape. For the Co and the Fe adatom the center of the COT molecule in the relaxed configuration stays on top of the adatom. on the Au and the Mn adatom the COT molecule adsorbs with a C=C double bond on top of the adatom. Table 5.1 lists the results regarding the adsorption energies, the distances between the Au(111) surface and the adatom and between the adatom and the COT molecule, as well as the magnetic moments of the adatoms. The binding strength expressed by the adsorption energies calculated with the PBE functional for the adatoms on Au(111) as well as for the COT molecule adsorbed on top of an adatom decreases from Co, Fe, Mn to Au. Compared to the clean Au(111) surface, where the adsorption energy of COT calculated with the PBE functional is -0.162 eV, COT is bound strongly to the Au adatom with an adsorption energy of -0.901 eV. The distances between the adatoms and the Au(111) surface are increased upon the adsorption of the COT molecule. The bond lengths between the adatom and the COT molecule are 1.88 Å for Au, 1.36 Å for Co, 1.24 Å for Fe, and 1.63 Å for Mn. These distances to the adatoms are significantly shorter than the molecule surface distance of COT directly adsorbed on the Au(111) surface. The magnetic moments of the adatoms are decreased with respect to those of the adatoms adsorbed on Au(111) without the COT molecule on top to 1.51 μ_B for Co,

2.49 μ_B for Fe and 3.53 μ_B for Mn. Again the magnetic moment of the studied $3d$ metal adatoms decreases by roughly 0.7 μ_B upon the adsorption of a COT molecule on top of it with respect to the magnetic moment of the adatom without molecule adsorbed on Au(111).

The adsorption on the adatoms significantly changes the electronic structure of COT compared to what has been shown in the last section for COT adsorbed on a clean Au(111) surface. The projection onto the p_z orbitals of COT adsorbed on Au(111) is reprinted in Figure 5.2 for a convenient comparison with the PDOS calculated for COT adsorbed on Au, Co, Fe and Mn adatoms on Au(111). The sharp molecular peaks located at -0.7 eV and 1.75 eV for COT adsorbed on Au(111) are shifted by ≈ 0.5 eV towards lower energies when the COT molecule is adsorbed on a Au adatom. Although the interaction between the Au adatom and the molecule is much stronger than that between the COT molecule and the Au(111) surface the peaks in the p PDOS remain sharp and are not too broadened due to hybridization. This is due to the fact that COT is interacting only with a single adatom which does not lead to the formation of broad hybrid metallic bands as on the strongly interacting (100) metal surfaces discussed in the last chapter. When we replace the Au adatom by a Co adatom the highest occupied orbital type peak becomes spin split by 148 meV and the lowest unoccupied type peak by 91 meV upon the hybridization of the p_z states of the C atoms of the COT molecule with the spin split d states of the Co atom. With the Fe adatom this spin splitting of the sharp molecular orbitals at -1.75 eV and 1.5 eV increases to 178 meV and 497 meV. On the contrary for the Mn adatom the peak in the PDOS for the unoccupied states is broadened due to the hybrid state formed near the Fermi energy. The difference between the Mn adatom on the one hand and the Fe and Co adatoms on the other hand is the position of the COT molecule relative to the adatom. The Fe and the Co adatom are beneath the center of the COT molecule. The Mn adatom in contrast is underneath a C=C double bond, which leads to stronger hybridization. With the COT molecule adsorbed on top of all three magnetic adatoms the d_{z^2} part of the PDOS shows sharp peaks, while those of the adatom without COT are slightly broadened. This becomes more evident when we compare the PDOS for the occupied states of the adatoms with a COT molecule on top to that of the adatoms adsorbed on Au(111) shown in Figure 5.3. Due to the fact that the adatoms are further away from the Au(111) surface when the COT molecule is adsorbed on top of them, the interaction with the substrate is decreased.

The magnetic anisotropy energies for COT adsorbed on Mn, Fe and Co adatoms on the Au(111) surface as well as for the adatoms without molecule on Au(111) are given in Table 5.2. The magnetic anisotropy energies for the adatoms on the Au(111) surface have been calculated for consistency reasons in the same large supercell which was also used for the adsorption of the COT molecule. It has been reported by S. Bornemann *et al.* [206] that magnetic $3d$ adatoms on Au(111) have a rather large magnetic anisotropy energy between the magnetization aligned parallel to an in-plane direction with respect to the magnetization aligned in the out-of-plane direction i.e. 11.45 meV for Fe and 9.02 meV

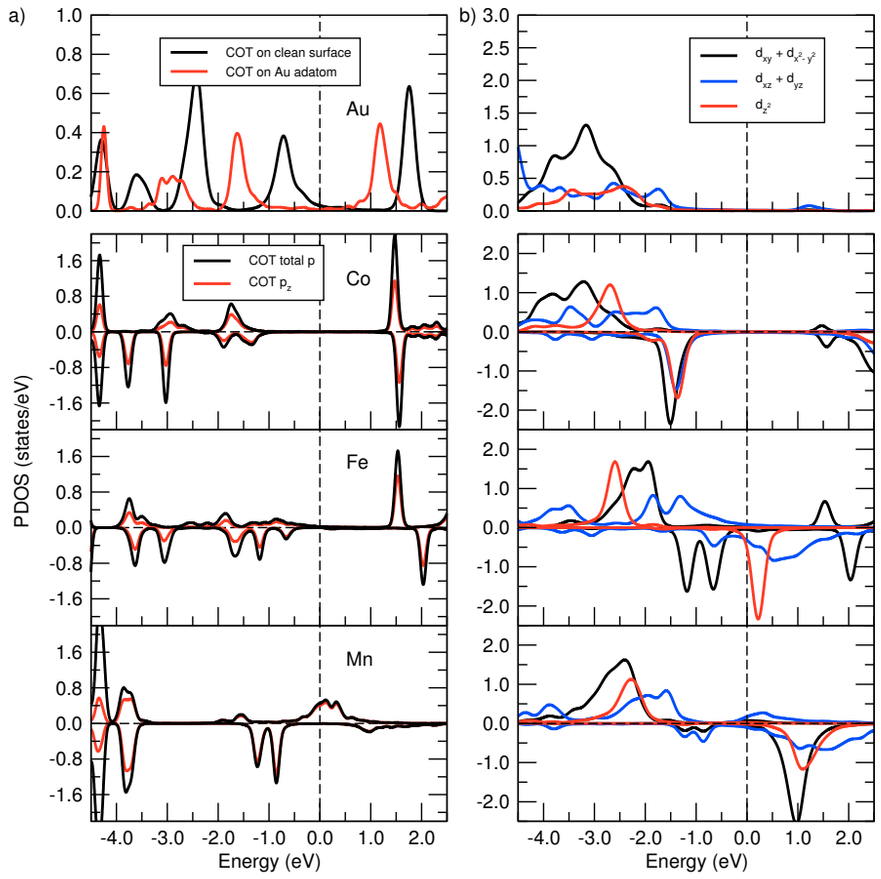

Figure 5.2.: (a) Projected density of states on the p orbitals of COT adsorbed on the clean Au(111) surface and on a Au, Co, Fe, as well as a Mn adatom. (b) PDOS on the in-plane $d_{xy} + d_{x^2-y^2}$ and the out-of-plane $d_{xz} + d_{yz}$,d_{z^2} d orbitals of the corresponding adatom adsorbed on the Au(111) surface. The PDOS has been broadened by a 0.1 eV Gaussian.

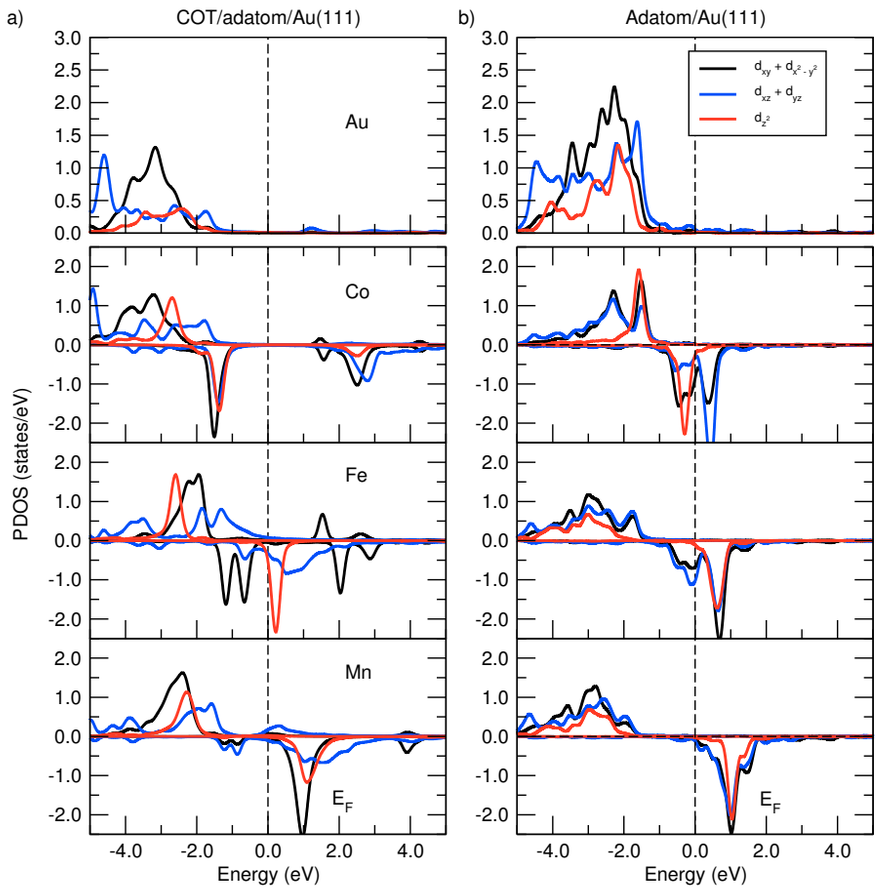

Figure 5.3.: Comparison between the (a) Projected density of states on the in-plane $d_{xy} + d_{x^2-y^2}$ and the out-of-plane $d_{xz} + d_{yz}$,d_{z^2} d orbitals of the Au, Co, Fe, and Mn adatom adsorbed on the Au(111) surface with COT adsorbed on top of the adatom and (b) without the COT molecule. The PDOS has been broadened by a 0.1 eV Gaussian.

Table 5.2.: Magnetic anisotropy energies in meV for COT adsorbed on Fe, Co and Mn adatoms as well as for the adatoms without the molecule on the Au(111) surface. The easy axis has a magnetic anisotropy energy of zero.

Direction	[110]		[11$\bar{2}$]		[111]	
k-points	**Γ**	2×2	**Γ**	2×2	**Γ**	2×2
COT 1Co/Au(111)	0.00	0.00	0.60	0.21	0.14	0.12
COT 1Fe/Au(111)	0.00	0.00	0.45	0.35	0.08	0.08
COT 1Mn/Au(111)	0.10	0.16	0.00	0.00	0.49	0.51
1Co/Au(111)	0.00	0.00	0.05	1.45	1.06	2.88
1Fe/Au(111)	0.00	0.00	-	-	0.01	0.42
1Mn/Au(111)	0.00	0.00	0.01	4.21	0.38	4.50

for Co. These results have been obtained with a non periodic supercell approach and the authors emphasized that a direct comparison to periodic supercell calculations has been shown to be problematic [206]. In the work of S. Bornemann *et al.* [206] the position of the magnetic adatom was fixed to the position which an additional Au bulk atom would have and the experimental lattice constant 4.08 Å of Au has been used. We already mentioned in the paragraph concerning the adsorption of the adatoms on the Au(111) surface that the relaxed distance between the adatom and the Au(111) surface differs significantly from the interlayer distance of the Au(111) surface. In addition a different xc-functional i.e. LSDA has been applied in [206]. Turning to our calculations for both Fe and Co adatoms on Au(111) the magnetic anisotropy energies obtained with the $2\times2\times1$ Monkhorst-Pack **k**-point grid are with 2.88 meV for Co and 0.42 meV for Fe much smaller than those presented in [206]. In addition our calculations predict an in-plane easy axis aligned along the [110] direction. Also with the **Γ**-point only calculations we obtain an in-plane easy axis. For a complete ML of Co on Au(111) an in-plane magnetization with a MAE of ≈ 0.65 meV has been reported by B. Újfalussy *et al.* [220]. Also for the Mn adatom we obtain an in-plane easy axis with a MAE of 4.50 meV. When COT is adsorbed on top of the adatoms the magnetic anisotropy energies calculated with the $2\times2\times1$ **k**-point set are decreased to 0.21 meV for Co, 0.35 meV for Fe and 0.51 meV for Mn. The changes of the MAE when increasing the number of **k**-points from the **Γ**-point only calculations are less drastic than for the adatoms without COT molecule adsorbed on Au(111). However, a large number of **k**-points for the BZ integration is required for the convergence of MAEs and thus results using only the **Γ**-point are certainly not converged. The direction of the easy axis stays the same for Co and Fe but due to the small energy differences between the configurations with the magnetization aligned along the [110] direction and along the [111] direction in the case of Fe it is necessary to speak of an easy plane rather than an easy axis anisotropy.

5.2. Paracyclophane on Fe/W(110)

The goal of this and the following section is to propose a concept for embedding magnetic units into a ferromagnetic substrate by the adsorption of an organic molecule which in addition shows spin-filter characteristics with sharp molecular features in the electronic structure. The conceptual challenge to achieve this is that the molecule should ideally be chemisorbed on the substrate such that the molecule-surface interaction can locally modify the magnetic properties of the substrate atoms leading to an organic based magnetic unit [14]. The requirement of chemisorption however leads to the formation of broad spin unbalanced hybrid molecule-metal bands [221] around the Fermi level. This conflicts with the requirement of having sharp molecular peaks in the electronic structure for the spin filter functionality, which occurs in the case of physisorption [14]. To solve this dilemma we propose the usage of biplanar π-conjugated nonmagnetic organic molecules chemisorbed on a ferromagnetic surface. In particular we have investigated the adsorption of [2,2]paracyclophane (PCP) on the ferromagnetic Fe/W(110) surface. PCP consists of two parallel benzene rings connected by sp^3 hybridized C atoms. In contrast to the last section were the formation of sharp spin split molecular features has been achieved by exploiting the discrete electronic structure of magnetic adatoms, in this case the biplanar structure of the PCP molecule will protect the molecular peaks at one of the two planes. Our investigations on PCP will serve as a blueprint for a more general study as PCP is a prototype of a whole class of biplanar structured molecules. Most of the results presented in this section have been published in [15].

Monolayers of Fe on W(110) have been studied intensively both by STM experiments and DFT calculations as they show a rich variety of different magnetic properties depending on the Fe coverage. In combination with this a pseudomorphic growth behavior [222] of Fe on W and a large spin orbit coupling of the W surface make the system attractive. Up to 60% coverage of the first monolayer [223] Fe forms non magnetic islands. Beyond that the Fe islands show a ferromagnetic order till the completion of the first full monolayer. The orientation of the magnetic easy axis is along the $[1\bar{1}0]$ in-plane direction as reported by both experiments [224–228] and theoretical calculations [229–233]. When the coverage reaches around 1.5 ML the islands of the second monolayer show a long range antiferromagnetic order [227, 234, 235]. While an out-of-plane magnetization direction is found in [227, 235–238], after annealing the sample the system shows an in-plane easy axis in [239]. For a complete second monolayer of Fe on W(110) both an in-plane easy axis [230] and an out-of-plane easy axis [238] have been reported calculated by means of the FLAPW method. Calculations using the VASP code support the out-of-plane magnetization for two ML of Fe on W(110) [221]. Energy differences between the ferromagnetic ground state and an antiferromagnetic configuration, from which the nearest neighbor magnetic exchange coupling constant can be extracted, have been done with the FLAPW method by A. T. Costa *et al.* [233] and with the VASP code by D. Spišák and J. Hafner [231].

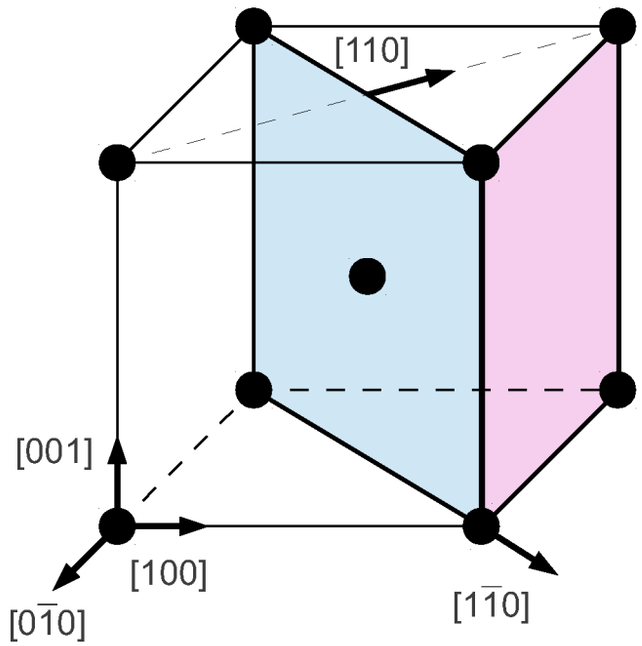

Figure 5.4.: Schematic of the bcc cell to visualize the crystallographic directions needed throughout the discussion in this chapter. The blue area represents the (110) surface plane of the bcc lattice and the red area the (100) surface plane. For the (110) surface the out-of-plane [110] direction and the long in-plane $[1\bar{1}0]$ direction are depicted.

For the adsorption configuration the Fe/W(110) surface has been modeled by a slab consisting of six layers of W with the calculated lattice constant of 3.174 Å and one or two monolayers of Fe adsorbed on one side of the slab. A (4×5) supercell has been used which leads to a distance between periodically repeated images of the PCP molecule of 17.95 Å in $[1\bar{1}0]$ direction and 15.87 in [001] direction. 18 Å of vacuum separate two periodic images of the slab in [110] direction. As starting configuration the magnetic moments of all Fe atoms were aligned ferromagnetically with the clean surface magnetic moment of 2.48 μ_B for the single monolayer and 2.25 μ_B as well as 2.88 μ_B for the first and the second Fe layer respectively in the case of two Fe monolayers. The cutoff energy was set to 500 eV and for the relaxations only the Γ-point has been used for BZ sampling.

On the (110) surface of the bcc lattice depicted as blue area in Figure 5.4 there are three high symmetry sites namely the top site, the hollow site in the center between

two surface atoms along the [100] direction and the bridge site in the center of the shortest distance between two surface atoms. On each site several different orientations of the PCP molecule have been chosen as starting configurations, which differ by the number of C atoms interacting with Fe surface atoms. The most stable adsorption configuration is the one with the center of the PCP molecule occupying the hollow site with the long axis of the molecule oriented parallel to the [100] direction. This configuration has two C atoms adsorbed directly on top of two Fe atoms (Fe1) and two C=C double bonds on top of two other Fe atoms (Fe2). The PCP molecule is slightly twisted clockwise around the C_2 axis in the center of the molecule pointing into the [110] direction, which brakes the mirror symmetry of the system with respect to the $(1\bar{1}0)$ plane. Except for the configuration adsorbing PCP with its center on a bridge site oriented in the $[1\bar{1}0]$ direction all other starting configurations relaxed towards the most stable one. The distance between the molecule and the surface is 1.95 Å and the corresponding adsorption energy is −2.457 eV. The inclusion of corrections regarding dispersion interactions via the DFT-D3 method did not lead to further relaxations. Only the adsorption energy changes to −3.482 eV. Due to the adsorption of PCP on the Fe/W(110) surface the magnetic moments of the four Fe atoms directly interacting with the molecule are reduced with respect to the magnetic moment 2.48 μ_B of the Fe atoms of the clean surface. The magnetic moments of the two Fe atoms underneath a C atom are decreased to 2.09 μ_B and the magnetic moments of the two Fe atoms underneath a C=C double bond to 2.32 μ_B. The rest of the Fe atoms has the magnetic moment of the clean surface. The difference between the magnetic moments of Fe1 and Fe2 is related to the slightly different Fe-C distance of 2.06 Å and 2.24 Å, indicating a different strength of hybridization. In the same way also the magnetic moments of the four Fe atoms underneath the PCP molecule on the two ML Fe/W(110) surface is decreased from the clean surface value 2.88 μ_B to 2.52 μ_B and 2.70 μ_B for the Fe atoms underneath the C atoms and the Fe atoms underneath the C=C double bonds respectively.

According to the small molecule surface distance and the large absolute value of the adsorption energy a strong interaction of PCP with the Fe/W(110) surface is expected. The PDOS on σ and π states of the lower part of the PCP molecule, which directly binds to the substrate, depicted in Figure 5.5 confirms this expectation by showing no distinct molecular features but only a broad band of hybrid states. While the PDOS of the free PCP in the gas phase is spin symmetric, this symmetry is broken when the molecule adsorbs on the surface due to the hybridization with states of the magnetic Fe atoms. However, the PCP molecule itself does not show a magnetization. In contrast to the broad bands observed on the lower ring the PDOS on the σ and π states of the upper part of the PCP molecule shows sharp peaks at energies of −2.3 eV (P1) and −1.8 eV for the occupied states as well as 2.5 eV for the unoccupied states. All three peaks in the PDOS of the upper part of the PCP molecule are exchange split with splittings of 65 meV, 57 meV and 88 meV for P1, P2 and P3 respectively. This shows the peculiarity of the choice of PCP to functionalize the Fe/W(110) surface. The lower part of the molecule interacts strongly with the surface and mediates an exchange splitting via spin

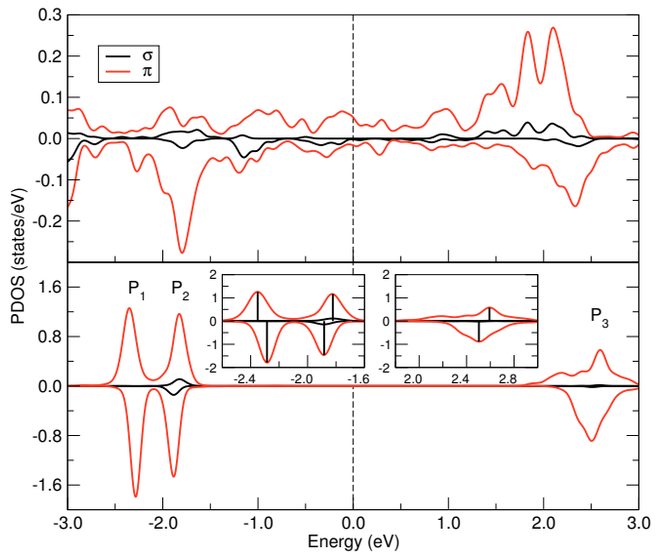

Figure 5.5.: The PDOS on the σ and π states of the lower ring and the upper ring of the PCP molecule adsorbed on 1 ML of Fe on W(110). The lower ring binds to the substrate which leads to the formation of broad spin polarized hybrid molecule surface bands. The PDOS of the upper ring shows in contrast sharp and spin split molecular orbital like peaks. The PDOS has been broadened by a 0.1 eV Gaussian.

unbalanced π-*pi* interaction. The molecule itself stays non magnetic. PCP adsorbed on Fe/W(110) thus shows the characteristics of a molecular spin filter. This effect could be used in STM experiments to access different spin polarizations of the upper ring depending on how many spin majority and spin minority states are within the energy interval under consideration. The effect is still present when PCP is adsorbed on a two Fe layers coated W(110) surface, which can be seen from the corresponding PDOS depicted in Figure 5.6. Again the lower ring strongly hybridizes with the metal states while the upper ring shows sharp spin split peaks. Here the splittings are 93 meV, 41 meV and meV respectively. The main difference between the single Fe monolayer and the Fe double layer is the magnetic moment of 2.88 μ_B of the second layer at the vacuum interface which is higher than the magnetic moment of 2.48 μ_B of the monolayer adsorbed on W(110). But, as it becomes clear from the above results, the larger magnetic moment does not translate into a larger spin splitting. The magnetic moments of the Fe ML at the W side of the interface are unaffected by the adsorption of the PCP molecule.

In the previous paragraph we have seen that due to the adsorption and the caused

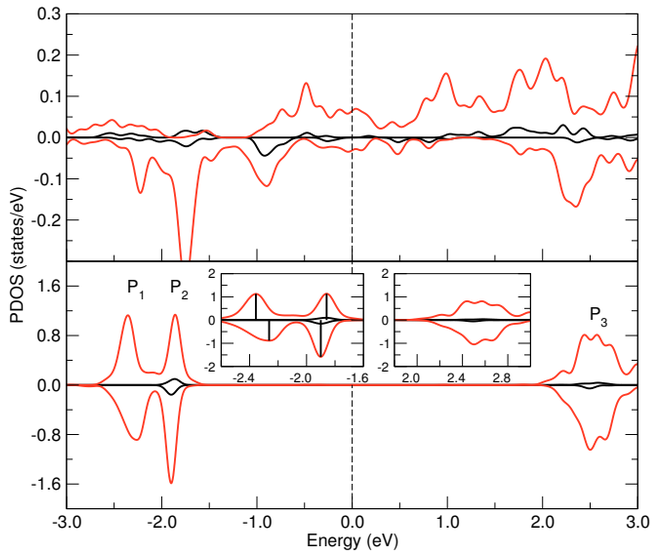

Figure 5.6.: The PDOS on the σ and π states of the lower ring and the upper ring of the PCP molecule adsorbed on 2 ML of Fe on W(110). The insets show close ups of the spin split peaks in the PDOS of the upper ring of the PCP molecule. The PDOS has been broadened by a 0.1 eV Gaussian.

hybridization of the PCP molecule on the Fe/W(110) surface the magnetic moments of the four Fe atoms underneath the PCP molecule are decreased. In order to investigate how the adsorption of PCP influences other magnetic properties like the magnetic exchange coupling constants J and the anisotropy K we have to do a set of additional calculations. The magnetic exchange coupling constants can be extracted by mapping our system onto a Heisenberg-model with the Hamiltonian

$$\mathcal{H} = -\sum_{i<j} J_{ij}\mathbf{S}_i\mathbf{S}_j \tag{5.1}$$

where the indices i, j run over all spins in the system and J_{ij} is the magnetic exchange coupling constant coupling the spins i and j. We will consider here only nearest neighbor interactions. Thus, the additional condition that i and j are nearest neighbors has to be imposed on the indices. Based on the analysis of the magnetic moments of the Fe atoms, we have to deal with three different kinds of Fe atoms in the surface layer: those which are directly underneath a C atom denoted as Fe1 in Figure 5.7 (b), those underneath C-C double bonds called Fe2 and all the other Fe atoms. Thus, if only nearest neighbor

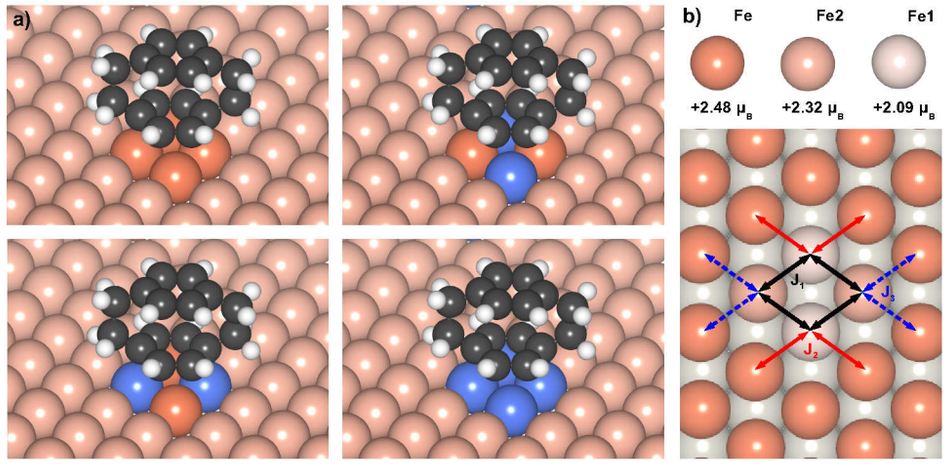

Figure 5.7.: (a) Visualization of the magnetic configurations used to calculate the magnetic exchange coupling constants J. Red atoms have a positive magnetization while the orientation of the magnetization of the blue atoms points in the opposite direction. (b) Definition of the magnetic exchange coupling constants J_1, J_2 and J_3.

interactions are taken into account, three different exchange coupling constants J_k have to be considered. J_1 is the magnetic exchange coupling constant of the interaction of Fe1 with Fe2, J_2 the magnetic exchange coupling constant of the interaction of Fe1 with other surface atoms and J_3 the magnetic exchange coupling constant of the interaction of Fe2 with other surface atoms. With these definitions and the Heisenberg model introduced above the energy difference caused by rotating a set of spins from parallel to antiparallel alignment with respect to the ferromagnetic ground state can be expressed as

$$\Delta E = -2 \sum_k J_k N_k m_{1,k} m_{2,k} \tag{5.2}$$

where N_k is either zero or four depending on wether the Fe atoms corresponding to this k are coupled ferromagnetically or antiferromagnetically in the second magnetic configuration and $m_{1,k}, m_{2,k}$ are the magnetic moments of the two Fe atoms corresponding to k. The three magnetic exchange coupling constants J_k can be obtained by performing calculations for additional three different magnetic configurations which are depicted in Figure 5.7 (a). First all four Fe1 and Fe2 atoms are oriented antiferromagnetically with respect to the other surface atoms. Second either the two Fe1 or the two Fe2 atoms have to be oriented in the opposite direction. The energy differences evaluated with Equation 5.2 between the ferromagnetic configuration and the three antiferromagnetic configurations lead to a set of equations from which the magnetic exchange coupling

constants J_1, J_2 and J_3 can be extracted.

$$\begin{aligned} E_{\mathrm{FM}} - E_{\mathrm{AFM1}} &= -8J_2 - 8J_3 \\ E_{\mathrm{FM}} - E_{\mathrm{AFM2}} &= -8J_1 - 8J_2 \\ E_{\mathrm{FM}} - E_{\mathrm{AFM3}} &= -8J_1 - 8J_3 \end{aligned} \tag{5.3}$$

These equations arise from the Heisenberg model discussed above and in Section 1.4, where the magnetic anisotropy terms vanish as in both configurations the spins are oriented parallel or antiparallel to the same axis and the terms for unchanged spin pairs cancel each other when taking the differences. With the obtained energy differences $E_{\mathrm{FM}} - E_{\mathrm{AFM1}} = -0.473$ eV, $E_{\mathrm{FM}} - E_{\mathrm{AFM2}} = -0.778$ eV, and $E_{\mathrm{FM}} - E_{\mathrm{AFM3}} = -0.796$ eV the magnetic exchange coupling constants given per pair of Fe atoms and divided by the magnetic moments are $J_1 = 15.65$ meV$/\mu_{\mathrm{B}}^2$, $J_2 = 5.84$ meV$/\mu_{\mathrm{B}}/\mu_{\mathrm{B}}^2$ and $J_3 = 5.17$ meV$/\mu_{\mathrm{B}}^2$. As a first observation the coupling constants describing the interactions of Fe1 and Fe2 with the other Fe atoms of the surface slightly differ from the value of the clean surface which is $J_{\mathrm{S}} = 5.42$ meV$/\mu_{\mathrm{B}}^2$. The latter has been calculated in a c(1×1) cell. We can compare our result for the magnetic exchange coupling constant of the clean surface to previous calculations within the FLAPW framework done by A. T. Costa *et al.* [233] and with VASP calculations by D. Spišák and J. Hafner [231]. In our units the FLAPW calculations resulted in a nearest neighbor magnetic exchange coupling constant $J_{\mathrm{S}} = 6.48$ meV$/\mu_{\mathrm{B}}^2$ [233] and the VASP calculations $J_{\mathrm{S}} = 6.15$ meV$/\mu_{\mathrm{B}}^2$ [231]. For both calculations the total magnetic moments of the Fe atoms were different from ours i.e. 2.56 μ_{B} and 2.41 μ_{B} for the ferromagnetic state as well as ± 2.56 μ_{B} and ± 2.31 μ_{B} for the antiferromagnetic state. In the FLAPW calculation besides of the all electron method a symmetric five layers W slab with an Fe slab on each side has been used[233]. In the VASP calculations the cutoff energy has been 280 eV, which leads to a larger W lattice constant and in consequence a different relaxation of the surface layer. This leads to energy differences between the two magnetic states slightly deviating from our calculations. Returning to the discussion on a PCP molecule adsorbed on Fe/W(110) more obvious is the change of the magnetic exchange coupling constant J_1 between Fe1 and Fe2 which is roughly three times larger than the clean surface value. Due to the strong magnetic exchange coupling between the four Fe atoms underneath the PCP molecule the four Fe atoms together with the PCP molecule can be considered as a magnetic unit embedded into the ferromagnetic surface. The fact that the magnetic exchange coupling constants J_2 and J_3 of Fe1 and Fe2 to the rest of the surface Fe atoms do not deviate much from the clean surface value shows that this magnetic hardening effect is restricted to a small part of the surface. In addition the small change of J_1 and J_2 differs from the previously found result by K. V. Raman *et al.* [14]. In their case the molecular unit formed by a phenalenyl based molecule and the underlying Co surface layer was decoupled from the rest of the surface, due to a significant decrease of the nearest neighbor magnetic exchange coupling constant to the second Co layer.

The analysis of the PDOS on the d states of the Fe atoms for the ferromagnetic and

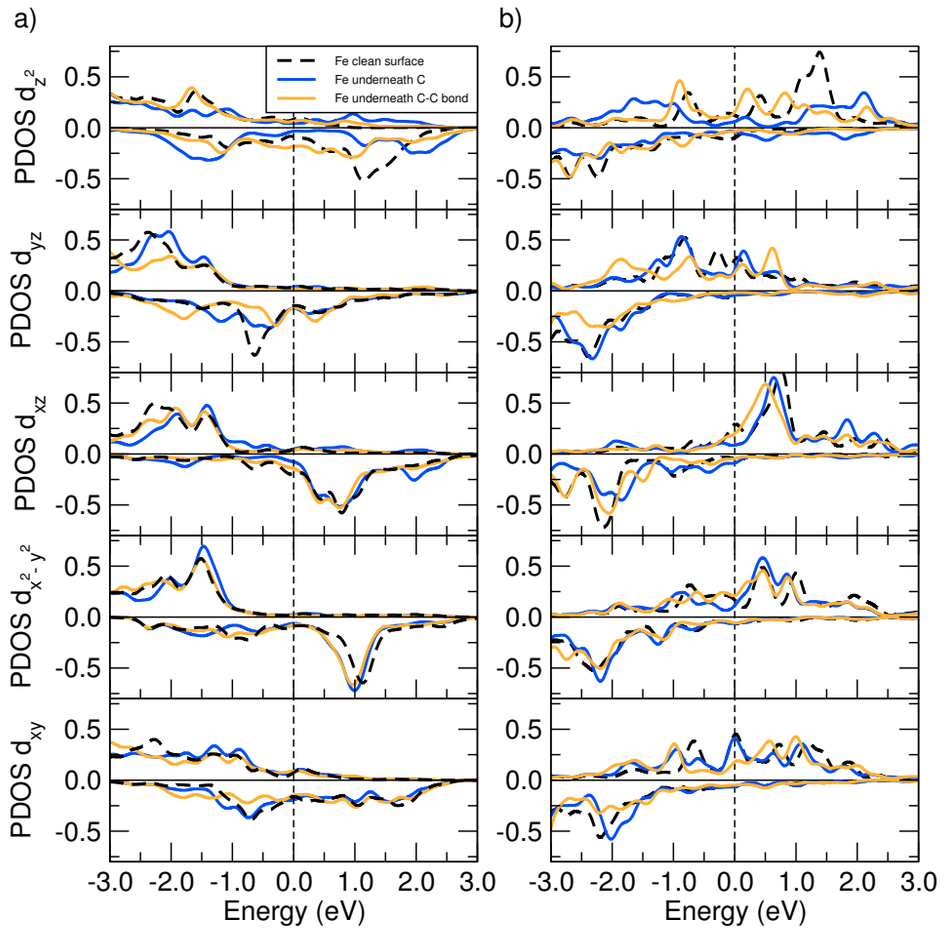

Figure 5.8.: PDOS on the Fe *d* states of an Fe atom on the clean Fe/W(110) surface (black), the Fe1 atom (blue) and the Fe2 atom (orange) for the ferromagnetic configuration (a) and the antiferromagnetic configuration (b) as depicted in Figure 5.7. The PDOS has been broadened by a 0.1 eV Gaussian.

Table 5.3.: Magnetic anisotropy energies per Fe atom in meV for PCP adsorbed on one ML of Fe on W(110), for the molecular unit defined by PCP and the four Fe atoms underneath in a large empty box and for the clean W(110) surface covered by one ML of Fe. The easy axis has a magnetic anisotropy energy of zero.

Direction	[1$\bar{1}$0]		[100]		[110]	
k-points	**Γ**	2×2	**Γ**	2×2	**Γ**	2×2
PCP Fe/W(110)	0.00	0.00	-2.94	1.68	-2.22	1.34
PCP + 4 Fe	0.49	-	0.00	-	0.20	-
Fe/W(110)	0.00	0.00	5.04	2.92	3.02	2.61

the antiferromagnetic configurations depicted in Figure 5.8 will help us to identify the magnetic hardening mechanism responsible for the enhanced interaction of the Fe atoms directly underneath the PCP molecule. With respect to the PDOS of the Fe atom from the clean surface the PDOS on the d_{xz}, d_{yz} and d_{z^2} orbitals of the Fe1 and the Fe2 atom shows significant differences over a large energy interval around the Fermi energy. This is due to the strong hybridization of these states - referred to as $d_\pi = d_{xz} + d_{yz} + d_{z^2}$- with the π orbitals of the PCP molecule. The contribution of the Fe1 and the Fe2 atoms to common $d_\pi - \pi$ hybrid orbitals leads to a stronger coupling between the d_π orbitals of those Fe atoms mediated by the hybrid orbitals, similar to the general mechanism of indirect exchange [15, 67]. In addition this mechanism based on the overlap of the $d_\pi - \pi$ states will not influence the magnetic exchange coupling constants J_2 and J_3 of Fe1 and Fe2 to the rest of the surface like the one based on charge transfer between the molecule and the surface mentioned in [14] leading to a large decrease of the coupling constants would. The PDOS on the d_{xy} and $d_{\mathrm{x}^2-\mathrm{y}^2}$ orbitals which couple the Fe1 and the Fe2 atoms to the rest of the Fe ML changes in a minor way upon the adsorption of the PCP molecule, which is a hint for only a slight modification of the overlap of those orbitals. This in turn leads to only a slight difference in J_2 and J_3 compared to J_{S}. As a simple test whether the magnetic hardening occurs due to the adsorption of the PCP molecule and not due to the change of the geometric structure of the Fe/W(110) surface we calculated the magnetic exchange coupling constants J_k with the same distorted geometry of the surface but without the PCP molecule. The obtained values are $J_1 = 7.56$ meV/μ_{B}^2, $J_2 = 3.11$ meV/μ_{B}^2 and $J_3 = 5.65$ meV/μ_{B}^2. Especially J_1 is significantly smaller without the molecule than with the PCP molecule. It is however still larger than the clean surface value. Hence, there is a contribution to the change of the magnetic exchange coupling constants, but the major part stems from the hybridization with the orbitals of the PCP molecule. The increase of the magnetic hardening effect when the PCP molecule is adsorbed on top of the Fe/W(110) surface compared to the contribution from the geometrical change of the Fe layer further supports our proposed mechanism.

The second very important quantity determining the magnetic switching behavior

is the magnetic anisotropy energy, which is the total energy difference between two magnetic configurations with different orientations of the magnetization due to spin orbit coupling. Together with the magnetic exchange coupling constant it determines the size of magnetic domains and domain walls. In order to calculate the magnetic anisotropy spin orbit coupling has to be included into the calculations and configurations with the magnetic moments pointing in [110] (out-of-plane magnetization), [100] (in-plane magnetization along the short axis) and $[1\bar{1}0]$ (in-plane magnetization along the long axis) have to be considered. The magnetization direction with the lowest energy is the $[1\bar{1}0]$ direction. Hence, the easy axis of the clean Fe/W(110) and after the adsorption of PCP are the same. The average MAE over all the Fe atoms in the unit cell for the out of plane direction [110] and the second in plane axis [001] are 2.50 meV and 4.24 meV when only the $\mathbf{\Gamma}$-point is used for BZ sampling. Increasing the number of $\mathbf{k}$-points by using a $2\times2\times1$ Monkhorst-Pack-grid leads to MAEs of 2.49 meV and 2.80 meV. In the previous paragraphs we have shown that the properties of the four Fe atoms underneath the PCP molecule are changed, while the other Fe atoms have the same magnetic properties as those of the clean surface. Thus, we subtract from the total energy difference the contribution of the Fe atoms, which do not interact with the C atoms, in order to obtain the MAE of the four Fe atoms directly interacting with the PCP molecule listed in Table 5.3. Using this procedure we obtain magnetic anisotropy energies of 1.34 meV and 1.68 meV for the [110] and the [001] direction respectively with the $2 \times 2 \times 1$ $\mathbf{k}$-point set. The numbers obtained from the calculations using the Γ-point are negative due to the overestimation of the clean surface MAE discussed later. Due to the magnetic hardening effect discussed above the Fe atoms underneath the PCP molecule would not rotate separately. Thus, for the MAE given in [15] we considered them together with the molecule as a magnetic unit, which leads to the large increase of the MAE to 5.35 meV and 6.71 meV with respect to the clean surface value. The convergence with respect to the number of $\mathbf{k}$-points used for the BZ-integration is hard to reach for MAEs. As we are restricted due to the system size to relatively small $\mathbf{k}$-point sets, we compare our MAE for the clean surface to already published results. In the large cell containing forty Fe atoms with the $2 \times 2 \times 1$ $\mathbf{k}$-point set we obtain an MAE of 2.92 meV per Fe atom. T. Andersen *et al.* [232] have done an extensive study on the MAE of Fe/W(110) as a function of the number of W layers and the number of $\mathbf{k}$-points in the irreducible BZ by means of FLAPW calculations. Their $\mathbf{k}$-point converged result for six layers of W is 2.79 meV. This value is under the above mentioned restrictions very close to our result. The adsorption configuration of the PCP molecule shows as already stated a broken mirror symmetry with respect to the $(1\bar{1}0)$ plane. Thus, we attempted to see if there is an energy difference between magnetic configurations with the magnetization pointing in positive or negative [110] direction but within the accuracy of our calculations there was no energy difference. Unfortunately there are still two possibilities: the effect of the twist of the molecule on the electronic structure of the Fe atoms is too small to be visible or our calculations are not accurate enough.

Having both quantities the magnetic exchange coupling constants J as well as the

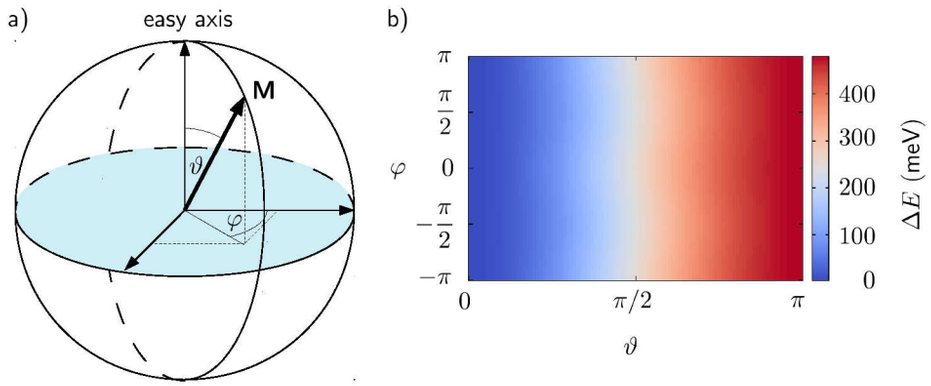

Figure 5.9.: (a) Schematic of the coordinate system used for the Heisenberg-model in Equation 5.4. The magnetization direction with $\vartheta = \varphi = 0$ corresponds to the easy axis. (b) Energy difference ΔE in meV between a magnetization direction given by ϑ and φ and the ferromagnetic ground state under the assumption that the magnetization of the molecular unit consisting of the PCP molecule and the four Fe atoms underneath can be rotated separately from the surface.

anisotropy K at hand we can further study a Heisenberg type model, where we account for the magnetic anisotropy terms for this particular system. Under the assumption that the defined molecular unit could be switched independently of the rest of the Fe monolayer, we can investigate the energy difference between the ferromagnetic ground state and a state with a changed orientation φ, ϑ of the magnetization of the four Fe atoms underneath the PCP molecule as a function of the orientation of the magnetization in order to identify wether or not there exist two stable energy minima with different orientations which would define a magnetic switch. This energy difference between the ferromagnetic ground state and the state $E(\varphi, \vartheta)$ is given by:

$$E(\varphi,\vartheta) - E_{\mathrm{FM}} = -2(J_2 m_S m_2 + J_3 m_S m_3 (\cos(\vartheta) - 1) + 4(K_1 + K_1' \cos(2\varphi)) \sin^2(\vartheta) \quad (5.4)$$

where the two angles ϑ and φ describing the direction of the magnetization are defined in Figure 5.9 (a). Inserting the calculated values for J_2, J_3 and the two anisotropy constants K_1 and K_1', which correspond to the [001] and the [110] direction, leads to the energy landscape depicted in Figure 5.9 (b). The energy difference between the state with arbitrary magnetization direction and the ferromagnetic ground state is governed by the magnetic exchange contribution. Thus, the energy difference shows a monotonic increase when rotating the magnetization direction from $\vartheta = 0$ to $\vartheta = \pi$. The contribution of the magnetic anisotropy is hardly visible as the $\sin^2 \varphi$ distortion of the $\vartheta = \pi/2$ line. An external magnetic field can be included in Equation 5.4 by adding a term $\mathbf{B} \cdot \mathbf{S} = B_x m \cos(\vartheta) \sin(\varphi) + B_y m \sin(\vartheta) \sin(\varphi) + B_z m(\cos(\vartheta) - 1)$ where the z component of the

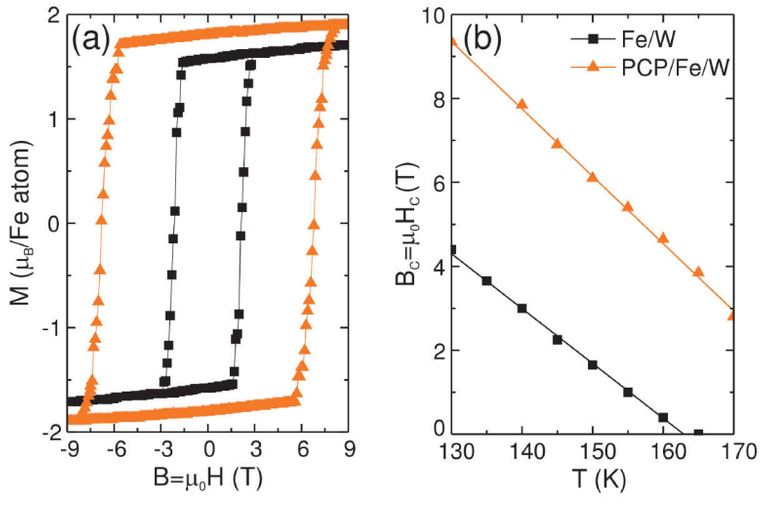

Figure 5.10.: Results of the Monte Carlo simulation of the magnetization reversal process at $T = 145$ K (a) and the coercivity field H_c below the ordering temperature for the clean (squares) and the PCP covered (triangles) magnetic Fe monolayer. The figure has been taken from [15]. Copyright (2013) by the American Physical Society.

magnetic field corresponds to the direction of the easy axis. The last term corresponding to the component of the magnetic field aligned along the direction of the easy axis compensates the loss of energy due to the magnetic exchange coupling when changing the orientation of the magnetization from ferromagnetic to antiferromagnetic coupling. None of the terms is able to introduce a second energy minimum. In addition the large energy difference between the ferromagnetically and the antiferromagnetically coupled molecular unit to the rest of the surface renders the assumption of an independent switching behavior unrealistic. For that a drastic decrease of J_2 and J_3 would be required such that the strength of the magnetic exchange coupling becomes comparable to or smaller than the magnetic anisotropy.

The impact of the magnetic hardening effect on experimentally measurable quantities like the coercivity field H_C and the Curie-temperature T_C, which are also relevant for technological applications, have been investigated by Nikolai Kiselev by means of Monte-Carlo simulations of a magnetization reversal process at finite temperature as part of our collaboration published in [15]. We will shortly review the results here to complete the discussion about the magnetic hardening of the Fe/W(110) surface upon adsorption of a PCP molecule. The simulations have been done on a bare Fe film described by the extended Heisenberg Hamiltonian containing magnetic exchange terms, magnetic anisotropy and Zeeman terms. Four of the Fe atoms contained in the Fe thin film adopted

the magnetic exchange coupling constants and magnetic anisotropy energies of Fe1 and Fe2 while the other Fe atoms were described by the clean surface values. The coverage has been chosen smaller than in the DFT calculations to one magnetic unit consisting of four Fe atoms per 24 Fe atoms in order to clearly show the impact of the magnetic hardening. The effects were however also present for smaller coverages. The simulated magnetization curves shown in Figure 5.10 (a) calculated at a fixed temperature provide an estimate for the coercivity field H_C necessary to switch the magnetization direction. The magnetization curve for the system with PCP adsorbed at the described coverage shows a much larger coercivity field than the magnetization curve of the clean surface. As a function of the temperature the coercivity field for both systems almost decreases linearly. Thus, the Fe/W(110) surface with an adsorbed PCP molecule has an around 4 T higher coercivity field than the clean surface in the studied temperature interval. The increase of the coercivity field due to the adsorption of graphene on Co coated Ir(111) has been recently observed in an experiment done by R. Decker *et al.* [240]. Their explanation for the increase of the coercivity field is an enhanced out-of-plane magnetic anisotropy. In our analysis the magnetic exchange coupling is in the focus, which goes in hand with a change of the magnetic anisotropy, due to the formation of the molecular magnetic unit. The difference between the coercivity fields of the clean Fe/W(110) surface and the PCP covered surface increases as a function of the coverage. In particular a calculation done for a four of twelve coverage resulted in an almost two times larger coercivity field than the previously discussed four of 24 coverage. The Curie temperature increases by 27 K. Together with the increase of the coercivity field the Monte-Carlo simulations clearly show an increased barrier for domain wall nucleation.

5.3. Paracyclophane on Fe/W(100)

In contrast to the ferromagnetic Fe/W(110) surface considered in the last section first experiments investigating the magnetic properties of the Fe/W(100) surface exhibit the absence of remanent magnetization [241, 242] for sub to one monolayer coverages. To explain the disappearance of the ferromagnetic order an antiferromagnetic order has been proposed based on LDA calculations [243] within the FLAPW method, whereas no stable ferromagnetic groundstate has been found. In one GGA study [244] a ferromagnetic groundstate has been calculated but the AFM case has not been studied while another [231] included both the FM and the AFM solution with the latter being more stable. Finally A. Kubetzka *et al.* [245] proved by a combined DFT and spin polarized STM study the antiferromagnetic order of the Fe layer on W(100) which explained the previous experimental results. Including spin orbit coupling in their calculations the authors in addition found an out-of-plane easy axis with a magnetic anisotropy energy of 2.4 meV for the antiferromagnetic configuration of Fe/W(100) [245]. M. L. Sandratskii *et al.* [246], M. Bode *et al.* [247] and A. Kubetzka *et al.* [245] have reported magnetic exchange coupling parameters for 1 ML of Fe on W(100) obtained by means of FLAPW calculations and

D. Spišák and J. Hafner [231] with the VASP code. References to the details of the calculations presented in [247] point towards [245]. Thus, we cite both publications but discuss mainly the latter one.

To model the surface a (6×6) unit cell containing a six layers slab of W(100) covered on one side by one or two layers of Fe has been used. As in the previous section the theoretical lattice constant of W taken to construct the surface has been 3.174 Å. The distance between periodically repeated images of the PCP molecule has been 19.04 Å in x- and in y-direction. The vacuum region between two slabs in z-direction was 18 Å large. The PCP molecule, the Fe layers and the upper three W layers have been allowed to relax until the forces became smaller than 0.003 eV/Å. For relaxations only the Γ-point has been taken into account for the BZ sampling. To calculate the electronic and magnetic properties larger k-point sets as described in the corresponding paragraphs have been used.

On the bcc (100) surface depicted as red area in Figure 5.4 there are three adsorption positions of high symmetry namely the top site, the hollow site above an atom of the second layer and the bridge site on the center between two nearest neighbor surface atoms. These high symmetry positions have been used as starting points for the geometrical center of the PCP molecule. On all three positions we tested orientations of the PCP molecule where either two C atoms or two C=C double bonds are directly on top of Fe atoms. On the Fe/W(100) surface only one of the starting configurations led to a stable minimum. In this stable adsorption configuration the center of the PCP molecule is on a hollow site. The two C atoms at the interconnections between both rings of the molecule are adsorbed on top of Fe atoms. Like on the Fe/W(110) the symmetry of the PCP molecule is broken due to a twist of the molecule. The upper part of the molecule is rotated clockwise with respect to the lower part. The molecule surface distance is 1.90 Å and the adsorption energy is −2.191 eV calculated using the PBE functional. The inclusion of corrections for vdW interactions with the DFT-D3 approach does not influence the adsorption site or the molecule surface distance. The adsorption energy changes to −2.870 eV. While on the Fe/W(110) the adsorption of a PCP molecule led to a slight decrease of the magnetic moments of the two Fe atoms directly binding to the molecule with respect to the magnetic moment of the clean surface, on the Fe/W(100) this effect is more drastic. The magnetic moment decreases from $\pm 2.36\ \mu_B$ to $\pm 1.09\ \mu_B$.

In Figure 5.11 the PDOS on the σ and π type states of the lower and the upper benzene ring of the PCP molecule adsorbed on Fe/W(100) is shown. Like on the (110) surface the hybridization of the molecules π states with the d states of the surface leads to the formation of broad spin split hybrid bands around the Fermi level in the PDOS of the lower ring. At the upper ring sharp molecular features are conserved. The peaks denoted as P_1 and P_2 are in contrast to the (110) surface spin split by only a few meV. The peaks around P_3 in the unoccupied states are spin split by 30 meV which is a relatively small spin splitting compared to what we have observed on the (110) surface. The picture is identical on the Fe/W(100) surface with two ML of Fe.

Also for PCP adsorbed on the Fe/W(100) surface we calculated the nearest neighbor

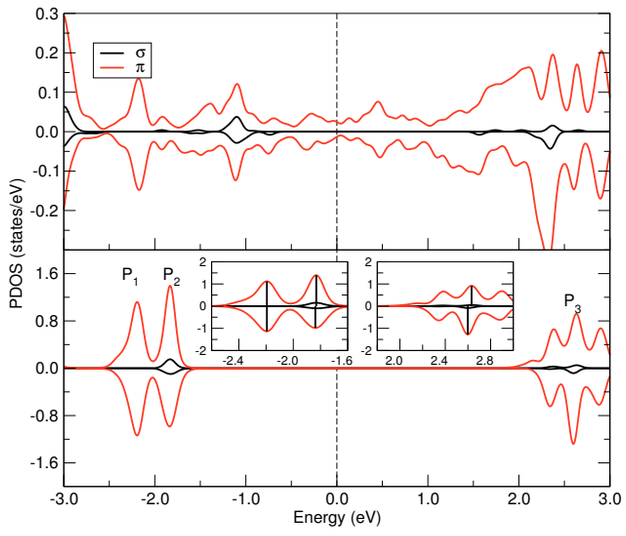

Figure 5.11.: The PDOS on the σ and π states of the lower ring and the upper ring of the PCP molecule adsorbed on 1 ML of Fe on W(100). The PDOS has been broadened by a 0.1 eV Gaussian.

magnetic exchange coupling constants J_k in order to see how the magnetic hardening effect of organic molecules adsorbed on ferromagnetic surfaces discovered in the last section works in the case of a surface showing an antiferromagnetic coupling. Although the four Fe atoms underneath the PCP molecule have the same magnetic moment, we assume a similar model of the magnetic exchange coupling on the Fe/W(100) surface with three different coupling constants J_1, J_2 and J_3 like in the last section on Fe/W(110). J_1 as defined in Figure 5.12 (d) is the magnetic exchange coupling between the four Fe atoms with the reduced magnetic moment due to the direct interaction with the PCP molecule, J_2 describes the coupling of the other surface atoms to the two Fe atoms underneath a C-C double bonds and J_3 the coupling of the other surface atoms to the two Fe atoms directly underneath a carbon atom. The different magnetic configurations required to extract the three magnetic exchange coupling constants J_1, J_2 and J_3 from our calculations are shown in Figure 5.12. The magnetic exchange coupling to the rest of the surface atoms can be obtained from the energy difference of the antiferromagnetic ground state shown in (a) and the configuration with the opposite sign of the magnetization for all four Fe atoms underneath the molecule depicted in (b). In this case the magnetic exchange coupling terms entering the Heisenberg model involving those four Fe atoms do not change their sign and thus cancel each other when taking the energy

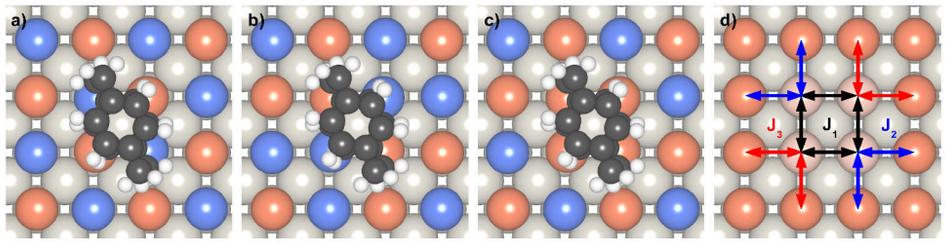

Figure 5.12.: (a-c) Visualization of the magnetic configurations AFM (a), AFM2 (b) and FM/FM2 (c) used to calculate the magnetic exchange coupling constants J_k. Red atoms have a positive magnetization while the orientation of the magnetization of the blue atoms points in the opposite direction. (b) Definition of the magnetic exchange constants J_1, J_2 and J_3 for PCP adsorbed on the Fe/W(100) surface. The brighter Fe atoms directly interacting with the PCP molecule have a smaller magnetic moment than the rest of the surface atoms.

difference. The other two magnetic configurations needed couple the four Fe atoms underneath the PCP molecule ferromagnetically as shown in Figure 5.12 (c) with both positive and negative magnetization. This leads to a similar set of equations like in the Fe/W(110) case:

$$\begin{aligned} E_{\mathrm{FM2}} - E_{\mathrm{AFM}} &= -8J_1 - 8J_2 \\ E_{\mathrm{FM1}} - E_{\mathrm{AFM}} &= -8J_1 - 8J_3 \end{aligned} \tag{5.5}$$

By solving this set of equations we obtain magnetic exchange coupling constants $J_1 = -17.12$ meV/μ_{B}^2, $J_2 = -3.38$ meV/μ_{B}^2 and $J_3 = -3.23$ meV/μ_{B}^2 per pair of Fe atoms, which are listed in Table 5.4. The negative signs on all of them show that the antiferromagnetic configuration is indeed favored over the ferromagnetic configuration. The magnetic exchange coupling constant $J_S = -7.42$ meV/μ_{B}^2 per pair of Fe atoms of the clean Fe/W(100) surface, calculated in a (2×2) cell with a $20 \times 20 \times 1$ **k**-point mesh, is more than a factor of two larger than the two coupling constants J_2 and J_3 of the Fe atoms underneath the PCP molecule to the rest of the surface. Our magnetic exchange coupling constant for the clean surface can be compared to previously published results using the FLAPW method [245–247] and calculations with the VASP code [231]. M. L. Sandratskii *et al.* [246] obtained an magnetic exchange coupling constant converted to our units $J_{\mathrm{S}} = -5.87$ meV/μ_{B}^2, M. Bode *et al.* [245, 247] -7.03 meV/μ_{B}^2 and D. Spišák and J. Hafner [231] -7.75 meV/μ_{B}^2. The coupling constant J_2 of the Fe atom directly underneath a C atom to the rest of the surface is slightly stronger than the coupling constant J_3 of the Fe atom underneath a C=C double bond to the rest of the surface. The magnetic exchange coupling between the four Fe atoms underneath the PCP molecule J_1 is about three times stronger than J_{S} of the clean surface. In total

Table 5.4.: Magnetic anisotropy energies K per Fe atom in meV and magnetic exchange coupling constants J in meV/μ_B^2 for PCP adsorbed on Fe/W(100) and for the clean W(100) surface covered by one ML of Fe. Positive numbers of the MAE correspond to an out-of-plane easy-axis and negative numbers to an in-plane easy-axis.

	K (meV)		J_1 (meV/μ_B^2)	J_2 (meV/μ_B^2)	J_3 (meV/μ_B^2)
	$\mathbf{\Gamma}$	$2\times2\times1$			
PCP Fe/W(100)	-6.78	-6.48	-17.12	-3.38	-3.32
Fe/W(100)	1.20	2.42		-7.42	

we observe the magnetic hardening effect of the four Fe atoms underneath the PCP molecule which has been already shown for the ferromagnetic Fe/W(110) surface also on the antiferromagnetic Fe/W(100) surface. In addition we observe on the Fe/W(100) surface a decoupling of the molecular unit consisting of the PCP molecule and the four Fe atoms underneath from the rest of the surface as J_2 and J_3 are significantly smaller than the magnetic exchange coupling constant of the clean surface J_S.

The MAEs for PCP adsorbed on one ML of Fe on W(100) as well as for the corresponding clean surface are listed in Table 5.4. Our MAE of 2.42 meV with an out-of-plane easy-axis for the clean Fe on W(100) surface obtained in the (6×6) cell with the $2\times2\times1$ **k**-point grid agrees reasonably well with the 2.4 meV with the same direction of the easy-axis from previous FLAPW calculations [245]. The average MAE per Fe atom of the Fe/W(100) surface with PCP adsorbed calculated with the $2\times2\times1$ **k**-point mesh is 1.43 meV, which is significantly smaller than the clean surface value. The same holds true for the $\mathbf{\Gamma}$-point calculation where the average MAE per Fe atom is 0.31 meV. If we calculate the MAE for the four Fe atoms underneath the PCP molecule in the same way as proposed in the last section, where we have subtracted the number of unaffected Fe atoms times the MAE of a clean surface atom from the total energy difference, we obtain -6.78 meV with the $\mathbf{\Gamma}$-point and -6.49 meV with the $2\times2\times1$ **k**-point set. In both cases following this approach an in-plane magnetization with a large MAE is favored by the four Fe atoms underneath the PCP molecule. In the last section the change of the sign of the MAE for the $\mathbf{\Gamma}$-point calculation was ascribed to the overestimation of the clean surface MAE. In the case of Fe/W(100) calculated with the $2\times2\times1$ **k**-point mesh the MAE is in good agreement with previous calculations.

6 Summary

We have investigated hybrid organic-metallic materials, which are model systems with possible applications in molecular electronics and molecular spintronics. For these systems an accurate description of the geometry and the electronic structure of the molecule metal interface is vital. Characterized by their binding strength, π conjugated molecules adsorbed on metal surfaces are often found between physisorption and weak chemisorption, where van der Waals (vdW) interactions are of high importance. The first part of this work thus dealt with the adsorption of small π conjugated molecules adsorbed on noble metal surfaces in order to test the accuracy of different methods for the description of vdW interactions within density functional theory (DFT). Based on the insights gained in the first part, the second part was dedicated to magnetic systems, which are suitable candidates for future applications in molecular spintronics devices.

Our study on single thiophene and 4-thiophene adsorbed on Cu(111) showed that these molecules are weakly chemisorbed and vdW interactions are the most important contribution to the binding. Due to the availability of experimental data regarding the adsorption geometry and adsorption energy, we were able to assess the performance of the PBE functional, the semi-empirical DFT-D2 and DFT-D3 methods and the non-local correlation functionals vdW-DF1, vdW-DF2 and rVV10 for correctly describing the adsorption parameters. Among the tested methods the semi-empirical DFT-D3 method, which takes into account the chemical environment of the atoms, agreed the best with the experiment for both the molecule surface distance and the adsorption energy. The adsorption energies of thiophene on Cu(111) obtained with the PBE functional and the vdW-DF functional differ by almost one order of magnitude. This difference is due to the substantially different spatial distribution of the correlation energy densities of those two functionals.

The neutral cyclooctatetraene (COT) molecule in the gas phase adopts a tub shape while anions and cations have a flat shape. For the two times charged COT molecule the flat shape can be explained by Hückel's rule of aromaticity. The change of conformation

of the COT molecule upon charging could be utilized in a conformational switch. Our study of tub and flat shaped COT adsorbed on the (100) surfaces of Cu, Ag and Au as well as on the Au(111) surface lead to the conclusion that varying the hybridization strength can change the shape of COT and take the role played by charging in the gas phase. The strongly interacting (100) noble metal surfaces were a test system for methods to correct for vdW interactions in DFT in the limit of minor importance of vdW interactions. While the *ab initio* methods of the vdW-DF type lead to adsorption energies comparable to the PBE functional, they overestimated the molecule surface distance. With the DFT-D3 method a molecule surface distance close to the PBE result has been obtained while the adsorption energy has been overestimated.

The COT molecule adsorbed on noble metal surfaces is another example for the following dilemma, which had to be faced later when developing molecular spintronic devices. On the weakly interacting Au(111) surface the COT molecule is physisorbed and thus the projected density of states (PDOS) showed sharp molecular orbital like peaks. On the strong interacting noble metal (100) surfaces the COT molecule is chemisorbed and the PDOS showed broad hybrid states around the Fermi Level. For applications in molecular spintronics, both sharp molecular orbital like states and a strong interaction with the substrate are required. COT is a building block for molecule transition metal sandwiches, which are candidates for spintronic devices. Thus, we extended our study of COT adsorbed on Au(111) to COT adsorbed on magnetic transition metal adatoms on Au(111). Adsorbed on the adatoms COT adopts in addition to the tub and the flat shape also an L like shape. The discrete electronic spectrum of the magnetic adatoms allows to form significantly spin split molecular orbitals by hybridization of the COT orbitals with the states of the magnetic adatoms. The magnetic anisotropy energy of the magnetic adatoms decreased upon the adsorption of the COT molecule.

The paracyclophane (PCP) molecule has been found to be chemisorbed on Fe/W(110) and Fe/W(100). In this case the biplanar structure of the PCP molecule protected the molecular states of the upper ring from broadening due to hybridization with the substrate states. At the same time the strong interaction of the lower ring with the magnetic substrate lead to spin splitting of the molecular states on Fe/W(110). With sharp and spin split molecular states at the upper ring of the PCP molecule the system could be used as a spin filter. In addition we have shown that the adsorption of organic molecules on magnetic surfaces can change the magnetic properties of the surface. In particular the adsorption of the PCP molecule on the Fe/W(110) as well as the Fe/W(100) surface strongly increases the magnetic exchange coupling constants of the Fe atoms directly coupled to the PCP molecule. This is due to an increased overlap of the d_π orbitals by the contribution of those Fe atoms to common $d_\pi - \pi$ orbitals. The increased magnetic exchange coupling of the Fe atoms underneath the PCP molecule manifests in the prediction of a higher coercivity field and a higher Curie temperature. The adsorption of organic molecules on magnetic surfaces offers a new road to design magnetic materials with predefined properties.

A

Ansatz for a spin dependent version of vdW-DF

The derivation of vdW-DF from the ACFD-theorem is somewhat involved when one goes really into detail and these details are scattered over a large number of documents [19, 248–250] which have been source for this appendix. The purpose is to gather a complete version of the derivation in one document. Each part of the derivation has been written in at least one of the given references. We just collect them here and add some detail where it seemed to be necessary for our understanding.

The second purpose of this appendix is to write down the formalism explicitly including the spin variable. An extension of vdW-DF to the spin polarized case is not straight forward and has not been done up to now. We will give the formulas where possible and also the corresponding references where available. In the beginning the derivation of the ACFD theorem is based on the overview given by J. F. Dobson [251] and the work of M. Lein *et al.* [252]. The overall shape of the derivation is however very similar to the spin unpolarized case and omitting the spin indices and summations will lead to the normal version of this derivation.

A.1. XC-Functional from the ACFD-theorem

The adiabatic connection formula gives an exact expression for the sum of the Hartree energy and the exchange correlation energy $E_{\mathrm{xc+H}}$ [106–108]:

$$E_{\mathrm{xc+H}} = \frac{1}{2}\int_0^1 \mathrm{d}\lambda \int \mathrm{d}^3\mathbf{r}\,\mathrm{d}^3\mathbf{r}' \sum_{\sigma,\sigma'} \frac{1}{|\mathbf{r}-\mathbf{r}'|} n_{2,\lambda}^{\sigma\sigma'}(\mathbf{r},\mathbf{r}'), \tag{A.1}$$

where $\mathbf{r}$ is the spatial and σ the spin coordinate[1], and λ is the coupling constant of the adiabatic connection. The usual equations without spin can be obtained by carrying out the spin summations and $n(\mathbf{r}) = \sum_\sigma n^\sigma(\mathbf{r})$. In the equation above $n_{2,\lambda}^{\sigma\sigma'}(\mathbf{r},\mathbf{r}') = n^\sigma(\mathbf{r})n^{\sigma'}(\mathbf{r}') + n^\sigma(\mathbf{r})n_{\mathrm{xc}}^{\sigma\sigma'}(\mathbf{r},\mathbf{r}')$ is the (λ dependent) pair density. The latter can be related with help of the fluctuation dissipation theorem to the density response function $\chi_\lambda^{\sigma\sigma'}(\mathbf{r},\mathbf{r}',\omega)$

$$-\int_0^\infty \frac{\mathrm{d}u}{\pi}\chi_\lambda^{\sigma\sigma'}(\mathbf{r},\mathbf{r}',iu) = n_{2,\lambda}^{\sigma\sigma'}(\mathbf{r},\mathbf{r}') - n^\sigma(\mathbf{r})n^{\sigma'}(\mathbf{r}') + n^\sigma(\mathbf{r})\delta^{\sigma\sigma'}\delta(\mathbf{r}-\mathbf{r}'). \tag{A.2}$$

If we insert Equation A.2 into Equation A.1 we arrive at a spin polarized version [252] of the adiabatic connection fluctuation dissipation (ACFD) theorem

$$E_{\mathrm{xc+H}} = -\frac{1}{2}\int_0^1 \mathrm{d}\lambda \int \mathrm{d}^3\mathbf{r}\,\mathrm{d}^3\mathbf{r}' \sum_{\sigma,\sigma'} v(\mathbf{r}-\mathbf{r}')\left(\int_0^\infty \frac{\mathrm{d}u}{\pi}\chi_\lambda^{\sigma\sigma'}(\mathbf{r},\mathbf{r}',iu) + n^\sigma(\mathbf{r})\delta^{\sigma\sigma'}\delta(\mathbf{r}-\mathbf{r}')\right) \tag{A.3}$$

$$+ \int \mathrm{d}^3\mathbf{r}\,\mathrm{d}^3\mathbf{r}' \sum_{\sigma,\sigma'} \frac{n^\sigma(\mathbf{r})n^{\sigma'}(\mathbf{r}')}{|\mathbf{r}-\mathbf{r}'|}$$

$$= -\frac{1}{2\pi}\int_0^1 \mathrm{d}\lambda \int_0^\infty \mathrm{d}u \sum_{\sigma,\sigma'} \mathrm{Tr}\left[v\,\chi_\lambda^{\sigma\sigma'}(iu)\right] - E_{\mathrm{self}} + \int \mathrm{d}^3\mathbf{r}\,\mathrm{d}^3\mathbf{r}' \sum_{\sigma,\sigma'} \frac{n^\sigma(\mathbf{r})n^{\sigma'}(\mathbf{r}')}{|\mathbf{r}-\mathbf{r}'|} \tag{A.4}$$

where $E_{\mathrm{self}} = \frac{1}{2}\int_0^1 \mathrm{d}\lambda \int \mathrm{d}^3\mathbf{r}\,\mathrm{d}^3\mathbf{r}' \sum_{\sigma,\sigma'} v(\mathbf{r}-\mathbf{r}')n^\sigma(\mathbf{r})\delta^{\sigma\sigma'}\delta(\mathbf{r}-\mathbf{r}')$ is an infinite self energy term which should be canceled by a corresponding term from the first integral. In the last term the only spin dependent quantities are the densities $n^\sigma(\mathbf{r})$ thus we can safely carry out the spin summations. When doing this one arrives at the usual expression for the Hartree energy E_{H} which we subtract in order to have a formula for E_{xc} only. In the second step we also interpreted v and $\chi_\lambda^{\sigma\sigma'}$ as matrices of two continuous indices $\mathbf{r}$ and $\mathbf{r}'$ for which the following conventions should be given:

$$1 = \delta(\mathbf{r},\mathbf{r}') \tag{A.5}$$

$$\mathrm{Tr}\,[A] = \int \mathrm{d}^3\mathbf{r} A(\mathbf{r},\mathbf{r}) \tag{A.6}$$

$$AB = \int \mathrm{d}^3\mathbf{r}'' A(\mathbf{r},\mathbf{r}'')B(\mathbf{r}'',\mathbf{r}') \tag{A.7}$$

[1]The spin variable is not in the arguments list of e.g. $n^\sigma(\mathbf{r})$ but written as superscript in order to remind that it takes only the two values $\uparrow$ and $\downarrow$ in contrast to the continuos variable $\mathbf{r}$. For the same reason the spin summation $\sum_{\sigma,\sigma'}$ is explicitly written. This notation will also be used, when we switch back and forth between matrix and normal notation later on.

which means that the unity operator 1 is a delta function, Tr means integration over the diagonal elements and the product of two operators is defined in analogy to the usual matrix product as summation over connecting indices. If A and B are not symmetric one can immediately see that $AB \neq BA$ (i.e. $[A, B] \neq 0$).

A.2. The response function $\chi_\lambda^{\sigma\sigma'}$ and the Full-Potential-Approximation

The full response function $\chi_\lambda^{\sigma\sigma'}$ is the density response $\delta n_\lambda^\sigma = \sum_{\sigma'} \chi_\lambda^{\sigma\sigma'} \delta\Phi_{\text{ext}}^{\sigma'}$ of the λ interacting system to a (in general spin dependent e.g. by an applied magnetic field) change in the external potential $\delta\Phi_{\text{ext}}^{\sigma'}$. Without matrix notation the relation between the change of the density δn_λ^σ and the change of the external potential $\delta\Phi_{\text{ext}}^{\sigma'}$ reads

$$\delta n_\lambda^\sigma(\mathbf{r}, \omega) = \sum_{\sigma'} \int \mathrm{d}^3\mathbf{r}' \chi_\lambda^{\sigma\sigma'}(\mathbf{r}, \mathbf{r}', \omega) \delta\Phi_{\text{ext}}^{\sigma'}(\mathbf{r}', \omega) \tag{A.8}$$

$$\delta n_\lambda^\sigma(\mathbf{r}, \omega) = \sum_{\sigma'} \int \mathrm{d}^3\mathbf{r}' \tilde{\chi}_\lambda^{\sigma\sigma'}(\mathbf{r}, \mathbf{r}', \omega) \delta\Phi_{\text{scr},\lambda}^{\sigma'}(\mathbf{r}', \omega) \tag{A.9}$$

$$\delta n_\lambda^\sigma(\mathbf{r}, \omega) = \sum_{\sigma'} \int \mathrm{d}^3\mathbf{r}' \chi_{\text{KS}}^{\sigma\sigma'}(\mathbf{r}, \mathbf{r}', \omega) \delta\Phi_{\text{eff},\lambda}^{\sigma'}(\mathbf{r}', \omega) \tag{A.10}$$

The second equation defines the screened response $\tilde{\chi}_\lambda$ to a change in the screened potential $\delta\Phi_{\text{scr},\lambda}^{\sigma'} = \delta\Phi_{\text{ext}}^{\sigma'} + \delta\Phi_{\text{ind},\lambda}^{\sigma'}$ which is the sum of the external potential change and the change of the induced potential $\delta\Phi_{\text{scr},\lambda}^{\sigma} = v_\lambda^{\sigma\sigma'} \delta n_\lambda^{\sigma'}$. The third equation introduces the Kohn-Sham response function $\chi_{\text{KS}}^{\sigma\sigma'}$ of the non interacting KS system to a change $\delta\Phi_{\text{eff},\lambda}^{\sigma'}(\mathbf{r}', \omega)$ in the effective potential. The first two response functions can be related by a Dyson like equation which we are going to derive in the following.

$$\chi_\lambda^{\sigma\sigma'}(iu) = \sum_{\tau'} \frac{\tilde{\chi}_\lambda^{\tau'\sigma'}(iu)}{\delta^{\sigma\tau'} - \sum_\tau \lambda \tilde{\chi}_\lambda^{\sigma\tau}(iu) v^{\tau\tau'}} \tag{A.11}$$

The response functions $\chi_\lambda^{\sigma\sigma'}$ and $\tilde{\chi}_\lambda^{\sigma\sigma'}$ are defined for all coupling constants λ which gives combining Equation A.8 and Equation A.9

$$\sum_{\sigma'} \chi_\lambda^{\sigma\sigma'} \delta\Phi_{\text{ext}}^{\sigma'} = \sum_{\sigma'} \tilde{\chi}_\lambda^{\sigma\sigma'} \delta\Phi_{\text{scr},\lambda}^{\sigma'} \tag{A.12}$$

$$= \sum_{\sigma'\tau} \tilde{\chi}_\lambda^{\sigma\tau} \left(\delta^{\tau\sigma'} \delta\Phi_{\text{ext}}^{\sigma'} + v_\lambda^{\tau\sigma'} \delta n_\lambda^{\sigma'} \right) \tag{A.13}$$

$$= \sum_{\tau\tau'\sigma'} \tilde{\chi}_\lambda^{\sigma\tau} \left(\delta^{\tau\tau'} \delta^{\tau'\sigma'} \delta\Phi_{\text{ext}}^{\sigma'} + v_\lambda^{\tau\tau'} \chi_\lambda^{\tau'\sigma'} \delta\Phi_{\text{ext}}^{\sigma'} \right) \tag{A.14}$$

where $v_\lambda^{\sigma\sigma'} = \lambda v$ is the spin blind and scaled Coulomb interaction. From the above equation we can immediately read the following Dyson equation like relation between the full response $\chi_\lambda^{\sigma\sigma'}$ and the screened response $\tilde{\chi}_\lambda^{\sigma\sigma'}$:

$$\chi_\lambda^{\sigma\sigma'} = \tilde{\chi}_\lambda^{\sigma\sigma'} + \sum_{\tau\tau'} \tilde{\chi}_\lambda^{\sigma\tau} v_\lambda^{\tau\tau'} \chi_\lambda^{\tau'\sigma'} \tag{A.15}$$

which when solved for $\chi_\lambda^{\sigma\sigma'}$ gives Equation A.11. In this case we related the full response $\chi_\lambda^{\sigma\sigma'}$ to the screened response $\tilde{\chi}_\lambda^{\sigma\sigma'}$ which should not be interchanged with the usually used non interacting or Kohn-Sham response $\chi_{\mathrm{KS}}^{\sigma\sigma'}$. For the latter instead of a screened potential $\Phi_{\mathrm{scr},\lambda}^{\sigma'}$ one has to use an effective potential $\Phi_{\mathrm{eff},\lambda}^{\sigma'}$ which then leads to a structural slightly different Dyson like equation:

$$\chi_\lambda^{\sigma\sigma'} = \chi_{\mathrm{KS}}^{\sigma\sigma'} + \sum_{\tau,\tau'} \chi_{\mathrm{KS}}^{\sigma\tau} \left(v_\lambda^{\tau\tau'} + f_{\mathrm{xc},\lambda}^{\tau\tau'} \right) \chi_\lambda^{\tau'\sigma'} \tag{A.16}$$

where the exchange correlation kernel $f_{\mathrm{xc},\lambda}^{\sigma\sigma'}$ is the second functional derivative of the xc energy functional with respect to the density. When we insert the Dyson like equation Equation A.11 into the expression for the xc-energy within the ACFD-theorem Equation A.4 we arrive at

$$E_{\mathrm{xc}} = -\frac{1}{2\pi} \int_0^1 \mathrm{d}\lambda \int_0^\infty \mathrm{d}u \sum_{\sigma,\sigma'} \sum_{\tau'} \mathrm{Tr} \left[\frac{\tilde{\chi}_\lambda^{\tau'\sigma'}(iu) v^{\sigma'\sigma}}{\delta^{\sigma\tau'} - \sum_\tau \lambda \tilde{\chi}_\lambda^{\sigma\tau}(iu) v^{\tau\tau'}} \right] - E_{\mathrm{self}}. \tag{A.17}$$

At this point we will make the so called Full-Potential-Approximation (FPA) in which it is assumed that the screened response function $\tilde{\chi}_\lambda^{\sigma\sigma'}$ which carries all the information of the dielectric function equals the response function $\tilde{\chi}_1^{\sigma\sigma'} := \tilde{\chi}^{\sigma\sigma'}$ for $\lambda = 1$ for all values of the coupling constant λ. When assuming this we can perform the coupling constant integration. With help of $\frac{\mathrm{d}}{\mathrm{d}\lambda} \ln\left[1 - \sum_\tau \lambda \tilde{\chi}^{\sigma\tau} v^{\tau\sigma}\right] = -\sum_{\tau'\sigma'} \frac{\tilde{\chi}^{\tau'\sigma'}(iu) v^{\sigma'\sigma}}{\delta^{\sigma\tau'} - \sum_\tau \lambda \tilde{\chi}^{\sigma\tau}(iu) v^{\tau\tau'}}$ we arrive at

$$E_{\mathrm{xc}} = \frac{1}{2\pi} \int_0^\infty \mathrm{d}u \sum_\sigma \mathrm{Tr} \left[\ln \left(1 - \sum_\tau \tilde{\chi}^{\sigma\tau}(iu) v^{\tau\sigma} \right) \right] - E_{\mathrm{self}}. \tag{A.18}$$

The FPA is formally similar to the random phase approximation (RPA) in which the xc-kernel $f_{\mathrm{xc},\lambda}^{\sigma\sigma'}$ in the Dyson like equation Equation A.16 connecting $\chi_\lambda^{\sigma\sigma'}$ and $\chi_{\mathrm{KS}}^{\sigma\sigma'}$ is set to zero. This leads then to the use of the non interacting $\chi_{\mathrm{KS}}^{\sigma\sigma'}$ for all coupling constants. In contrast to the RPA the FPA is not justified in the short range regime, but these terms will be subtracted later.

Dion *et al.* proceeded by relating for a non spin polarized system the screened density response $\tilde{\chi}(\mathbf{r}, \mathbf{r}', \omega)$ to the dielectric function $\epsilon(\mathbf{r}, \mathbf{r}', \omega)$ by calculating the induced electric field $\mathbf{E}(\mathbf{r}, \omega)$ of the system as the negative gradient of the screened potential $\Phi_{\mathrm{scr}}(\mathbf{r}', \omega)$. Attempting to follow the same way we will run into trouble which will be clarified in the following. First of all we have to take a close look at the change of the screened

potential $\delta\Phi^\sigma_{\rm scr}(\mathbf{r}',\omega)$. In equation Equation A.13 we already have used an expression for $\delta\Phi^\sigma_{\rm scr}(\mathbf{r}',\omega)$

$$\delta\Phi^\sigma_{\rm scr}(\mathbf{r},\omega) = \delta\Phi^\sigma_{\rm ext}(\mathbf{r},\omega) + \sum_{\sigma'}\int \mathrm{d}^3\mathbf{r}' v^{\sigma\sigma'}(\mathbf{r},\mathbf{r}')\delta n^{\sigma'}(\mathbf{r}',\omega) \tag{A.19}$$

$$= \delta\Phi^\sigma_{\rm ext}(\mathbf{r},\omega) + \sum_{\tau\sigma'}\int \mathrm{d}^3\mathbf{r}'\mathrm{d}^3\mathbf{r}'' \frac{\chi^{\sigma'\tau}_{\rm KS}(\mathbf{r}',\mathbf{r}'',\omega)\delta\Phi^\tau_{\rm eff}(\mathbf{r}'',\omega)}{|\mathbf{r}-\mathbf{r}'|} \tag{A.20}$$

The Kohn-Sham response function $\chi^{\sigma\sigma'}_{\rm KS}(\mathbf{r},\mathbf{r}',\omega)$ had to be introduced in order to relate the change in the screened potential $\delta\Phi^\sigma_{\rm scr}(\mathbf{r},\omega)$ to the effective potential change $\delta\Phi^\sigma_{\rm eff}(\mathbf{r},\omega)$ for which we know the analytic form as reported e.g. in [253]

$$\delta\Phi^\sigma_{\rm eff}(\mathbf{r},\omega) = \delta\Phi^\sigma_{\rm ext}(\mathbf{r},\omega) + \sum_{\sigma'}\int \mathrm{d}^3\mathbf{r}' \frac{\delta n^{\sigma'}(\mathbf{r}',\omega)}{|\mathbf{r}-\mathbf{r}'|} + \frac{\delta E_{\rm xc}\left[n(\mathbf{r},\omega), m_{\rm z}(\mathbf{r},\omega)\right]}{\delta n^\sigma(\mathbf{r},\omega)} \tag{A.21}$$

$$= \delta\Phi_{\rm ext}(\mathbf{r},\omega) + \sigma_{\rm z}^{\sigma\sigma}B_{\rm ext,z}(\mathbf{r},\omega) + \int \mathrm{d}^3\mathbf{r}' \frac{\delta n(\mathbf{r}',\omega)}{|\mathbf{r}-\mathbf{r}'|} + v_{\rm xc}(\mathbf{r},\omega) + \sigma_{\rm z}^{\sigma\sigma}B_{\rm xc,z}(\mathbf{r},\omega) \tag{A.22}$$

$$= \delta\Phi_{\rm eff}(\mathbf{r},\omega) + \sigma_{\rm z}^{\sigma\sigma}\left[B_{\rm ext,z}(\mathbf{r},\omega) + B_{\rm xc,z}(\mathbf{r},\omega)\right] \tag{A.23}$$

$$= \delta\Phi_{\rm eff}(\mathbf{r},\omega) + \sigma_{\rm z}^{\sigma\sigma}B_{\rm z}(\mathbf{r},\omega), \tag{A.24}$$

where we have separated the change in the effective potential in its spin dependent part $\sigma_{\rm z}^{\sigma\sigma}B_{\rm z}(\mathbf{r},\omega)$ and its spin independent part $\delta\Phi_{\rm effective}(\mathbf{r},\omega)$. The first of these two parts of the potential $\sigma_{\rm z}^{\sigma\sigma}B_{\rm z}(\mathbf{r},\omega)$ arises from the z-component[2] of the external magnetic field $B_{\rm ext,z}(\mathbf{r},\omega)$ and also from the contribution to the magnetic potential originated in the exchange correlation potential $B_{\rm xc,z}(\mathbf{r},\omega) = \frac{\delta E_{\rm xc}[n(\mathbf{r},\omega),m_{\rm z}(\mathbf{r},\omega)]}{\delta m_{\rm z}(\mathbf{r},\omega)}$. The $\sigma_{\rm z}^{\sigma\sigma}$ coming from the second part of the chain rule $\frac{\delta m_{\rm z}(\mathbf{r},\omega)}{\delta n^\sigma(\mathbf{r},\omega)}$ are the entries of the third Pauli matrix which makes notation more convenient. The difference between the two spin components of $\delta\Phi^\sigma_{\rm eff}(\mathbf{r},\omega)$ is just the sign of $B_{\rm z}(\mathbf{r},\omega)$. Reinserting the effective potential change $\delta\Phi^\sigma_{\rm eff}(\mathbf{r},\omega)$ in Equation A.20 for the screened potential change $\delta\Phi^\sigma_{\rm scr}(\mathbf{r},\omega)$ leaves us with

$$\delta\Phi^\sigma_{\rm scr}(\mathbf{r},\omega) = \delta\Phi^\sigma_{\rm ext}(\mathbf{r},\omega) + \sum_{\tau\sigma'}\int \mathrm{d}^3\mathbf{r}'\mathrm{d}^3\mathbf{r}'' \frac{\chi^{\sigma'\tau}_{\rm KS}(\mathbf{r}',\mathbf{r}'',\omega)}{|\mathbf{r}-\mathbf{r}'|}\left[\Phi_{\rm eff}(\mathbf{r}'',\omega) + \sigma_{\rm z}^{\tau\tau}B_{\rm z}(\mathbf{r}'',\omega)\right] \tag{A.25}$$

The spin summation in the second term ensures that electrons from one spin channel also feel the potential generated by the other spin channel. If we now introduce the KS electron density response $\chi^{\rm nn}_{\rm KS} = \chi^{\uparrow\uparrow}_{\rm KS} + \chi^{\uparrow\downarrow}_{\rm KS} + \chi^{\downarrow\uparrow}_{\rm KS} + \chi^{\downarrow\downarrow}_{\rm KS}$ and the KS spin density response

[2] That we deal here only with the z-component is due to the assumption of collinear magnetism in which all magnetic moments are aligned in the same direction.

$\chi_{\mathrm{KS}}^{\mathrm{nm}} = \chi_{\mathrm{KS}}^{\uparrow\uparrow} - \chi_{\mathrm{KS}}^{\uparrow\downarrow} + \chi_{\mathrm{KS}}^{\downarrow\uparrow} - \chi_{\mathrm{KS}}^{\downarrow\downarrow}$ as it has been done in [253] we arrive at a simpler formula

$$\begin{aligned}\delta\Phi_{\mathrm{scr}}^{\sigma}(\mathbf{r},\omega) = \delta\Phi_{\mathrm{ext}}^{\sigma}(\mathbf{r},\omega) \\ + \int \mathrm{d}^3\mathbf{r}'\mathrm{d}^3\mathbf{r}'' \frac{\chi_{\mathrm{KS}}^{\mathrm{nn}}(\mathbf{r}',\mathbf{r}'',\omega)\Phi_{\mathrm{eff}}(\mathbf{r}'',\omega) + \chi_{\mathrm{KS}}^{\mathrm{nm}}(\mathbf{r}',\mathbf{r}'',\omega)B_{\mathrm{z}}(\mathbf{r}'',\omega)}{|\mathbf{r}-\mathbf{r}'|}\end{aligned} \tag{A.26}$$

As long as we consider a non zero external magnetic field the change of the screened potential $\delta\Phi_{\mathrm{scr}}^{\sigma}$ will be spin dependent. In addition also the polarization $\mathbf{P}$ has a more complicated form as it depends on the external magnetic field due to e.g. the magneto-electric effect:

$$P_i = \alpha_{ij}^{(1)}E_j + \alpha_{ijk}^{(2)}E_jE_k + \beta_{ij}^{(1)}H_j + \beta_{ijk}^{(2)}H_jH_k + \ldots \tag{A.27}$$

where the indices i, j and k run over the three spatial coordinates. Here the polarization has been expanded in a Taylor series with respect to the electric and magnetic fields where for instance $\alpha_{ij}^{(1)}$ is the usual polarizability tensor which is approximated by a scalar function by Dion *et al.* and $\beta_{ij}^{(1)}$ is the so called magnetoelectric tensor. From here on we will omit the external magnetic field, which implies that we consider intrinsically magnetic systems. By this we can arrive at a similar formalism as Dion *et al.* did for the unpolarized case. A spin polarized dielectric function $\epsilon^{\sigma\sigma'}(\mathbf{r},\mathbf{r}',\omega)$ can be defined [254] as

$$\sum_{\sigma'}\int \mathrm{d}^3\mathbf{r}'\epsilon^{\sigma\sigma'}(\mathbf{r},\mathbf{r}',\omega)\Phi_{\mathrm{scr}}(\mathbf{r}',\omega) = \Phi_{\mathrm{ext}}(\mathbf{r},\omega) \tag{A.28}$$

$$\sum_{\sigma'}\int \mathrm{d}^3\mathbf{r}'\epsilon^{\sigma\sigma'}(\mathbf{r},\mathbf{r}',\omega)\mathbf{E}(\mathbf{r}',\omega) = \mathbf{D}(\mathbf{r},\omega) \tag{A.29}$$

where $\mathbf{D}(\mathbf{r},\omega)$ is the electric displacement field.

The change of the charge density δn^{σ} can also be written as the divergence $-\nabla\cdot\mathbf{P}^{\sigma}$ of the induced polarization $\mathbf{P}^{\sigma} = \sum_{\sigma'}\alpha^{\sigma\sigma'}\mathbf{E}$ due to the internal electric field $\mathbf{E}$ in a medium with polarizability $\alpha^{\sigma\sigma'}$ which is related to the dielectric function $\epsilon^{\sigma\sigma'}$ via $4\pi\alpha^{\sigma\sigma'} = \epsilon^{\sigma\sigma'} - \delta^{\sigma\sigma'}$. Without matrix notation these equations read

$$\mathbf{P}^{\sigma}(\mathbf{r},\omega) = \sum_{\sigma'}\int \mathrm{d}^3\mathbf{r}'\alpha^{\sigma\sigma'}(\mathbf{r},\mathbf{r}',\omega)\cdot\mathbf{E}(\mathbf{r}',\omega) \tag{A.30}$$

This leads to the relation

$$\delta n^{\sigma}(\mathbf{r},\omega) = -\nabla_{\mathbf{r}}\cdot\sum_{\sigma'}\int \mathrm{d}^3\mathbf{r}'\alpha^{\sigma\sigma'}(\mathbf{r},\mathbf{r}',\omega)\mathbf{E}(\mathbf{r}',\omega) \tag{A.31}$$

$$= \sum_{\sigma'}\int \mathrm{d}^3\mathbf{r}'\nabla_{\mathbf{r}}\cdot\alpha^{\sigma\sigma'}(\mathbf{r},\mathbf{r}',\omega)\nabla_{\mathbf{r}'}\delta\Phi_{\mathrm{scr}}(\mathbf{r}',\omega) \tag{A.32}$$

Having a look at the defining equation for the screened response function $\tilde{\chi}^{\sigma\sigma'}(\mathbf{r},\mathbf{r}',\omega)$

$$\delta n^\sigma(\mathbf{r},\omega) = \sum_{\sigma'} \int \mathrm{d}^3\mathbf{r}' \tilde{\chi}^{\sigma\sigma'}(\mathbf{r},\mathbf{r}',\omega)\Phi_{\mathrm{scr}}(\mathbf{r}',\omega) \tag{A.33}$$

we can identify $\tilde{\chi}^{\sigma\sigma'}$ with the operator $\nabla\cdot\alpha^{\sigma\sigma'}\nabla$

$$\tilde{\chi}^{\sigma\sigma'}(\mathbf{r},\mathbf{r}',\omega) = \nabla_{\mathbf{r}}\cdot\alpha^{\sigma\sigma'}(\mathbf{r},\mathbf{r}',\omega)\nabla_{\mathbf{r}'} \tag{A.34}$$

With this identification at hand we can relate the screened density response $\tilde{\chi}^{\sigma\sigma'}(\mathbf{r},\mathbf{r}',\omega)$ to the dielectric function $\epsilon^{\sigma\sigma'}(\mathbf{r},\mathbf{r}',\omega)$ which we will need in the next section on our way to an expression for a non local correlation functional. In the following equation we will switch back and forth between normal and matrix notation.

$$1-\sum_\tau \tilde{\chi}^{\sigma\tau}v^{\tau\sigma} = \delta(\mathbf{r},\mathbf{r}') - \sum_\tau \int \mathrm{d}^3\mathbf{r}''\nabla_{\mathbf{r}}\cdot\alpha^{\sigma\tau}(\mathbf{r},\mathbf{r}'',\omega)\nabla_{\mathbf{r}''}v^{\tau\sigma}(\mathbf{r}'',\mathbf{r}') \tag{A.35}$$

$$= \delta(\mathbf{r},\mathbf{r}') + \sum_\tau \int \mathrm{d}^3\mathbf{r}''\nabla_{\mathbf{r}}\cdot\left(\delta(\mathbf{r},\mathbf{r}'')\delta^{\sigma\tau} - \epsilon^{\sigma\tau}(\mathbf{r},\mathbf{r}'',\omega)\right)\nabla_{\mathbf{r}''}\frac{v^{\tau\sigma}(\mathbf{r}'',\mathbf{r}')}{4\pi} \tag{A.36}$$

$$= \delta(\mathbf{r},\mathbf{r}') - \nabla_{\mathbf{r}}\cdot\sum_\tau \int \mathrm{d}^3\mathbf{r}''\delta(\mathbf{r},\mathbf{r}'')\delta^{\sigma\tau}\nabla_{\mathbf{r}''}G^{\tau\sigma}(\mathbf{r}'',\mathbf{r}') \tag{A.37}$$

$$+\sum_\tau \int \mathrm{d}^3\mathbf{r}''\nabla_{\mathbf{r}}\cdot\epsilon^{\sigma\tau}(\mathbf{r},\mathbf{r}'',\omega)\nabla_{\mathbf{r}''}G^{\tau\sigma}(\mathbf{r}'',\mathbf{r}')$$

$$= \delta(\mathbf{r},\mathbf{r}') - \sum_\tau \delta^{\sigma\tau}\nabla^2_{\mathbf{r}}G^{\tau\sigma}(\mathbf{r},\mathbf{r}') \tag{A.38}$$

$$+\sum_\tau \int \mathrm{d}^3\mathbf{r}''\nabla_{\mathbf{r}}\cdot\epsilon^{\sigma\tau}(\mathbf{r},\mathbf{r}'',\omega)\nabla_{\mathbf{r}''}G^{\tau\sigma}(\mathbf{r}'',\mathbf{r}')$$

$$= \sum_\tau \nabla\cdot\epsilon^{\sigma\tau}\nabla G^{\tau\sigma} \tag{A.39}$$

In the first step we insert our identification of the density response function $\tilde{\chi}^{\sigma\sigma'}(\mathbf{r},\mathbf{r}',\omega)$ with the operator $\nabla_{\mathbf{r}}\cdot\alpha^{\sigma\sigma'}(\mathbf{r},\mathbf{r}',\omega)\nabla_{\mathbf{r}'} = -\frac{1}{4\pi}\nabla_{\mathbf{r}}\cdot\left(\delta(\mathbf{r},\mathbf{r}')\delta^{\sigma\sigma'} - \epsilon^{\sigma\sigma'}(\mathbf{r},\mathbf{r}',\omega)\right)\nabla_{\mathbf{r}'}$ and wrote down the integrations explicitly. In Equation A.38 we have inserted the Coulomb Greensfunction $G^{\sigma\sigma'}(\mathbf{r},\mathbf{r}')$ which equals $-\frac{v^{\sigma\sigma'}(\mathbf{r}'',\mathbf{r}')}{4\pi}$ in atomic units and satisfies the equation $\nabla^2_{\mathbf{r}}G^{\sigma\sigma'}(\mathbf{r},\mathbf{r}') = \delta(\mathbf{r},\mathbf{r}')$. By carrying out the $\mathbf{r}''$ integration in the second term we obtain exactly this defining equation of the Coulomb Greensfunction which than gives us the required $\delta(\mathbf{r},\mathbf{r}')$ to cancel the first term. The third term then leads to the very short notation of the result $\sum_{\sigma'}\nabla\cdot\epsilon^{\sigma\sigma'}\nabla G^{\sigma'\sigma}$.

In order to obtain this result the order of $v\tilde{\chi}^{\sigma\sigma'}$ has been changed to $\tilde{\chi}^{\sigma\sigma'}v$ which is allowed under the protection of the trace only. Otherwise the identification we obtained

for $\tilde{\chi}^{\sigma\sigma'}$ will not commute with the coulomb potential and the more familiar identification

$$\epsilon^{-1} = 1 + v\chi \tag{A.40}$$
$$\epsilon = 1 - v\tilde{\chi} \tag{A.41}$$

needs to be applied. We can obtain the commutator of $\tilde{\chi}$ and v by combining Equation A.39 and Equation A.41 which results in $[v,\tilde{\chi}] = \epsilon - \nabla \cdot \epsilon^{\sigma\sigma'} \nabla G$. This commutator vanishes in the case of an isotropic system which will be the subject of the next section.

Inserting the result from Equation A.39 into Equation A.18 we finally arrive at an expression for the xc-energy in terms of the dielectric function $\epsilon^{\sigma\sigma'}(\mathbf{r}, \mathbf{r'}, \omega)$ of the system

$$E_{\mathrm{xc}} = \frac{1}{2\pi} \int_0^\infty \mathrm{d}u \sum_\sigma \mathrm{Tr} \left[\ln \left(\sum_{\sigma\prime} \nabla \cdot \epsilon^{\sigma\sigma'}(iu) \nabla G^{\sigma'\sigma} \right) \right] - E_{\mathrm{self}}. \tag{A.42}$$

A.3. The mostly local part of E_{xc}

The expression for the xc-energy in Equation A.42 contains both local and non local contributions from exchange and correlation. But it is not clear and not necessary that assuming the response of the system equals the full response for all coupling constants in the FPA covers also the correct description of the local or short ranged in the sense of locality parts of the xc-energy. Not necessary means that there is quite a large number of different local or semi-local xc-functionals already developed. We should rely on them and just have a look at non local corrections to these functionals. By subtracting the mostly local parts of the xc-energy from Equation A.42 we obtain the non local correction to the correlation energy which includes the van der Waals interactions

$$E_{\mathrm{c}}^{\mathrm{nl}}[n] = E_{\mathrm{xc}}[n] - E_{\mathrm{xc}}^{0}[n]. \tag{A.43}$$

In addition in this step we also make the approximation that non local exchange contributions can be neglected. This should be reconsidered with a critical view as we explicitly want to treat magnetic systems with this functional.

For the mostly local contribution to the exchange correlation energy we make an LDA by looking at Equation A.42 for the homogenous electron gas. In this case the dielectric function $\epsilon^{\sigma\sigma'}(\mathbf{r}, \mathbf{r'}, \omega) = \epsilon^{\sigma\sigma'}(\mathbf{r} - \mathbf{r'}, \omega)$ is isotropic i.e. depends only on the distance not on the spatial coordinates directly. For isotropic functions however due to the chain rule the derivative with respect to one of the two variables only changes the sign when one differentiates with respect to the other variable

$$\nabla_{\mathbf{r}} \cdot \epsilon^{\sigma\sigma'}(\mathbf{r} - \mathbf{r'}) = \frac{\mathrm{d}\epsilon^{\sigma\sigma'}}{\mathrm{d}\mathbf{R}} \nabla_{\mathbf{r}} \cdot \mathbf{R} = -\frac{\mathrm{d}\epsilon^{\sigma\sigma'}}{\mathrm{d}\mathbf{R}} \nabla_{\mathbf{r'}} \cdot \mathbf{R} = -\nabla_{\mathbf{r'}} \cdot \epsilon^{\sigma\sigma'}(\mathbf{r} - \mathbf{r'}) \tag{A.44}$$

This we can exploit when we calculate the mostly local part of the xc-energy by inserting an isotropic dielectric function $\epsilon^{\sigma\sigma'}(\mathbf{r}-\mathbf{r}',\omega)$ into Equation A.42

$$E_{\mathrm{xc}}^{0} = \frac{1}{2\pi}\int_0^\infty \mathrm{d}u \ \sum_\sigma \mathrm{Tr}\left[\ln\left(\sum_{\sigma'}\int \mathrm{d}^3\mathbf{r}'\nabla_{\mathbf{r}}\cdot\epsilon^{\sigma\sigma'}(\mathbf{r}-\mathbf{r}',iu)\nabla_{\mathbf{r}'}G^{\sigma'\sigma}(\mathbf{r}',\mathbf{r}'')\right)\right] - E_{\mathrm{self}} \tag{A.45}$$

$$= \frac{1}{2\pi}\int_0^\infty \mathrm{d}u \ \sum_\sigma \mathrm{Tr}\left[\ln\left(-\sum_{\sigma'}\int \mathrm{d}^3\mathbf{r}'\nabla_{\mathbf{r}'}\cdot\epsilon^{\sigma\sigma'}(\mathbf{r}-\mathbf{r}',iu)\nabla_{\mathbf{r}'}G^{\sigma'\sigma}(\mathbf{r}',\mathbf{r}'')\right)\right] - E_{\mathrm{self}} \tag{A.46}$$

$$= \frac{1}{2\pi}\int_0^\infty \mathrm{d}u \ \sum_\sigma \mathrm{Tr}\left[\ln\left(\sum_{\sigma'}\int \mathrm{d}^3\mathbf{r}'\epsilon^{\sigma\sigma'}(\mathbf{r}-\mathbf{r}',iu)\nabla^2_{\mathbf{r}'}G^{\sigma'\sigma}(\mathbf{r}',\mathbf{r}'')\right)\right] - E_{\mathrm{self}} \tag{A.47}$$

$$= \frac{1}{2\pi}\int_0^\infty \mathrm{d}u \ \sum_\sigma \mathrm{Tr}\left[\ln\left(\sum_{\sigma'}\int \mathrm{d}^3\mathbf{r}'\epsilon^{\sigma\sigma'}(\mathbf{r}-\mathbf{r}',iu)\delta(\mathbf{r}'-\mathbf{r}'')\right)\right] - E_{\mathrm{self}} \tag{A.48}$$

$$= \frac{1}{2\pi}\int_0^\infty \mathrm{d}u \ \sum_\sigma \mathrm{Tr}\left[\ln\sum_{\sigma'}\epsilon^{\sigma\sigma'}(iu)\right] - E_{\mathrm{self}} \tag{A.49}$$

where we have used Equation A.44, partial integration and once again the definition of the Coulomb Greensfunction.

A.4. Derivation of vdW-DF continued

When subtracting the mostly local part E_{xc}^{0} of the xc-energy from Equation A.42 and also assuming that non local exchange contributions are negligible we arrive at an expression for the non local correlation energy

$$E_{\mathrm{c}}^{\mathrm{nl}} = \frac{1}{2\pi}\int_0^\infty \mathrm{d}u \ \sum_\sigma \mathrm{Tr}\left[\ln\left(\sum_{\sigma'}\nabla\epsilon^{\sigma\sigma'}(iu)\nabla G^{\sigma'\sigma}\right) - \ln\sum_{\sigma'}\epsilon^{\sigma\sigma'}(iu)\right]. \tag{A.50}$$

We will now expand this expression in terms of $S^{\sigma\sigma'} = \delta^{\sigma\sigma'} - \frac{1}{\epsilon^{\sigma\sigma'}} \Leftrightarrow \epsilon^{\sigma\sigma'} = \frac{1}{\delta^{\sigma\sigma'}-S^{\sigma\sigma'}}$. We obtain $\epsilon^{\sigma\sigma'} = \delta^{\sigma\sigma'} + S^{\sigma\sigma'} + \sum_\tau S^{\sigma\tau}\cdot S^{\tau\sigma'} + \mathcal{O}(S^3)$. Inserting this into Equation A.50 and expanding the matrix logarithm in a second step according to $\ln(1+X) = X - \frac{X^2}{2} + \mathcal{O}(X^3)$

we obtain:

$$E_{\mathrm{c}}^{\mathrm{nl}} = \frac{1}{2\pi}\int_0^\infty \mathrm{d}u \ \sum_\sigma \mathrm{Tr}\left[\ln\left(\sum_{\sigma'}\nabla\epsilon^{\sigma\sigma'}(iu)\nabla G^{\sigma'\sigma}\right) - \ln\sum_{\sigma'}\epsilon^{\sigma\sigma'}(iu)\right] \tag{A.51}$$

$$= \frac{1}{2\pi}\int_0^\infty \mathrm{d}u \ \sum_\sigma \mathrm{Tr}\left[\ln\left(\sum_{\sigma'}\nabla\left(\delta^{\sigma\sigma'} + S^{\sigma\sigma'} + \sum_\tau S^{\sigma\tau}\cdot S^{\tau\sigma'}\right)\nabla G^{\sigma'\sigma}\right)\right. \tag{A.52}$$
$$\left. - \ln\sum_{\sigma'}\left(\delta^{\sigma\sigma'} + S^{\sigma\sigma'} + \sum_\tau S^{\sigma\tau}\cdot S^{\tau\sigma'}\right)\right]$$

$$= \frac{1}{2\pi}\int_0^\infty \mathrm{d}u \ \sum_\sigma \mathrm{Tr}\left[\ln\left(1 + \nabla\left(\sum_{\sigma'} S^{\sigma\sigma'} + \sum_{\tau\sigma'} S^{\sigma\tau}\cdot S^{\tau\sigma'}\right)\nabla G^{\sigma'\sigma}\right)\right. \tag{A.53}$$
$$\left. - \sum_{\sigma'} S^{\sigma\sigma'} - \sum_{\tau\sigma'} S^{\sigma\tau}\cdot S^{\tau\sigma'} + \frac{1}{2}\left(\sum_{\sigma'} S^{\sigma\sigma'}\right)^2 + \mathcal{O}(S^3)\right]$$

$$= \frac{1}{2\pi}\int_0^\infty \mathrm{d}u \ \sum_\sigma \mathrm{Tr}\left[\sum_{\sigma'}\nabla\left(S^{\sigma\sigma'} + \sum_\tau S^{\sigma\tau}\cdot S^{\tau\sigma'}\right)\nabla G^{\sigma'\sigma}\right.$$
$$\left. -\frac{1}{2}\left(\sum_{\sigma'}\nabla\left(S^{\sigma\sigma'} + \sum_\tau S^{\sigma\tau}\cdot S^{\tau\sigma'}\right)\nabla G^{\sigma'\sigma}\right)^2\right. \tag{A.54}$$
$$\left. - \sum_{\sigma'} S^{\sigma\sigma'} - \sum_{\tau\sigma'} S^{\sigma\tau}\cdot S^{\tau\sigma'} + \frac{1}{2}\left(\sum_{\sigma'} S^{\sigma\sigma'}\right)^2 + \mathcal{O}(S^3)\right]$$

$$= \frac{1}{2\pi}\int_0^\infty \mathrm{d}u \ \sum_\sigma \mathrm{Tr}\left[\sum_{\sigma'}\nabla S^{\sigma\sigma'}\nabla G^{\sigma'\sigma} - \sum_{\sigma'} S^{\sigma\sigma'} + \nabla\sum_{\tau\sigma'} S^{\sigma\tau}\cdot S^{\tau\sigma'}\nabla G^{\sigma'\sigma}\right. \tag{A.55}$$
$$\left. - \sum_{\tau\sigma'} S^{\sigma\tau}\cdot S^{\tau\sigma'} - \frac{1}{2}\left(\sum_{\sigma'}\nabla S^{\sigma\sigma'}\nabla G^{\sigma'\sigma}\right)^2 + \frac{1}{2}\left(\sum_{\sigma'} S^{\sigma\sigma'}\right)^2\right]$$

where we have in the last step omitted all the terms of the order of $\mathcal{O}(S^3)$ arising from $\left(\nabla\sum_{\sigma'}(S^{\sigma\sigma'} + \sum_\tau S^{\sigma\tau}\cdot S^{\tau\sigma'})\nabla G^{\sigma'\sigma}\right)^2$ and rearranged them in a way they will cancel after the following considerations. For the first term we obtain

$$\mathrm{Tr}\sum_{\sigma'}\nabla S^{\sigma\sigma'}\nabla G^{\sigma'\sigma} = \int \mathrm{d}^3\mathbf{r}\mathrm{d}^3\mathbf{r}'\sum_{\sigma'}\nabla_{\mathbf{r}} S^{\sigma\sigma'}(\mathbf{r},\mathbf{r}')\nabla_{\mathbf{r}'} G^{\sigma'\sigma}(\mathbf{r}',\mathbf{r}) \tag{A.56}$$

$$= -\int \mathrm{d}^3\mathbf{r}\mathrm{d}^3\mathbf{r}'\sum_{\sigma'} S^{\sigma\sigma'}(\mathbf{r},\mathbf{r}')\nabla_{\mathbf{r}}\nabla_{\mathbf{r}'} G^{\sigma'\sigma}(\mathbf{r}',\mathbf{r}) \tag{A.57}$$

$$= \int \mathrm{d}^3\mathbf{r}\mathrm{d}^3\mathbf{r}'\sum_{\sigma'} S^{\sigma\sigma'}(\mathbf{r},\mathbf{r}')\delta(\mathbf{r}',\mathbf{r}) \tag{A.58}$$

$$= \mathrm{Tr} \sum_{\sigma'} S^{\sigma\sigma'} \tag{A.59}$$

To see this we have used partial integration over $\mathbf{r}$ in the first step and then used the property $\nabla_{\mathbf{r}'}\nabla_{\mathbf{r}} G(\mathbf{r},\mathbf{r}') = -\delta(\mathbf{r},\mathbf{r}')$ of the Coulomb Greensfunction [3]. The same trick can be applied to $\nabla \sum_{\tau\sigma'} S^{\sigma\tau} \cdot S^{\tau\sigma'} \nabla G^{\sigma'\sigma}$

$$\mathrm{Tr}\nabla \sum_{\tau\sigma'} S^{\sigma\tau} \cdot S^{\tau\sigma'} \nabla G^{\sigma'\sigma} = \int \mathrm{d}^3\mathbf{r}\mathrm{d}^3\mathbf{r}'\mathrm{d}^3\mathbf{r}''\nabla_{\mathbf{r}} \sum_{\tau\sigma'} S^{\sigma\tau}(\mathbf{r},\mathbf{r}') \cdot S^{\tau\sigma'}(\mathbf{r}',\mathbf{r}'')\nabla_{\mathbf{r}''} G^{\sigma'\sigma}(\mathbf{r}'',\mathbf{r}) \tag{A.60}$$

$$= -\int \mathrm{d}^3\mathbf{r}\mathrm{d}^3\mathbf{r}'\mathrm{d}^3\mathbf{r}'' \sum_{\tau\sigma'} S^{\sigma\tau}(\mathbf{r},\mathbf{r}') \cdot S^{\tau\sigma'}(\mathbf{r}',\mathbf{r}'')\nabla_{\mathbf{r}}\nabla_{\mathbf{r}''} G^{\sigma'\sigma}(\mathbf{r}'',\mathbf{r}) \tag{A.61}$$

$$= \int \mathrm{d}^3\mathbf{r}\mathrm{d}^3\mathbf{r}'\mathrm{d}^3\mathbf{r}'' \sum_{\tau\sigma'} S^{\sigma\tau}(\mathbf{r},\mathbf{r}') \cdot S^{\tau\sigma'}(\mathbf{r}',\mathbf{r}'')\delta(\mathbf{r}'',\mathbf{r}) \tag{A.62}$$

$$= \mathrm{Tr} \sum_{\tau\sigma'} S^{\sigma\tau} \cdot S^{\tau\sigma'} \tag{A.63}$$

By this the first four terms in Equation A.55 cancel each other and we arrive at

$$E_{\mathrm{c}}^{\mathrm{nl}} = \frac{1}{4\pi}\int_0^\infty \mathrm{d}u \ \sum_{\sigma} \mathrm{Tr}\left[\left(\sum_{\sigma'} S^{\sigma\sigma'}\right)^2 - \left(\sum_{\sigma'} \nabla S^{\sigma\sigma'} \nabla G^{\sigma'\sigma}\right)^2\right] \tag{A.64}$$

In the above equation $\left(\sum_{\sigma'} \nabla S^{\sigma\sigma'} \nabla G^{\sigma'\sigma}\right)^2 = \sum_{\sigma'\tau\tau'} \nabla S^{\sigma\sigma'} \nabla G^{\sigma'\tau} \nabla S^{\tau\tau'} \nabla G^{\tau'\sigma}$ has been used as a shorthand notation. Finally we want to Fourier transform this expression to reciprocal space. This is rather lengthy so we will treat both terms independently.

$$\mathrm{Tr} \sum_{\sigma'\tau\tau'} S^{\sigma\sigma'} \cdot S^{\tau\tau'} = \int \mathrm{d}^3\mathbf{r}\ \mathrm{d}^3\mathbf{r}' \sum_{\sigma'\tau\tau'} S^{\sigma\sigma'}(\mathbf{r},\mathbf{r}')S^{\tau\tau'}(\mathbf{r}',\mathbf{r}) \tag{A.65}$$

$$= \int \mathrm{d}^3\mathbf{r}\ \mathrm{d}^3\mathbf{r}' \int \mathrm{d}^3\mathbf{k_1}\ \mathrm{d}^3\mathbf{k_2}\ \mathrm{d}^3\mathbf{k_3}\ \mathrm{d}^3\mathbf{k_4} \sum_{\sigma'\tau\tau'} S^{\sigma\sigma'}(\mathbf{k_1},\mathbf{k_2})S^{\tau\tau'}(\mathbf{k_3},\mathbf{k_4})e^{i(\mathbf{r}\cdot(\mathbf{k_1}-\mathbf{k_4})+\mathbf{r}'\cdot(\mathbf{k_3}-\mathbf{k_2}))} \tag{A.66}$$

$$= \int \mathrm{d}^3\mathbf{k_1}\ \mathrm{d}^3\mathbf{k_2}\ \mathrm{d}^3\mathbf{k_3}\ \mathrm{d}^3\mathbf{k_4} \sum_{\sigma'\tau\tau'} S^{\sigma\sigma'}(\mathbf{k_1},\mathbf{k_2})S^{\tau\tau'}(\mathbf{k_3},\mathbf{k_4})\delta(\mathbf{k_1}-\mathbf{k_4})\delta(\mathbf{k_3}-\mathbf{k_2}) \tag{A.67}$$

[3] This can be verified explicitly calculating the gradient of the Coulomb potential. If we now take the divergence with respect to $\mathbf{r}'$ only the sign will change:

$$\nabla_{\mathbf{r}'} \cdot \nabla_{\mathbf{r}} G(\mathbf{r},\mathbf{r}') = -\frac{1}{4\pi}\nabla_{\mathbf{r}'} \cdot \frac{\mathbf{r}-\mathbf{r}'}{|\mathbf{r}-\mathbf{r}'|^3} = \frac{1}{4\pi}\nabla_{\mathbf{r}} \cdot \frac{\mathbf{r}-\mathbf{r}'}{|\mathbf{r}-\mathbf{r}'|^3} = -\nabla_{\mathbf{r}}^2 G(\mathbf{r},\mathbf{r}') = -\delta(\mathbf{r},\mathbf{r}')$$

It is actually a special case of what we have shown already in Equation A.44.

$$= \int \mathrm{d}^3\mathbf{k}\ \mathrm{d}^3\mathbf{k}' \sum_{\sigma'\tau\tau'} S^{\sigma\sigma'}(\mathbf{k},\mathbf{k}')S^{\tau\tau'}(\mathbf{k}',\mathbf{k}) \tag{A.68}$$

$$\begin{aligned}\mathrm{Tr}\ (\nabla S^{\sigma\sigma'}\nabla G^{\sigma'\sigma})^2 = \int \mathrm{d}^3\mathbf{r}\ \mathrm{d}^3\mathbf{r}'\ \mathrm{d}^3\mathbf{r}''\ \mathrm{d}^3\mathbf{r}'''\ \sum_{\sigma'\tau\tau'} \nabla_{\mathbf{r}} S^{\sigma\sigma'}(\mathbf{r},\mathbf{r}')\nabla_{\mathbf{r}'} G^{\sigma'\tau}(\mathbf{r}',\mathbf{r}'') \\ \nabla_{\mathbf{r}''} S^{\tau\tau'}(\mathbf{r}'',\mathbf{r}''')\nabla_{\mathbf{r}'''} G^{\tau'\sigma}(\mathbf{r}''',\mathbf{r})\end{aligned} \tag{A.69}$$

$$= \int \mathrm{d}^3\mathbf{r}\ \mathrm{d}^3\mathbf{r}'\ \mathrm{d}^3\mathbf{r}''\ \mathrm{d}^3\mathbf{r}''' \int \mathrm{d}^3\mathbf{k_1}\ \mathrm{d}^3\mathbf{k_2}\ \mathrm{d}^3\mathbf{k_3}\ \mathrm{d}^3\mathbf{k_4}\ \mathrm{d}^3\mathbf{k_5}\ \mathrm{d}^3\mathbf{k_6}\ \mathrm{d}^3\mathbf{k_7}\ \mathrm{d}^3\mathbf{k_8} \tag{A.70}$$

$$\sum_{\sigma'\tau\tau'} i\mathbf{k_1} S^{\sigma\sigma'}(\mathbf{k_1},\mathbf{k_2}) i\mathbf{k_3} G^{\sigma'\tau}(\mathbf{k_3},\mathbf{k_4}) i\mathbf{k_5} S^{\tau\tau'}(\mathbf{k_5},\mathbf{k_6}) i\mathbf{k_7} G^{\tau'\sigma}(\mathbf{k_7},\mathbf{k_8})$$

$$e^{i\mathbf{r}\cdot(\mathbf{k_1}-\mathbf{k_8})} e^{i\mathbf{r}'\cdot(\mathbf{k_3}-\mathbf{k_2})} e^{i\mathbf{r}''\cdot(\mathbf{k_5}-\mathbf{k_4})} e^{i\mathbf{r}'''\cdot(\mathbf{k_7}-\mathbf{k_6})}$$

$$= \int \mathrm{d}^3\mathbf{k_1}\ \mathrm{d}^3\mathbf{k_2}\ \mathrm{d}^3\mathbf{k_3}\ \mathrm{d}^3\mathbf{k_4}\ \mathrm{d}^3\mathbf{k_5}\ \mathrm{d}^3\mathbf{k_6}\ \mathrm{d}^3\mathbf{k_7}\ \mathrm{d}^3\mathbf{k_8} \tag{A.71}$$

$$\sum_{\sigma'\tau\tau'} \mathbf{k_1} S^{\sigma\sigma'}(\mathbf{k_1},\mathbf{k_2})\mathbf{k_3} G^{\sigma'\tau}(\mathbf{k_3},\mathbf{k_4})\mathbf{k_5} S^{\tau\tau'}(\mathbf{k_5},\mathbf{k_6})\mathbf{k_7} G^{\tau'\sigma}(\mathbf{k_7},\mathbf{k_8})$$

$$\delta(\mathbf{k_1}-\mathbf{k_8})\delta(\mathbf{k_3}-\mathbf{k_2})\delta(\mathbf{k_5}-\mathbf{k_4})\delta(\mathbf{k_7}-\mathbf{k_6})$$

$$= \int \mathrm{d}^3\mathbf{k_1}\ \mathrm{d}^3\mathbf{k_3}\ \mathrm{d}^3\mathbf{k_5}\ \mathrm{d}^3\mathbf{k_7}\ \mathbf{k_1}\mathbf{k_3}\mathbf{k_5}\mathbf{k_7} \tag{A.72}$$

$$\sum_{\sigma'\tau\tau'} S^{\sigma\sigma'}(\mathbf{k_1},\mathbf{k_3}) G^{\sigma'\tau}(\mathbf{k_3},\mathbf{k_5}) S^{\tau\tau'}(\mathbf{k_5},\mathbf{k_7}) G^{\tau'\sigma}(\mathbf{k_7},\mathbf{k_1})$$

$$= \int \mathrm{d}^3\mathbf{k_1}\ \mathrm{d}^3\mathbf{k_3}\ \mathrm{d}^3\mathbf{k_5}\ \mathrm{d}^3\mathbf{k_7}\ \frac{\mathbf{k_1}\mathbf{k_3}\mathbf{k_5}\mathbf{k_7}}{k_3^2 k_7^2} \tag{A.73}$$

$$\sum_{\sigma'\tau\tau'} S^{\sigma\sigma'}(\mathbf{k_1},\mathbf{k_3})\delta(\mathbf{k_3}-\mathbf{k_5}) S^{\tau\tau'}(\mathbf{k_5},\mathbf{k_7})\delta(\mathbf{k_7}-\mathbf{k_1})$$

$$= \int \mathrm{d}^3\mathbf{k_1}\ \mathrm{d}^3\mathbf{k_5}\ \sum_{\sigma'\tau\tau'} \frac{\mathbf{k_1}\mathbf{k_5}\mathbf{k_5}\mathbf{k_1}}{k_5^2 k_1^2} S^{\sigma\sigma'}(\mathbf{k_1},\mathbf{k_5}) S^{\tau\tau'}(\mathbf{k_5},\mathbf{k_1}) \tag{A.74}$$

$$= \int \mathrm{d}^3\mathbf{k}\ \mathrm{d}^3\mathbf{k}'\ \sum_{\sigma'\tau\tau'} \left(\hat{\mathbf{k}}\hat{\mathbf{k}}'\right)^2 S^{\sigma\sigma'}(\mathbf{k},\mathbf{k}') S^{\tau\tau'}(\mathbf{k}',\mathbf{k}) \tag{A.75}$$

During this we have used the explicit form $G(\mathbf{k},\mathbf{k}') = \frac{\delta(\mathbf{k}-\mathbf{k}')4}{k^2}$ of the Coulomb Greens-function in reciprocal space. Putting now together the just derived results we finally

[4] In order to obtain the matrix element $G(\mathbf{r},\mathbf{r}')$ in momentum space we need the following equation:

$$G(\mathbf{r},\mathbf{r}') = \langle \mathbf{r}|G|\mathbf{r}'\rangle = \sum_{\mathbf{kk}'} \langle \mathbf{r}|\mathbf{k}\rangle \langle \mathbf{k}|G|\mathbf{k}'\rangle \langle \mathbf{k}'|\mathbf{r}'\rangle = \sum_{\mathbf{kk}'} e^{i\mathbf{k}\cdot\mathbf{r}} G(\mathbf{k},\mathbf{k}') e^{-i\mathbf{k}'\cdot\mathbf{r}'} = \mathcal{F}^{-1}_{\mathbf{rk}}\left(\mathcal{F}_{\mathbf{r}'\mathbf{k}'}\left(G(\mathbf{k},\mathbf{k}')\right)\right),$$

where $\mathcal{F}_{\mathbf{rk}}$ denotes the Fourier transform corresponding to the variable pair $\mathbf{r}$ and $\mathbf{k}$ and $\mathcal{F}^{-1}_{\mathbf{rk}}$ its inverse. The matrix element in momentum space is then given by $G(\mathbf{k},\mathbf{k}') = \mathcal{F}^{-1}_{\mathbf{r}'\mathbf{k}'}\left(\mathcal{F}_{\mathbf{rk}}\left(G(\mathbf{r},\mathbf{r}')\right)\right)$. The

arrive at the following expression for the non local part of the correlation energy

$$E_{\mathrm{c}}^{\mathrm{nl}} = \int_0^\infty \frac{\mathrm{d}u}{4\pi} \int \mathrm{d}^3\mathbf{k}\ \mathrm{d}^3\mathbf{k}'\ \sum_\sigma \left(1 - \left(\hat{\mathbf{k}}\hat{\mathbf{k}}'\right)^2\right) \sum_{\sigma'\tau\tau'} S^{\sigma\sigma'}(\mathbf{k}, \mathbf{k}') S^{\tau\tau'}(\mathbf{k}', \mathbf{k}) \tag{A.76}$$

A.5. A model for $S(\mathbf{k}, \mathbf{k}', \omega)$

In the last section we arrived at an expression for the non-local correlation energy which depends on the function $S(\mathbf{k}, \mathbf{k}', \omega)$ which is $1 - \epsilon^{-1}$. Only a number of analytic limits and constraints are known for the full non-local nonmagnetic dielectric function. Thus, we have to find a model for $S(\mathbf{k}, \mathbf{k}', iu)$ which at first fulfills these asymptotic forms and second also leads to a more or less simple expression which allows to carry out some of the integrations in Equation A.76. Starting from this point one could try to find a different approximation based on a more sophisticated ansatz for the dielectric function in order to improve the non local correlation functional with respect to the one originally proposed by Dion *et al.*. Vydrov *et al.* pursued this way for their VV10 functional. An earlier version of that functional (i.e. VV09) did not satisfy all imposed limits and was therefore harshly criticized. Unfortunately the newer version of that functional did not inherit the attempt to include spin effects into the non-local functional from its predecessor. We will nevertheless give a short overview about both vdW-DF and VV10 to shed some light on their structure.

Starting with vdW-DF the form of $S(\mathbf{k}, \mathbf{k}', iu)$ is inspired by the plasmon pole model

$$S(\mathbf{k}, \mathbf{k}', \omega) = \frac{1}{2}\tilde{S}(\mathbf{k}, \mathbf{k}', \omega) + \frac{1}{2}\tilde{S}(-\mathbf{k}, -\mathbf{k}', \omega) \tag{A.77}$$

$$\tilde{S}(\mathbf{k}, \mathbf{k}', \omega) = \int \mathrm{d}^3\mathbf{r}\ e^{-i(\mathbf{k}-\mathbf{k}')\mathbf{r}} \frac{4\pi n(\mathbf{r})}{[\omega + \omega_k(\mathbf{r})]\,[-\omega + \omega_{k'}(\mathbf{r})]} \tag{A.78}$$

where the dispersion is approximated by $\omega_k = k^2/\left[2h(k/k_0)\right]$ which uses a switching function $h(k/k_0)$ as well as k_0 will be defined in Section A.6. Equation A.77 ensures the time reversal symmetry of $S(\mathbf{k}, \mathbf{k}', \omega)$. Besides this Dion *et al.* name three more properties and limits which $S(\mathbf{k}, \mathbf{k}', \omega)$ needs to fulfill. First the high frequency limit

$$\lim_{\omega\to\infty} S(\mathbf{k}, \mathbf{k}', \omega) = -\frac{4\pi}{\omega^2} n_{\mathbf{k}-\mathbf{k}'}, \tag{A.79}$$

---

first Fourier transform we obtain from the Fourier transform of the Poisson equation $\Delta_{\mathbf{r}} G(\mathbf{r}, \mathbf{r}') = \delta(\mathbf{r} - \mathbf{r}') \Leftrightarrow -k^2 G(\mathbf{k}, \mathbf{r}') = e^{-i\mathbf{k}\cdot\mathbf{r}'}$. Now applying $\mathcal{F}^{-1}_{\mathbf{r}'\mathbf{k}'}$ leads to

$$G(\mathbf{k}, \mathbf{k}') = -\int \mathrm{d}^3\mathbf{r}'\ \frac{e^{-i\mathbf{k}\cdot\mathbf{r}'}}{k^2} e^{i\mathbf{k}'\cdot\mathbf{r}'} = \frac{1}{k^2}\int \mathrm{d}^3\mathbf{r}'\ e^{-i(\mathbf{k}'-\mathbf{k})\cdot\mathbf{r}'} = \frac{\delta(\mathbf{k}' - \mathbf{k})}{k^2} = \frac{\delta(\mathbf{k} - \mathbf{k}')}{k^2}$$

where we have in the second step changed the variable from $\mathbf{r}'$ to $-\mathbf{r}'$ in order to get rid of the negative sign.

second the large k limit where N is the total number of electrons

$$\lim_{k\to\infty}\int_{-\infty}^{\infty}\mathrm{d}u\ S(\mathbf{k},\mathbf{k}',iu)=\frac{8\pi^2 N}{k^2}, \tag{A.80}$$

and last the charge conservation which translates to the condition of $S(\mathbf{k},\mathbf{k}',\omega)$ staying finite for $\omega\neq 0$ and $\mathbf{k}=0$ or $\mathbf{k}'=0$.

To reach the final form of the non local correlation energy as a double spatial integral over the charge densities and the kernel function $\phi(\mathbf{r},\mathbf{r}')$ as given in Equation 3.16 we have to insert the definition of $S(\mathbf{k},\mathbf{k}',\omega)$ from Equation A.78 into Equation A.76 and to do the frequency integration and the angular parts of the k integrations. with the abbreviation

$$f(k,k',\omega)=\frac{2\pi}{[\omega+\omega_k(\mathbf{r})]\,[-\omega+\omega_{k'}(\mathbf{r})]}+\frac{2\pi}{[\omega+\omega_{k'}(\mathbf{r})]\,[-\omega+\omega_k(\mathbf{r})]} \tag{A.81}$$

$$S(\mathbf{k},\mathbf{k}',\omega)=\int\mathrm{d}^3\mathbf{r}\ e^{-i(\mathbf{k}-\mathbf{k}')\mathbf{r}}f(k,k',\omega)n(\mathbf{r}) \tag{A.82}$$

where $f(k,k',\omega)$ depends only on the length of k we arrive at the expression

$$E_{\mathrm{c}}^{\mathrm{nl}}=\int\mathrm{d}^3\mathbf{r}\ \mathrm{d}^3\mathbf{r}'n(\mathbf{r})n(\mathbf{r}')\left[\int_0^\infty\mathrm{d}k\int_0^\infty\mathrm{d}k'\ k^2k'^2\int_0^\infty\frac{\mathrm{d}u}{2\pi}f(k,k',iu,\mathbf{r})f(k',k,iu,\mathbf{r}')\right.$$
$$\left.\int\mathrm{d}\theta\ \mathrm{d}\theta'\left(1-\left(\hat{\mathbf{k}}\hat{\mathbf{k}}'\right)^2\right)e^{-i(\mathbf{k}-\mathbf{k}')\mathbf{r}}e^{i(\mathbf{k}-\mathbf{k}')\mathbf{r}'}\right] \tag{A.83}$$

for the non local correlation energy, where the θ-integration denotes the angular part of the $\mathbf{k}$-integration and part contained in the square brackets constitutes the kernel $\phi(\mathbf{r},\mathbf{r}')$. The corresponding integrals can be evaluated and the result will be given in Section A.6.

A.6. The kernel function ϕ

In the original paper from Dion *et al.* [19] from which we also adopt the nomenclature the kernel $\phi(\mathbf{r},\mathbf{r}')$ is defined by the following equation:

$$\phi(\mathbf{r},\mathbf{r}')=\int_0^\infty\mathrm{d}k\int_0^\infty\mathrm{d}k'\ k^2k'^2\int_0^\infty\frac{\mathrm{d}u}{2\pi}f(k,k',iu,\mathbf{r})f(k',k,iu,\mathbf{r}')$$
$$\int\mathrm{d}\theta\ \mathrm{d}\theta'\left(1-\left(\hat{\mathbf{k}}\hat{\mathbf{k}}'\right)^2\right)e^{-i(\mathbf{k}-\mathbf{k}')\mathbf{r}}e^{i(\mathbf{k}-\mathbf{k}')\mathbf{r}'}, \tag{A.84}$$

which is the part in square brackets of Equation A.83. The frequency integration and the angular integrations can be done independently and analytically. With $W(a,b)$ being the angular integral and $T(v(a),v(b),v'(a),v'(b))$ being the frequency integral we finally reach the form of the kernel as given by Dion *et al.*:

$$\phi(\mathbf{r},\mathbf{r}') = \int_0^\infty a^2 \int_0^\infty b^2 \; W(a,b)\, T(v(a),v(b),v'(a),v'(b))\,\mathrm{d}a\,\mathrm{d}b \tag{A.85}$$

$$T(w,x,y,z) = \frac{1}{2}\left[\frac{1}{(w+x)} + \frac{1}{(y+z))}\right]\left[\frac{1}{(w+y)(x+z)} + \frac{1}{(w+z)(x+y)}\right] \tag{A.86}$$

$$W(a,b) = \frac{2}{a^3b^3}\left[\left(3-a^2\right) b\cos b\sin a + \left(3-b^2\right) a\cos a\sin b\right. \tag{A.87}$$

$$\left. + \left(a^2+b^2-3\right)\sin a\sin a - 3\,ab\cos a\cos b\right] \tag{A.88}$$

$v(y) = y^2/2h(y/d)$ and $v'(y)) = y^2/2h(y/d')$ contain the $\mathbf{r}$ dependence of ϕ by $d = |\mathbf{r}-\mathbf{r}'|\, q_0(\mathbf{r})$ and $d' = |\mathbf{r}-\mathbf{r}'|\, q_0(\mathbf{r}')$ where $h(y) = 1 - e^{-\frac{4\pi}{9}y^2}$ is a switching function from small q to large q regime and $q_0(\mathbf{r})$ has the form:

$$q_0(\mathbf{r}) = q_0\left[n(\mathbf{r}), \nabla n(\mathbf{r})\right] = \left[1 + \frac{\epsilon_\mathrm{c}^{\mathrm{LDA}}(n(\mathbf{r}))}{\epsilon_\mathrm{x}^{\mathrm{LDA}}(n(\mathbf{r}))} - \frac{Z_{ab}}{9}\left(\frac{\nabla n(\mathbf{r})}{2n(\mathbf{r})k_F}\right)^2\right] k_F \tag{A.89}$$

$k_F = (3\pi^2 n)^{\frac{1}{3}}$ is the usually defined Fermi wave vector. The constant $Z_{ab} = -0.8491$ from the original Dion paper has been adjusted by Lee *et al.* [158] to $Z_{ab} = -1.887$ which then gives the more accurate so called vdW-DF2 functional. The kernel can be tabulated in advance so there are now all ingredients to evaluate the integral in Equation 3.16 and calculate the non local contribution to the xc-functional.

The double integral makes the evaluation of the non local correlation Energy very expensive even for modern computers. Recently G. Román-Pérez and J. M. Soler [115] have proposed a different way to deal with this problem which reduces the costs dramatically and by this also allows self consistent calculations employing vdW-DF.

A.7. The VV10 kernel

The kernel proposed by O. A. Vydrov and T. van Voorhis [163] has a slightly different even simpler form. Unfortunately no full derivation of this form is given in [163] except for that it is build on insights gained in [165, 166, 255, 256]. In [256] a derivation based on the Clausius Mosotti formula as relation between the polarizability α and the dielectric function ϵ. This argumentation leads to a form of the dispersion energy which is similar to the non local correction introduced [256]. The starting point is an expression for the dispersion interaction of two polarizable systems A and B separated by a large distance R for which $\mathbf{r}$ denotes the domain of A and $\mathbf{r}'$ the domain of B and the local polarizability $\alpha(\mathbf{r},\omega)$ is defined on both domains:

$$E_\mathrm{disp} = -\frac{3}{\pi}\int_0^\infty \mathrm{d}u \int_\mathrm{A} \mathrm{d}^3\mathbf{r} \int_\mathrm{B} \mathrm{d}^3\mathbf{r}' \frac{\alpha(\mathbf{r},iu)\alpha(\mathbf{r}',iu)}{|\mathbf{r}-\mathbf{r}'|^6} \tag{A.90}$$

The authors obtain the polarizability via the Clausius Mossotti equation:

$$\alpha(\mathbf{r},\omega) = \frac{3}{4\pi}\left[\frac{\epsilon(\mathbf{r},\omega)-1}{\epsilon(\mathbf{r},\omega)+2}\right] \tag{A.91}$$

with the zero wave vector dielectric function for a semiconductor with a finite gap $\epsilon(\mathbf{r},iu) = 1+\frac{\omega_p^2}{\omega_g^2+u^2}$ where $\omega_g = C\left|\frac{n(\nabla\mathbf{r})}{n(\mathbf{r})}\right|^4$ is a 'local' gap and C is a parameter which has to be adjusted. This leads to a polarizability:

$$\alpha(\mathbf{r},iu) = \frac{1}{4\pi}\frac{\omega_p^2}{\frac{\omega_p^2}{3}+\omega_g^2+u^2} \tag{A.92}$$

Inserting this into the expression for the dispersion energy and calling $\omega_0^2 = \omega_p^2/3+\omega_g^2$ leads to the form of the kernel similar to what has been used in VV10:

$$E_{\text{disp}} = -\frac{3}{32\pi^2}\int_{\text{A}}\mathrm{d}^3\mathbf{r}\int_{\text{B}}\mathrm{d}^3\mathbf{r}'\frac{\omega_p^2(\mathbf{r})\omega_p^2(\mathbf{r}')}{\omega_0(\mathbf{r})\omega_0(\mathbf{r}')\left(\omega_0(\mathbf{r})+\omega_0(\mathbf{r}')\right)} \tag{A.93}$$

In order to obtain the non local correlation energy E_{c}^{nl} for the VV10 functional the above formula has been slightly modified. First the authors introduced a function $g = \omega_0(\mathbf{r})\left|\mathbf{r}-\mathbf{r}'\right|^2+\kappa(\mathbf{r})$ where $\kappa(\mathbf{r}) = 3b\omega_p(\mathbf{r})/k_s^2$ is added to control the short range damping. k_s is the Fermi wave vector and b is a second parameter which has to be adjusted. The second major difference are the domains of integration. In the just shown formulas the integration run only over the confined domains of systems A and B. In VV10 these integrations run over the whole space which leads to a factor of one half to avoid double counting.

$$E_{\text{c}}^{\text{nl}} = -\frac{1}{32\pi^2}\frac{3}{2}\int\mathrm{d}^3\mathbf{r}\int\mathrm{d}^3\mathbf{r}'\frac{\omega_p^2(\mathbf{r})\omega_p^2(\mathbf{r}')}{gg'\left(g+g'\right)} \tag{A.94}$$

$$= \frac{1}{2}\int\mathrm{d}^3\mathbf{r}\int\mathrm{d}^3\mathbf{r}'n(\mathbf{r})\phi(\mathbf{r},\mathbf{r}')n(\mathbf{r}'), \tag{A.95}$$

with the kernel function defined as $\phi(\mathbf{r},\mathbf{r}') = -\frac{3}{2}\frac{1}{gg'(g+g')}$ The total correlation functional $E_{\text{c}}^{\text{VV10}}$ of VV10 is than defined as

$$E_{\text{c}}^{\text{VV10}} = \int\mathrm{d}^3\mathbf{r}n(\mathbf{r})\left(\beta+\int\mathrm{d}^3\mathbf{r}'\phi(\mathbf{r},\mathbf{r}')n(\mathbf{r}')\right) \tag{A.96}$$

where β is minus the density independent correlation energy density of a uniform density. This construction ensures that $E_{\text{c}}^{\text{VV10}}$ vanishes in the uniform density limit. The correlation part of the VV10 functional is then added to PBE correlation. For the exchange the same refitted PW86 as in vdW-DF2 is used.

Regarding the presented derivation and the xc-functional used in combination with the VV10 correlation the VV10 functional appears to be similar to the semi empirical

approach used by A. Tkatchenko and M. Scheffler [136]. In the case of VV10 a dispersion correction is added to a certain GGA. Also in that method the C_6 coefficients are calculated from polarizabilities α which again are calculated based on the density. The dispersion energy is then added to the total energy obtained from the DFT calculations. Of course the consistency of a vdW functional with Equation A.90 is usually checked and also for vdW-DF this has been shown in the thesis of M. Dion [248]. From this point of view as consistency with Equation A.90 is a general feature of vdW functionals the relation between VV10 and the Tkatchenko-Scheffler method might not survive of a closer second look. Unfortunately in the given references there is no hint how to obtain the final version of VV10 from $S(\mathbf{r}, \mathbf{r}', \omega)$.

A.8. Additional thoughts based on modern theory of polarization

Before continu/ing with the detailed description of the Soler scheme for the implementation of vdW-DF we would like to take a step back and look again at E_{xc} in the ACFDT

$$E_{\mathrm{xc}} = -\frac{1}{2\pi}\int_0^1 \mathrm{d}\lambda \int_0^\infty \mathrm{d}u \ \mathrm{Tr}\left[v\,\chi_\lambda(iu)\right] - E_{\mathrm{self}} \tag{A.97}$$

$$= -\frac{1}{2\pi}\int_0^1 \mathrm{d}\lambda \int_0^\infty \mathrm{d}u \ \mathrm{Tr}\left[v\,\frac{\delta n_\lambda(iu)}{\delta\phi_{\mathrm{ext}}}\right] - E_{\mathrm{self}} \tag{A.98}$$

regarding the modern theory of polarization[5] as the polarization has turned out to be one key ingredient during the derivation of vdW-DF. In the second step we have rewritten the responsefunction χ_λ as the functional derivative of the charge density with respect to the potential as defined by Equation A.8. The change of the charge density is also given by the divergence of the polarization

$$\delta n_\lambda(\mathbf{r}, \omega) = \nabla_{\mathbf{r}} \cdot \mathbf{P}_\lambda(\mathbf{r}, \omega) \tag{A.99}$$

which has been used during the derivation of vdW-DF. In the literature there is a generalization of DFT for materials with a finite gap to make a correspondence between charge density and polarization $\{n, \mathbf{P}\}$ and the potential and an electric field elaborated by X. Gonze, R. Godby and Ph. Ghosez [258] and further discussed in [259, 260]. This extension of DFT is proposed because of the problem occurring with the original Hohenberg Kohn theorems for a system in an electric field when there is no well defined lowest energy state anymore.

For the formulation of DFT with the polarization $\mathbf{P}_\lambda(\mathbf{r}, \omega)$ as a second variable it is necessary to keep its value fixed along the variation λ. As a consequence of Equation A.99 also the induced charge density $\delta n_\lambda(\mathbf{r}, \omega)$ becomes independent of the coupling constant

[5] a topical review on the subject has been written by R. Resta [257]

λ which in addition leads to a λ-independence of the fully interacting response function $\chi_\lambda(\mathbf{r}, \mathbf{r}', \omega)$. Hence, the λ integration in Equation A.98 can be carried out trivially and we arrive at

$$E_{\mathrm{xc}} = -\frac{1}{2\pi} \int_0^\infty \mathrm{d}u \ \mathrm{Tr}\left[v\, \chi(iu)\right] - E_{\mathrm{self}} \tag{A.100}$$

In the modern theory of polarization the polarization is associated with the berry curvature.

B

An efficient implementation of vdW-DF: The Soler scheme

B.1. Decomposition of the kernel

This section will repeat basically the Soler paper and give additional information on the derivation of some of the formulas. To get rid of the expensive double integral in Equation 3.16 Fourier method will be applied. First one rewrites Equation 3.16 with the explicit dependencies:

$$E_{\mathrm{c}}^{\mathrm{NL}}[n] = \frac{1}{2} \iint n(\mathbf{r_1})\, \phi(q_1, q_2, r_{12})\, n(\mathbf{r_2})\, \mathrm{d}^3\mathbf{r_1}\, \mathrm{d}^3\mathbf{r_2} \tag{B.1}$$

If q_1 and q_2 where fixed values and thus independent of $\mathbf{r_1}$ and $\mathbf{r_2}$ Equation B.1 would be a simple convolution. Soler et al. managed to achieve this in the following way. They expanded the kernel ϕ as:

$$\phi(q_1, q_2, r_{12}) \backsimeq \sum_{\alpha,\beta} \phi(q_\alpha, q_\beta, r_{12}) p_\alpha(q_1) p_\beta(q_2) \tag{B.2}$$

$$= \sum_{\alpha,\beta} \phi_{\alpha\beta}(r_{12}) p_\alpha(q_1) p_\beta(q_2) \tag{B.3}$$

To see this we start by expanding a function of one variable $f(x) \backsimeq \sum_\alpha f(x_\alpha)\, p_\alpha(x) = \sum_\alpha f_\alpha\, p_\alpha(x)$ where $p_\alpha(x)$ are the functions resulting from the interpolation of $f_\beta = \delta_{\alpha\beta}$. This can be applied two times if the function depends on two variables $f(x, y) \backsimeq \sum_\alpha f(x, y_\alpha)\, p_\alpha(y) = \sum_\alpha f_\alpha(x)\, p_\alpha(y) \backsimeq \sum_{\alpha,\beta} f_\alpha(x_\beta)\, p_\alpha(y)\, p_\beta(x) = \sum_{\alpha,\beta} f_{\alpha\beta}\, p_\alpha(y)\, p_\beta(x)$. The functions $p_\alpha(x)$ are independent of the function $f(x)$ but depend on the interpolation scheme and the set of points x_α. In Equation B.3 we have interpolated a function of

three variables using two of them. According to [115] the interpolation points q_α should be chosen appropriate for the third variable r_{12}.

Due to the shape of $\phi(q_\alpha, q_\beta, r_{12})$ a logarithmic mesh for the interpolation points q_α is proposed:

$$(q_{\alpha+1} - q_\alpha) = \lambda\,(q_\alpha - q_{\alpha-1}) \tag{B.4}$$

$\lambda > 1$ (i.e. $\lambda = 1.2$) is a scaling factor for the mesh. The authors state that $N_\alpha = 20$ interpolation points is enough for proper description of ϕ up to a cut off radius $q_c = 5$ a.u.. Higher q values result from high electron densities which can occur in the core regions but there the non local contribution to E_{xc} is negligible compared to the other contributions. Due to this the function $q_0\,(n, \nabla n)$ will be artificially saturated.

$$q_0^{\mathrm{sat}}\,(n, \nabla n) = h\,[q_0\,(n, \nabla n)\,, q_c] = q_c \left[1 - \exp\left(-\sum_{m=1}^{m_c} \frac{(q/q_c)^m}{m}\right)\right] \tag{B.5}$$

Another technical detail is the logarithmic divergence of $\phi(d_1, d_2)$ for $d_1, d_2 \to 0$ which prevents a straightforward interpolation of the function. For this reason the kernel is softened for small values of d by the formula:

$$\phi_s(d_1, d_2) = \begin{cases} \phi_0 + \phi_2 d^2 + \phi_4 d^4 & \text{if } d < d_s \\ \phi(d_1, d_2) & \text{otherwise.} \end{cases} \tag{B.6}$$

The parameters d_s and ϕ_0 have to be chosen carefully. ϕ_2 and ϕ_4 are used to match the kernel ϕ and the softened kernel ϕ_s in value and slope at d_s. This softening of the kernel leads to an artificial error in the non local energy $E_{\mathrm{c}}^{\mathrm{NL}}$. This is corrected by a local density approximation

$$\Delta E_{\mathrm{c}}^{\mathrm{NL}} = \int n(\mathbf{r}) \Delta\epsilon_{\mathrm{c}}^{\mathrm{NL}}(\mathbf{r}) \mathrm{d}^3\mathbf{r} \tag{B.7}$$

$$\Delta\epsilon_{\mathrm{c}}^{\mathrm{NL}}(\mathbf{r}) = \frac{n(\mathbf{r})}{2} \int_0^\infty 4\pi r'^2 \left[\phi(q, q, r') - \phi_s(q, q, r')\right] \mathrm{d}r' \tag{B.8}$$

where $q = q_0\,[n(\mathbf{r}), \nabla n(\mathbf{r})]$. This correction is calculated by using a method to efficiently evaluate xc-energy and potential on a real-space grid developed by Balbás *et al.* [261] and will be described in a later section.

After this technical paragraph considering the interpolation and some details about the evaluation of the kernel we can return to the initial problem of decomposing the kernel. For this we plug in the interpolated kernel from Equation B.3 into Equation B.1:

$$E_{\mathrm{c}}^{\mathrm{NL}}\,[n] = \frac{1}{2} \sum_{\alpha,\beta} \iint n(\mathbf{r_1})\, p_\alpha(q_1)\, n(\mathbf{r_2})\, p_\beta(q_2)\, \phi_{\alpha\beta}(r_{12})\, \mathrm{d}^3\mathbf{r_1}\, \mathrm{d}^3\mathbf{r_2} \tag{B.9}$$

$$= \frac{1}{2} \sum_{\alpha,\beta} \iint \Theta_\alpha(\mathbf{r_1})\, \Theta_\beta(\mathbf{r_2})\, \phi_{\alpha\beta}(r_{12})\, \mathrm{d}^3\mathbf{r_1}\, \mathrm{d}^3\mathbf{r_2} \tag{B.10}$$

Finally by using Fourier transformation we can eliminate one of the two integrals. For this we define forward Fourier transform as

$$f(\mathbf{k}) = \int \mathrm{d}^3\mathbf{r}\, f(\mathbf{r}) e^{-i\,\mathbf{k}\cdot\mathbf{r}} \tag{B.11}$$

and the convolution $(f * g)(x)$ of two functions f and g as

$$(f * g)(x) = \int \mathrm{d}y\, f(y)\, g(x-y) \tag{B.12}$$

The integral over $\mathbf{r_2}$ in Equation B.10 can be identified as a convolution which leads to

$$E_\mathrm{c}^\mathrm{NL}[n] = \sum_{\alpha,\beta} \int \Theta_\alpha(\mathbf{r_1})\,(\Theta_\beta * \phi_{\alpha\beta})(\mathbf{r_1})\,\mathrm{d}^3\mathbf{r_1} \tag{B.13}$$

Now we express $\Theta_\alpha(\mathbf{r_1})$ and $(\Theta_\beta * \phi_{\alpha\beta})(\mathbf{r_1})$ by their Fourier transforms $\Theta_\alpha(\mathbf{k_1})$ and $\Theta_\beta(\mathbf{k_2})\,\phi_{\alpha\beta}(\mathbf{k_2})$ by using the convolution theorem for Fourier transforms.

$$E_\mathrm{c}^\mathrm{NL}[n] = \sum_{\alpha,\beta} \int \Theta_\alpha(\mathbf{k_1})\,\Theta_\beta(\mathbf{k_2})\,\phi_{\alpha\beta}(\mathbf{k_2})\, e^{-i\,\mathbf{r_1}\cdot(\mathbf{k_1}+\mathbf{k_2})}\,\mathrm{d}^3\mathbf{r_1}\,\mathrm{d}^3\mathbf{k_1}\,\mathrm{d}^3\mathbf{k_2} \tag{B.14}$$

$$= \sum_{\alpha,\beta} \int \Theta_\alpha(\mathbf{k_1})\,\Theta_\beta(\mathbf{k_2})\,\phi_{\alpha\beta}(\mathbf{k_2})\,\delta(\mathbf{k_1}+\mathbf{k_2})\,\mathrm{d}^3\mathbf{k_1}\,\mathrm{d}^3\mathbf{k_2} \tag{B.15}$$

where we have used one of the representations of the δ-function i.e. $\delta(\mathbf{k}) = \int \mathrm{d}^3\mathbf{r}\, e^{-i\mathbf{r}\cdot\mathbf{k}}$. By the δ-function we can eliminate the $\mathbf{k_1}$-integration. Renaming of the variables and $\Theta_\alpha(-\mathbf{k}) = \Theta_\alpha^*(\mathbf{k})$ for every real function $\Theta_\alpha(\mathbf{r})$ finally leads to the expression for the non local correlation energy from [115]:

$$E_\mathrm{c}^\mathrm{NL}[n] = \frac{1}{2}\sum_{\alpha,\beta} \int \Theta_\alpha^*(\mathbf{k})\,\Theta_\beta(\mathbf{k})\,\phi_{\alpha\beta}(k)\,\mathrm{d}^3\mathbf{k} \tag{B.16}$$

In order to get the non local correlation contribution to E_{xc} we now have to Fourier transform several quantities and do one integration in reciprocal space. This is significantly faster than directly evaluating Equation 3.16 in real space.

B.2. Adjustments of the VV10 functional

As it has been reported by R. Sabatini et al. [116] the Soler scheme cannot be directly applied to the VV10 functional due to the definition of g in the kernel where one cannot separate the dependence on the two spatial coordinates and the distance in order to expand the kernel in those spatial coordinates which is necessary for the trick with the Fourier transform to work. The authors of et al. [116] did some modifications to the

VV10 kernel in order to fix this problem. The authors rewrote the VV10 kernel given in Equation A.94 by introducing $z(\mathbf{r}) = \frac{\omega_0(\mathbf{r})}{\kappa(\mathbf{r})}R^2 + 1$ such that $g(\mathbf{r}) = z(\mathbf{r})/\kappa(\mathbf{r})$. This leads to

$$\phi^{\mathrm{VV10}}(\mathbf{r},\mathbf{r}') = -\frac{3}{2}\frac{1}{\kappa(\mathbf{r})^{\frac{3}{2}}\kappa(\mathbf{r}')^{\frac{3}{2}}}\frac{1}{z(\mathbf{r})z(\mathbf{r}')\left(\sqrt{\frac{\kappa(\mathbf{r})}{\kappa(\mathbf{r}')}}z(\mathbf{r}) + \sqrt{\frac{\kappa(\mathbf{r}')}{\kappa(\mathbf{r})}}z(\mathbf{r}')\right)}. \tag{B.17}$$

The only term left to prevent the kernel from the expansion following the Soler scheme is $\frac{\kappa(\mathbf{r})}{\kappa(\mathbf{r}')}$. R. Sabatini *et al.* analyzed this term for the S22 test set and showed that $\frac{\kappa(\mathbf{r})}{\kappa(\mathbf{r}')} \approx 1$ for a large range of distances R. It is thus valid to neglect these factors and rewrite the kernel in the form:

$$\phi^{\mathrm{VV10}}(\mathbf{r},\mathbf{r}') - \frac{3}{2}\frac{\kappa(\mathbf{r})^{-\frac{3}{2}}\kappa(\mathbf{r}')^{-\frac{3}{2}}}{(q(\mathbf{r})R^2+1)(q(\mathbf{r}')R^2+1)(q(\mathbf{r})R^2+q(\mathbf{r}')R^2+2)}, \tag{B.18}$$

where $q(\mathbf{r}) = \omega_0(\mathbf{r})/\kappa(\mathbf{r}')$. The factors $\kappa(\mathbf{r})^{-\frac{3}{2}}$ will be absorbed in the charge densities and the rest of the kernel can be expanded in q_α as described in the last sections.

With this we can use the implementation of the Soler scheme with only a few small modifications. Namely the calculation of q_0 has to be adjusted, Θ has to be scaled by $1/\kappa^{3/2}$ and a different kernel file which fits to the changed values of q_0 has to be precalculated.

B.3. The potential $v_{\mathrm{c}}^{\mathrm{nl}}$

In order to get a self consistent implementation of vdW-DF we also need the non local contribution to the potential which is the functional derivative of $E_{\mathrm{c}}^{\mathrm{nl}}$ with respect to the density $n(\mathbf{r})$:

$$v_{\mathrm{c}}^{\mathrm{nl}} = \frac{\delta E_{\mathrm{c}}^{\mathrm{nl}}}{\delta n(\mathbf{r})} = \frac{\partial f}{\partial n(\mathbf{r})} - \nabla\cdot\frac{\partial f}{\partial \nabla n(\mathbf{r})} \tag{B.19}$$

where f is defined by $E_{\mathrm{c}}^{\mathrm{nl}} = \int f(n(\mathbf{r}),\nabla n(\mathbf{r}))\,\mathrm{d}^3\mathbf{r}$. In [115] a method applying finite differences to calculate the potential has been proposed. We will follow another approach from White and Bird [262] which is based on FFT.

On a grid with N points the formula for the potential reads:

$$\tilde{v}_{\mathrm{c}}^{\mathrm{nl}}(\mathbf{r}) = \frac{\partial f}{\partial n(\mathbf{r})} - \frac{1}{N}\sum_{\mathbf{G},\mathbf{r}'} i\mathbf{G}\cdot\frac{\nabla n(\mathbf{r}')}{|\nabla n(\mathbf{r}')|}\frac{\partial f}{\partial\,|\nabla n(\mathbf{r}')|}\,e^{i\mathbf{G}(\mathbf{r}-\mathbf{r}')} \tag{B.20}$$

where $\mathbf{r},\mathbf{r}'$ are lattice vectors and $\mathbf{G}$ is a reciprocal lattice vector. The two sums over (G) and $\mathbf{r}'$ together with the exponential $e^{i\mathbf{G}(\mathbf{r}-\mathbf{r}')}$ corresponds to a discrete forward FFT and a discrete backward FFT respectively which we additionally have to perform in order to

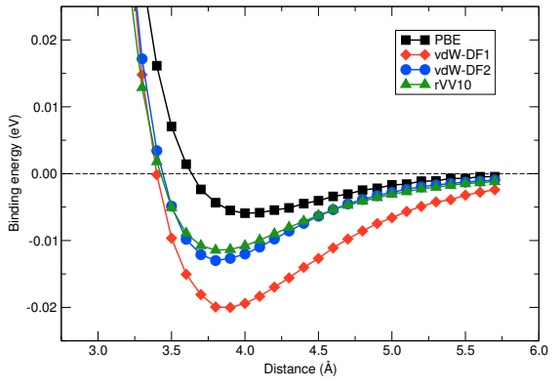

Figure B.1.: Binding energy of an Ar dimer with the PBE, vdW-DF1, vdW-DF2 and the rVV10 functional implemented selfconsistently in the JuRS code.

calculate the potential. Inserting $f = \frac{1}{2}\sum_{\alpha,\beta}\int \mathrm{d}^3\mathbf{r}''\,\Theta_\alpha(\mathbf{r})\,\Theta_\beta(\mathbf{r}'')\,\phi_{\alpha\beta}(\mathbf{r}-\mathbf{r}'')$ leads to:

$$\tilde{v}_\mathrm{c}^\mathrm{nl}(\mathbf{r}) = \frac{1}{2}\sum_\alpha \left(u_\alpha(\mathbf{r})\,\frac{\partial\Theta_\alpha(\mathbf{r})}{\partial n(\mathbf{r})} - \frac{1}{N}\sum_{\mathbf{G},\mathbf{r}'} i\mathbf{G}\,\frac{\nabla n(\mathbf{r}')}{|\nabla n(\mathbf{r}')|}\,u_\alpha(\mathbf{r}')\,\frac{\partial\Theta_\beta(\mathbf{r}')}{\partial\,|\nabla n(\mathbf{r}')|}\,e^{i\mathbf{G}(\mathbf{r}-\mathbf{r}')} \right) \quad \text{(B.21)}$$

Here $u_\alpha(\mathbf{r}) = \Delta\Omega\sum_\beta\sum_{\mathbf{r}'}\theta_\beta(\mathbf{r}')\phi_{\alpha\beta}(\mathbf{r}-\mathbf{r}')$ has been introduced as an abbreviation where $\Delta\Omega$ is the volume per grid point. This is also the convolution which one would have to evaluate to get the non local energy density.

B.4. Test calculations

In order to evaluate the quality of the results obtained with the implemented Soler scheme we did a number of test calculations. With the stand alone program as well with the self consistent implementation in juRS we have calculated interaction energy curves of an Ar dimer. The correlation binding energy density plots for three small organic molecules namely Benzene (C_6H_6), Borazine ($B_3N_3H_6$) and Triazine ($C_3N_3H_3$) adsorbed on graphene published in [263] have been calculated with the stand alone subroutines.

For the Ar dimer a -12.3 meV binding energy and a 3.757 Å equilibrium distance can be extracted from a pair interaction potential reported by R. A. Aziz [264]. This potential has been fitted to reproduce experimentally obtained ultraviolet rotation-vibration spectra. The interaction energy as a function of the distance for the Ar dimer calculated

with the PBE functional and the selfconsistent implementations of vdW-DF1, vdW-DF2 and rVV10 in the juRS are depicted in Figure B.1. The PBE functional underestimates the interaction energy with -6 meV and overestimates the equilibrium distance with 4 Å. The vdW-DF1 functional leads to a larger interaction energy of -19.9 meV and a shorter equilibrium distance of 3.85 Å but both values are still away from the experimental results. In this calculations the rVV10 yields the closest result with an interaction energy of -11.6 meV and an equilibrium distance of 3.75 Å but the vdW-DF2 functional performs only slightly worse with an adsorption energy of -13 meV and the same equilibrium distance. In the article by R. Sabatini *et al.* [116] also the Ar dimer has been studied as a test case for their implementation of the rVV10 functional. While for the rVV10 functional our interaction energy and the equilibrium distance agrees well with those published in Ref. [116], the interaction energies obtained with both vdW-DF1 and vdW-DF2 differ by 3 meV.

The adsorption energy of benzene, borazine and triazine on graphene calculated with the PBE functional is around -30 meV. The comparison with the experimental value of the adsorption energy -500 meV for a low coverage of benzene on graphite [265] shows that the PBE functional leads to a too weak binding. The adsorption energy obtained with the vdW-DF1 functional with PBE exchange is -687 meV. This value is much closer to the experiment and the reason for the large difference between the PBE value and the vdW-DF value lies in the spatial distribution of the correlation binding energy density, representing the semi-local or the non-local nature of the corresponding functional. The general shape of the correlation binding energy densities of benzene on graphene is similar for the other two molecules. The LDA correlation binding energy density follows the charge density difference, which shows no net charge transfer and only charge rearrangement. The semi-local correction to the correlation binding energy density is important only at the tails of the wavefunctions, where Pauli repulsion leads to charge rearrangement. The spatial distribution of the non-local correlation binding energy density is substantially different, which leads to the difference in the adsorption energies obtained with the semi-local PBE and the non-local vdW-DF1 functional with PBE exchange. The spatial shape of the correlation binding energy densities depends on the position of the C, B and N atoms with respect to the surface and on the chemical nature of the atoms. In the case of benzene adsorbed on graphene the correlation binding energy density shows an asymmetry depending on wether the C atom from the benzene molecule adsorbs on top of a graphene C atom or not. This asymmetry is more pronounced when a more electronegative atom i.e. B is involved.

Bibliography

[1] F. Chen, J. Hihath, Z. Huang, X. Li, and N. Tao, *Measurement of single-molecule conductance* Annual Review of Physical Chemistry **58**, 535 (2007).

[2] J. C. Cuevas and E. Scheer, *Molecular Electronics: An Introduction to Theory and Experiment* (World Scientific Publishing, Singapore, 2010), ISBN 978-981-4282-58-1.

[3] J. R. Heath and M. A. Ratner, *Molecular electronics* Physics Today **56**, 43 (2003).

[4] N. Robertson and C. A. McGowan, *A comparison of potential molecular wires as components for molecular electronics* Chem. Soc. Rev. **32**, 96 (2003).

[5] L. D. A. Siebbeles and F. C. Grozema, *Charge and Exciton transport through molecular wires* (Wiley-VCH, Weinheim, 2011), ISBN 978-3-527-32501-6.

[6] M. Ratner, *A brief history of molecular electronics* Nat. Nano. **8**, 378 (2013).

[7] S. Sanvito, *Molecular spintronics* Chem. Soc. Rev. **40**, 3336 (2011).

[8] L. Bogani and W. Wernsdorfer, *Molecular spintronics using single-molecule magnets* Nature Materials **7**, 179 (2008).

[9] M. Shiraishi and T. Ikoma, *Molecular spintronics* Physica E: Low-dimensional Systems and Nanostructures **43**, 1295 (2011).

[10] A. R. Rocha, V. M. Garcia-suarez, S. W. Bailey, C. J. Lambert, J. Ferrer, and S. Sanvito, *Towards molecular spintronics* Nat. Mater. **4**, 335 (2005).

[11] W. J. M. Naber, S. Faez, and W. G. van der Wiel, *Organic spintronics* Journal of Physics D: Applied Physics **40**, R205 (2007).

[12] M. H. Pilkuhn, *Molecular electronics: Beyond the limits of conventional electronics* International Journal of Polymeric Materials **44**, 305 (1999).

[13] D. D. Awschalom and M. E. Flatte, *Challenges for semiconductor spintronics* Nature Physics **3**, 153 (2007).

[14] K. V. Raman, A. M. Kamerbeek, A. Mukherjee, N. Atodiresei, T. K. Sen, P. Lazic, V. Caciuc, R. Michel, D. Stalke, S. K. Mandal, et al., *Interface-engineered templates for molecular spin memory devices* Nature **493**, 509 (2013).

[15] M. Callsen, V. Caciuc, N. Kiselev, N. Atodiresei, and S. Blügel, *Magnetic hardening induced by nonmagnetic organic molecules* Phys. Rev. Lett. **111**, 106805 (2013).

[16] M. Callsen, N. Atodiresei, V. Caciuc, and S. Blügel, *Semiempirical van der waals interactions versus ab initio nonlocal correlation effects in the thiophene-cu(111) system* Phys. Rev. B **86**, 085439 (2012).

[17] H. Harutyunyan, M. Callsen, T. Allmers, V. Caciuc, S. Blügel, N. Atodiresei, and D. Wegner, *Hybridisation at the organic-metal interface: a surface-scientific analogue of hückel's rule?* Chem. Commun. **49**, 5993 (2013).

[18] S. Grimme, *Semiempirical GGA-type density functional constructed with a long-range dispersion correction* Journal of Computational Chemistry **27**, 1787 (2006).

[19] M. Dion, H. Rydberg, E. Schröder, D. C. Langreth, and B. I. Lundqvist, *Van der waals density functional for general geometries* Phys. Rev. Lett. **92**, 246401 (2004).

[20] A. Aviram and M. A. Ratner, *Molecular rectifiers* Chemical Physics Letters **29**, 277 (1974).

[21] G. J. Ashwell, J. R. Sambles, A. S. Martin, W. G. Parker, and M. Szablewski, *Rectifying characteristics of mg/(c16h33-q3cnq lb film)/pt structures* J. Chem. Soc., Chem. Commun. pp. 1374–1376 (1990).

[22] A. S. Martin, J. R. Sambles, and G. J. Ashwell, *Molecular rectifier* Phys. Rev. Lett. **70**, 218 (1993).

[23] R. M. Metzger, B. Chen, U. Höpfner, M. V. Lakshmikantham, D. Vuillaume, T. Kawai, X. Wu, H. Tachibana, T. V. Hughes, H. Sakurai, et al., *Unimolecular electrical rectification in hexadecylquinolinium tricyanoquinodimethanide* Journal of the American Chemical Society **119**, 10455 (1997).

[24] R. M. Metzger, *Electrical rectification by a molecule: the advent of unimolecular electronic devices* Accounts of Chemical Research **32**, 950 (1999).

[25] R. M. Metzger, J. W. Baldwin, W. J. Shumate, I. R. Peterson, P. Mani, G. J. Mankey, T. Morris, G. Szulczewski, S. Bosi, M. Prato, et al., *Electrical rectification in a langmuir−blodgett monolayer of dimethyanilinoazafullerene sandwiched between gold electrodes* The Journal of Physical Chemistry B **107**, 1021 (2003).

[26] K. B. Blodgett, *Films built by depositing successive monomolecular layers on a solid surface* Journal of the American Chemical Society **57**, 1007 (1935).

[27] I. I. Oleynik, M. A. Kozhushner, V. S. Posvyanskii, and L. Yu, *Rectification mechanism in diblock oligomer molecular diodes* Phys. Rev. Lett. **96**, 096803 (2006).

[28] T. Kudernac, N. Katsonis, W. R. Browne, and B. L. Feringa, *Nano-electronic switches: Light-induced switching of the conductance of molecular systems* J. Mater. Chem. **19**, 7168 (2009).

[29] D. Dulić, S. J. van der Molen, T. Kudernac, H. T. Jonkman, J. J. D. de Jong, T. N. Bowden, J. van Esch, B. L. Feringa, and B. J. van Wees, *One-way optoelectronic switching of photochromic molecules on gold* Phys. Rev. Lett. **91**, 207402 (2003).

[30] B.-Y. Choi, S.-J. Kahng, S. Kim, H. Kim, H. W. Kim, Y. J. Song, J. Ihm, and Y. Kuk, *Conformational molecular switch of the azobenzene molecule: A scanning tunneling microscopy study* Phys. Rev. Lett. **96**, 156106 (2006).

[31] Y. Wang, J. Kröger, R. Berndt, and W. A. Hofer, *Pushing and pulling a sn ion through an adsorbed phthalocyanine molecule* Journal of the American Chemical Society **131**, 3639 (2009).

[32] A. Aviram, *Molecules for memory, logic, and amplification* Journal of the American Chemical Society **110**, 5687 (1988).

[33] S. J. Tans, A. R. M. Verschueren, and C. Dekker, *Room-temperature transistor based on a single carbon nanotube* Nature **393**, 49 (1998).

[34] H. Song, Y. Kim, Y. H. Jang, H. Jeong, M. A. Reed, and T. Lee, *Observation of molecular orbital gating* Nature **462**, 1039 (2009).

[35] M. M. Shulaker, G. Hills, N. Patil, H. Wei, H.-Y. Chen, H.-S. P. Wong, and S. Mitra, *Carbon nanotube computer* Nature **501**, 526 (2013).

[36] B. Xu and N. J. Tao, *Measurement of single-molecule resistance by repeated formation of molecular junctions* Science **301**, 1221 (2003).

[37] S. Ho Choi, B. Kim, and C. D. Frisbie, *Electrical resistance of long conjugated molecular wires* Science **320**, 1482 (2008).

[38] N. Hamada, S.-i. Sawada, and A. Oshiyama, *New one-dimensional conductors: Graphitic microtubules* Phys. Rev. Lett. **68**, 1579 (1992).

[39] S. J. Tans, M. H. Devoret, H. Dai, A. Thess, R. E. Smalley, L. J. Geerligs, and C. Dekker, *Individual single-wall carbon nanotubes as quantum wires* Nature **386**, 474 (1997).

[40] H. L. Anderson, *Building molecular wires from the colours of life: conjugated porphyrin oligomers* Chem. Commun. pp. 2323–2330 (1999).

[41] D. Kim and A. Osuka, *Directly linked porphyrin arrays with tunable excitonic interactions* Accounts of Chemical Research **37**, 735 (2004).

[42] H. Ishii, K. Sugiyama, E. Ito, and K. Seki, *Energy level alignment and interfacial electronic structures at organic/metal and organic/organic interfaces* Advanced Materials **11**, 605 (1999).

[43] T. R. Ohno, Y. Chen, S. E. Harvey, G. H. Kroll, J. H. Weaver, R. E. Haufler, and R. E. Smalley, c_{60} *bonding and energy-level alignment on metal and semiconductor surfaces* Phys. Rev. B **44**, 13747 (1991).

[44] J. B. Neaton, M. S. Hybertsen, and S. G. Louie, *Renormalization of molecular electronic levels at metal-molecule interfaces* Phys. Rev. Lett. **97**, 216405 (2006).

[45] J. M. Garcia-Lastra, C. Rostgaard, A. Rubio, and K. S. Thygesen, *Polarization-induced renormalization of molecular levels at metallic and semiconducting surfaces* Phys. Rev. B **80**, 245427 (2009).

[46] D. C. Langreth, B. I. Lundqvist, S. D. Chakarova-Käck, V. R. Cooper, M. Dion, P. Hyldgaard, A. Kelkkanen, J. Kleis, L. Kong, S. Li, et al., *A density functional for sparse matter* Journal of Physics: Condensed Matter **21**, 084203 (2009).

[47] D. Loffreda, D. Simon, and P. Sautet, *Molecular and dissociative chemisorption of no on palladium and rhodium (100) and (111) surfaces: A density-functional periodic study* The Journal of Chemical Physics **108**, 6447 (1998).

[48] C. Morin, A. Eichler, R. Hirschl, P. Sautet, and J. Hafner, *Dft study of adsorption and dissociation of thiophene molecules on ni(1 1 0)* Surface Science **540**, 474 (2003).

[49] N. Atodiresei, J. Brede, P. Lazić, V. Caciuc, G. Hoffmann, R. Wiesendanger, and S. Blügel, *Design of the local spin polarization at the organic-ferromagnetic interface* Phys. Rev. Lett. **105**, 066601 (2010).

[50] M. C. Lennartz, V. Caciuc, N. Atodiresei, S. Karthäuser, and S. Blügel, *Electronic mapping of molecular orbitals at the molecule-metal interface* Phys. Rev. Lett. **105**, 066801 (2010).

[51] M. Jullière, *Tunneling between ferromagnetic films* Physics Letters A **54**, 225 (1975).

[52] G. Binasch, P. Grünberg, F. Saurenbach, and W. Zinn, *Enhanced magnetoresistance in layered magnetic structures with antiferromagnetic interlayer exchange* Phys. Rev. B **39**, 4828 (1989).

[53] M. N. Baibich, J. M. Broto, A. Fert, F. N. Van Dau, F. Petroff, P. Etienne, G. Creuzet, A. Friederich, and J. Chazelas, *Giant magnetoresistance of (001)fe/(001)cr magnetic superlattices* Phys. Rev. Lett. **61**, 2472 (1988).

[54] N. F. Mott, *The electrical conductivity of transition metals* Proceedings of the Royal Society of London. Series A - Mathematical and Physical Sciences **153**, 699 (1936).

[55] T. S. Santos, J. S. Lee, P. Migdal, I. C. Lekshmi, B. Satpati, and J. S. Moodera, *Room-temperature tunnel magnetoresistance and spin-polarized tunneling through an organic semiconductor barrier* Phys. Rev. Lett. **98**, 016601 (2007).

[56] B. N. Limketkai, P. Jadhav, and M. A. Baldo, *Electric-field-dependent percolation model of charge-carrier mobility in amorphousorganic semiconductors* Phys. Rev. B **75**, 113203 (2007).

[57] A. N. Pasupathy, R. C. Bialczak, J. Martinek, J. E. Grose, L. A. K. Donev, P. L. McEuen, and D. C. Ralph, *The kondo effect in the presence of ferromagnetism* Science **306**, 86 (2004).

[58] J. R. Petta, S. K. Slater, and D. C. Ralph, *Spin-dependent transport in molecular tunnel junctions* Phys. Rev. Lett. **93**, 136601 (2004).

[59] V. Dediu, M. Murgia, F. Matacotta, C. Taliani, and S. Barbanera, *Room temperature spin polarized injection in organic semiconductor* Solid State Communications **122**, 181 (2002).

[60] Z. H. Xiong, D. Wu, Z. Valy Vardeny, and J. Shi, *Giant magnetoresistance in organic spin-valves* Nature **427**, 821 (2004).

[61] D. Wu, Z. H. Xiong, X. G. Li, Z. V. Vardeny, and J. Shi, *Magnetic-field-dependent carrier injection at* $\mathrm{la_{2/3}sr_{1/3}mno_3}$*/ and organic semiconductors interfaces* Phys. Rev. Lett. **95**, 016802 (2005).

[62] T. L. Francis, O. Mermer, G. Veeraraghavan, and M. Wohlgenannt, *Large magnetoresistance at room temperature in semiconducting polymer sandwich devices* New Journal of Physics **6**, 185 (2004).

[63] G.-H. Kim and T.-S. Kim, *Electronic transport in single-molecule magnets on metallic surfaces* Phys. Rev. Lett. **92**, 137203 (2004).

[64] R. Vincent, S. Klyatskaya, M. Ruben, W. Wernsdorfer, and F. Balestro, *Electronic read-out of a single nuclear spin using a molecular spin transistor* Nature **488**, 357 (2012).

[65] S. Heinze, K. von Bergmann, M. Menzel, J. Brede, A. Kubetzka, R. Wiesendanger, G. Bihlmayer, and S. Blügel, *Spontaneous atomic-scale magnetic skyrmion lattice in two dimensions* Nat. Phys. **7**, 713 (2011).

[66] S. Blügel, *Magnetische anisotropie und magnetostriktion*, Lecture notes, http://www.fz-juelich.de/SharedDocs/Downloads/PGI/PGI-1/DE/mca_pdf.pdf (2010).

[67] R. Skomski, *Simple models of magnetism*, Oxford Graduate Texts (Oxford Univ. Press, Oxford, 2008).

[68] W. Heisenberg, *Zur theorie des ferromagnetismus* Zeitschrift für Physik **49**, 619 (1928).

[69] N. Akulov, *Über das magnetische quadrupolmoment des eisenatoms* Zeitschrift für Physik **57**, 249 (1929).

[70] M. Born and R. Oppenheimer, *Zur quantentheorie der molekeln* Annalen der Physik **389**, 457 (1927).

[71] I. Shavitt, *The history and evolution of configuration interaction* Molecular Physics **94**, 3 (1998).

[72] R. J. Needs, M. D. Towler, N. D. Drummond, and P. L. Ríos, *Continuum variational and diffusion quantum monte carlo calculations* Journal of Physics: Condensed Matter **22**, 023201 (2010).

[73] D. M. Ceperley, *Path integrals in the theory of condensed helium* Rev. Mod. Phys. **67**, 279 (1995).

[74] A. L. Fetter and J. D. Walecka, *Quantum Theory of Many-Particle-Systems* (Dover Publications, 2003).

[75] P. Hohenberg and W. Kohn, *Inhomogeneous electron gas* Phys. Rev. **136**, B864 (1964).

[76] W. Kohn and L. J. Sham, *Self-consistent equations including exchange and correlation effects* Phys. Rev. **140**, A1133 (1965).

[77] G. Kresse and J. Furthmüller, *Efficient iterative schemes for ab initio total-energy calculations using a plane-wave basis set* Phys. Rev. B **54**, 11169 (1996).

[78] G. Kresse and J. Furthmüller, *Efficiency of ab-initio total energy calculations for metals and semiconductors using a plane-wave basis set* Computational Materials Science **6**, 15 (1996).

[79] G. Kresse and J. Hafner, *Ab initio molecular dynamics for liquid metals* Phys. Rev. B **47**, 558 (1993).

[80] E. Runge and E. K. U. Gross, *Density-functional theory for time-dependent systems* Phys. Rev. Lett. **52**, 997 (1984).

[81] U. von Barth and L. Hedin, *A local exchange-correlation potential for the spin polarized case. i* Journal of Physics C: Solid State Physics **5**, 1629 (1972).

[82] C. Fiolhais, F. Nogueira, and M. Marques, *A Primer in density functional theory* (Springer, Berlin [etc.], 2003), ISBN 3540030832 9783540030836.

[83] A. H. MacDonald and S. H. Vosko, *A relativistic density functional formalism* Journal of Physics C: Solid State Physics **12**, 2977 (1979).

[84] P. Blonski, S. Dennler, and J. Hafner, *Strong spin–orbit effects in small pt clusters: Geometric structure, magnetic isomers and anisotropy* The Journal of Chemical Physics **134**, 034107 (pages 12) (2011).

[85] D. M. Ceperley and B. J. Alder, *Ground state of the electron gas by a stochastic method* Phys. Rev. Lett. **45**, 566 (1980).

[86] J. P. Perdew and A. Zunger, *Self-interaction correction to density-functional approximations for many-electron systems* Phys. Rev. B **23**, 5048 (1981).

[87] V. N. Staroverov, G. E. Scuseria, J. Tao, and J. P. Perdew, *Tests of a ladder of density functionals for bulk solids and surfaces* Phys. Rev. B **69**, 075102 (2004).

[88] P. Bagno, O. Jepsen, and O. Gunnarsson, *Ground-state properties of third-row elements with nonlocal density functionals* Phys. Rev. B **40**, 1997 (1989).

[89] J. P. Perdew, J. A. Chevary, S. H. Vosko, K. A. Jackson, M. R. Pederson, D. J. Singh, and C. Fiolhais, *Atoms, molecules, solids, and surfaces: Applications of the generalized gradient approximation for exchange and correlation* Phys. Rev. B **46**, 6671 (1992).

[90] J. P. Perdew, K. Burke, and M. Ernzerhof, *Generalized gradient approximation made simple* Phys. Rev. Lett. **77**, 3865 (1996).

[91] J. P. Perdew, A. Ruzsinszky, J. Tao, V. N. Staroverov, G. E. Scuseria, and G. I. Csonka, *Prescription for the design and selection of density functional approximations: More constraint satisfaction with fewer fits* The Journal of Chemical Physics **123**, 062201 (pages 9) (2005).

[92] Y. Zhang and W. Yang, *Comment on "generalized gradient approximation made simple"* Phys. Rev. Lett. **80**, 890 (1998).

[93] S. Kurth, J. P. Perdew, and P. Blaha, *Molecular and solid-state tests of density functional approximations: Lsd, ggas, and meta-ggas* International Journal of Quantum Chemistry **75**, 889 (1999).

[94] J. P. Perdew, A. Ruzsinszky, G. I. Csonka, O. A. Vydrov, G. E. Scuseria, L. A. Constantin, X. Zhou, and K. Burke, *Restoring the density-gradient expansion for exchange in solids and surfaces* Phys. Rev. Lett. **100**, 136406 (2008).

[95] J. P. Perdew, A. Ruzsinszky, G. I. Csonka, L. A. Constantin, and J. Sun, *Workhorse semilocal density functional for condensed matter physics and quantum chemistry* Phys. Rev. Lett. **103**, 026403 (2009).

[96] A. D. Becke, *A new mixing of hartree–fock and local density-functional theories* The Journal of Chemical Physics **98**, 1372 (1993).

[97] P. J. Stephens, F. J. Devlin, C. F. Chabalowski, and M. J. Frisch, *Ab initio calculation of vibrational absorption and circular dichroism spectra using density functional force fields* The Journal of Physical Chemistry **98**, 11623 (1994).

[98] J. Heyd, G. E. Scuseria, and M. Ernzerhof, *Hybrid functionals based on a screened coulomb potential* The Journal of Chemical Physics **118**, 8207 (2003).

[99] C. Adamo and V. Barone, *Toward reliable density functional methods without adjustable parameters: The pbe0 model* The Journal of Chemical Physics **110**, 6158 (1999).

[100] P. Lazić, M. Alaei, N. Atodiresei, V. Caciuc, R. Brako, and S. Blügel, *Density functional theory with nonlocal correlation: A key to the solution of the co adsorption puzzle* Phys. Rev. B **81**, 045401 (2010).

[101] J. Tao, J. P. Perdew, V. N. Staroverov, and G. E. Scuseria, *Climbing the density functional ladder: Nonempirical meta–generalized gradient approximation designed for molecules and solids* Phys. Rev. Lett. **91**, 146401 (2003).

[102] L. Ferrighi, G. K. H. Madsen, and B. Hammer, *Self-consistent meta-generalized gradient approximation study of adsorption of aromatic molecules on noble metal surfaces* The Journal of Chemical Physics **135**, 084704 (pages 7) (2011).

[103] Y. Zhao and D. G. Truhlar, *A new local density functional for main-group thermochemistry, transition metal bonding, thermochemical kinetics, and noncovalent interactions* The Journal of Chemical Physics **125**, 194101 (pages 18) (2006).

[104] J. P. Perdew and K. Schmidt, *Jacob's ladder of density functional approximations for the exchange-correlation energy* AIP Conference Proceedings **577**, 1 (2001).

[105] J. P. Perdew, V. N. Staroverov, J. Tao, and G. E. Scuseria, *Density functional with full exact exchange, balanced nonlocality of correlation, and constraint satisfaction* Phys. Rev. A **78**, 052513 (2008).

[106] D. Langreth and J. Perdew, *The exchange-correlation energy of a metallic surface* Solid State Communications **17**, 1425 (1975).

[107] D. C. Langreth and J. P. Perdew, *Exchange-correlation energy of a metallic surface: Wave-vector analysis* Phys. Rev. B **15**, 2884 (1977).

[108] O. Gunnarsson and B. I. Lundqvist, *Exchange and correlation in atoms, molecules, and solids by the spin-density-functional formalism* Phys. Rev. B **13**, 4274 (1976).

[109] H.-V. Nguyen and G. Galli, *A first-principles study of weakly bound molecules using exact exchange and the random phase approximation* The Journal of Chemical Physics **132**, 044109 (pages 8) (2010).

[110] J. Harl and G. Kresse, *Cohesive energy curves for noble gas solids calculated by adiabatic connection fluctuation-dissipation theory* Phys. Rev. B **77**, 045136 (2008).

[111] J. Harl and G. Kresse, *Accurate bulk properties from approximate many-body techniques* Phys. Rev. Lett. **103**, 056401 (2009).

[112] J. Paier, X. Ren, P. Rinke, G. E. Scuseria, A. Grüneis, G. Kresse, and M. Scheffler, *Assessment of correlation energies based on the random-phase approximation* New Journal of Physics **14**, 043002 (2012).

[113] J. Hafner, *Ab-initio simulations of materials using vasp: Density-functional theory and beyond* Journal of Computational Chemistry **29**, 2044 (2008).

[114] P. Lazić, N. Atodiresei, M. Alaei, V. Caciuc, S. Blügel, and R. Brako, *Junolo - jülich nonlocal code for parallel post-processing evaluation of vdw-df correlation energy* Computer Physics Communications **181**, 371 (2010).

[115] G. Román-Pérez and J. M. Soler, *Efficient implementation of a van der waals density functional: Application to double-wall carbon nanotubes* Phys. Rev. Lett. **103**, 096102 (2009).

[116] R. Sabatini, T. Gorni, and S. de Gironcoli, *Nonlocal van der waals density functional made simple and efficient* Phys. Rev. B **87**, 041108 (2013).

[117] H. J. Monkhorst and J. D. Pack, *Special points for brillouin-zone integrations* Phys. Rev. B **13**, 5188 (1976).

[118] P. E. Blöchl, *Projector augmented-wave method* Phys. Rev. B **50**, 17953 (1994).

[119] G. Kresse and D. Joubert, *From ultrasoft pseudopotentials to the projector augmented-wave method* Phys. Rev. B **59**, 1758 (1999).

[120] A. D. Mcnaught and A. Wilkinson, *IUPAC. Compendium of Chemical Terminology, 2nd ed. (the "Gold Book").* (WileyBlackwell; 2nd Revised edition edition, 1997), ISBN 978-0865426849.

[121] R. Eisenschitz and F. London, *Über das verhältnis der van der waalsschen kräfte zu den homöopolaren bindungskräften* Zeitschrift für Physik **60**, 491 (1930).

[122] F. London, *Zur theorie und systematik der molekularkräfte* Zeitschrift für Physik **63**, 245 (1930).

[123] H. B. G. Casimir and D. Polder, *The influence of retardation on the london-van der waals forces* Phys. Rev. **73**, 360 (1948).

[124] S. Y. Buhmann, *Dispersion Forces I*, vol. 247 of *Springer tracts in modern physics* (Springer, Berlin, 2012), ISBN 978-3-642-32483-3.

[125] T. Björkman, A. Gulans, A. V. Krasheninnikov, and R. M. Nieminen, *Are we van der waals ready?* Journal of Physics: Condensed Matter **24**, 424218 (2012).

[126] J. Klimeš and A. Michaelides, *Perspective: Advances and challenges in treating van der waals dispersion forces in density functional theory* The Journal of Chemical Physics **137**, 120901 (pages 12) (2012).

[127] C. Kittel, *Introduction to Solid State Physics* (John Wiley & Sons, Inc., New York, 2004), 8th ed.

[128] C. Mavroyannis and M. Stephen, *Dispersion forces* Molecular Physics **5**, 629 (1962).

[129] B. M. Axilrod and E. Teller, *Interaction of the van der waals type between three atoms* The Journal of Chemical Physics **11**, 299 (1943).

[130] C. Farina, F. C. Santos, and A. C. Tort, *A simple model for the nonretarded dispersive force between an electrically polarizable atom and a magnetically polarizable one* American Journal of Physics **70**, 421 (2002).

[131] G. Feinberg and J. Sucher, *General theory of the van der waals interaction: A model-independent approach* Phys. Rev. A **2**, 2395 (1970).

[132] V. N. Staroverov, G. E. Scuseria, J. Tao, and J. P. Perdew, *Comparative assessment of a new nonempirical density functional: Molecules and hydrogen-bonded complexes* The Journal of Chemical Physics **119**, 12129 (2003).

[133] M. Mura, A. Gulans, T. Thonhauser, and L. Kantorovich, *Role of van der waals interaction in forming molecule-metal junctions: flat organic molecules on the au(111) surface* Phys. Chem. Chem. Phys. **12**, 4759 (2010).

[134] F. Ortmann, F. Bechstedt, and W. G. Schmidt, *Semiempirical van der waals correction to the density functional description of solids and molecular structures* Phys. Rev. B **73**, 205101 (2006).

[135] S. Grimme, J. Antony, S. Ehrlich, and H. Krieg, *A consistent and accurate ab initio parametrization of density functional dispersion correction (dft-d) for the 94 elements h-pu* The Journal of Chemical Physics **132**, 154104 (pages 19) (2010).

[136] A. Tkatchenko and M. Scheffler, *Accurate molecular van der waals interactions from ground-state electron density and free-atom reference data* Phys. Rev. Lett. **102**, 073005 (2009).

[137] S. Grimme, S. Ehrlich, and L. Goerigk, *Effect of the damping function in dispersion corrected density functional theory* Journal of Computational Chemistry **32**, 1456 (2011).

[138] P. L. Silvestrelli, *Van der waals interactions in dft made easy by wannier functions* Phys. Rev. Lett. **100**, 053002 (2008).

[139] A. Ambrosetti and P. L. Silvestrelli, *van der waals interactions in density functional theory using wannier functions: Improved C_6 and C_3 coefficients by a different approach* Phys. Rev. B **85**, 073101 (2012).

[140] P. L. Silvestrelli and A. Ambrosetti, *Inclusion of screening effects in the van der waals corrected dft simulation of adsorption processes on metal surfaces* Phys. Rev. B **87**, 075401 (2013).

[141] W. Hujo and S. Grimme, *Comparison of the performance of dispersion-corrected density functional theory for weak hydrogen bonds* Phys. Chem. Chem. Phys. **13**, 13942 (2011).

[142] A. Tkatchenko, R. A. DiStasio, R. Car, and M. Scheffler, *Accurate and efficient method for many-body van der waals interactions* Phys. Rev. Lett. **108**, 236402 (2012).

[143] T. Bučko, S. Lebègue, J. Hafner, and J. G. Ángyán, *Tkatchenko-scheffler van der waals correction method with and without self-consistent screening applied to solids* Phys. Rev. B **87**, 064110 (2013).

[144] K. Tonigold and A. Gross, *Adsorption of small aromatic molecules on the (111) surfaces of noble metals: A density functional theory study with semiempirical corrections for dispersion effects* The Journal of Chemical Physics **132**, 224701 (pages 10) (2010).

[145] W. Hujo and S. Grimme, *Performance of non-local and atom-pairwise dispersion corrections to dft for structural parameters of molecules with noncovalent interactions* Journal of Chemical Theory and Computation **9**, 308 (2013).

[146] N. Marom, A. Tkatchenko, M. Rossi, V. V. Gobre, O. Hod, M. Scheffler, and L. Kronik, *Dispersion interactions with density-functional theory: Benchmarking semiempirical and interatomic pairwise corrected density functionals* Journal of Chemical Theory and Computation **7**, 3944 (2011).

[147] P. Jurečka, J. Šponer, J. Černý, and P. Hobza, *Benchmark database of accurate (mp2 and ccsd(t) complete basis set limit) interaction energies of small model complexes, dna base pairs, and amino acid pairs* Phys. Chem. Chem. Phys. **8**, 1985 (2006).

[148] J. Řezáč, K. E. Riley, and P. Hobza, *S66: A well-balanced database of benchmark interaction energies relevant to biomolecular structures* Journal of Chemical Theory and Computation **7**, 2427 (2011).

[149] L. Goerigk and S. Grimme, *A general database for main group thermochemistry, kinetics, and noncovalent interactions – assessment of common and reparameterized (meta-)gga density functionals* Journal of Chemical Theory and Computation **6**, 107 (2010).

[150] E. R. McNellis, J. Meyer, and K. Reuter, *Azobenzene at coinage metal surfaces: Role of dispersive van der waals interactions* Phys. Rev. B **80**, 205414 (2009).

[151] G. Mercurio, E. R. McNellis, I. Martin, S. Hagen, F. Leyssner, S. Soubatch, J. Meyer, M. Wolf, P. Tegeder, F. S. Tautz, et al., *Structure and energetics of azobenzene on ag(111): Benchmarking semiempirical dispersion correction approaches* Phys. Rev. Lett. **104**, 036102 (2010).

[152] K. Toyoda, I. Hamada, K. Lee, S. Yanagisawa, and Y. Morikawa, *Density functional theoretical study of pentacene/noble metal interfaces with van der waals corrections: Vacuum level shifts and electronic structures* The Journal of Chemical Physics **132**, 134703 (pages 9) (2010).

[153] K. Lee, K. Berland, M. Yoon, S. Andersson, E. Schröder, P. Hyldgaard, and B. I. Lundqvist, *Benchmarking van der waals density functionals with experimental data: potential-energy curves for h 2 molecules on cu(111), (100) and (110) surfaces* Journal of Physics: Condensed Matter **24**, 424213 (2012).

[154] B. I. Lundqvist, Y. Andersson, H. Shao, S. Chan, and D. C. Langreth, *Density functional theory including van der waals forces* International Journal of Quantum Chemistry **56**, 247 (1995).

[155] E. Hult, Y. Andersson, B. I. Lundqvist, and D. C. Langreth, *Density functional for van der waals forces at surfaces* Phys. Rev. Lett. **77**, 2029 (1996).

[156] H. Rydberg, B. I. Lundqvist, D. C. Langreth, and M. Dion, *Tractable nonlocal correlation density functionals for flat surfaces and slabs* Phys. Rev. B **62**, 6997 (2000).

[157] J. Wellendorff and T. Bligaard, *On the importance of gradient-corrected correlation for van der waals density functionals* Topics in Catalysis **54**, 1143 (2011).

[158] K. Lee, E. D. Murray, L. Kong, B. I. Lundqvist, and D. C. Langreth, *Higher-accuracy van der waals density functional* Phys. Rev. B **82**, 081101 (2010).

[159] J. Klimeš, D. R. Bowler, and A. Michaelides, *Chemical accuracy for the van der waals density functional* Journal of Physics: Condensed Matter **22**, 022201 (2010).

[160] V. R. Cooper, *Van der waals density functional: An appropriate exchange functional* Phys. Rev. B **81**, 161104 (2010).

[161] J. Klimeš, D. R. Bowler, and A. Michaelides, *Van der waals density functionals applied to solids* Phys. Rev. B **83**, 195131 (2011).

[162] F. Hanke, M. S. Dyer, J. Björk, and M. Persson, *Structure and stability of weakly chemisorbed ethene adsorbed on low-index cu surfaces: performance of density functionals with van der waals interactions* Journal of Physics: Condensed Matter **24**, 424217 (2012).

[163] O. A. Vydrov and T. V. Voorhis, *Nonlocal van der waals density functional: The simpler the better* The Journal of Chemical Physics **133**, 244103 (pages 9) (2010).

[164] O. Vydrov and T. Van Voorhis, *Benchmark assessment of the accuracy of several van der waals density functionals* Journal of Chemical Theory and Computation **8**, 1929 (2012).

[165] O. A. Vydrov and T. Van Voorhis, *Nonlocal van der waals density functional made simple* Phys. Rev. Lett. **103**, 063004 (2009).

[166] D. C. Langreth and B. I. Lundqvist, *Comment on "nonlocal van der waals density functional made simple"* Phys. Rev. Lett. **104**, 099303 (2010).

[167] L. Romaner, D. Nabok, P. Puschnig, E. Zojer, and C. Ambrosch-Draxl, *Theoretical study of ptcda adsorbed on the coinage metal surfaces, ag(111), au(111) and cu(111)* New Journal of Physics **11**, 053010 (2009).

[168] N. Atodiresei, V. Caciuc, P. Lazić, and S. Blügel, *Chemical versus van der waals interaction: The role of the heteroatom in the flat absorption of aromatic molecules* $\mathbf{c_6h_6}$*,* $\mathbf{c_5}\mathrm{nh_5}$*, and* $\mathbf{c_4n_2h_4}$ *on the cu(110) surface* Phys. Rev. Lett. **102**, 136809 (2009).

[169] A. Gulans, M. J. Puska, and R. M. Nieminen, *Linear-scaling self-consistent implementation of the van der waals density functional* Phys. Rev. B **79**, 201105 (2009).

[170] C. Ambrosch-Draxl, D. Nabok, P. Puschnig, and C. Meisenbichler, *The role of polymorphism in organic thin films: oligoacenes investigated from first principles* New Journal of Physics **11**, 125010 (2009).

[171] P. Sony, P. Puschnig, D. Nabok, and C. Ambrosch-Draxl, *Importance of van der waals interaction for organic molecule-metal junctions: Adsorption of thiophene on cu(110) as a prototype* Phys. Rev. Lett. **99**, 176401 (2007).

[172] M. Vanin, J. J. Mortensen, A. K. Kelkkanen, J. M. Garcia-Lastra, K. S. Thygesen, and K. W. Jacobsen, *Graphene on metals: A van der waals density functional study* Phys. Rev. B **81**, 081408 (2010).

[173] G. Li, I. Tamblyn, V. R. Cooper, H.-J. Gao, and J. B. Neaton, *Molecular adsorption on metal surfaces with van der waals density functionals* Phys. Rev. B **85**, 121409 (2012).

[174] J. Carrasco, J. Klimeš, and A. Michaelides, *The role of van der waals forces in water adsorption on metals* The Journal of Chemical Physics **138**, 024708 (pages 9) (2013).

[175] M. Obata, M. Nakamura, I. Hamada, and T. Oda, *Implementation of van der waals density functional approach to the spin-polarized system: Interaction potential between oxygen molecules* Journal of the Physical Society of Japan **82**, 093701 (2013).

[176] T. Thonhauser, V. R. Cooper, S. Li, A. Puzder, P. Hyldgaard, and D. C. Langreth, *Van der waals density functional: Self-consistent potential and the nature of the van der waals bond* Phys. Rev. B **76**, 125112 (2007).

[177] M. Frigo and S. G. Johnson, *The design and implementation of FFTW3* Proceedings of the IEEE **93**, 216 (2005).

[178] E. C. P. Smits, S. G. J. Mathijssen, P. A. van Hal, S. Setayesh, T. C. T. Geuns, K. A. H. A. Mutsaers, E. Cantatore, H. J. Wondergem, O. Werzer, R. Resel, et al., *Bottom-up organic integrated circuits* Nature **455**, 956 (2008).

[179] J. Repp, P. Liljeroth, and G. Meyer, *Coherent electron-nuclear coupling in oligothiophene molecular wires* Nature Physics **6**, 975 (2010).

[180] N. Sändig, F. Biscarini, and F. Zerbetto, *Driving force for the adsorption of sexithiophene on gold* The Journal of Physical Chemistry C **112**, 19516 (2008).

[181] F. Ercolessi, M. Parrinello, and E. Tosatti, *Simulation of gold in the glue model* Philosophical Magazine A **58**, 213 (1988).

[182] H. Orita and N. Itoh, *Adsorption of thiophene on ni(1 0 0), cu(1 0 0), and pd(1 0 0) surfaces: ab initio periodic density functional study* Surface Science **550**, 177 (2004).

[183] T. Kakudate, S. Tsukamoto, M. Nakaya, and T. Nakayama, *Initial stage of adsorption of octithiophene molecules on cu(111)* Surface Science **605**, 1021 (2011).

[184] P. Milligan, J. MNamarra, B. Murphy, B. C. C. Cowie, D. Lennon, and M. Kadodwala, *A nixsw and nexafs investigation of thiophene on cu(111)* Surface Science **412-413**, 166 (1998).

[185] P. K. Milligan, B. Murphy, D. Lennon, B. C. C. Cowie, and M. Kadodwala, *A complete structural study of the coverage dependence of the bonding of thiophene on cu(111)* The Journal of Physical Chemistry B **105**, 140 (2001).

[186] G. B. D. Rousseau, N. Bovet, S. M. Johnston, D. Lennon, V. Dhanak, and M. Kadodwala, *The structure of a coadsorbed layer of thiophene and co on cu(1 1 1)* Surface Science **511**, 190 (2002).

[187] A. Imanishi, T. Yokoyama, Y. Kitajima, and T. Ohta, *Structural and electronic properties of adsorbed thiophene on cu(111) studied by s k-edge x-ray absorption spectroscopy* Bulletin of the Chemical Society of Japan **71**, 831 (1998).

[188] M. Kofranek, T. Kovář, H. Lischka, and A. Karpfen, *Ab initio studies on heterocyclic conjugated polymers: structure and vibrational spectra of thiophene, oligothiophenes and polythiophene* Journal of Molecular Structure: Theochem **259**, 181 (1992).

[189] G. A. Diaz-Quijada, N. Weinberg, S. Holdcroft, and B. M. Pinto, *Investigation of barriers to conformational interchange in oligothiophenes and oligo(thienyl)furans* The Journal of Physical Chemistry A **106**, 1266 (2002).

[190] X. Shi, R. Q. Zhang, C. Minot, K. Hermann, M. A. Van Hove, W. Wang, and N. Lin, *Complex molecules on a flat metal surface: Large distortions induced by chemisorption can make physisorption energetically more favorable* The Journal of Physical Chemistry Letters **1**, 2974 (2010).

[191] G.-J. Su, H.-M. Zhang, L.-J. Wan, and C.-L. Bai, *Phase transition of thiophene molecules on au(1 1 1) in solution* Surface Science **531**, L363 (2003).

[192] A. Nambu, H. Kondoh, I. Nakai, K. Amemiya, and T. Ohta, *Film growth and x-ray induced chemical reactions of thiophene adsorbed on au(1 1 1)* Surface Science **530**, 101 (2003).

[193] M. May, S. Gonzalez, and F. Illas, *A systematic density functional study of ordered sulfur overlayers on cu(1 1 1) and ag(1 1 1): Influence of the adsorbate coverage* Surface Science **602**, 906 (2008).

[194] P. C. Rusu, G. Giovannetti, C. Weijtens, R. Coehoorn, and G. Brocks, *First-principles study of the dipole layer formation at metal-organic interfaces* Phys. Rev. B **81**, 125403 (2010).

[195] M. Kiguchi, G. Yoshikawa, and K. Saiki, *Temperature and thickness dependence of molecular orientation of ?-sexithienyl on cu(111)* J. Appl. Phys. **94**, 4866 (2003).

[196] J. Tersoff and D. R. Hamann, *Theory and application for the scanning tunneling microscope* Phys. Rev. Lett. **50**, 1998 (1983).

[197] H. S. Kaufman, I. Fankuchen, and H. Mark, *Structure of cyclo-octatetraene* Nature **161**, 165 (1948).

[198] T. J. Katz, *The cycloöctatetraenyl dianion* Journal of the American Chemical Society **82**, 3784 (1960).

[199] P. G. Wenthold, D. A. Hrovat, W. T. Borden, and W. C. Lineberger, *Transition-state spectroscopy of cyclooctatetraene* Science **272**, 1456 (1996).

[200] C. Nacci, J. Lagoute, X. Liu, and S. Fölsch, *Conformational switching of single 1,5-cyclooctadiene molecules on si(001) induced by inelastic electron tunneling* Phys. Rev. B **77**, 121405 (2008).

[201] C. Nacci, S. Fölsch, K. Zenichowski, J. Dokić, T. Klamroth, and P. Saalfrank, *Current versus temperature-induced switching in a single-molecule tunnel junction: 1,5 cyclooctadiene on si(001)* Nano Letters **9**, 2996 (2009).

[202] J. V. Barth, H. Brune, G. Ertl, and R. J. Behm, *Scanning tunneling microscopy observations on the reconstructed au(111) surface: Atomic structure, long-range superstructure, rotational domains, and surface defects* Phys. Rev. B **42**, 9307 (1990).

[203] Y. Wang, N. S. Hush, and J. R. Reimers, *Simulation of the* Au(111)-$(22 \times \sqrt{3})$ *surface reconstruction* Phys. Rev. B **75**, 233416 (2007).

[204] E. Kawabe, H. Yamane, R. Sumii, K. Koizumi, Y. Ouchi, K. Seki, and K. Kanai, *A role of metal d-band in the interfacial electronic structure at organic/metal interface: Ptcda on au, ag and cu* Organic Electronics **9**, 783 (2008).

[205] F. Muinoz, A. H. Romero, J. Mejía-López, and J. L. Morán-López, *Monoatomic and dimer mn adsorption on the au(111) surface from first principles* Phys. Rev. B **83**, 205423 (2011).

[206] S. Bornemann, O. Šipr, S. Mankovsky, S. Polesya, J. B. Staunton, W. Wurth, H. Ebert, and J. Minár, *Trends in the magnetic properties of fe, co, and ni clusters and monolayers on ir(111), pt(111), and au(111)* Phys. Rev. B **86**, 104436 (2012).

[207] M. Elbing, R. Ochs, M. Koentopp, M. Fischer, C. von Hänisch, F. Weigend, F. Evers, H. B. Weber, and M. Mayor, *A single-molecule diode* Proceedings of the National Academy of Sciences of the United States of America **102**, 8815 (2005).

[208] I. Díez-Pérez, J. Hihath, Y. Lee, L. Yu, L. Adamska, M. A. Kozhushner, I. I. Oleynik, and N. Tao, *Rectification and stability of a single molecular diode with controlled orientation* Nat. Chem. **1**, 635 (2009).

[209] C. Dimitrakopoulos and P. Malenfant, *Organic thin film transistors for large area electronics* Advanced Materials **14**, 99 (2002).

[210] V. C. Sundar, J. Zaumseil, V. Podzorov, E. Menard, R. L. Willett, T. Someya, M. E. Gershenson, and J. A. Rogers, *Elastomeric transistor stamps: Reversible probing of charge transport in organic crystals* Science **303**, 1644 (2004).

[211] M. Urdampilleta, S. Klyatskaya, J.-P. Cleuziou, M. Ruben, and W. Wernsdorfer, *Supramolecular spin valves* Nature Materials **10**, 502 (2011).

[212] L. Zhu, K. L. Yao, and Z. L. Liu, *Molecular spin valve and spin filter composed of single-molecule magnets* Applied Physics Letters **96**, 082115 (pages 3) (2010).

[213] S. Barraza-Lopez, K. Park, V. García-Suárez, and J. Ferrer, *First-principles study of electron transport through the single-molecule magnet* mn_{12} Phys. Rev. Lett. **102**, 246801 (2009).

[214] A. Lodi Rizzini, C. Krull, T. Balashov, J. J. Kavich, A. Mugarza, P. S. Miedema, P. K. Thakur, V. Sessi, S. Klyatskaya, M. Ruben, et al., *Coupling single molecule magnets to ferromagnetic substrates* Phys. Rev. Lett. **107**, 177205 (2011).

[215] N. Atodiresei, P. H. Dederichs, Y. Mokrousov, L. Bergqvist, G. Bihlmayer, and S. Blügel, *Controlling the magnetization direction in molecules via their oxidation state* Phys. Rev. Lett. **100**, 117207 (2008).

[216] K. Miyajima, M. B. Knickelbein, and A. Nakajima, *Stern−gerlach study of multidecker lanthanide−cyclooctatetraene sandwich clusters* The Journal of Physical Chemistry A **112**, 366 (2008).

[217] K. Xu, J. Huang, S. Lei, H. Su, F. Y. C. Boey, Q. Li, and J. Yang, *Efficient organometallic spin filter based on europium-cyclooctatetraene wire* The Journal of Chemical Physics **131**, 104704 (pages 6) (2009).

[218] K. Tao, V. S. Stepanyuk, P. Bruno, D. I. Bazhanov, V. V. Maslyuk, M. Brandbyge, and I. Mertig, *Manipulating magnetism and conductance of an adatom-molecule junction on a metal surface: An ab initio study* Phys. Rev. B **78**, 014426 (2008).

[219] D. Wegner, private communication.

[220] B. Újfalussy, L. Szunyogh, P. Bruno, and P. Weinberger, *First-principles calculation of the anomalous perpendicular anisotropy in a co monolayer on au(111)* Phys. Rev. Lett. **77**, 1805 (1996).

[221] N. Atodiresei, V. Caciuc, P. Lazić, and S. Blügel, *Engineering the magnetic properties of hybrid organic-ferromagnetic interfaces by molecular chemical functionalization* Phys. Rev. B **84**, 172402 (2011).

[222] U. Gradmann, M. Przybylski, H. Elmers, and G. Liu, *Ferromagnetism in the thermodynamically stable monolayer fe(110) on w(110), coated by ag* Applied Physics A **49**, 563 (1989).

[223] H. J. Elmers, J. Hauschild, H. Höche, U. Gradmann, H. Bethge, D. Heuer, and U. Köhler, *Submonolayer magnetism of fe(110) on w(110): Finite width scaling of stripes and percolation between islands* Phys. Rev. Lett. **73**, 898 (1994).

[224] U. Gradmann, J. Korecki, and G. Waller, *In-plane magnetic surface anisotropies in fe(110)* Applied Physics A **39**, 101 (1986).

[225] H. Elmers and U. Gradmann, *Magnetic anisotropies in fe(110) films on w(110)* Applied Physics A **51**, 255 (1990).

[226] H. J. Elmers, T. Furubayashi, M. Albrecht, and U. Gradmann, *Analysis of magnetic anisotropies in ultrathin films by magnetometry in situ in uhv (invited)* Journal of Applied Physics **70**, 5764 (1991).

[227] H. J. Elmers, J. Hauschild, H. Fritzsche, G. Liu, U. Gradmann, and U. Köhler, *Magnetic frustration in ultrathin fe films* Phys. Rev. Lett. **75**, 2031 (1995).

[228] M. Bode, O. Pietzsch, A. Kubetzka, and R. Wiesendanger, *Shape-dependent thermal switching behavior of superparamagnetic nanoislands* Phys. Rev. Lett. **92**, 067201 (2004).

[229] X. Qian and W. Hübner, *First-principles calculation of structural and magnetic properties for fe monolayers and bilayers on w(110)* Phys. Rev. B **60**, 16192 (1999).

[230] X. Qian and W. Hübner, *Ab initio magnetocrystalline anisotropy calculations for fe/w(110) and fe/mo(110)* Phys. Rev. B **64**, 092402 (2001).

[231] D. Spišák and J. Hafner, *Diffusion of fe atoms on w surfaces and* Fe/W *films and along surface steps* Phys. Rev. B **70**, 195426 (2004).

[232] T. Andersen and W. Hübner, *Substrate effects on surface magnetism of* Fe/W(110) *from first principles* Phys. Rev. B **74**, 184415 (2006).

[233] A. T. Costa, R. B. Muniz, J. X. Cao, R. Q. Wu, and D. L. Mills, *Magnetism of an fe monolayer on w(110)* Phys. Rev. B **78**, 054439 (2008).

[234] D. Sander, R. Skomski, C. Schmidthals, A. Enders, and J. Kirschner, *Film stress and domain wall pinning in sesquilayer iron films on w(110)* Phys. Rev. Lett. **77**, 2566 (1996).

[235] O. Pietzsch, A. Kubetzka, M. Bode, and R. Wiesendanger, *Real-space observation of dipolar antiferromagnetism in magnetic nanowires by spin-polarized scanning tunneling spectroscopy* Phys. Rev. Lett. **84**, 5212 (2000).

[236] N. Weber, K. Wagner, H. J. Elmers, J. Hauschild, and U. Gradmann, *Nanoscale spatial switching of magnetic anisotropy in pseudomorphic fe(110) on w(110)* Phys. Rev. B **55**, 14121 (1997).

[237] H. J. Elmers, J. Hauschild, and U. Gradmann, *Onset of perpendicular magnetization in nanostripe arrays of fe on stepped w(110) surfaces* Phys. Rev. B **59**, 3688 (1999).

[238] M. Heide, G. Bihlmayer, and S. Blügel, *Dzyaloshinskii-moriya interaction accounting for the orientation of magnetic domains in ultrathin films: Fe/w(110)* Phys. Rev. B **78**, 140403 (2008).

[239] D. Sander, A. Enders, C. Schmidthals, D. Reuter, and J. Kirschner, *Mechanical stress and magnetism of ferromagnetic monolayers* Surface Science **402–404**, 351 (1998).

[240] R. Decker, J. Brede, N. Atodiresei, V. Caciuc, S. Blügel, and R. Wiesendanger, *Atomic-scale magnetism of cobalt-intercalated graphene* Phys. Rev. B **87**, 041403 (2013).

[241] G. A. Mulhollan, R. L. Fink, J. L. Erskine, and G. K. Walters, *Local spin correlations in ultrathin fe/w(100) films* Phys. Rev. B **43**, 13645 (1991).

[242] J. Chen and J. L. Erskine, *Surface-step-induced magnetic anisotropy in thin epitaxial fe films on w(001)* Phys. Rev. Lett. **68**, 1212 (1992).

[243] R. Wu and A. J. Freeman, *Magnetic properties of fe overlayers on w(001) and the effects of oxygen adsorption* Phys. Rev. B **45**, 7532 (1992).

[244] X. Qian and W. Hübner, *Symmetry and substrate effects on magnetic interactions from first principles: A comparison between fe/w(100) and fe/w(110)* Phys. Rev. B **67**, 184414 (2003).

[245] A. Kubetzka, P. Ferriani, M. Bode, S. Heinze, G. Bihlmayer, K. von Bergmann, O. Pietzsch, S. Blügel, and R. Wiesendanger, *Revealing antiferromagnetic order of the fe monolayer on w(001): Spin-polarized scanning tunneling microscopy and first-principles calculations* Phys. Rev. Lett. **94**, 087204 (2005).

[246] L. M. Sandratskii, E. Şaşıoğlu, and P. Bruno, *Exchange interactions and néel temperature of a fe monolayer on w(001): A first-principles study* Phys. Rev. B **73**, 014430 (2006).

[247] M. Bode, E. Y. Vedmedenko, K. von Bergmann, A. Kubetzka, P. Ferriani, S. Heinze, and R. Wiesendanger, *Atomic spin structure of antiferromagnetic domain walls* Nature Materials **5**, 477 (2006).

[248] M. Dion, Phd thesis, Rutgers University (2004).

[249] D. C. Langreth, M. Dion, H. Rydberg, E. Schröder, P. Hyldgaard, and B. I. Lundqvist, *Van der waals density functional theory with applications* International Journal of Quantum Chemistry **101**, 599 (2005).

[250] K. Berland, Licentiate thesis, Department of Microtechnology and Nanoscience, MC2, Chalmers (2009).

[251] J. F. Dobson, in *Fundamentals of Time-Dependent Density Functional Theory*, edited by M. Marques, N. Maitra, F. Nogueira, E. Gross, and A. Rubio (Springer-Verlag Berlin Heidelberg, 2012), vol. 837 of *Lecture Notes in Physics*, chap. 22.

[252] M. Lein, J. F. Dobson, and E. K. U. Gross, *Toward the description of van der waals interactions within density functional theory* Journal of Computational Chemistry **20**, 12 (1999).

[253] M. B. Torres and L. C. Balbás, *Linear response to spin-dependent and spin-independent fields of alkali metal clusters* Journal of Physics: Condensed Matter **12**, 4365 (2000).

[254] J. S. Kim and K. Yi, *Spin-resolved dielectric functions of spin-polarized electrons* Journal of Korean Physical Society **51**, 111 (2007).

[255] O. A. Vydrov and T. V. Voorhis, *Improving the accuracy of the nonlocal van der waals density functional with minimal empiricism* The Journal of Chemical Physics **130**, 104105 (pages 7) (2009).

[256] O. A. Vydrov and T. Van Voorhis, *Dispersion interactions from a local polarizability model* Phys. Rev. A **81**, 062708 (2010).

[257] R. Resta, *Electrical polarization and orbital magnetization: the modern theories* Journal of Physics: Condensed Matter **22**, 123201 (2010).

[258] X. Gonze, P. Ghosez, and R. W. Godby, *Density-polarization functional theory of the response of a periodic insulating solid to an electric field* Phys. Rev. Lett. **74**, 4035 (1995).

[259] R. M. Martin and G. Ortiz, *Functional theory of extended coulomb systems* Phys. Rev. B **56**, 1124 (1997).

[260] D. Vanderbilt, *Nonlocality of kohn-sham exchange-correlation fields in dielectrics* Phys. Rev. Lett. **79**, 3966 (1997).

[261] L. C. Balbás, J. L. Martins, and J. M. Soler, *Evaluation of exchange-correlation energy, potential, and stress* Phys. Rev. B **64**, 165110 (2001).

[262] J. A. White and D. M. Bird, *Implementation of gradient-corrected exchange-correlation potentials in car-parrinello total-energy calculations* Phys. Rev. B **50**, 4954 (1994).

[263] V. Caciuc, N. Atodiresei, M. Callsen, P. Lazić, and S. Blügel, *Ab initio and semi-empirical van der waals study of graphene–boron nitride interaction from a molecular point of view* Journal of Physics: Condensed Matter **24**, 424214 (2012).

[264] R. A. Aziz, *A highly accurate interatomic potential for argon* The Journal of Chemical Physics **99**, 4518 (1993).

[265] R. Zacharia, H. Ulbricht, and T. Hertel, *Interlayer cohesive energy of graphite from thermal desorption of polyaromatic hydrocarbons* Phys. Rev. B **69**, 155406 (2004).

Acknowledgements

First I want to express my Gratitude to Prof. Dr. Stefan Blügel for the opportunity to work on my PhD thesis in the inspiring environment of the famous Peter Grünberg Institut at the Forschungszentrum Jülich. Many great scientists are attracted for working or presenting their results here, which together with his enthusiasm for science and support for young scientists creates the perfect boundary conditions for learning and doing science.

I am very grateful to Prof. Dr. Arne Lüchow for being the second referee of my thesis.

I would like to thank Dr. Nicolae Atodiresei for co-supervising and proof reading my thesis. I owe him my deepest thanks for integrating me into the molecular spintronics team, the neverending input of new ideas, discussions about results and constantly encouraging me to present my work apart from this thesis in talks and articles.

I thank Dr. Vasile Caciuc for in-depth help with the programming related part of the thesis, for many discussions about the results and proof reading of my thesis.

Many thanks go to all members of the institute for providing a hospitable and inspiring working environment. Among them I would especially like to thank Ute Winkler. Without her finishing a PhD thesis in time while dealing with often unforeseen administrative challenges would not be possible. Also in particular I would like to thank Dr. Konstantin Rushchanskii, Dr. Ivetta Slipukhina, Dr. Nikolai Kiselev, Dr. Shigeru Tsukamoto and Dr. Daria Popova for the enjoyable time we spent together.

I would like to acknowledge my longer term office mates Matthias C. D. T. Müller and Rico Friedrich for a productive working atmosphere and frequently joining discussions about whatever was written to the whiteboard.

I thank my family and friends for giving me courage and strength throughout the three years of writing the thesis.

Publications

Parts of this thesis and results from this thesis have been published already or are submitted for publication. The status of each article is indicated.

1. M. Callsen, V. Caciuc, N. Kiselev, N. Atodiresei, and S. Blügel, *"Magnetic hardening induced by nonmagnetic organic molecules"*,
   Phys. Rev. Lett. **111**, 106805 (2013).
   Selected as an *Editor's Suggestion* and featured in a Viewpoint in Physics **6**, 96 (2013). (http://link.aps.org/doi/10.1103/PhysRevLett.111.106805)

2. H. Harutyunyan, M. Callsen, T. Allmers, V. Caciuc, S. Blügel, N. Atodiresei, and D. Wegner, *"Hybridisation at the organic-metal interface: a surface-scientific analogue of Hückel's rule?"*,
   Chem. Commun. **49**, 5993 (2013).

3. V. Caciuc, N. Atodiresei, M. Callsen, P. Lazić, and S. Blügel, *"Ab initio and semi-empirical van der Waals study of graphene–boron nitride interaction from a molecular point of view"*,
   J. Phys.: Condens. Matter **24**, 424214 (2012).

4. M. Callsen, N. Atodiresei, V. Caciuc, and S. Blügel, *"Semiempirical van der Waals interactions versus ab initio nonlocal correlation effects in the thiophene-Cu(111) system"*,
   Phys. Rev. B **86**, 085439 (2012).

Schriften des Forschungszentrums Jülich
Reihe Schlüsseltechnologien / Key Technologies

Band / Volume 79
Development of a relativistic full-potential first-principles multiple scattering Green function method applied to complex magnetic textures of nano structures at surfaces
D. Bauer (2014), 193 pp
ISBN: 978-3-89336-934-8

Band / Volume 80
Identifizierung von artifiziellen Liganden eines in Nanodiscs inkorporierten integralen Membranproteins
M. Pavlidou (2014), 106 pp
ISBN: 978-3-89336-942-3

Band / Volume 81
Interdomain Functional Dynamics of Phosphoglycerate Kinase Studied by Single-Molecule FRET
M. Gabba (2014), v, 179 pp
ISBN: 978-3-89336-943-0

Band / Volume 82
Silizium Nanoribbon Feld-Effekt Transistoren zur Kopplung an elektroaktive Zellen
M. Jansen (2014), xvi, 181 pp
ISBN: 978-3-89336-944-7

Band / Volume 83
Microscopic description of the inverse Faraday effect at subpicosecond time scales
D. Popova (2014), 183 pp
ISBN: 978-3-89336-962-1

Band / Volume 84
Neutron Scattering
Lectures of the JCNS Laboratory Course held at Forschungszentrum Jülich and at the Heinz Maier-Leibnitz Zentrum Garching
edited by Th. Brückel, G. Heger, D. Richter, G. Roth and R. Zorn (2014),
ca. 360 pp
ISBN: 978-3-89336-965-2

Band / Volume 85
Neutron Scattering
Experiment Manuals of the JCNS Laboratory Course held at Forschungszentrum Jülich and at the Heinz Maier-Leibnitz Zentrum Garching
edited by Th. Brückel, G. Heger, D. Richter, G. Roth and R. Zorn (2014),
ca. 195 pp
ISBN: 978-3-89336-966-9

Schriften des Forschungszentrums Jülich
Reihe Schlüsseltechnologien / Key Technologies

Band / Volume 86
Development and Characterization of a Microfluidic Magnetic Oscillation Reactor for Enzymes
D. Jussen (2014), xxi, 131 pp
ISBN: 978-3-89336-974-4

Band / Volume 87
Submolecular imaging with single particle atomic force sensors
G. Kichin (2014), 140 pp
ISBN: 978-3-89336-976-8

Band / Volume 88
Multiscale Multimodel Simulation of Micromagnetic Singularities
C. Andreas (2014), xix, 188 pp
ISBN: 978-3-89336-983-6

Band / Volume 89
***Ab initio* description of transverse transport due to impurity scattering in transition-metals**
B. C. Zimmermann (2014), 164 pp
ISBN: 978-3-89336-985-0

Band / Volume 90
Ladungstransport durch Graphenschichten und GaAs-Nanodrähte untersucht mit einem Multispitzen-Rastertunnelmikroskop
S. Korte (2014), 96 pp
ISBN: 978-3-89336-990-4

Band / Volume 91
6th Georgian-German School and Workshop in Basic Science
A. Kacharava (Ed.) (2014), CD
ISBN: 978-3-89336-991-1

Band / Volume 92
Ab initio investigations of π-conjugated-molecule-metal interfaces for molecular electronics and spintronics
M. Callsen (2014), viii, 155 pp
ISBN: 978-3-89336-992-8

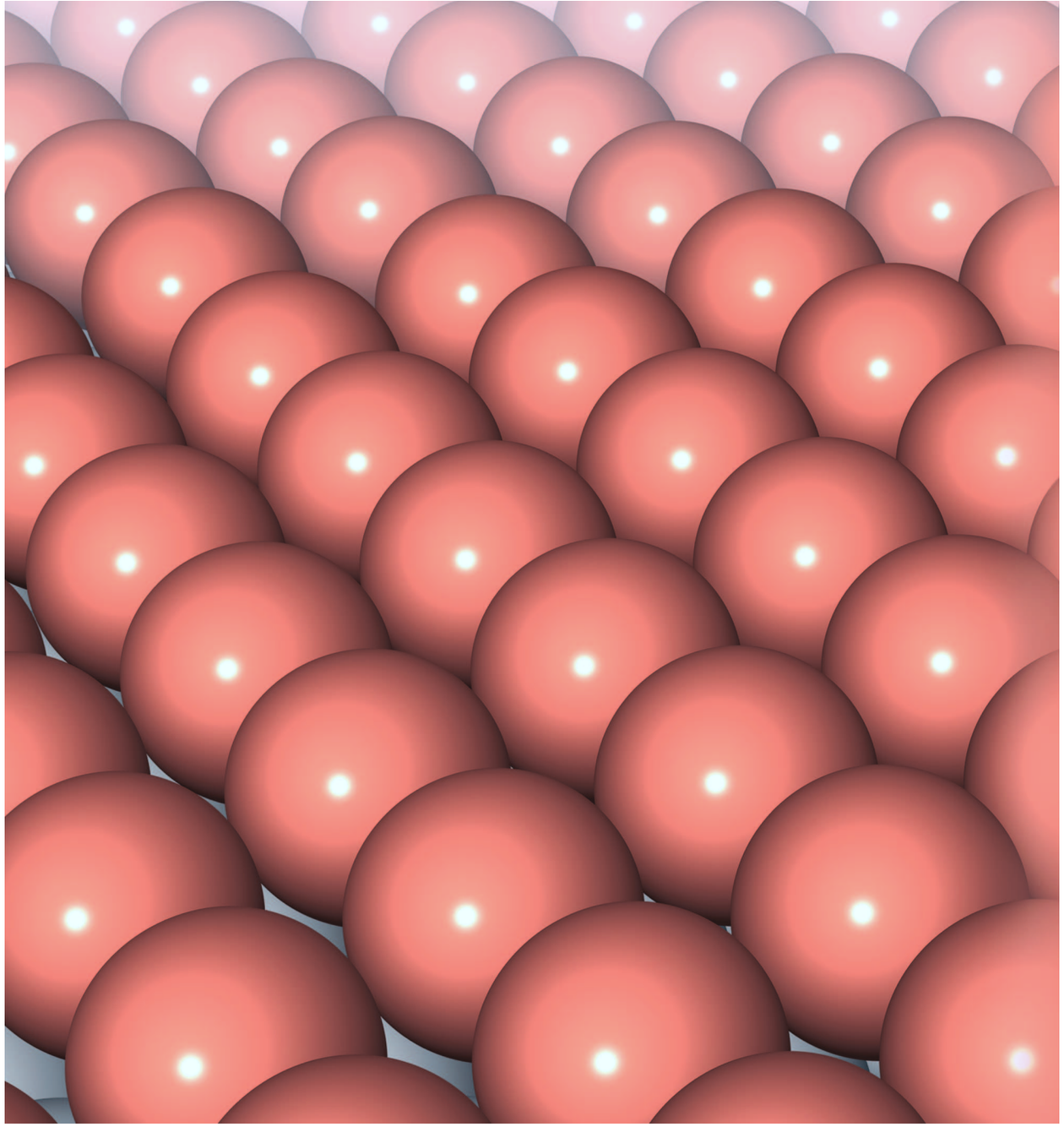

Schlüsseltechnologien / Key Technologies
Band / Volume 92
ISBN 978-3-89336-992-8

JÜLICH
FORSCHUNGSZENTRUM